KATHOLIEKE UNIVERSITEIT LEUVEN
FACULTEIT INGENIEURSWETENSCHAPPEN
DEPARTEMENT ELEKTROTECHNIEK
Kasteelpark Arenberg 10, 3001 Leuven (Heverlee)

SIGNAL PROCESSING AND CLASSIFICATION FOR MAGNETIC RESONANCE SPECTROSCOPIC DATA WITH CLINICAL APPLICATIONS

Anca Ramona Croitor Sava

Jury:

Prof. dr. ir.	xxx, president
Prof. dr. ir.	S. Van Huffel, promoter
Dr.	D.M. Sima, co-promoter
Prof. dr	U. Himmelreich
Prof. dr. ir.	D. Vandermeulen
Prof. dr.	A.-M. De Meyer
Prof. dr.	A. Heerschap (RUMCN Nijmegen)
Prof. dr.	B. Celda (UVEG Valencia)
Dr. ir.	D. Graveron-Demilly (INSA Lyon)

Dissertation presented in partial fulfillment of the requirements for the degree of Doctor in Engineering

November 2011

© Katholieke Universiteit Leuven – Faculty of Engineering
Kasteelpark Arenberg 1/2200, B-3001 Leuven (Belgium)

Alle rechten voorbehouden. Niets uit deze uitgave mag worden vermenigvuldigd en/of openbaar gemaakt worden door middel van druk, fotocopie, microfilm, elektronisch of op welke andere wijze ook zonder voorafgaande schriftelijke toestemming van de uitgever.

All rights reserved. No part of the publication may be reproduced in any form by print, photoprint, microfilm or any other means without written permission from the publisher.

D/2011/X/X
ISBN X

Abstract

Over the past decades, Magnetic Resonance Imaging (MRI) has taken a leading role in the study of human body and it is widely used in clinical diagnosis. *In vivo* and *ex vivo* Magnetic Resonance Spectroscopic (MRS) techniques can additionally provide valuable metabolic information as compared to MRI and are gaining more clinical interest. The analysis of MRS data is a complex procedure and requires several preprocessing steps aiming to improve the quality of the data and to extract the most relevant features before any classification algorithm can be successfully applied.

In this thesis a new approach to quantify magnetic resonance spectroscopic imaging (MRSI) data and therefore to obtain improved metabolite estimates is proposed. Then, an important part is focusing on improving the diagnosis of glial brain tumors which are characterized by an extensive heterogeneity since various intratumoral histopathological properties such as viable tumor cells, necrotic tissue and infiltration with normal tissue can be identified in the tumor region. For a reliable diagnosis of the glial tumor type and grade this thesis proposes a first screening between these intratumoral histopathological properties. To this aim, cluster analysis and several blind source separation methods are tested on *ex vivo* HR-MAS and *in vivo* MRSI data. Moreover, several approaches to fuse multimodal information coming from MRI, MRSI and HR-MAS for the classification of glial brain tumors are considered.

MRS techniques are nowadays successfully considered for the analysis of body fluids. A pilot research to study the amniotic fluid from fetuses with congenital diaphragmatic hernia using high resolution MRS spectroscopy is proposed.

Nomenclature

Ala	Alanine
ALS	Alternating least squares algorithms
AF	Amniotic fluid
AMARES	Advanced method for accurate, robust and efficient spectral fitting
ANOVA	Analysis of variance
AQSES	Automated quantitation of short echo time MRS spectra
BOLD	Blood-oxygenation-level dependent
BSS	Blind source separation
CAMNS	Convex analysis of mixtures of non-negative sources
CBTRUS	Central Brain Tumor Registry of the United States
CCA	Canonical correlation analysis
Cho	Choline
CDH	Congenital diaphragmatic hernia
CNS	Central nervous system
CRB	Cramer-Rao bounds
Cr	Creatine
CSF	Cerebrospinal fluid
CSI	Chemical shift imaging
CT	Computed tomography
dB	Decibels
DSS	Decision support system
DTI	Diffusion tensor imaging
DWI	Diffusion-weighted imaging
ECC	Eddy current correction
FD	Frequency domain
FIDDLE	Free induction decay deconvolution for lineshape enhancement
FETO	Fetoscopic endoluminal tracheal occlusion
FFT	Fast Fourier transform
FID	Free induction decay
FIR	Finite impulse response
FLAIR	Fluid attenuated inversion recovery
FLENI	Fundacion para la Lucha contra las Enfermedades Neurologicas de la Infancia
fMRI	Functional MRI
FOV	Field of view
GAMMA	General approach to magnetic resonance mathematical analysis
Gd	Gadolinium
GE	General Electric
Glc	Glucose
Gln	Glutamine
Glu	Glutamate

Glx	Glutamate + Glutamine
Gly	Glycine
GPCho	Glycerophosphocholine
GUI	Graphical user interface
HSVD	Hankel singular value decomposition
HLSVD	Hankel Lanczos singular value decomposition
HLSVD-PRO	HLSVD with partial reorthogonalization
HR-MAS	High-resolution magic angle spinning
ICA	Independent component analysis
ICM	Iterated conditional modes
K-NN	K-nearest neighbor
KL	Krzanowski and Lai index
Lac	Lactate
LCModel	Linear combination of model spectra
LDA	Linear discriminant analysis
Lip	Lipid
LS-SVM	Least squares support vector machine
Myo	Myo-inositol
MM	Macromolecule
MP-FIR	Maximum phase finite impulse response
MR	Magnetic resonance
MRI	Magnetic resonance imaging
MRS	Magnetic resonance spectroscopy
MRSI	Magnetic resonance spectroscopic imaging
ms	Milliseconds
MSE	Mean squared error
NAA	N-acetyl-aspartate
NLLS	Nonlinear least squares
nICA	Non-negative ICA
NMR	Nuclear magnetic resonance
NMR-SCOPE	NMR spectra calculation using operators
NNMF	Non-negative matrix factorization
NNMFSC	Non-negative matrix factorization with sparsity constraints
PCA	Principal component analysis
PCho	Phosphocholine
PCr	Phosphocreatine
PD	Proton density
Pdf	Probability density function
PET	Positron emission tomography
PRESS	Point-resolved spectroscopy
ppm	Parts per million
RMSE	Relative mean-squared error
QUALITY	Quantification improvement by converting lineshapes to the Lorentzian type
QUECC	QUALITY and eddy current correction
QUEST	Quantitation based on quantum estimation
RBF	Radial basis function

RF	Radio frequency
RMSE	Root mean squared error
RUMCN	Radboud University Medical Center Nijmegen
rTO	Reversal of tracheal occlusion
SNR	Signal-to-noise ratio
SSR	Sum of squared residuals
STEAM	Stimulated echo acquisition mode
SPID	Simulation package based on in vitro databases
SVD	Singular value decomposition
SVM	Support vector machine
SW	Spectral width
T	Tesla
Tau	Taurine
TE	Echo time
TR	Repetition time
TO	Tracheal occlusion
tCho	Total choline
tCr	Total creatine
UVEG	Universitat de Valencia-Estudi General
VARPRO	Variable projection
WHO	World Health Organization
VOI	Volume of interest

Contents

Abstract

Nomenclature

Contents

1. Introduction 1
1.1 Goals of the thesis 1
1.2 Magnetic resonance 2
1.2.1. Basic concepts of magnetic resonance 2
1.2.2 *In vivo* nuclear magnetic resonance 7
1.2.3 Magnetic resonance imaging 8
1.2.4 Magnetic resonance spectroscopy 9
1.2.5 Magnetic resonance spectroscopic imaging 12
1.2.6 *Ex vivo* nuclear magnetic resonance 13
1.3 Nuclear magnetic resonance for clinical applications 15
1.3.1 Brain tumors and nuclear magnetic resonance 15
1.3.2 Pregnancy and nuclear magnetic resonance 22
1.4 Organization of the thesis 25
1.5 Personal contribution and research partners 28
1.6 Conclusions 30

2. Signal processing and preprocessing 31
2.1 Preprocessing methods..... 31
2.1.1 SNR improvement 32
2.1.2 Frequency alignment 33
2.1.3 Phase correction 33
2.1.4 Eddy current correction 34
2.1.5 Lineshape correction 34
2.1.6 Water filtering 34
2.1.7 Signal normalization 35
2.1.8 Baseline correction 36
2.2 Metabolite extraction methods 37
2.2.1 Feature extraction 37
2.2.2 Extraction of features with biomedical information 38
2.2.3 Peak integration 38
2.2.4 Model-based methods 40

2.2.5 AQSES 42
2.2.6 QUEST 45
2.2.7 LCModel 47
2.2.8 Quantification of multivoxel MRSI data 48
2.2.9 Extraction of features using statistical criteria 50
2.3 Conclusions 52

3. Pattern recognition methods in MRS 53
3.1 Supervised classification 53
3.1.1 K-nearest neighbor 53
3.1.2 Linear discriminant analysis 54
3.1.3 Support vector machines 54
3.1.4 Canonical correlation analysis 55
3.2. Unsupervised classification 57
3.2.1 Cluster analysis in MRS 57
3.2.2 Blind signal separation 58
3.2.3 Non-negative matrix factorization 58
3.2.4 Independent component analysis 59
3.2.5 Convex analysis of mixtures of non-negative sources 61
3.3 Performance measures 62
3.3.1 Krzanovski-Lai 62
3.3.2 The weighted inter-intra index 63
3.3.3 Silhouette index 64
3.3.4 Homogeneity index 64
3.3.5 Kruskal-Wallis index 65
3.3.6 Tukey multiple comparison 66
3.4 Software 67
3.5 Fusion of several MR modalities 67
3.6 From MRSI to nosologic imaging 69
3.7 Conclusions 70

4. AQSES-MRSI for the quantification of MRSI data using spatial information 71
4.1 Introduction 71
4.2 The proposed method 73
4.2.1 Modalities of exploiting spatial information 73
4.3 Experimental results using simulations and real-life examples 78
4.3.1 Simulation experiments 79
4.3.2 *In vivo* MRSI studies 81
4.4 Results 83
4.4.1 AQSES-MRSI performance 81
4.4.2 The effect of including spatial prior knowledge when analyzing MRSI data 85
4.5 Discussion 92

4.6 Conclusions 94

5. Classification of HR-MAS signals for Tumor tissue typing in adult human gliomas 95
5.1 Introduction 95
5.2 Materials 97
5.2.1 HR-MAS data acquisition 97
5.2.2 HR-MAS data preprocessing 98
5.2.3 Histological analysis 99
5.3 Methods 99
5.4 Correlation with histopathology 101
5.5 Results 102
5.6 Discussion 107
5.7 Conclusions 113

6. Non-negative blind source separation techniques for brain tumor tissue typing 114
6.1 Application to ex vivo HR-MAS spectroscopy 114
6.1.1 Introduction 114
6.1.2 Materials 116
6.1.3 Methods 117
6.1.4 Application to HR-MAS 119
6.1.5 Results 121
6.1.6 Discussion 126
6.2 Application to *in vivo* MRSI data 130
6.2.1. Introduction 130
6.2.2 Data 130
6.2.3 Methods 131
6.2.4 Results 132
6.3 Conclusions 136

7. Fusing *in vivo* and *ex vivo* NMR for brain tumor classification 137
7.1 Introduction 137
7.2. Materials 139
7.2.1 Tumor data description 139
7.2.2 Harmonization of multimodal data 140
7.3 Methods 142
7.3.1 Model-based CCA 142
7.3.2 Simulation study 144
7.3.3 *In vivo* study 146
7.4 Results 147
7.4.1 Simulation study 147

7.4.2 *In vivo* study 149
7.5 Discussion 150
7.6 Conclusions 152

8. High resolution ^{1}H NMR spectroscopy for the classification of fetuses with congenital diaphragmatic hernia 153
8.1 Introduction 153
8.2 Materials 154
8.3 Methods 155
8.4 Results and discussion 156
8.5 Conclusions 158

9. Conclusions and future work 159
9.1 Summary 159
9.2 Future work 161

Bibliography 163

Publication list 188

Curriculum vitae 192

Chapter 1

Introduction

This chapter presents the aim of the thesis and introduces the general concepts of magnetic resonance (MR) with the focus on different MR modalities that will be considered for the medical applications presented in this thesis, i.e., brain tumors diagnosis and pregnancy follow up. Section 1.2 is a theoretical overview of MR principle, in vivo MR modalities, such as MR imaging, MR spectroscopy, MR spectroscopic imaging, and ex vivo MR techniques. Section 1.3 provides medical background about brain tumors and abnormal pregnancies such as congenital diaphragmatic hernia and underlines the potential of MR techniques for the diagnosis of these clinical conditions. An overview of the organization of the thesis and the personal contributions are summarized in Sections 1.4 and 1.5, respectively.

1.1 Goals of the thesis

The aim of the research presented in this thesis is to improve and facilitate the clinical application of nuclear magnetic resonance (NMR) techniques by the development of advanced methods for the interpretation and preprocessing of magnetic resonance (MR) data as well as for developing advanced classifiers with adaptive learning abilities combining segmentation, signal processing and pattern recognition. The study is performed in close collaboration with clinical centers from Belgium and abroad. The direct application in diagnosis, prognosis and treatment selection of adult's brain tumor is foreseen. Another clinical application is the prediction of certain complicated pregnancies using NMR techniques.

This thesis approaches mainly two topics in the (pre)processing of NMR data: the quantification and classification. These topics are closely related since for obtaining reliable classifiers, firstly relevant information needs to be extracted from the acquired data. Quantification represents the process of deriving physically meaningful parameter estimates from the given data. In this thesis, the focus is mainly on the quantification of magnetic resonance spectroscopic imaging (MRSI) data for which retrieving accurate estimates of the most relevant metabolite concentrations remains a challenging problem due to low spectral quality as a result of the spatial/spectral trade-off. For improving the accuracy of quantification of MRSI data the available spatial information is exploited.

The second main goal of the thesis is the development of classifiers that can assist clinicians for an improved diagnosis and prognosis of brain tumors. This part of the thesis focuses on glial brain tumors which are characterized by a very high heterogeneity. One purpose is to identify histopathological tissue properties using unsupervised classification methods such as cluster analysis and blind source separation (BSS). A first screening of these tumors at a microscale level can further help in an improved diagnosis and prognosis of the tumor type and grade. Moreover, using BSS methods the contribution (abundance) of each tumor tissue to the profile of the spectra is predicted. Another important aspect which is studied is the combination of different sources of NMR data, by fusing *in vivo* MRSI, *ex vivo* high resolution magic angle spinning (HR-MAS) spectroscopic information and magnetic resonance imaging (MRI) for improved diagnosis. For the visualization of the obtained classification results nosologic images are considered.

Furthermore, automatic feature reduction methods in combination with automated classification techniques are considered for analyzing whether the metabolic information contained in the amniotic fluid (AF) coming from fetuses presenting congenital diaphragmatic hernia (CDH) reflects the status of the disease.

1.2 Magnetic resonance

NMR technique is based on the quantum-physical property of certain nuclei called *spin*. This concept was first introduced by Wolfgang Pauli in 1924. Then, in 1938 NMR was first described and measured in molecular beams by Isidor Rabi. In 1946, Felix Bloch and Edward Mills Purcell extended the technique to liquids and solids. They noticed that some magnetic nuclei, such as ^{1}H and ^{31}P, when placed in a magnetic field of strength specific to the identity of the nuclei, can absorb radio frequency (RF) energy. When this absorption occurs, the nucleus is referred to as being *in resonance*. Different atomic nuclei within a molecule resonate at different RFs for the same magnetic field strength. This enables the measurement of the chemical and structural information that characterizes a certain molecule.

1.2.1 Basic concepts of magnetic resonance

An NMR experiment usually involves:

A. A spin

Nucleons (protons and neutrons composing the atomic nucleus) have the quantum property of *spin*. As quantum mechanics describes, the *spin* is characterized by a nuclear spin quantum number, *I*, which depends on the number of protons and neutrons. If the number of both protons and neutrons is even then there is no overall *spin* and *I=0*. If the number of neutrons plus the number of protons is odd, then the nucleus has a half-integer spin (*i.e. I = 1/2, 3/2,*

5/2). If the number of neutrons and the number of protons are both odd, then the nucleus has an integer spin (*i.e. I = 1, 2, 3*).
The non-zero spin can be represented as a rotational motion of the particle around its own axis, see Figure 1.1.a. This motion generates a small magnetic field and therefore the nucleus possesses a magnetic moment, μ , which is proportional to its spin, *I*:

$$\mu = \frac{\gamma I h}{2\pi} \tag{1.1}$$

where γ is the *gyromagnetic ratio constant* and has a different value for each nucleus. *h* is *Planck's constant*.

B. A static external field B_0

In the absence of an external magnetic field the individual spins have random orientations, summing up to a null overall magnetization, see Figure 1.1.a. On the other hand, if an external magnetic field, B_0, is applied, then the individual spins align with B_0 and therefore enter an angular momentum state. The nuclei will thus rotate about their own axis and precess about the axis of the magnetic field B_0 with a frequency f_0 (called the *Larmor frequency*) which is a function of the strength of the magnetic field and the *gyromagnetic ratio*

$$f_0 = \frac{\gamma B_0}{2\pi} \tag{1.2}$$

For any given nucleus, the total number of angular momentum states, *m*, also called magnetic quantum number, is *2I + 1*. Thus, an *I =1/2* nucleus can only give rise to two distinct angular momentum states, an *I=1* nucleus to three and so on.

Our discussion will be further limited to *I = 1/2* nuclei. They are of particular interest for NMR since they can take two spin states and therefore their analysis is fairly straightforward. Nuclei of *I=1/2,* when placed in an external magnetic field B_0 will align along or against B_0, see Figure 1.1.b. When the nuclei align along the external field, B_0, their magnetic moment *m* = *+1/2* and the nuclei are described as being in low energy spin state. An alignment opposed to the field (*m = -1/2*) is less stable as it matches with a higher energy spin state.

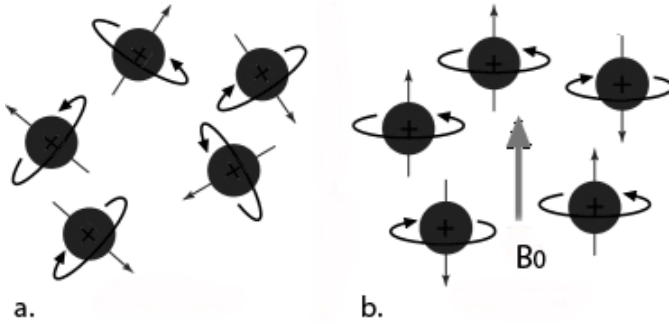


Figure 1.1 *Atomic nuclei spinning around their own axis and having random orientations in the absence of an external magnetic field, see a. In b. spinning nuclei align up parallel or opposed to the applied field, B_o.*

The energy corresponding to each possible state *m* is calculated as:

$$E_m = \gamma m B_0 \frac{h}{2\pi} \tag{1.3}$$

As the energy is proportional to the strength of the magnitude of the external field, the two spin states have the same energy when the external field is zero, but differ as the field increases, see Figure 1.2.

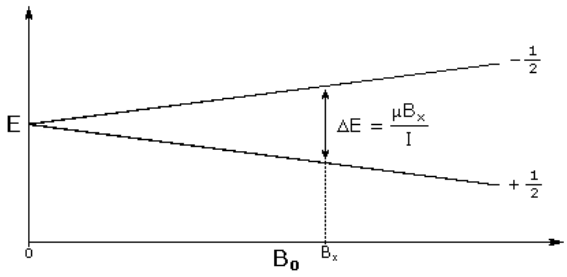


Figure 1.2 *Magnetic field strength effect on NMR energies.*

Thus, at a field equal to B_x there will be a difference in energy between the low and high energy level. The energy difference, also called transition energy, is computed as:

$$\Delta E = E_{-1/2} - E_{+1/2} = \gamma B_x \frac{h}{2\pi} \tag{1.4}$$

In relation to (1.1) ΔE becomes:

$$\Delta E = \frac{\mu B_x}{I} \tag{1.5}$$

This means that ΔE is increased for an increased magnetic field, B_x, and for relatively large *gyromagnetic ratio*.

C. An oscillating magnetic field

It is possible to make a nucleus flip from the more stable energy spin state to the less stable one, by supplying exactly the right amount of energy. To induce transitions between these states an oscillating magnetic field, B_1, is applied in a plane perpendicular to the direction of the static external field B_0. Since the B_0 field is much stronger than the B_1 field, by many orders of magnitude, if the B_1 field was static, it would have a negligible influence onto the spins. However, the B_1 field is not static but rotates about the axis of B_0 with a frequency that is very similar to the precession frequency of the spins, see Eq. 1.2. The radio frequency (RF) of the oscillating field matches the energy difference between the nuclear spin levels in a constant magnetic field of appropriate strength. During RF pulses, spins which are exactly on resonance (e.g., whose precession frequency is equal to the precession frequency of the B_1 field) react to the B_1 field. They will start to precess about the axis of the B_1 field until the B_1 field is turned off again, see Figure 1.3.

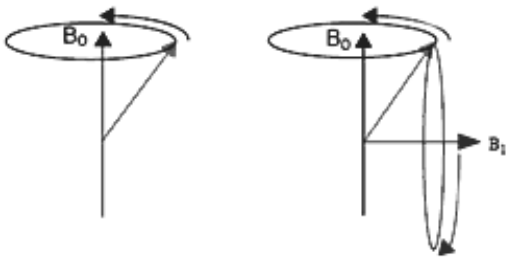


Figure 1.3 *Precession of a nuclear moment in a B_0 field (left). During the RF pulse the nucleus precesses about the axis of B_1 (right).*

NMR explores the property of some nuclei to absorb this RF energy and therefore to enter the state of being *in resonance*. The NMR signal originates from the process of energy absorption when making a transition from the lower energy state to the higher energy state, and energy emission when making a transition from the higher energy state to the lower energy state. The signal intensity is thus proportional to the amount of energy absorbed and emitted by the nuclei and therefore depends also on the population difference between the states.

The relative population of the states can be calculated from the Boltzmann distribution:

$$N^{-1/2} \Big/ N^{+1/2} = e^{\Delta E / kT} \tag{1.6}$$

where k is the *Boltzman constant* and T the temperature.

The number of spins in the low energy level $N^{+1/2}$ is slightly larger than the number of spins in the high energy level $N^{-1/2}$. This causes a net magnetic field or a net magnetization in the direction of B_0. Still, the energy difference in NMR experiments is very small and therefore the signal is weak, thus a low signal-to-noise ratio (SNR) is registered. To overcome this problem, the RF pulse is usually repeated several times to allow the signals to be averaged and thus better identified from the background noise.

Important parameters in NMR

Except the three main elements which define an NMR experiment (the spin, the external magnetic field and the oscillating magnetic field), for a successful NMR signal acquisition, one has to consider other important parameters:

- the type of nucleus to be considered in an NMR experiment. From all nuclei that possess a spin, the most commonly used in NMR are presented in Table 1.1. They are chosen due to their high *gyromagnetic ratio* and consequently stronger magnetic moment, but also due to their abundance in the human body.

Table 1.1 *The most common nuclei considered in NMR experiments*

Nucleus	γ	**Human body elemental abundance in %**
^{1}H	2.675	10
^{13}C	0.673	18
^{19}F	2.517	0.01
^{15}N	-0.271	3
^{31}P	1.083	1.2

- the temperature, T, of the sample. As shown in Eq. 1.6, a higher intensity is obtained for higher B_0 and smaller T. During *ex vivo* HR-MAS experiments the samples are usually kept at 4 ^0C. Yet, for *in vivo* experiments, the temperature is fixed (body temperature) and therefore it does not allow the manipulation of T for improving the measurements.

- the echo time (TE). It represents the time in milliseconds between the application of the 90◦ pulse and the peak of the echo signal in spin echo and inversion recovery pulse sequences.

- the repetition time (TR). TR is the amount of time between successive pulse sequences.

- the pulse sequence. The most common pulse sequences considered during MRS experiments are Point-RESolved Spectroscopy (PRESS) which uses a 90◦ excitation and two 180◦ refocusing pulses and STimulated Echo Acquisition Mode (STEAM) when all three pulses are 90◦ excitation pulses.

While the parameters above can be chosen as part of the NMR acquisition protocol, the following parameters characterize the effect of the experiment:

- the relaxation time T_1, also called the spin-lattice relaxation time, is the time constant characterizing the exponential return to equilibrium of the longitudinal magnetization (i.e., component of the magnetization vector in the direction of B_0) after the RF pulse.

- the time constant T_2, which describes the exponential return to equilibrium of the transverse magnetization (i.e., component of the magnetization vector in the plane perpendicular to B_0), and is called the spin-spin relaxation time.

How exactly these parameters influence an NMR experiment will be detailed in the following sections.

1.2.2 *In vivo* nuclear magnetic resonance

Nowadays, NMR represents a sophisticated and powerful analytical tool that has found a variety of applications in many disciplines of scientific research, medicine, as well as in various industries. NMR is in particular commonly considered in medical sciences since it is extremely versatile and allows for a whole family of modalities that record different anatomical and physiological properties that can help in the diagnosis and prognosis of various clinical states. With conventional magnetic resonance imaging (MRI) techniques, which focus on anatomical abnormalities, we can essentially assess the anatomy of the tissue under investigation. More functional magnetic resonance (MR) methods are currently being

explored such as MR of vessel perfusion, of water diffusion and of metabolite distribution. In contrast to the first two, which rely on the measurement of the signal intensity of water, the latter is able to assess abnormal signal levels of certain metabolites in, e.g., brain tumors. This technique is called MR spectroscopy (MRS) and, if performed in a multi-voxel approach, magnetic resonance spectroscopic imaging (MRSI). The latter allows the spatial mapping of metabolites and is more and more used in the clinical MR community. All of the above mentioned *in vivo* NMR techniques are non-invasive.

1.2.3 Magnetic resonance imaging

The most common NMR application is MRI. Unlike other clinical imaging modalities, such as for example Computer Tomography (CT) or Positron Emission Tomography (PET), which make use of potentially harmful radiations (X-rays), MRI has the advantage that the images are acquired completely non-invasively without causing any radiation risk to the patient. In addition it provides very good contrast between the different soft tissues of the body and therefore is very useful in studying the brain, the heart, muscles and cancers.

MRI is based on the detection of water signals. The resonance signals from the protons (^{1}H) of water molecules and their spatial origin are recorded. The basic principles of NMR, which are presented in Section 1.1.1, are applied to generate *in vivo* images of the tissues under investigation. In addition gradients corresponding to a linear variation in the magnetic field as a function of distance need to be applied to the external magnetic field B_0. If no gradient is applied, we would acquire a signal that corresponds to the global response of all spins and no information about their spatial distribution would be available.
By applying different *TE* and *TR*, which are basic parameters of an MRI image acquisition, MRI images of different contrast can be obtained. On a T_2-weighted MRI (longer *TE* and *TR*), tissues containing water and/or fluid are bright and fat-containing tissues appears dark. With T_1-weighted images (short *TR* and *TE*) mostly the reverse of a T_2-weighted MRI is obtained. Proton density (PD) images, based on a long *TR* and a short *TE*, reveal changes coming from differences in the amount of available spins (^{1}H nuclei in water). In addition, contrast agents, such as Gadolinium (Gd), can be injected intravenously to enhance tissue characteristics on the obtained MRI image.

Beyond these conventional MR sequences, more advanced MR modalities can be used to obtain specialized MRI scans. By considering an additional RF pulse and additional manipulation of the magnetic gradients, a T_2-weighted sequence can be converted to a Fluid Attenuated Inversion Recovery (FLAIR**)** sequence. On FLAIR images the signal from fluids appears dark, but edema tissue remains bright. Thus they are often used in brain imaging to bring out the periventricular hyperintense lesions, such as multiple sclerosis plaques. By measuring the diffusion of water molecules in biological tissues we can obtain diffusion MRI. Two known applications for diffusion MRI are diffusion-weighted imaging (DWI) which is highly sensitive to the changes occurring in the lesion and diffusion tensor imaging (DTI) which is very helpful for fiber directions detection and connectivity of

different regions in the brain inspection. Functional MRI (fMRI) measures signal changes in the brain that occur due to neural activity. For example, the BOLD (blood-oxygenation-level dependent) effect is used to visualize brain activity. Although the specialized MRI scans are very interesting for research, they are nowadays not commonly used for clinical purposes. In Figure 1.4, several MRI images of different contrast as well as specialized MRI scans are acquired for a patient diagnosed with glioblastoma.

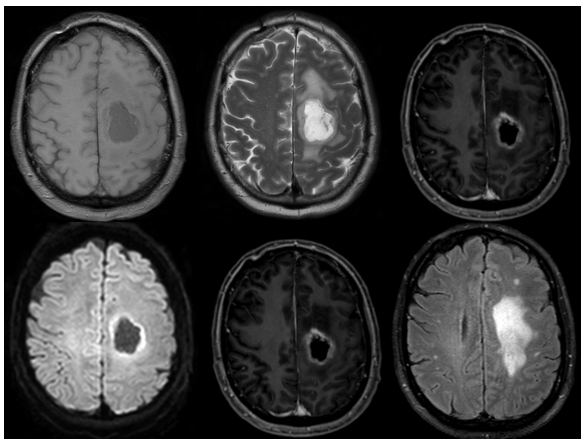


Figure 1.4: *Brain MRI data. From top-left to bottom-right: T_1-weighted MRI without contrast, T_2-weighted MRI, T_1-weighted MRI with contrast, FLAIR, DWI with sequence b-value of 0 mm/s² , DWI with sequence b-value of 1000 mm/s².*

1.2.4 Magnetic resonance spectroscopy

Another very interesting NMR application is MRS. Compared to conventional MRI, which essentially assesses anatomy, MRS reveals biochemical information on the tissue under investigation by exhibiting peaks at frequencies specific to the molecular composition of the tissue under investigation. It measures the levels of different metabolites in the tissue, which appear in the MR signal as a spectrum of resonances that correspond to different metabolites. The technology can thus provide relevant information on cancer metabolism, as well as on the biochemical composition of body fluids.

What makes it possible to separate between the resonances coming from different metabolites is the shielding effect also called chemical shift. When an atom is placed in a magnetic field, its electrons circulate about the direction of the applied magnetic field creating a small magnetic field which opposes the externally applied field, creating the chemical shift effect. The effective magnetic field at the nucleus of the same atom, but belonging to a different molecule, is slightly different, by a fraction σ , and is described by:

$$B_{eff} = B_0 \cdot (1 - \sigma) \tag{1.7}$$

where σ is called the *shielding constant.* Its value is specific to each atom in a molecule and depends on the electrical environment of a nucleus. The chemical shift effect is seen as if the nuclei's *Larmor frequency* is shifted relative to the reference frequency corresponding to the static field B_0 (i.e., the spectrometer frequency):

$$f_{eff} = \frac{\gamma \cdot (1 - \sigma) \cdot B_0}{2\pi} \tag{1.8}$$

This shift in frequency makes the nuclei from a different chemical environment (molecules) to emit signals with different frequencies. The chemical shift can be expressed in Hz or parts-per-million (ppm). The latter version is commonly preferred because it is independent from the spectrometer frequency. If a metabolite resonates at a certain ppm value for a spectrometer frequency of 63.8 MHz (corresponding to a 1.5 Tesla scanner), it will resonate at the same ppm-value for a spectrometer frequency of 500 MHz. The ppm value of a resonance *M* is defined by:

$$ppm_M = \frac{f_{Hz} 10^6}{f_S} + ppm_{ref} \tag{1.9}$$

where f_{Hz} is the resonance frequency in Hz and f_S is the spectrometer frequency in Hz. ppm_{ref} is the value of the reference resonance. Usually the resonance of water at 4.7 ppm is chosen as reference.

The MRS signal is acquired as a time domain signal and is commonly referred to as free induction decay (FID) signal since it corresponds to a sum of complex-damped exponentially decaying sinusoids. For the ease of visualization and sometimes interpretation the time domain signal can be Fourier transformed into a complex frequency domain signal commonly called spectrum, see Figure 1.5.

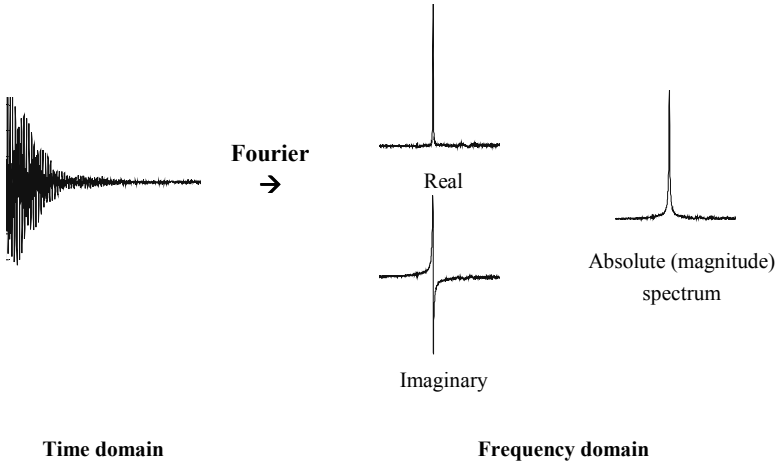


Figure 1.5 *FID signal (left), the real and imaginary parts of the Fourier transformed signal (middle) and the magnitude spectrum (right).*

Each metabolite has a specific spectrum, see Figure 1.6, and the MRS spectrum coming from the tissue under investigation will thus be a linear combination of spectra from individual metabolites present in the tissue. The intensity of each metabolite signal is proportional to the number of nuclei that contribute to it and this allows one to quantify the concentration of each metabolite in the spectra.

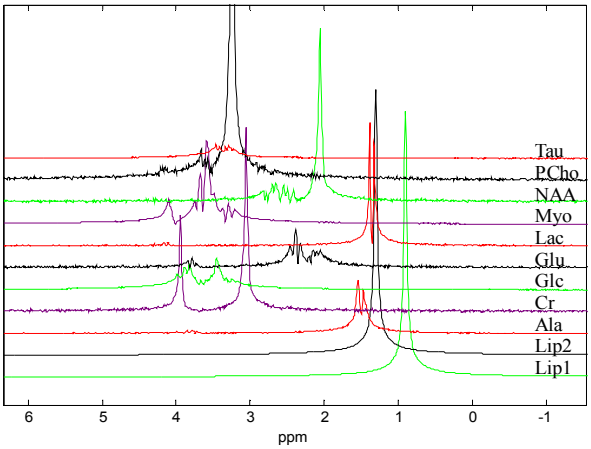


Figure 1.6 *Set of metabolite profiles measured in vitro at 3T, PRESS sequence, TE = 35ms. The magnitude spectra are visualized.*

The metabolic resolution of the MRS spectra can be influenced by the acquisition parameters such as the *TE* value. Short *TEs* (*e.g.*, 30 ms) provide more metabolic information than long *TEs* (*e.g.*, 135 ms), see Figure 1.7, but a low SNR. To improve the SNR, usually repeated measurements are consecutively performed and the final signal is the average of all measured signals. As mentioned in Section 1.1.1, the static magnetic field also has a high influence on the signal, i.e., for high magnetic field the spectral resolution is increased.

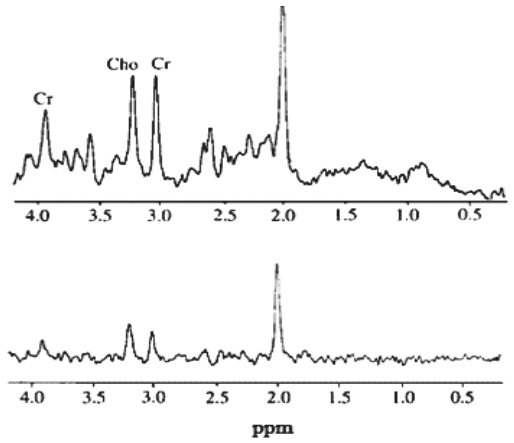


Figure 1.7 *^{1}H MR spectra at, from top to bottom, short echo time (TE=35 ms) and long echo time (TE=272 ms). Figure adapted from Devos, 2005.*

1.2.5 Magnetic resonance spectroscopic imaging

When MRS is performed as a multi-voxel approach, MRSI images are obtained, see Figure 1.8. The technique, also called Chemical Shift Imaging (CSI) or multi-voxel spectroscopy is a combination of both MRI and MRS, since it allows the spatial mapping of metabolites. This makes it more and more popular in the clinical MR community.

The MRSI signals are acquired in a two dimensional or three dimensional matrix with, for example, dimensions 16x16(x16) or 32x32(x32). To get enough signal intensity from the metabolites, the MRSI voxel size is much bigger than those used in MRI reaching usually 1cm x 1cm (x 1cm).

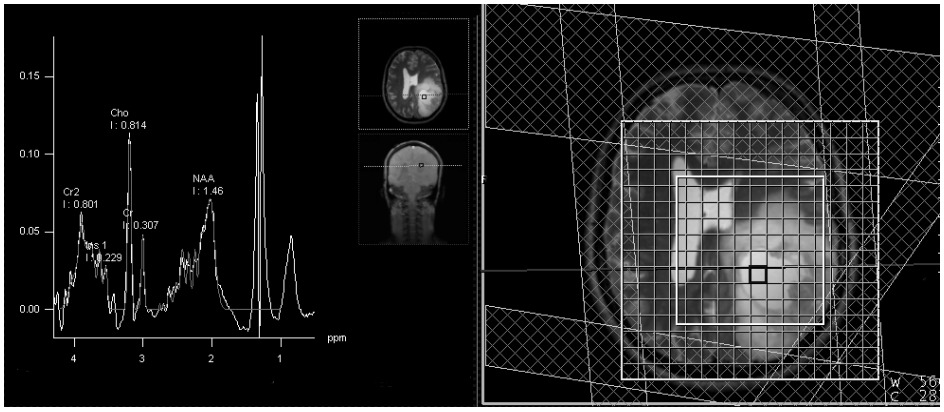


Figure 1.8 *Screenshot from the 3T Siemens scanner for in vivo brain MRSI data acquired using a semi-laser, 30ms TE sequence. The data are provided by Radboud University Medical Center Nijmegen (RUMCN).*

1.2.6 *Ex vivo* nuclear magnetic resonance

Ex vivo high resolution NMR techniques, although invasive, are of high clinical interest in the study of body tissue and fluids since they provide an accurate biochemical profile of human tissue and therefore are very helpful for the assignment of well-resolved spectra of cellular metabolites. When performing *in vivo* MRS spectroscopy one may be confronted with poor spectral resolution and overlapping peaks due to B_0 inhomogeneity, dipolar coupling, T_2 relaxation and low field strength. Moreover *in vivo* NMR experiments at very high field strengths are not possible due to technical limitation and for patient safety. When the NMR experiment is performed *ex vivo* higher field strength can be used, which yields higher spectral resolution, better spectral quality and therefore many of the limitations of *in vivo* MRS are overcome. Compared to *in vivo* MRS, *ex vivo* high resolution NMR techniques allow the identification of a large number of metabolites, see Figure 1.9.

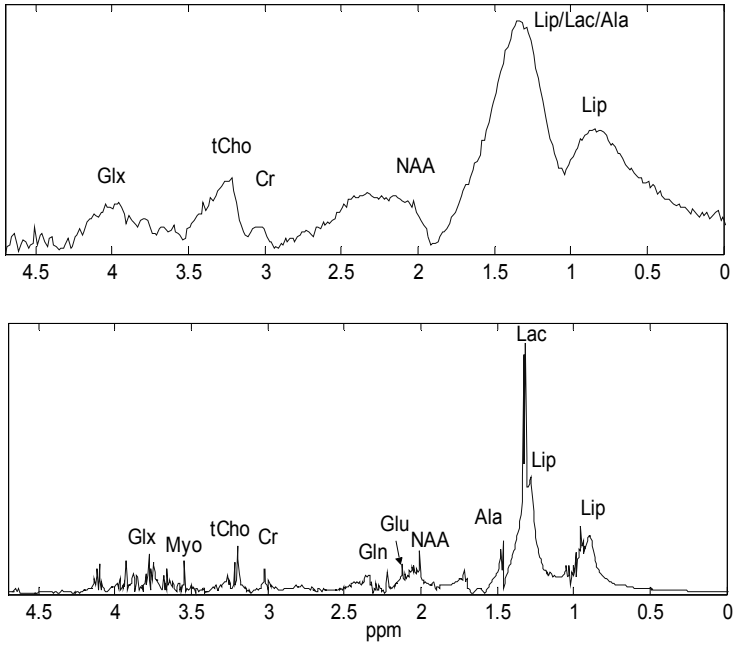


Figure 1.9 *Comparison between an in vivo MRSI spectrum (top) and an ex vivo spectrum (bottom) for glioblastoma brain tissue in the area of interest [0.25, 4.5] ppm. The spectra were obtained by computing the mean over several cases.*

***Ex vivo* HR-MAS**

HR-MAS is an *ex vivo* NMR technique that provides spectra characterized by narrow line widths and high SNR ratios. According to the available literature, it allows the most detailed assignment of biochemical compounds obtained in intact human tissue, in particular in brain tumor tissue. Since a good correlation between *ex vivo* HR-MAS and *in vivo* MRS has been reported (Barton et al., 1999; Opstad et al., 2010), the HR-MAS technique is often considered for improving the interpretation of the metabolic biomarkers that are visible with *in vivo* NMR. Additionally, with *ex vivo* HR-MAS the tissue integrity is mainly conserved (Martínez-Bisbal et al., 2010) and this is an advantage since it allows one to perform, on the same tissue sample, multimodal studies including subsequent genomic, proteomic or histopathological analyses and, therefore, to obtain a direct comparison between all these techniques.

For acquiring HR-MAS spectra, the NMR principles described in Section 1.1.1 are still valid. Specific for this technique is that the sample is placed in a small rotor filled in with a solvent, *e.g.*, D_2O solution. The rotor is then spun at high angular velocities, of a few kHz, and at a certain angle, called *magic angle*, θ_m, with respect to the direction of the static magnetic field, B_0, see Figure 1.10.

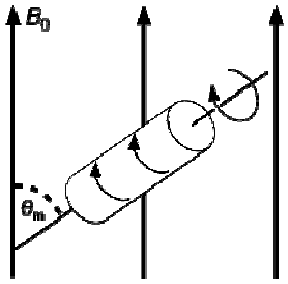


Figure 1.10 *HR-MAS experiment. The sample placed in the scanner rotor is rotating with high frequency inside the main magnetic field (B_0) at magic angle* $\theta_m = \arccos\frac{1}{\sqrt{3}} \approx 54.7^\circ$.

1.3 Nuclear magnetic resonance for clinical applications

NMR techniques have various applications in many medical fields, chemistry, as well as in various industries. In the medical field NMR imaging and spectroscopy are often considered for the diagnosis, prognosis and/or follow up of cancer in different organs (e.g. breast, prostate) and brain (Mueller-Lisse and Scherr, 2007; Callot et al., 2008; Dorrius et al., 2011), pediatric diseases (Dezortova and Hajek, 2008), liver and muscle diseases (Machann et al., 2008) brain diseases (e.g. ischemia, multiple sclerosis, Alzheimer's disease, epilepsy (Frederick et al., 2004; Mader et., 2008; Hajek et al., 2008)) and cardiovascular diseases (den Hollander et at., 2005). Alterations in metabolite concentrations were reported in fluids, such as amniotic fluid (AF), and correlate with the health of the fetus and caring mother (Graca et al., 2007; 2008; 2009). This thesis mainly focuses on the use of NMR techniques in the study of brain tumors and for identifying abnormal pregnancies by AF spectroscopic analysis.

1.3.1 Brain tumors and nuclear magnetic resonance

Brain tumors represent an important challenge in oncology because of their relative high mortality. The World Health Organization (WHO) classification discriminates between different brain tumor types, subtypes and different grades of malignancy (Louis et al., 2007). Additionally, brain tumors are known for their extensive heterogeneity both at the level of tumor type and grade, as well as at a microscale level. These characteristics pose serious difficulties in the diagnosis, prognosis and treatment of brain tumors. Consequently, many

researchers are now focusing on understanding this disease from the metabolomic, genomic and proteomic points of view. NMR techniques can thus play an important role in the diagnosis and prognosis of brain tumors. *In vivo* and *ex vivo* high-resolution MRS techniques are especially interesting since they offer a clinically feasible metabolic assessment, providing significant biochemical information on the molecules of the brain tissue under investigation.

About brain tumors

A brain tumor is an abnormal growth of cells within the brain or the central spinal canal. It is the effect of an abnormal and uncontrolled cell division, either in the brain itself, in the cranial nerves, in the brain envelopes, skull, pituitary and pineal gland.

There are over 120 different types of brain tumors, which make effective treatment complicated. They can be, based on their origin, primary or secondary. The latter refers to those tumors that originate from other organs and spread in the brain and are known as metastatic brain tumors. By behavior brain tumors can be cancerous (malignant) or non-cancerous (benign). Based on which cells are affected we can distinguish meningiomas, which appear in the meninges, the tissue membrane that surrounds the brain and separate the skull from the brain. Brain tumors of the glial cells are called glioma or glial brain tumors. The grade of a tumor reflects the degree of malignancy. Grading is based on how abnormal the cancer cells are and how quickly the tumor is likely to grow and spread. Low grade tumors, such as Grade I and Grade II tumors, grow slowly and rarely spread to other tissues. Still some of these tumors may recur in a higher grade tumor. Grade III tumors are characterized by a fast growth and are likely to spread into nearby normal tissue. Grade IV tumors have a very fast growth and spread. Also, they mostly develop necrosis.

Although a recent statistical report at worldwide level is not publicly available, the CBTRUS (Central Brain Tumor Registry of the United States) reported in 2005 43.800 new cases of brain tumors ("Central Brain Tumor Registry of the United States, Primary Brain Tumors in the United States, Statistical Report, 2005–2006"). This accounted for 1.4 percent of all cancers, 2.4 percent of all cancer deaths, and 20–25 percent of pediatric cancers. CBTRUS also reports that males-females have a 0.67%-0.53% lifetime risk of being diagnosed with a primary malignant brain/central nervous system tumor and 0.48%- 0.39% chance of dying from a brain/central nervous system tumor. Additional statistics can be found from the Statistics from Accelerate Brain Cancer Cure (ABC2) (http://www.abc2.org), the American Cancer Society (http://www.cancer.org/) or the Brain Tumor Society and National Brain Tumor Foundation (http://www.tbts.org/).

The most common primary tumors among adults are the gliomas. They are characterized by an extensive heterogeneity reflected both at the level of the tumor type and grade, as well as at histopathological level since they can present areas with mostly necrotic tissue (dead cells) or a mixture of necrotic tissue and high cellular tumor tissue, see Figure 1.11. Moreover, glial tumors are highly infiltrative. A large part of this thesis is dedicated to the classification of glial brain tumors.

Diagnosis

Generally there is no specific or singular clinical symptom or sign for any brain tumor and the clinicians would typically not be confident to provide a diagnosis after a visual inspection of the patient. Thus, technology plays a very important role in the diagnosis and prognosis of this disease and especially imaging techniques are regularly used. Although the presence of an abnormal tissue growth or the existence of a tumor can be easily detected with the available imaging techniques, commonly the final diagnosis is confirmed by histological examination of tumor tissue samples.

Histology

The histological examination involves a brain biopsy or open surgery and is performed by an expert pathologist. It typically has three stages: interoperative examination of fresh tissue, preliminary microscopic examination of prepared tissues, and follow up examination of prepared tissues after immunohistochemical staining or genetic analysis. The histological examination is performed for the correct prognosis of the brain tumor and therefore for determining the appropriate treatment. Nowadays it is often considered the ground truth for tumor typing and grading and for providing detailed information on the mixture of tissues present in the sample under investigation, as well as the abundance of each tissue, see Figure 1.11. Histopathology has a few consistent drawbacks: it is invasive, time consuming and it only provides local information from the tumor, while tumors are known to be heterogeneous and infiltrative. Thus, there is a very high interest in considering alternative methods for the diagnosis of brain tumor at a level of accuracy similar to histopathology. As a result, *in vivo* NMR spectroscopy is gaining more and more importance in the diagnosis and prognosis of brain tumors.

Treatment

The standard treatments for brain tumors include surgery, radiation therapy, chemotherapy, or the combination of those. The main purpose of all these approaches is to remove or kill the tumor cells, while keeping the normal tissue unaffected. More recently, a new therapy based on Dendritic cell vaccination is tested (Ardon, 2011). For an effective treatment, it is very important to have an accurate diagnosis both in tumor type and malignancy. A correct detection of the contour of the tumor and the possible infiltrative areas is also essential before starting the treatment.

During the surgery the surgeon attempts to remove the entire tumor. Often a partial removal is performed in order not to damage vital brain tissue. In these circumstances the treatment is followed by radiation therapy or chemotherapy. The radiation therapy uses high-powered rays to selectively kill tumor cells. Radiation therapy may be given in two ways: external or internal radiation. An external radiation therapy involves multiple treatments (10 to 30 treatments, depending on the type of tumor). Although for each treatment both healthy and normal tissue is damaged, most of the normal cells can repair the damage within short time, while the tumor tissue cannot. When radiotherapy is performed internally, also called radiosurgery or the Gamma Knife, a computerized calculation is used to focus radiation at the

site of the tumor while minimizing the radiation dose to the surrounding brain. The treatment is given in just one session.

During the chemotherapy special drugs designed to kill tumor cells are administered to the patients. Chemotherapy is usually given in more cycles and each treatment cycle is followed by a recovery period. The drug administration is usually done orally or by injection into a blood vessel or muscle. Intrathecal chemotherapy involving the injection of the drugs into the cerebrospinal fluid is also possible. Recently a direct placement into the tumor cavity has been considered. Chemotherapy is highly toxic and the many side effects and the uncertain outcome of chemotherapy in brain tumors puts this treatment further down the line of treatment options for medical teams.

Brain tumor diagnosis and prognosis using nuclear magnetic resonance

NMR techniques are widely used in the diagnosis and prognosis of brain tumors. Conventional MRI techniques, such as PD, T_1 and T_2 weighted MRI, are routinely considered by clinicians to assess the anatomy and location of the tumor, but they are often not able to characterize the heterogeneous growth of cancer tissue and to identify tumor type or grade. To address these issues, more functional MR methods are currently being explored such as MR of vessel perfusion, of water diffusion and of metabolite distribution. The potential of *ex vivo* and *in vivo* NMR spectroscopy has been lately extensively exploited in the separation between normal brain and brain tumors (Rutter at al., 1995; Howe et al., 2003b), as well as for the characterization of different degrees of malignancy (Negendank at al., 1996; McKnight et al., 2004, 2007; Erb et al., 2008; Opstad et al., 2008a).

To avoid performing expensive histopathological examinations which, due to their invasive nature, are with high risk for the patients, MRSI is currently more and more used in clinical setting in conjunction with anatomical MRI to assess the presence, extent and type of brain tumors. Still, the accuracy of MRSI in differentiating and grading glial brain tumors is limited by the significant variability of *in vivo* spectra as an effect of intra-tumoral heterogeneity (Croitor Sava et al., 2011b). For example, in gliomas one can observe distinct histopathological tissue properties, such as viable tumor cells, necrotic tissue or regions where the tumor infiltrates normal brain.

Ex vivo high resolution NMR techniques are also often considered if one is interested in an accurate biochemical profile of brain tissue, since they are very helpful for the assignment of well-resolved spectra of cellular metabolites (Martinez-Bisbal et al., 2004). In this context, *ex vivo* HR-MAS is seen as a promising complementary NMR technique with potential applications in supporting tumor classification and diagnosis and a good correlation between *ex vivo* HR-MAS and *in vivo* MRS has been reported (Opstad et. al., 2010). Thus, HR-MAS can improve the interpretation of the metabolic biomarkers that are visible with *in vivo* NMR. Additionally, with *ex vivo* HR-MAS the tissue integrity is not extremely damaged (Martinez-Bisbal et al., 2010) and this is an advantage since it allows one to perform, on the same tissue sample, multimodal studies including subsequent genomic, proteomic or histopathological analyses and, therefore, to obtain a direct comparison between all these techniques. Moreover,

HR-MAS can help in predicting the growth characteristic within different regions of a tumor (McKnight et al., 2007), can help in differentiating between glial tumor grades (Erb et al., 2008) and can successfully reveal the status of tumor microheterogeneity (Cheng et al., 2000; Croitor Sava et al., 2011b; 2011c.). To have complete information on the contour of the tumor and the possible infiltrative areas, a first screening between the different intratumoral histopathological tissue properties is essential and would greatly assist in a correct diagnosis and prognosis of brain tumors.

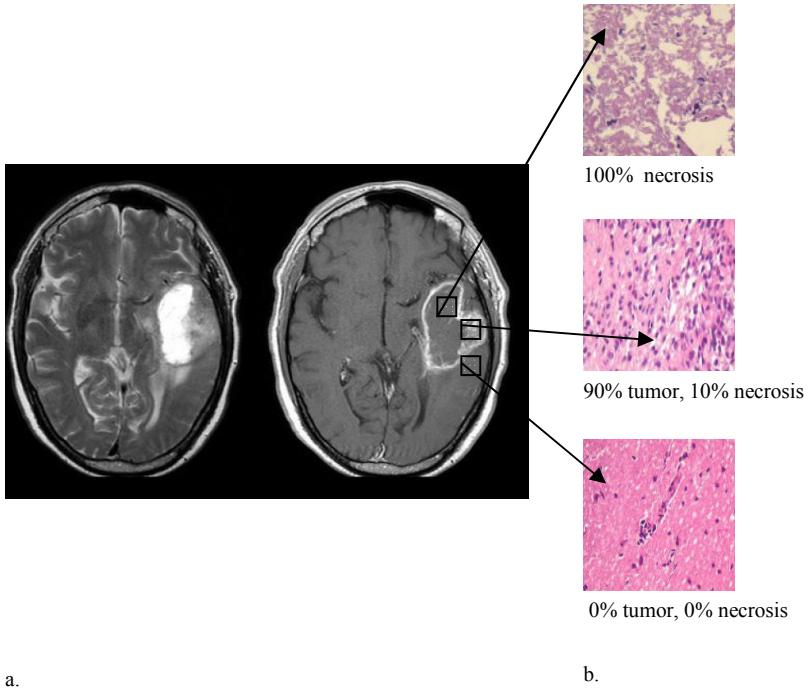


Figure 1.11 *In a. T2 (left) and T1 Gd enhanced (right) MRI images asses the location and size of the tumor and may provide information regarding the presence of necrotic tissue (see T2 MRI). In b. histopathological examination reveals the tumor type and grade and the contributions from different histopathological properties. Figure adapted from (Martinez-Bisbal et al., 2008).*

Metabolic biomarkers

An extensive list with the metabolites present in brain is described in *(*Govindaraju et al., 2000). The metabolites that best discriminate between different types and grades of tumor, as

well as between the different tumor tissue histopathological properties are visualized in Figure 1.12 and described bellow.

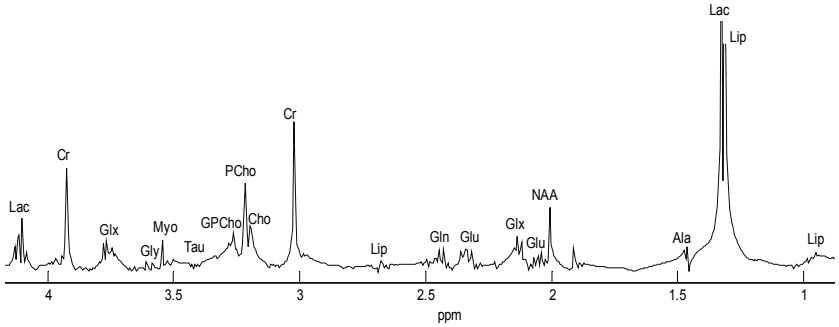


Figure 1.12 *HR-MAS spectra from a patient with high grade glial brain tumor. The most relevant metabolites in differentiating brain tumor are labeled. For Gly and Tau the area where they appear is marked although they are present in very low concentration in this tumor type and therefore not visible.*

Alanine (Ala) has two main resonances at 1.47 ppm and at 3.77 ppm. The first one is clearly detectable with *ex vivo* high resolution MRS techniques, but highly overlaps with the resonances from lipids in low magnetic field *in vivo* MRS measurements. The resonance at 3.77ppm is not visible in *in vivo* experiments *(*Govindaraju et al., 2000*)*. Ala is a biomarker for brain tumors and increased levels have been observed *in vivo* in meningiomas (Manton et al., 1995) and gliomas (Tong et al., 2004).

Creatine (Cr) presents two resonances at 3.03 and 3.9 ppm, respectively. It is a marker of the energetic status of the tissue. Compared with normal brain, Cr is reduced in gliomas and is almost absent in meningiomas, schwannomas and metastases, characteristics that are also observed *ex vivo*. Still, the significance of the Cr decreases in terms of tumor metabolism is not clear (Govindaraju et al., 2000). On the other hand, Cr is typically used as an internal reference due to its stability. In (Tong et al., 2004) the ratio of NAA/Cr was reported as significantly decreased compared to the same ratio in normal brain. The tCho/Cr ratios decrease in high grade gliomas with the malignancy of the tumor due to the low cellularity of high-grade gliomas, which contain a large amount of necrosis, while the ratio tCho/Cr may solve some tumor classification problems in (Majos et al., 2004).

Total Choline (tCho) group includes Choline (Cho), Phosphorylcholine (PCho) and Glycerophospholylcholine (GPCho) which resonate at about 3.22 ppm. tCho is associated with brain tumor progression when present in high concentrations. tCho elevation is thought to be due to accelerated membrane synthesis of rapidly dividing cancer cells. High tCho concentration in tumor regions of metastasis and GBM were found in (Fan et al., 2004),

reflecting increased cellularity during cancer cell growth (Usenius et al., 1994; Tedeschi, 1997; Podo, 1999). tCho group could not be used to differentiate low grade glioma from high grade glioma (Tong, 2004), but can act as a biomarker in differentiating tissue type as suggested in (Croitor Sava et al., 2011b) where it was shown that degradation in the tCho concentrations relates with the tissue heterogeneity. Thus, tCho values are the highest in high cellular tumor regions, relatively high in border regions, but are very low in necrosis.

Lipids (Lips) resonances at 0.9, 1.3 and 2.8 ppm are one of the most reliable markers of tumor progression and in increased concentrations indicate necrosis, which is a histopathological characterization of high grade tumors (Podo et al., 1999). *Ex vivo* studies have further supported this, showing not only a correlation between NMR-visible mobile lipids and percentage of necrosis (Andronesi et al., 2008), but also the presence of mobile lipids in tumors with no necrosis (Tong et al., 2004), while (Cheng et al., 2000) reported that concentrations of mobile lipids correlate linearly with the amount of necrosis. These findings were confirmed in (Croitor Sava et al., 2011b) where it has been shown additionally that the concentrations of lipids in border regions are almost negligible.

Lactate (Lac) presents a doublet at 1.33 ppm and a quartet resonating at 4.09 ppm. Since the latter may overlap with the water resonance (Govindaraju et al., 2000) it is mostly not considered in the metabolic analysis. For the *in vivo* experiments Lac is overlapping with the resonances from lipids while when performing *ex vivo* measurements Lac is more sensitive to external factors such as snap-freezing, the temperature conditions and the effect of organ perfusion with deuterated saline solution. Lac is the end product of anaerobic glycolysis. Although instable and hard to quantify, it is normally present in brain tissue at low concentrations, while in tumors it is often prominent (Govindaraju et al., 2000). In (Cheng et al., 2000) it is reported to correlate with the level of necrosis.

N-acetylaspartate (NAA), whose main resonance is a singlet signal at 2.01 ppm, is regarded as a neuronal marker found only in neurons, and since most brain tumors are of non-neuronal origin, NAA is reduced or absent in tumors (Peeling and Sutherland, 1992). Higher levels of NAA are expected in the border region of the tumor with respect to the active tumor region. NAA acts as a good biomarker for border tissue, but also for separating the necrosis from border tissue and high cellular tissue (Croitor Sava et al., 2011b).

Glycine (Gly) at 3.56 ppm is visible both in *ex vivo* and *in vivo* experiments. For the latter ones, the resonance may overlap with those of myo-inositol. Gly is a simple amino acid that acts as an inhibitory neurotransmitter and antioxidant. It is distributed throughout the brain and central nervous system. The concentrations of Gly are elevated in tumors (Govindaraju et al., 2000).

Glutamine and Glutamate (Gln and Glu) are known to be excitatory neurotransmitters. They present resonances at around 2.04, 2.35 and 3.74 ppm, the latter overlapping with a multiplet of NAA in *in vivo* experiments (Govindaraju et al., 2000). Although they can be quantified separately in *ex vivo* high resolution MRS spectra, they are often considered

together in *in vivo* experiments, being referred as Glx. Glx levels are elevated in highly malignant tumors and meningiomas (Manton et al., 1995).

Myo-inositol (Myo) resonates at 3.56 ppm. It is considered to be essential for cell growth, acting as an osmolite and a storage form for glucose. Alterations in Myo levels were associated with Alzheimer's disease (Zhu et al., 2006) and brain injury (Ross et al., 1998). It is reported absent or low in non-glial tumor like meningioma and in high level in low grade gliomas and astrocytomas (Govindaraju et al., 2000).

Taurine (Tau) resonates at 3.42 ppm. It is an amino acid that is responsible of the osmoregulation and modulation of the action of neurotransmitters. It is high in neonates and decreased in adults. In *in vivo* studies at low magnetic field its resonances overlap with the resonances of Myo and tCho (Govindaraju et al., 2000). Tau can differentiate gliomas from other tumors (Tong et al., 2004).

Among the described metabolites Cho, Cr, NAA, Myo, Glu, Gln, Gly, Lac, Lips, Tau and Ala are often considered for differentiating brain tumor (Howe and Opstad, 2003a), while Lips, NAA, tCho and Cr are biomarkers for tumor microheterogeneity (Cheng et al., 2000; Croitor Sava et al., 2011b).

1.3.2 Pregnancy and nuclear magnetic resonance

The pregnancy follow up, also known as prenatal screening, is a routine examination performed for checking the conditions in a fetus or embryo before it is born. It is of high interest for the parents and clinicians as it enables timely medical or surgical treatment before or soon after birth in case a health problem was detected, gives the parents the chance to "prepare" themselves psychologically, socially, and medically for a baby with a health problem or disability, or even to abort a fetus with a certain diagnosed condition.

For a routine prenatal screening most common non-invasive techniques such as ultrasonography are considered. If the results of the ultrasonography bring questions regarding the health of the fetus or of the mother, a more advanced testing might be necessary. In this situation commonly an amniocentesis is performed to extract a sample from the AF, the substance which surrounds the baby and plays a vital role in the development of internal organs, such as the lungs and kidneys. As organs start to prepare for independent functioning, the baby swallows the AF, filters it through its kidneys and passes it out again as urine. Moreover, some fluid from baby's lungs is also eliminated in the AF. Therefore, the analysis of the AF ca provide valuable prenatal information and can help in the diagnosis of birth defects such as neural tube defects, Down syndrome, chromosome abnormalities, genetic diseases and fetal infections.

About congenital diaphragmatic hernia

Congenital diaphragmatic hernia (CDH) is a birth defect with a birth prevalence of approximately 1 in 4000 (Deprest et al., 2004). It is characterized by a defect in the diaphragm (the thin muscle separating the chest from the abdominal cavity) which allows abdominal organs (intestines, stomach, liver) to protrude into the thorax. The impairment in lung development (pulmonary hypoplasia) that accompanies the diaphragmatic defect is associated with high rates of neonatal mortality and morbidity.

Diagnosis and Prognosis

CDH can be diagnosed by ultrasound during pregnancy. To assess lung size, liver herniation and possible additional malformations, fetal Magnetic Resonance Imaging (MRI) is often part of the CDH follow-up in specialized centers. Up to 30% of babies presenting with isolated CDH do not survive the early weeks of life as postnatal treatment options fall short for severe cases of pulmonary hypoplasia.

Therapy

Nowadays, fetoscopic endoluminal tracheal occlusion (FETO) can be offered to fetuses with severe lung hypoplasia as prenatal therapy in an experimental setting. Blocking the fetus` windpipe with an inflatable balloon (Figure 1.13), hence, entrapping lung liquid and thus increasing intrapulmonary pressure seems to stimulate lung growth and development. Early data comparing fetuses treated by FETO against fetuses only treated postnatally indicates an increased survival for the FETO group.

Treating CDH fetuses using FETO usually comprises two interventions: the insertion of the balloon around 26-30 weeks and the removal of the balloon around 34 weeks. The procedure is nowadays generally performed under combined fetal analgesia and immobilization as well as maternal spinal–epidural anesthesia. Then a thin-walled cannula is inserted under ultrasound-guidance into the amniotic cavity through the abdominal and uterine walls and directed towards the fetal mouth. A purpose-designed fetoscope is inserted via a 3.0-mm sheath and introduced into the trachea to position a detachable balloon between the carina and the vocal cords (see Figure 1.13). As the balloon blocks the fetal airways, it needs to be removed preferably before birth (reversal of tracheal occlusion (rTO). This can be done by an ultrasound-guided needle puncture or a second fetoscopic procedure.

NMR in the diagnosis and prognosis of CDH

Previous studies have shown that the use of magnetic resonance methods can aid in the clinical routine for monitoring pregnancies (McGowan et al., 1993). Compared to the ultrasound technique, which is mostly considered in the routine fetal follow up, with NMR we obtain not only detailed structural, but also biochemical and functional information, which cannot be obtained by ultrasound.

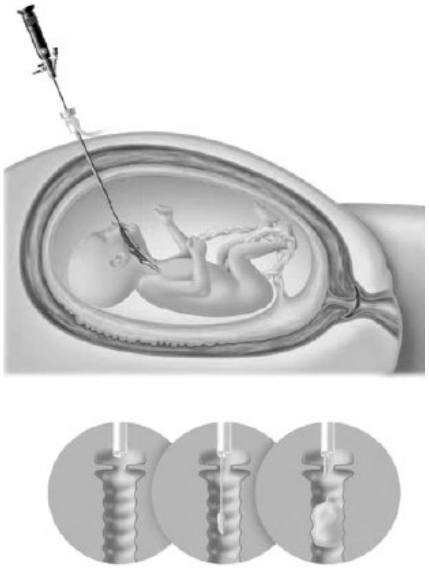


Figure 1.13 *FETO schematic illustration. Figure from (Deprest et al., 2004)*

Fetal MRI is of increasing interest in the diagnosis, prognosis and follow up of abnormal pregnancies. It is an important technique to study fetal lung growth during the second and third trimester. The excellent tissue contrast of MRI allows (Kasprian et al., 2006) to examine the structure of the fetal lung and offers more details on fetal pulmonary pathologies. In CDH, fetal MRI is applied to gain information on lung size, the nature and amount of herniated organs as well as potential further malformations.

Studies on human AF using NMR spectroscopy have shown the correlation between AF metabolites, gestational age, and the health status of the mother and fetuses. Therefore, several metabolites associated with fetal developmental abnormalities have previously been identified by MRS. In Figure 1.14 is illustrated a typical AF spectrum. Metabolic correlations with disorders such as spina bifida (Bock, 1994; Groenen et al., 2004), diabetes (McGowan, 1999), Down syndrome (Bock, 1994), cystic fibrosis (Le Moyec, 1994) and congenital malformations (Graca et al., 2009) were reported. Further information on changes in metabolic patterns related to fetal lung (Pearce et al., 1993; Clifton et al., 2006) and kidney maturation (Bock, 1994) exist. Moreover normative values were suggested for the second and third trimester (Cohen et al., 2009). Recently, high field NMR studies have identified several additional AF metabolites, determined the effects of freeze-thawing, and evaluated long term sample stability at room temperature, −20, and −70◦C (Graca et al., 2007). No studies focusing on the metabolic profile of fetuses with CHD using NMR spectroscopy exist so far.

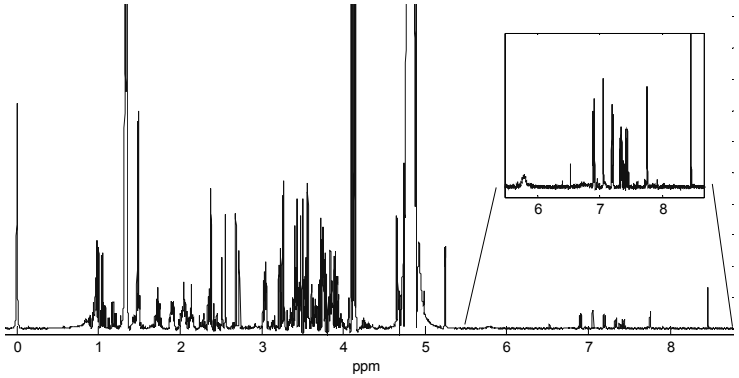


Figure 1.14 *Typical AF spectrum obtained with high resolution NMR spectroscopy.*

1.4 Organization of the thesis

The contents of this thesis is organized in nine chapters structured as follows (see also Figure 1.15).

Chapter 1 presents the basic principles of NMR with focus on different MR modalities (MRI, MRSI, *ex vivo* HR-MAS and high resolution MRS) which are used in the studies of this thesis. The characteristics of each of these modalities are summarized by emphasizing the differences, giving their advantages and limitations. A minimal medical background over brain tumors (statistics, diagnosis tools, treatments, main types of brain tumors) and the follow up of pregnancies based on the analyses of the AF is given. The links between metabolite concentrations and these two clinical conditions are shown. The chapter concludes with the goals of the thesis, gives a chapter-by-chapter overview, and presents the author's personal contributions.

Chapter 2 is an overview of the typical preprocessing and processing steps for MRS signals with focus on the methods used in this thesis in Chapters 4 to 8. It also introduces basic concepts in order to understand the following chapters.

Chapter 3 reviews briefly the pattern recognition methods considered in this thesis. Supervised classification, unsupervised classification and performance measurement methods are presented.

Chapter 4 describes a novel metabolite quantification method for MRSI data, AQSES-MRSI, in which the available spatial information is exploited. A nonlinear least squares algorithm is

proposed. Prior knowledge is included in the form of proximity constraints on the spectral parameters within a grid, optimized starting values and a penalty term that promotes a spatially smooth spectral parameter map. AQSES-MRSI's accuracy on simulated MRSI data with several types of disturbances and on short echo time *in vivo* proton MRSI data is presented. Moreover, AQSES-MRSI performance is compared against several existing quantification methods, AQSES, QUEST and LCModel.

Chapter 5 presents a methodology for characterizing glial brain tumors at a microscale level by identifying distinct histopathological tissue properties, such as viable tumor cells, necrotic tissue or regions where the tumor infiltrates normal brain using *ex vivo* HR-MAS spectroscopy. Cluster analysis on feature sets coming from various metabolites and metabolite ratios is considered for the identification of groups with distinct histopathological tissue properties for each glial tumor type. The statistically significant correlation between the considered feature sets and the predominant histopathological tissue properties is investigated. Representative metabolic tissue models for each histopathological tissue property are extracted. A statistical analysis examining which of the considered input feature values are most sensitive in revealing the predominant histopathological property is performed.

Chapter 6 presents a comparative study where three different blind source separation (BSS) methods: non-negative matrix factorization (NNMF), non-negative independent component analysis (nICA) and convex analysis of mixtures of non-negative sources (CAMNS) are applied on the full magnitude HR-MAS signals and on metabolic features extracted from the spectra. The BSS methods are used for obtaining characteristic profiles for necrosis, high cellular tumor and border tumor tissue, and for providing the contribution (abundance) of each tumor tissue to the profile of the spectra. The study presented in this chapter evaluates which of the considered non-negative BSS methods performs best. Different feature inputs spaces are considered. NNMF is further used also on MRSI data for quantifying the abundance of each intratumoral histopathological tissue property within each MRSI voxel. Nosologic images based on the extracted abundance maps and reflecting the presence of necrosis, viable tumor cells or infiltrations in the MRSI grid are obtained.

Chapter 7 presents a new methodology for investigating the potential and limitations of fusing *in vivo* short echo-time brain MRSI data, HR-MAS data and MRI data to detect brain tumors. A model-based canonical correlation analysis (CCA) algorithm is considered. We present various modalities of combining multimodal information, and we study the effect and the impact of using multimodal information for classifying MRSI brain glial tumor data. Additionally, we analyze which parameters influence our classification results by means of extensive simulation and *in vivo* studies. Special attention is drawn to the possibility of considering HR-MAS information as a complementary dataset when dealing with a lack of MRSI data needed to build a classifier.

Chapter 8 presents a pilot study to identify metabolic differences between the amniotic fluid from fetuses with congenital diaphragmatic hernia (CDH) undergoing temporary tracheal occlusion (TO) or its reversal (rTO) against healthy controls. Several feature reduction

methods are separately considered in combination with automated classification techniques to study the potential of NMR spectroscopy to differentiate CDH.

Chapter 9 is a summary of the main achievements of this thesis and presents a few open problems and their possible solutions for future research.

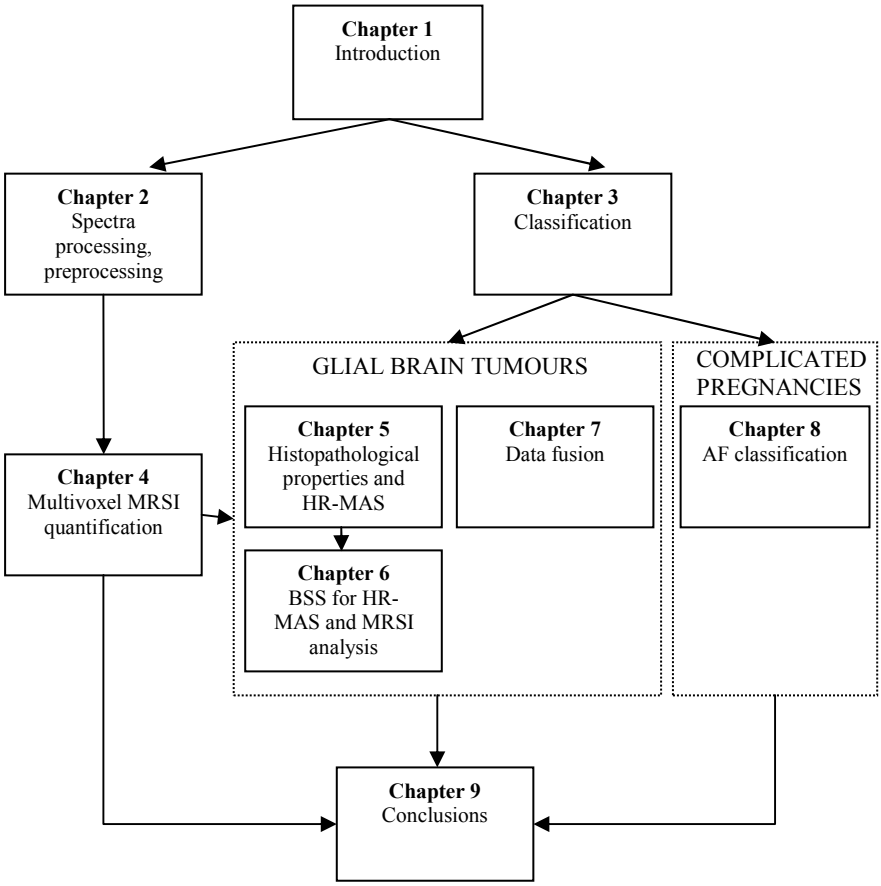


Figure 1.15: *Flowchart of the thesis.*

1.5 Personal contribution and research partners

The scientific work presented in this PhD thesis finds its application in two main clinical case studies: brain tumors and complicated pregnancies follow up.

When classifying brain tumors using MRSI data, the input used by the pattern recognition techniques is usually, due to computational matters, a set of metabolic features extracted from the spectra. Since metabolite concentration estimates from MRSI signals are the input variables for advanced classifiers for tissue type differentiation and tumor recognition, it is clear that reliable quantification results are very important. Therefore, an improved and robust quantification method is proposed for MRSI data, AQSES-MRSI, in which the available spatial information is considered in the form of proximity constraints on the spectral parameters within a grid and optimized starting values. A penalty term that promotes a spatially smooth spectral parameter map is added to the fitting algorithm. The newly proposed approach compares favorably against single-voxel approaches, as well as against the multivoxel approach embedded in the well-known quantification software LCModel (widely used in the NMR community). The method is presented in detail in Chapter 4 of this thesis. The mathematical principles underlying the AQSES-MRSI method are published as a book chapter in *Recent Advances in Optimization and its Applications in Engineering* (Sima et al., 2010). In addition, the method and its performance on *in vivo* and simulated MRSI data are presented in the international journal *NMR in Biomedicine (*Croitor Sava et al., 2011a*)*. This work was done in close collaboration with the Radboud University Medical Centre Nijmegen (RUMCN), Department of Radiology.

The most common brain tumor type, glioma, has a very unfavorable prognosis. The problem that can mostly interfere with a reliable diagnosis and grading of glial brain tumors is the heterogeneity that is reflected both at the level of the tumor type and grade, as well as at a microscale level along with viable tumor cells, necrotic regions or contributions from normal brain tissue. Since it is believed that a first screening between these different intratumoral histopathological tissue properties would greatly assist in correctly diagnosing and prognosing of gliomas, in this thesis the potential of *ex vivo* HR-MAS spectroscopy, in characterizing these properties is further explored. Using advanced statistical methodology applied on sets of metabolite concentrations and metabolite ratios extracted from HR-MAS recordings coming from patients with different grades of glial tumors we show a strong correlation between the histopathological tissue properties and the considered metabolic profiles, regardless of the malignancy grade. The results of this work are presented in Chapter 5 and are published in the journal *Magnetic Resonance in Medicine* (Croitor Sava et al., 2011b). This study was performed in very close collaboration with the Departamento de Química-Física, Facultad de Química, Universitat de Valencia, Valencia, Spain, CIBER-BBN, ISC-III, Universitat de Valencia, Valencia, Spain and Departamento de Patología, Facultad de Medicina, Universitat de Valencia, Valencia, Spain.

The study on intratumoral histopathological tissue properties is further extended through the extraction of characteristic profiles for pure necrosis, high cellular tumor and border tumor tissue, and through the quantification of the contribution (abundance) of each tumor tissue to the profile of the spectra using BSS techniques. The problem is formulated as a non-negative source separation problem using NNMF, nICA and CAMNS. This work is published in the proceedings of *Annual International Conference of the IEEE Engineering in Medicine and Biology Society,* 2010 and an extended study on this topic is submitted as journal paper to the *Journal of Chemometrics*. Furthermore, brain tumor tissue classification of *in vivo* MRSI data can benefit from a similar approach. To this aim we further explore non-negative BSS methods for quantifying the abundance within each MRSI voxel for each intratumoral histopathological tissue property. Additionally, nosologic images are drawn based on the extracted abundance maps, reflecting the presence of necrosis, viable tumor cells or infiltrations in the MRSI grid. An overview of the considered BSS methods and their application to *in vivo* MRSI and *ex vivo* HR-MAS for quantifying intratumoral histopathological tissue properties is presented in Chapter 6. Part of the research presented in Chapters 5 and 6 originates from the involvement in the eTUMOUR project (*Web accessible MR decision support system for brain tumour diagnosis and prognosis, incorporating in vivo and ex vivo genomic and metabolomic data*, 2004−2009, FP6-2002-LIFESCIHEALTH 503094). The aim of this project was to develop decision support systems (DSSs) to assist clinicians in brain tumor diagnosis based on various sources of data: MRI, MRS, MRSI, high-resolution magic angle spinning (HR-MAS), DNA microarrays and clinical information. Our involvement within this project is related to the development and integration of pattern recognition tools (i.e., classifiers) for brain tumor diagnosis based on MRI, MRS, MRSI and HR-MAS data.

From the studies presented in Chapters 5 and 6 we could conclude that *in vivo* and *ex vivo* MR spectroscopy techniques can complement each other and can provide distinct valuable information for the interpretation and diagnosis of brain tumors. Therefore, our next goal was to investigate the potential and limitations of using *in vivo* NMR information in combination with *ex vivo* NMR information. To this aim, we focused on supervised pattern recognition methods, whose performance directly depends on the available observations used in building these classifiers. Here, the possibility of using HR-MAS data as a complementary dataset when dealing with a lack of MRSI data needed to build a classifier is explored. This is particularly interesting when considering rare brain tumors, since it is unlikely to acquire sufficient cases to define their metabolite profiles using only *in vivo* NMR information, and we can use *ex vivo* HR-MAS for determining them. In Chapter 7 different approaches to combine HR-MAS data with *in vivo* MRSI and MRI data using Canonical Correlation Analyses (CCA) are described. We investigated which parameters influence the classification results by means of extensive simulations and *in vivo* studies. This work is accepted for publication in the journal *Measurement Science and Technology,* 2011 and was awarded at the *6th European Symposium on Biomedical Engineering, Chania,* 2008. This research is part the involvement in the HealthAgents project (*Agent-based distributed decision support system for brain tumour diagnosis and prognosis*, 2006−2008, IST–2004–27214) where we were responsible for the development and integration of pattern recognition tools (i.e., classifiers)

for brain tumor diagnosis based on different NMR modalities. The study was performed in close collaboration with the Department of Radiology, RUMCN.

Another relevant and very new clinical application of MRS is to study human AF and explore its potential in becoming a valuable technique for the evaluation of fetal health and development. In Chapter 8, a study on how to exploit spectral information contained within the AF to extract reliable biomarkers for identifying complicated pregnancies and separating between different pregnancy complications is presented. Results show that these purposes can be achieved by using dimensionality reduction methods in combination with automated classifiers. This work is performed in close collaboration with the Division Woman and Child, the Centre for Surgical Technologies, the Division of Medical Imaging and the Biomedical NMR Unit at the University Hospitals K.U.Leuven.

1.6 Conclusions

In this chapter the basic MR principles are introduced. Different MR modalities that record different anatomical and physiological properties are presented with the focus on MRI, MRS(I), HR-MAS and high resolution MRS data, since these data are considered in the studies presented in this thesis. A minimal medical background with regards to brain tumor diagnostics (facts, diagnosis tools, treatments, main types of brain tumors) is given underlying the potential of the above mentioned MR modalities in brain tumor diagnosis. The links between the metabolite concentrations and brain tumors as well as the MRS features that are most relevant for brain tumor diagnosis are presented. An overview of the possible follow up of a pregnancy behavior based on the AF analyses is given. The different goals of the thesis are addressed giving a chapter-by-chapter overview and outlining the author's personal contributions.

Chapter 2

Signal processing and preprocessing

This chapter is an overview of the typical processing and preprocessing steps performed in the analysis of MR spectra before the classification step. The focus mostly lies on those techniques that are considered in the studies presented in this thesis. In section 2.1 the SNR improvement, frequency alignment, phase and lineshape correction, water suppression, baseline correction and normalization preprocessing methods are outlined. Section 2.2 gives the theoretical background of the feature extraction methods used in the thesis. Firstly methods that exploit the biomedical information embedded in the spectra are presented. Then, mathematical methods where the features are extracted based on their statistical relevance are summarized.

2.1 Preprocessing methods

The quality of NMR signals is mostly hampered by the presence of artifacts, instrumental errors, noise and other unwanted components. Hence, before analyzing these signals, preprocessing steps that are aimed at removing irrelevant information, while enhancing the key features are needed. Most common preprocessing steps considered nowadays for NMR spectroscopy analysis are noise and artifact filtering, normalization, alignment, phase correction and baseline correction (in Figure 2.1 distorted MRS spectra are illustrated before and after correction). The order and the number of the preprocessing methods to be considered must be carefully chosen for each type of signals. This is due, on one hand, to the fact that the different instrumentations and protocols used in acquiring NMR data present different sensitivity to the artifacts listed above and, on the other hand, one step may influence another. Feature extraction and selection methods can also be regarded as a kind of preprocessing that helps in finding the most valuable information present in the data. In the following paragraphs the most relevant preprocessing methods are outlined.

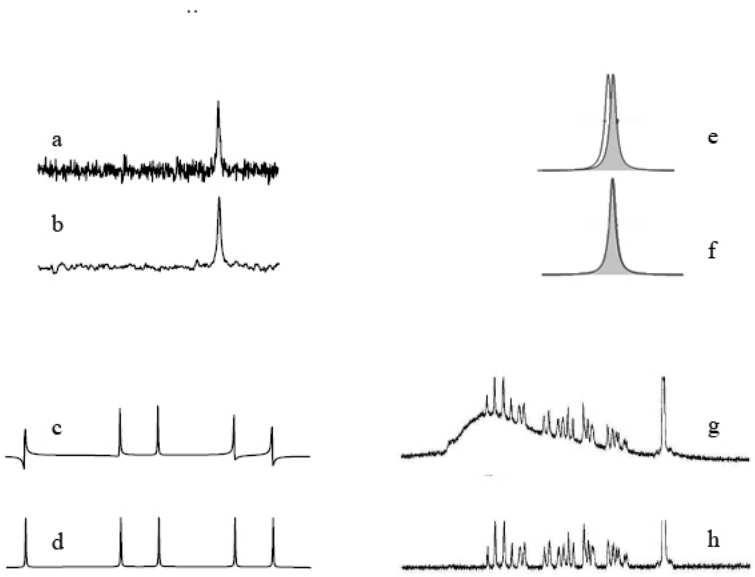


Figure 2.1 *Illustration of a. noisy spectrum and b. noise corrected spectrum; c. phase distorted and d. phase corrected spectrum; e. frequency shifted spectra and f. aligned spectra; g. baseline distorted and h. baseline corrected spectrum.*

2.1.1 SNR improvement

The NMR signals are essentially contaminated by noise and therefore suffering from a poor SNR. This artifact is particularly common for *in vivo* measurements, especially when a short echo time acquisition protocol was followed. High resolution *ex vivo* MRS measurements are characterized by higher SNR compared to *in vivo* MRS.

When the spectral resolution is too low to identify the resonances, increasing it can be achieved by truncating the last points of the time domain signal (which are considered to consist mainly of noise). Other techniques commonly used for improving spectral resolution in a measured NMR spectroscopy signal represented in the frequency domain include zero-filling and apodization.

Zero filling is the procedure of artificially extending the acquisition time by appending zeros to the acquired FIDs. The zero-filling procedure performed in the time-domain translates into a spectral interpolation in the frequency domain. Zero-filling beyond twice the number of original data points only leads to a trigonometric interpolation, which provides no further SNR enhancement (Bartholdi and Ernst, 1973; Ebel et al., 2006), and allows resolution enhancement only in rare cases (Lindon and Ferrige, 1980).

Apodization. Another widely used procedure for SNR improvement is apodization, i.e., the point-wise multiplication of the time-domain signal with a weighting function that typically attenuates the parts of the signal that exhibit low SNR (Ebel et al., 2006, De Graaf, 2007). Usually, an exponentially decaying weighting function is used for this purpose. In this way, the initial points of the FID get a higher weighting than the points at the end of the FID, which mainly contain noise. If an exponentially increasing weighting function is used, this leads to narrower peaks in the MR spectrum, but a decreased SNR because of the higher contribution of the points at the end of the FID.

In (Ebel et al., 2006) the importance of zero-filling in combination with apodization has been discussed in the context of 1D and 2D NMR spectroscopy, as well as MRSI. The combination of apodization with zero-filling could not provide higher sensitivity enhancement.

2.1.2 Frequency alignment

The chemical shift is dependent on the pH and temperature which may vary from one sample to another and thus complicates the alignment of the spectra. These effects are in particular noticeable for high resolution *ex vivo* MRS data. *In vivo* measurements can also suffer from frequency shifts. Since most feature extraction methods require a correct alignment of the spectra, special attention must be paid to this step.

For *in vivo* MR data, large peaks, such as NAA, Cho or Cr are generally used as reference for the alignment, while for *ex vivo* HR-MAS data doublets are preferred (*e.g.*, Ala or Lac doublet). If a reference chemical substance was added to the solution before the measurement, this reference peak is commonly used for the alignment. The spectra are shifted in the frequency domain for alignment and, if needed, transformed back into the time domain by the inverse Fourier transformation.

2.1.3 Phase correction

Phase corrections are meant to transform the acquired MRS signal such that its spectrum is in absorption mode, i.e., peaks in the real part of the spectrum are positive. The first-order phase shifts arise from the delay between the excitation pulse and the first point of the acquisition of the time domain signal and are linearly frequency-dependent. Zero-order phase correction is possible by multiplying the complex spectrum by a complex phase factor equal to the initial phase of the FID (Jiru, 2008).

2.1.4 Eddy current correction

Eddy currents artifact is induced by the rapid switching in the magnet coils and surrounding metal structures. It is described by the Faraday's law of induction (De Graaf, 2007). Eddy currents can be corrected by point-wise dividing the water suppressed signal by the phase term of the water unsuppressed signal in the time-domain (Klose, 1990).

2.1.5 Lineshape correction

The lineshape of MRS signals can be additionally distorted due to inhomogeneities of the magnetic field, which may be caused by tissue heterogeneity. Traditionally, Lorentzian lineshape for each spectral component, or correspondingly, complex damped exponential components in the time domain, are expected.

A typical assumption of the methods that deal with the lineshape corrections is that all spectral components in the signal are affected by the same spectral distortions. A fundamental difference in the methods used in correcting these artifacts concerns whether they use a reference signal or they do not. Reference deconvolution methods need a reference signal, which is either a separate measurement, or a spectral component extracted from the analyzed signal. Here we mention the FIDDLE (free induction decay deconvolution for lineshape enhancement) method proposed in (Morris, 1988; Morris et al., 1997) and the QUALITY (quantification improvement by converting lineshapes to the Lorentzian type) method proposed in (De Graaf, 1990). Further developments for automating these methods have been proposed in (Webb et al., 1992; Maudsley et al., 1994). The QUECC method (Bartha et al., 2000) is meant to benefit from the advantages of both QUALITY for a complete correction of the lineshape and Klose's eddy current correction method (ECC) (Klose, 1990), which can be applied when an additional water-unsuppressed reference signal is acquired.

When the goal of lineshape estimation is improving the quantitation results rather than visually correcting the spectrum, it is better to include the reference signal as part of the quantitation method. In (Maudsley, 1995), a self-deconvolution method which does not require the use of a reference signal is proposed. In (Sima et al., 2009) the self-deconvolution method for lineshape correction is combined with the quantification method AQSES. Later, an improvement of the method is proposed in (Osorio Garcia et al., 2011).

2.1.6 Water filtering

^{1}H NMR spectroscopy measurements fail to suppress completely the water resonance without affecting the metabolites of interest. Consequently, the so-called water suppressed MRS signals still contain a residual water contribution. The water resonance frequency region is

well known to be around 4.7 ppm and therefore it is close to the region where other metabolite resonances of interest are located. Hence, a water filtering step is mostly necessary when analyzing MRS data. Additionally, time-domain quantification methods cannot be used without accounting for the water components. Frequency-domain quantification methods (see, e.g., Mandelshtam et al., 1998; Mierisová and Ala-korpela, 2001; Hiltunen et al., 2002; Stoica et al., 2003; Gabr et al., 2006) can be applied directly to the water suppressed signal, because they can exclude in a straightforward way unwanted regions from the spectrum, but they should consider the water tails as part of the baseline.

Water filtering can be performed using convolution-based methods (Marion et al., 1989; Sodano and Delepierre, 1993; Cross, 1993; Sundin et al., 1999; Antoine et al., 2000, 2001; Günther et al., 2002, Poullet et al., 2009) which convolve the original signal with the coefficients of a filtering window. Water filtering can also be performed using a subspace-based modeling approach such as Hankel singular value decomposition (HSVD) (or its more computationally efficient implementations, Hankel Lanczos singular value decomposition (HLSVD) or HLSVD with partial reorthogonalization (HLSVD-PRO)) (Barkhuijsen et al., 1987; Pijnappel et al., 1992; Chen et al., 1996; Laudadio et al., 2002). In these methods the whole signal is fitted as a sum of complex damped exponentials. Afterwards, the components whose frequencies are estimated in the frequency region of the water resonance are subtracted. These filtering methods are sometimes embedded in the quantification algorithm, such as AQSES (Poullet et al., 2007a).

2.1.7 Signal normalization

When analyzing datasets of MRS signals one might observe signal intensity differences between the spectra. This phenomenon is mostly obvious if the data are acquired by several clinical centers, on various scanners or with different acquisition protocols. Even if similar acquisition conditions were followed, the difference in the type of tissue under investigation can also lead to intensity differences between the spectra. Normalization is the procedure used to compensate for these differences.

Typically two main normalization approaches are applied to MRS signals: normalization with respect to a particular mathematical norm and normalization by division to the intensity of a particular molecule.

Mathematical normalization. This approach involves division of each spectral value by the norm (e.g. *L1, L2*) of the spectrum, or a part of the spectrum. *L1*-norm is defined as the sum of the absolute value of the elements in a vector (this corresponds to the integral of the magnitude spectrum) and *L2*-norm is defined as the square root of the sum of the squares of the elements in a vector (Tate et al., 1996, 1998, 2003; Usenius et al., 1996).

Normalization by the intensity of a molecule. When analyzing brain tissue, commonly the amplitude of Cr (Preul et al., 1996), which is assumed to be constant, is used as reference for the signal normalization. Nevertheless, Li et al. (2003) found that this normalization approach increases variability. An alternative is to divide the spectrum by the intensity of water, in case an additional measurement of a corresponding water unsuppressed signal, acquired with the same acquisition parameters and originating from the same tissue is available (Usenius et al., 1996). The intensity of the water peak can be estimated for example by taking the highest value in the time domain signal, by peak integration in the frequency domain (Meyer et al., 1988) or by modeling the water unsuppressed signal using HSVD (Barkhuysen et al., 1987), HLSVD-PRO (Laudadio et al., 2002) or other modeling approaches. For *ex vivo* measurements a reference substance is frequently added to the solution in a known quantity before the measurement of the NMR signals. The signal normalization can therefore be performed with respect to this substance.

2.1.8 Baseline correction

When analyzing human tissue using NMR spectroscopy techniques, besides the metabolites, also other types of components might be captured in the MR spectra, such as lipids and macromolecules (MMs). MM signals are characterized by broad spectral lines (short T_2), which often overlap in the frequency domain with metabolite components. Thus, in the frequency domain, the lipids and MMs contamination is observed as an underlying profile called baseline. Another type of baseline is caused by the distortion of the initial FID data points due to instrumental imperfections (also called rolling baseline), but this does not form the subject of this thesis since the MRS signals analyzed here do not suffer from rolling baselines, but have instead a macromolecular baseline.

Many applications involving spectroscopic data analysis require a baseline correction. The goal is to disentangle the macromolecule contributions from the metabolite signals. One way is to measure an MM signal with an inversion recovery pulse (Hwang et al., 1996), but this significantly extends the measurement time. Other approaches include modeling the MMs signal using mathematical functions either as a preprocessing step such as: interpolation (Golotvin and Williams, 2000; Cobas et al., 2006), randomization (Williamson et al., 2006); iterative wavelet transform (Galloway et al., 2009), approximation using linear functions (Hiltunen et al., 1991) or analytical functions such as Fourier series (Stephenson and Binsch, 1980) or polynomials (Brown, 1995; Dietrich et al., 1991); in combination with quantification (see for *e.g.* Young et al., 1998; Soher et al., 2001) or embedded in the quantification step (see for *e.g.* Provencher, 1993; Elster et al., 2005; Ratiney et al., 2005; Poullet et al., 2007a). Modeling of the baseline can be done by Lorentzians, wavelets, polynomial or spline functions (Provencher, 1993; Bartha et al., 1999; Soher et al, 2001; Seeger et al., 1999, 2001, 2003; Ratiney et al., 2004; Cudalbu et al., 2009).

The baseline correction approaches considered in this thesis are:

- using an apodization function (Simonetti et al., 2003). The FID is point-wise multiplied in the time-domain with an exponentially decaying function. This requires only the decay as parameter to be selected. The resulting spectrum which mainly contains the broad baseline components (the baseline consists of broad fast decaying components and their main contribution is in the first part of the FID) is subsequently subtracted from the original spectrum, yielding the baseline-corrected signal.

- truncation of the initial points in the FID. This approach is applied by (Ratiney et al. 2004) as a sub-step of the method QUEST. Removing the initial part of the FID should suppress the baseline components. However, the disadvantage is that also part of the metabolite contributions might be suppressed.

- Non-parametric modeling of the baseline with spline functions in AQSES (Poullet et al., 2007a).

2.2 Metabolite extraction methods

2.2.1 Feature extraction

^{1}H MR spectroscopy, when combined with reliable and robust classification strategies can represent a powerful noninvasive tool for detecting and classifying diseases and/or disease stages. An important part of the classification strategies is the selection of the input space. When considering MRS data, the input used by the pattern recognition techniques is either the full spectra or a set of features extracted from the spectra. When dealing with metabolic data one may consider extracting features based on their biochemical relevance in the classification problem. This approach involves some prior knowledge with regards to the metabolites to be extracted as features, as well as their spectral model. Another possibility is to extract statistically significant features, relying strictly on their mathematical relevance in solving the classification problem. This approach is usually preferred when no prior knowledge on the metabolites present in the data is available *a priori*.

Full spectra
When considering the full spectra, all the points of the real or magnitude spectrum in the frequency region of interest are considered. In this thesis, for avoiding phasing problems and since only minor difference has been reported between performances based on magnitude spectra and real spectra (Devos et al., 2004; Opstad et al., 2007), the magnitude spectra have been used.

Why considering a feature space reduction?
A full spectra approach might not be suitable for all MR spectra of biomedical origin classification, whether *ex* or *in vivo*. One may deal with the complications that occur because such spectra are complex, noisy and with overlapping peaks. Additionally, the samples present an overabundance of spectral features since each spectrum consists typically of hundreds of attributes (the frequencies), with the majority redundant or correlated, coming from the contributing metabolites. If there were an infinite number of samples, then the classification accuracy would increase with increasing number of features. Yet, in real life we are dealing with classification problems with a finite number of samples. Therefore the so-called peaking phenomenon (Allais, 1966; Chandrasekaran and Jain, 1974) may occur and beyond a certain number of features the classifier performance will decrease. Thus, there is an optimal number of features and this number depends on the classifier, on the characteristics of the features and on the sample size. Consequently, the goal of feature selection/extraction is to preserve the most relevant information, to minimize redundancy and to exclude the noise and artifacts present in the spectrum. Moreover, it simplifies the calculation and therefore the computation time is reduced (Guyon et al., 2006a; 2006b; Liu and Motoda, 2007). Due to computational matters, using the metabolite tissue concentrations as input features is preferred, as previous studies reported high accuracy with such feature-based classification approaches (Devos et al., 2004; De Vos, 2009; Luts et al., 2009a).

2.2.2 Extraction of features with biomedical information

Since characteristic resonance peaks correspond to metabolites that are relevant biomarkers for classifying a clinical condition (Murphy et al., 1993; Mukherji, 1998; Smith and Stewart, 2002; Leclerc et al., 2002; Howe et al., 2003b; Bock, 1994; Clifton et al., 2006) it is then reasonable to use these peaks, resembling the metabolite concentration in the spectrum under investigation, as discriminatory features. For estimating the metabolite concentration, simple frequency domain methods can be considered, such as peak integration (Hoch and Stern, 1996), where the selected frequency regions are taken as intervals around the resonance frequencies (Govindaraju et al., 2000) of several characteristic metabolites; peak bucketing (points of the spectra in several particular disjoint frequency regions corresponding to the regions of interest are considered as features); binning (i.e., gathering adjacent spectral points). More accurate quantification methods are the model-based approaches, which can also work in frequency domain, such as LCModel (Provencher, 1993), or in time domain such as AMARES (Vanhamme et al., 1997; Lemmerling et al., 2002), QUEST (Ratiney et al., 2005) or AQSES (Poullet et al., 2007a).

2.2.3 Peak integration

In spite of the fact that, in the recent years, frequency-domain and time-domain fitting methods for spectral quantification have gained interest, spectral peak integration is still

widely used. Peak integration is a simple non-parametric method to estimate metabolite concentrations in the frequency domain. The method does not make any model assumptions; it is non-iterative, very fast and quite robust. To integrate the area under the peak, Simpson's rule or trapezoid rule can be considered. In this thesis the integration is performed based on the trapezoidal rule. Figure 2.2 is an illustration of the method. Peak integration results depend widely on the way the integration intervals are defined. One possibility is to consider symmetric regions around the theoretical resonance frequency of the peak (Devos et al., 2005). In reality it is well known that the metabolite resonances can be misaligned, due to variations in temperature, pH or physiological abnormalities. Consequently the resonance frequency can deviate from the theoretical one and therefore would lead to biased quantification results. Another approach is to consider dynamic integration intervals by finding the highest peak of the considered metabolites and then fix the bounds at those ppm values at which peak slopes return to baseline (Croitor Sava et al., 2011d). Regardless the approach used in integrating the area under the peak, the accuracy of this method can not always be guaranteed due to its sensitivity to the artifacts which are often present in the NMR signals. Moreover, the method does not succeed to extract reliable information from individual peaks when these are overlapping with each other. Residual baseline and low SNRs have also an influence on the peak-integrated values. Additionally, the tail of the peaks is also neglected by peak integration and the area under the peaks will therefore be underestimated, possibly by up to 40% (Meyer et al., 1988).

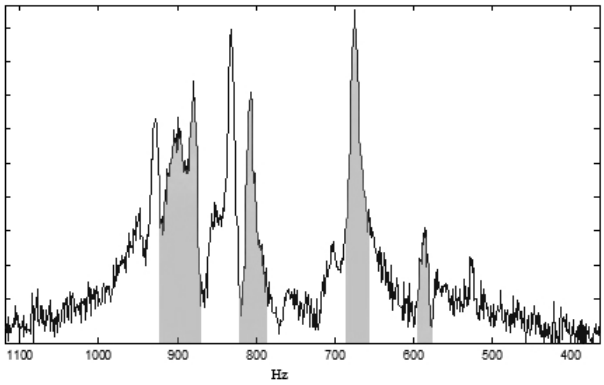


Figure 2.2 *Integration of peak areas. The selected regions to be integrated are indicated through the vertical grey bars.*

When applying peak integration, special attention must be paid to the correct preprocessing of the MR spectra, in particular to their alignment (see section 2.1.2) and phasing (see section 2.1.3). Because the chemical shift is dependent on pH and temperature and therefore may vary from one sample to another, the alignment of the spectra is not always straightforward. In what concerns the phasing, several studies prefer to use the magnitude of the spectra instead of their real part for performing peak integration, (Tate et al., 2003; Lukas et al., 2004; Devos

et al., 2004; Menze et al., 2006). In general, the advantage obtained from omitting phase correction by using the magnitude spectra outweighs the drawback of increasing linewidths, which could lead to more peak overlap in these magnitude spectra than in the real part spectra.

2.2.4 Model-based methods

MRS and MRSI signals are measured in the time-domain and are Fourier transformed for better visualization into frequency-domain spectra. In most of the model-based quantification methods an appropriate nonlinear model is fitted to the measured MRS signal by minimizing the sum of the squared residuals, which is the maximum likelihood solution under the assumption of additive white Gaussian noise. The fitting can be done in the time domain with methods as AMARES (Vanhamme et al., 1996), QUEST (Ratiney et al., 2005) and AQSES (Poullet et al., 2007a); in the frequency domain using for example LCModel (Provencher, 1993, 2001), or by combining both domains with TDFDfit (Slotboom et al., 1998). Methods such as LCModel, QUEST or AQSES use metabolite basis sets, which can be built up from simulated spectra (*e.g.*, via programs based on quantum mechanics such as NMR-SCOPE (Graveron-Demilly et al., 1993) or GAMMA (Smith et al., 1994)) or *in vitro* measured spectra. Using a metabolite basis set facilitates the disentangling of overlapping resonances and has been shown to provide better accuracy (Cavassila et al., 2000)

MRS model

The free induction decay (FID) signal can be modeled analytically in the time-domain (or, equivalently, its Fourier transform can be modeled in the frequency domain) as a linear combination of K possibly damped, phased and frequency-shifted metabolite templates. Hence, having a "metabolite basis set" $\{\nu_k$, for $k = 1,\ldots,K\}$ of complex-valued signals of length N, the typical mathematical model for an FID signal, $\hat{y}$, is expressed as:

$$\hat{y}(t) = \sum_{k=1}^{K} a_k \exp(j\phi_k)\exp(-d_k t + 2\pi j f_k t)v_k(t) + b(t) + w(t) \qquad (2.1)$$

where a_k are positive amplitudes of the metabolites in the basis set, ϕ_k are phase shifts, f_k are frequency shifts, d_k are Lorentzian damping factors that account for the necessary corrections of the basis set signals, $j = \sqrt{-1}$ and t denotes a particular time instant among the discrete measuring times $t_0, \ldots, t_{m-1}$. The $b(t)$ denotes the "baseline", which is the response of the macromolecules that are not included in the basis set, and $w(t)$ denotes the water component. The amplitudes are proportional to the concentration of the respective molecule.

This model contains useful prior knowledge due to the inclusion of the metabolite profiles, since many metabolites resonate at more than one frequency, depending on the molecular configuration.

Model fitting

An *in vivo* NMR signal *y*, which is also a complex-valued time series of length *N*, is assumed to satisfy:

$$y(t) = \hat{y}(t) + \varepsilon_t \tag{2.2}$$

where term ε_t denotes an unknown noise perturbation with zero mean.

Typically, a single voxel time-domain model-based quantification problem can be expressed as a nonlinear least squares (NLLS) problem of fitting model $\hat{y}(t)$ to a measured signal:

$$\min_{\substack{a_k,\phi_k,d_k,f_k \\ k=1,\ldots K}} \sum_{t=0}^{t_{N-1}} \left| y(t) - \hat{y}(t) \right|^2 \tag{2.3}$$

Figure 2.3 shows a measured basis set of metabolite spectra ν_k that are used for fitting the *in vivo* measured MRS signal from the human brain from Figure 2.4.

When considering a metabolite basis set the protocol used to simulate/acquire these metabolite signals should reproduce the same conditions as to the ones used to acquire the NMR signals to be quantified. Using measured or simulated basis sets on metabolite concentration estimates can provide slightly different results (Cudalbu et al., 2008). Additionally, the number of components used in the quantification may also have an influence on the robustness of the quantification method (Poullet et al., 2007a).

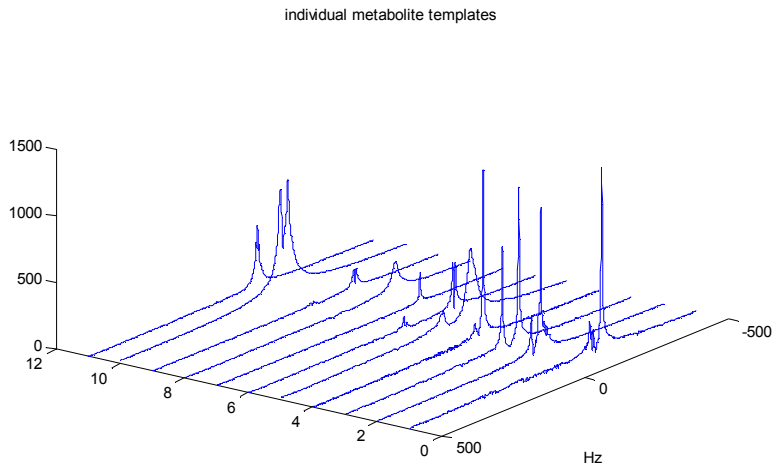


Figure 2.3 *Absolute part of a measured metabolite basis set spectra*

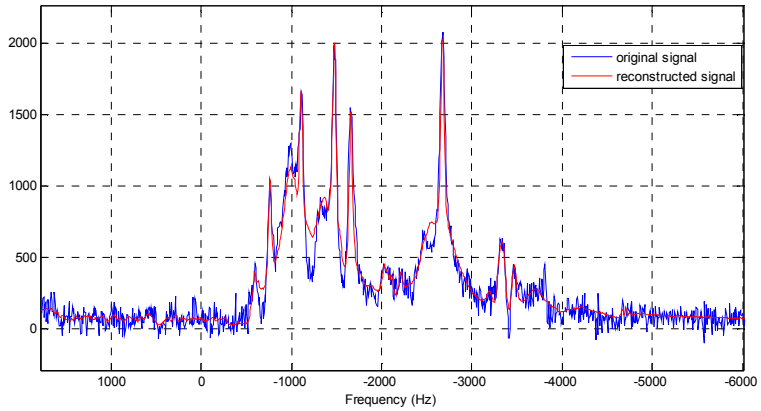


Figure 2.4 *An in vivo 1.5T MRS spectrum fitted with the metabolite basis set. The metabolite spectra are shifted in frequency with f_k Hz, broadened (by increasing d_k) and scaled to an appropriate amplitude a_k.*

2.2.5 AQSES

AQSES (Accurate Quantitation of Short-echo Time Magnetic Resonance Spectroscopic Signals) is a time-domain quantification method (Poullet et al., 2007a) that fits the whole complex measured signal in the time domain to a nonlinear model (Sima et al., 2007). The method AQSES is embedded in Java (AQSES GUI) and Matlab (SPID) software packages,

both available online at: http://homes.esat.kuleuven.be/~biomed/software.php. An illustration of the software is provided in Figure 2.5. AQSES method uses a database of metabolite profiles that are measured *in vitro* or quantum-mechanically simulated.

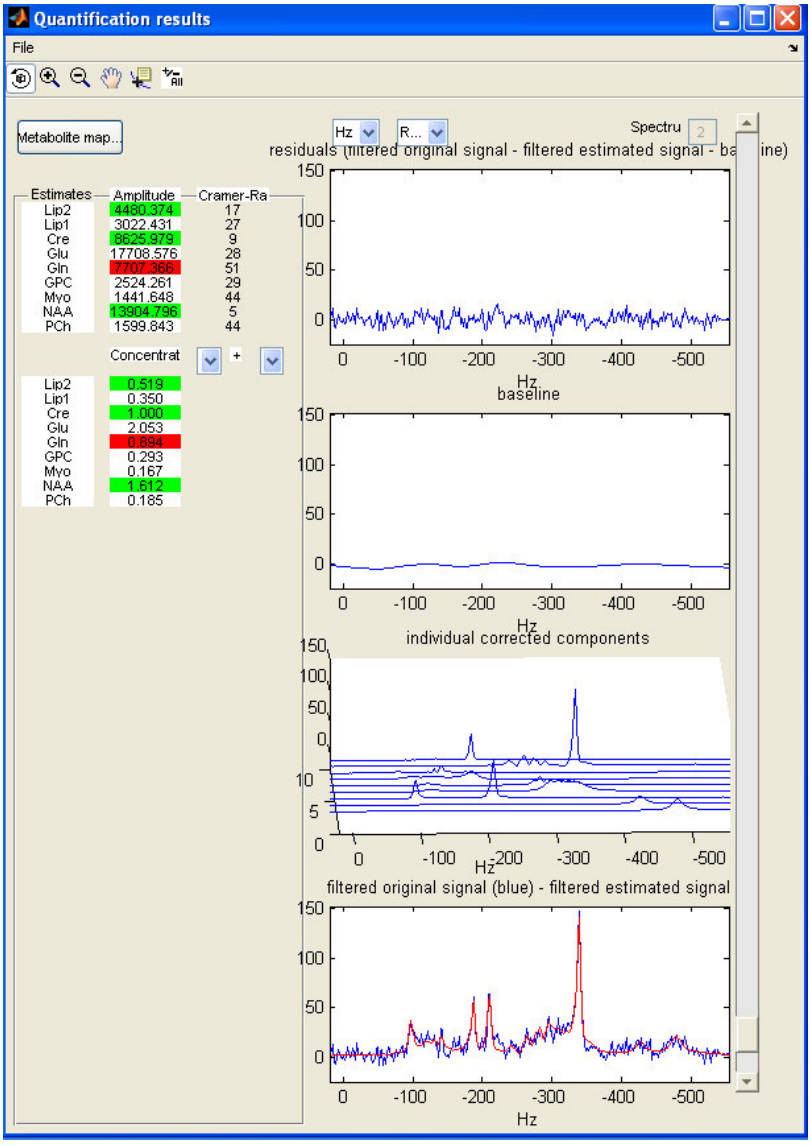


Figure 2.5 *Quantification results with AQSES for an in vivo ^{1}H MRS spectrum of a human brain acquired with an 3 T Phillips scanner. Print screen from SPID used interface.*

The method is designed to deal with the macromolecular contributions by incorporating the baseline *b* into the fit as a non-parametric model based on penalized splines. This typically requires less spline functions than smoothing splines, which are used for instance in LCModel. In order to model the baseline in the time-domain, a basis of splines is created and then passed through the discrete inverse Fourier transform; the resulting discretized functions are put as columns in a matrix *A*. Then the baseline *b* can be written in matrix notation as the product Ac. The coefficients in this linear combination, $c_1, \ldots c_s$ are unknowns that must be identified. AQSES solves the regularized NLLS criterion by fitting the model and the smooth baseline at the same time:

$$\min \frac{1}{N} \sum_{t=0}^{t_{N-1}} \left| y(t) - \hat{y}(t) \right|^2 + \lambda^2 \left\| Dc \right\|^2 \tag{2.4}$$

where $\hat{y}(t)$ is computed as defined in Eq 2.1. The term $\lambda^2 \left\| Dc \right\|^2$ imposes a certain degree of smoothness to the baseline *b*. The regularization matrix *D* measures the smoothness of the baseline in the frequency domain. The regularization parameter λ controls the degree of smoothness.

Neglecting the water filter for the sake of simplicity, the NLLS problem in Eq. 2.5 becomes:

$$\min_{a_k, \phi_k, d_k, f_k, c} \frac{1}{N} \sum_{i=0}^{N-1} \left| y(t_i) - \sum\nolimits_{k=1}^{K} a_k \exp(j\phi_k) \exp(-d_k t_i + 2\pi j f_k t_i) v_k(t_i) - (Ac)_i \right|^2 + \lambda^2 \left\| Dc \right\|^2 \tag{2.5}$$

which can be rewritten in a compact matrix form as:

$$\min_{a_k, \phi_k, d_k, f_k, c} \frac{1}{N} \left\| y - \Psi(\varsigma)\alpha - Ac \right\|^2 + \lambda^2 \left\| Dc \right\|^2 \tag{2.6}$$

with $y = [y(t_0) \ldots y(t_{N-1})]^T$, $\alpha = \left[a_1 \exp(\phi_1) \ldots a_K \exp(\phi_K)\right]^T$ and $\Psi(\varsigma)$ is an *N* x *K* matrix defined as:

$$\Psi_{ik} = \exp((-d_k + j2\pi f_k) t_i) v_k(t_i) \tag{2.7}$$

In AQSES, the water term *w(t)* in Eq. 2.1 is filtered and the region that should be filtered out of the signal must be specified by the user. The purpose of this step is to suppress all the components in the specified frequency region so that there the spectrum becomes smaller than an estimated noise level, while the frequency regions of interest are kept undistorted.

AQSES is implemented using a variant of the variable projection VARPRO algorithm (Golub and Pereyra, 2003). The parameters appearing linearly into the model (the complex amplitudes and phases) are projected out of the least squares problem. Only a smaller sized NLLS problem remains to be solved for the nonlinear variables d_k, f_k, via an iterative minimization algorithm of the Levenberg- Marquardt type. This procedure increases robustness of the parameters, in particular when the number of metabolites is not known a priori. Additionally, in AQSES, the classical VARPRO method is extended by imposing constraints on the nonlinear parameters (Sima, 2006) via upper and lower bounds or via linear equalities between some variables of the same type. Some constraints can be imposed also on linear parameters, such as non-negative amplitudes and equal phases.

The Levenberg-Marquardt algorithm needs good initial values for its variables, but the initial values for all the nonlinear parameters (frequency and damping corrections) are set in AQSES to zero, which means that the optimization starts with no spectral corrections to the signals in the database. In the equal phase case, an initial guess for the common phase corrections is estimated from a preliminary optimization round of the free phase algorithm.

AQSES is designed for the quantification of single voxel MRS data. It can be successfully used for quantifying MRSI signals, but each voxel signal is treated individually.

2.2.6 QUEST

QUEST is a semi-parametric time domain quantification method (Ratiney et al., 2005). It can be successfully used for quantifying single voxel MRS, as well as for HR-MAS signals (Rabeson et al., 2008). As AQSES, the method uses a Levenberg-Marquart algorithm to minimize the SSR (Sum of Squared Residuals) with the signal model (2.1). The method is implemented in the software package jMRUI- 4.0 (http://www.mrui.uab.es/mrui/), see Figure 2.6.

The NLLS problem in QUEST can be formulated as:

$$\min \frac{1}{N} \left\| y - \Psi(\varsigma)\alpha \right\|^2 \tag{2.8}$$

with the same notations as in Eq. 2.6. The NLLS fit method used in QUEST is described in (De Beer and van Ormondt, 1992).

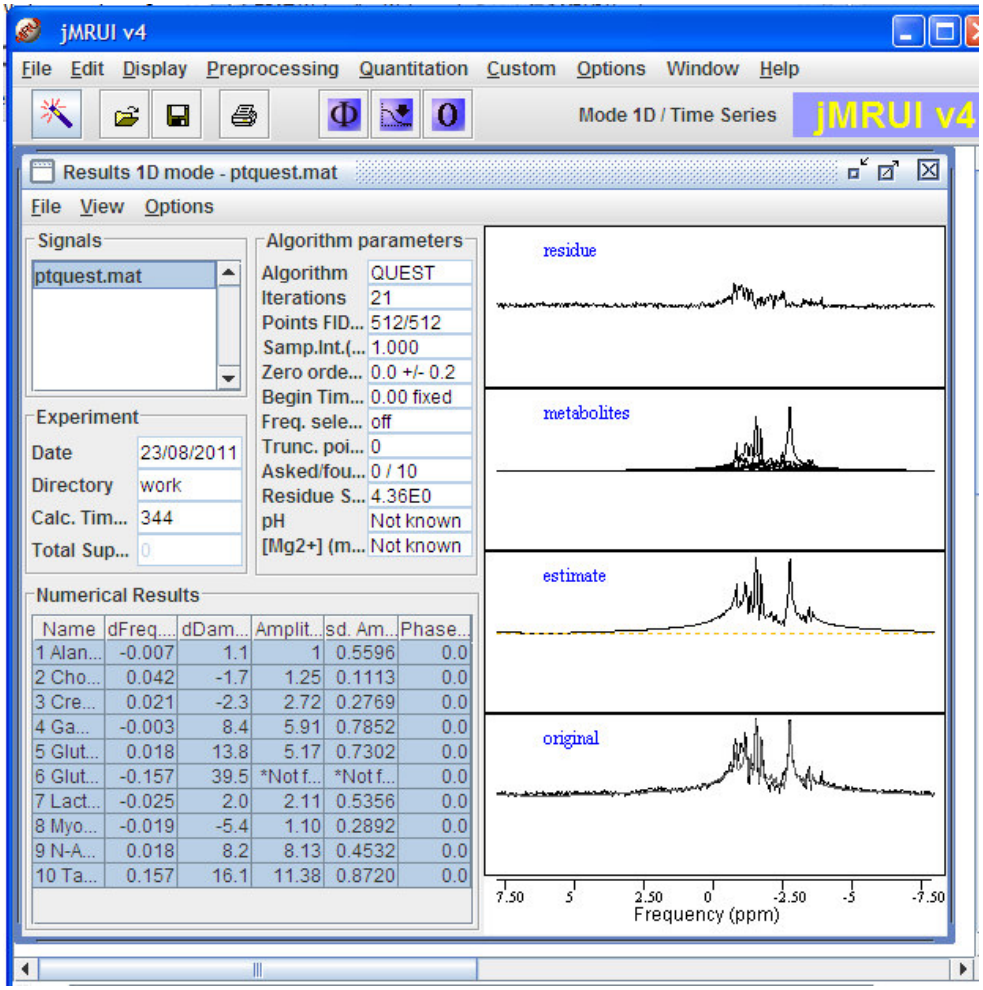


Figure 2.6. *^{1}H MRS spectrum of a 1.5T PRESS 23 obtained using a PRESS sequence, quantitated with QUEST.*

The method is also able to deal with the baseline via the following procedure (Ratiney et al., 2005):

- estimation of the model parameters by fitting a truncated version of the FID without its initial data points, which contain the macromolecular contribution

- back-extrapolation of the model towards the first time instant
- background signal (or baseline) estimation by subtracting the back-extrapolated model from the original FID
- modeling (or smoothing) of the background signal
- parametric NLLS fitting of the disentangled metabolite signal knowing the background

Water filtering is not integrated in QUEST. Therefore it has to be performed as a preprocessing step prior to the quantification. For quantifying MRSI data, with QUEST spatial knowledge is not considered and therefore each voxel signal is treated individually.

2.2.7 LCModel

LCModel is a semi-parametric frequency domain quantification method (Provencher, 1993, 2001). It models the spectrum as a linear combination of *in vitro* metabolite profiles. A baseline approximation, using splines, is also included in the method. The method is commercially available in the LCModel software package, see Figure 2.7.

LCModel fits only the real part of the frequency domain signal as:

$$\hat{Y}(\nu_p) = \exp(-j(\phi_0 + \nu_p\phi_1))\left(\sum_{i=1}^{B}\beta_i B_i(\nu_p) + \sum_{k=1}^{K} C_k \sum_{n=-S}^{S} S_n M_k(\nu_{j-n};\gamma_k,\lambda_k)\right) \quad (2.9)$$

with $C_k \geq 0, \gamma_k \geq 0$ and $\sum_{n=-S}^{S} S_n = 1$. C_k represents the concentration of the k^{th} metabolite ϕ_0 and ϕ_1 are the zero-order and first-order phase corrections, respectively. The *in vitro* metabolite spectra, $M_k(\nu\,;\,0,\,0)$, are broadened and shifted with the parameters γ_k, λ_k respectively, such that:

$$M_k(\nu;\gamma_k,\lambda_k) = FFT\{m_k(t)\exp(-(\gamma_k + j2\pi\lambda_k))t\} \quad (2.10)$$

with $m_k(t)$ the inverse Fourier transform of the model spectrum $M_k(\nu;\,0,\,0)$. The baseline is represented by cubic B-splines, $B_i(\nu)$ and the lineshape coefficients S_n take field inhomogeneities and eddy currents into account.

LCModel uses a Marquardt modification of a constrained Gauss-Newton least squares algorithm. The LCModel software package also offers the possibility to analyze MRSI data in one multivoxel run. For this it first analyzes a central voxel of the subset and then works outwards, in a row-by-row analysis, using Bayesian learning to get starting estimates and "soft constraints" for the first-order phase correction and the referencing shift from the preceding central voxels for the outer voxels. These are preceded by locating Cho and NAA peaks for a "preliminary analysis" for the improved estimation of phase and frequency adjustments.

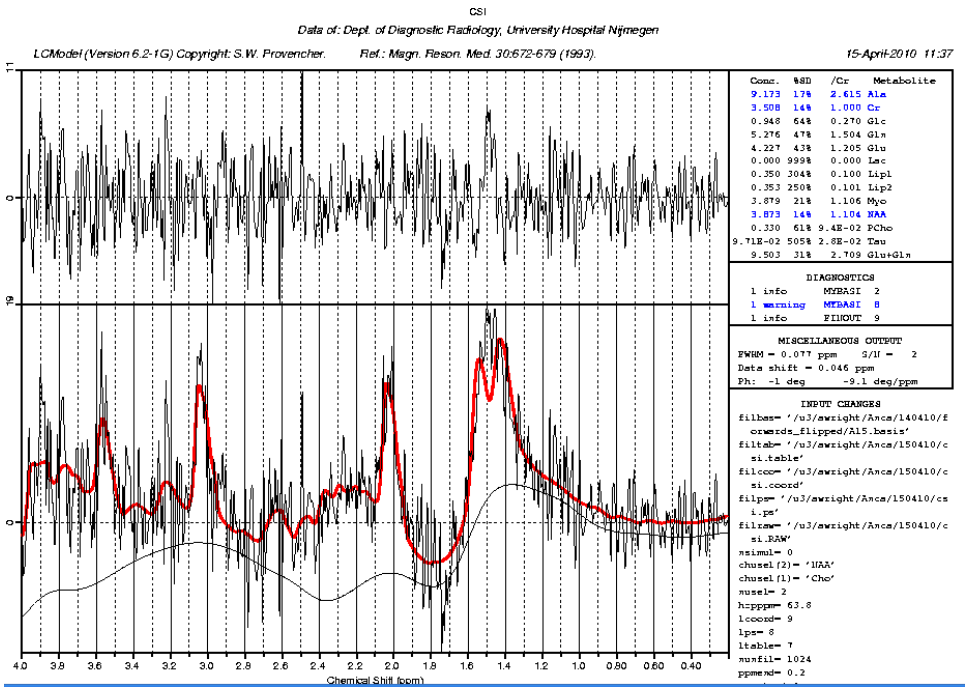


Figure 2.7 *LCModel quantification window for an ^{1}H MRS spectrum of a human brain at 1.5T. Image provided by RUMCN.*

2.2.8 Quantification of multivoxel MRSI data

Compared to *ex vivo* NMR measurements, *in vivo* MRS and especially *in vivo* MRSI data are obtained with a much lower spatial and spectral resolution. Thus, there is a considerable interest in improving the reconstruction of metabolite maps from MRSI. One way is to incorporate anatomical spatial information as a prior for improved reconstruction of metabolite images. This idea was exploited in several contributions that have considered the

spatial information in MRSI data analysis and mostly in the classification, starting with Szabo De Edelenyi *et al.* (2001).

The common hypothesis in these studies is that two adjacent voxels resemble each other in terms of metabolite concentration. Laudadio *et al.* (2005b) proposed to use a 3×3 spatial model when considering spatial information for improved MRSI classification.

Moreover, MRI images, which are acquired together with the MRSI data, can help to decide how similar two adjacent voxels are. For example, two adjacent voxels, one with glioblastoma tissue and the other with healthy tissue, should not influence each other in the parameter estimation. Therefore a weighting matrix constructed based on the MRI information could say to what extent a surrounding voxel influences the voxel under investigation by giving more weight to the voxels with similar tissue type and similar location.

For quantifying metabolites in a grid of MRSI voxels, a straightforward approach is to apply a single-voxel quantification method, such as QUEST, AQSES, AMARES or others, to each signal in the grid individually. MRSI signals usually have a much lower quality than single voxel, due to the spatial/spectral trade-off for the available measuring time. This also implies that metabolite components become more strongly overlapping in frequency and metabolites present in low concentration are almost embedded in noise. Therefore, these data are more prone to quantification errors. Supplementary spatial information expressed as constraints on the optimization parameters would be very valuable in analyzing this type of data. Thus, spatial information can be exploited in the MRSI quantification to prevent the optimization algorithm to converge toward a wrong local mimimum (Kelm, 2007).

AQSES-MRSI (Croitor Sava et al., 2011a), an advanced metabolite quantification method for MRSI data, in which the available spatial information is considered, is described in detail in Chapter 4. An illustration of AQSES-MRSI quantification window, which is embedded in SPID user interface, is presented in Figure 2.8. The method is an extension of AQSES and includes prior knowledge in the form of proximity constraints on the spectral parameters within a grid and optimized starting values, and a penalty term that promotes a spatially smooth spectral parameter map. Smoothness of a 2D parameter map can be locally measured at every voxel (ℓ, κ) in the grid by using the parameter value at the current location and the values in a certain neighborhood. We denote that two voxels are neighbors by ($\ell 1$, $\kappa 1$) ~ ($\ell 2$, $\kappa 2$). Because MRSI grids are rather coarse, we usually focus on 3x3 regions with the current voxel (ℓ, κ) in the center. When (ℓ, κ) is on the border of the MRSI grid, only the available neighbors are used. A possible measure for the smoothness at point (ℓ, κ) is given by the first order difference norm:

$$\sum_{(i,j)\sim(l,k)} (p_{lk} - p_{ij})^2 \tag{2.11}$$

where p stands for any of the parameters considered in the quantification (damping, frequency) for any k. Second order formulas are also possible, such as the second order differences:

$$(2p_{lk} - p_{l-1,k} - p_{l+1,k})^2 + (2p_{lk} - p_{l,k} - p_{l,k-1} - p_{l,k+1})^2 \quad (2.12)$$

$$(4p_{lk} - p_{l-1,k} - p_{l+1,k} - p_{l,k-1-}p_{l,k+1})^2 \quad (2.13)$$

The multi-voxel quantification approach AQSES-MRSI is more accurate than individually fitting each signal in the grid. The relevance of this approach on simulated and clinical MRSI data obtained from brain tumor patients has been evaluated in (Croitor Sava et al., 2011a) and is presented in Chapter 4.

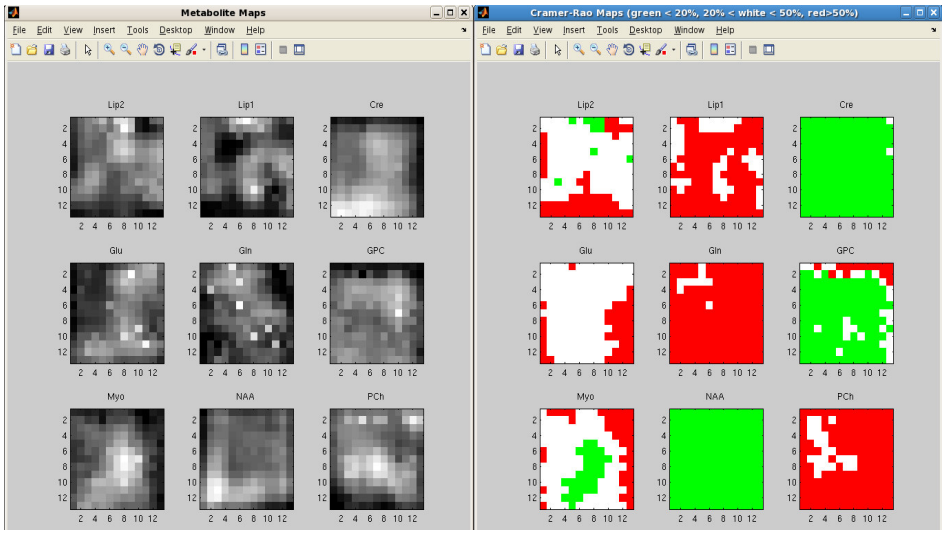


Figure 2.8 *An illustration of the quantification results window for AQSES-MRSI, as it is displayed in SPID user interface. Left: the obtained metabolite maps. Right: the Cramer-Rao confidence maps.*

2.2.9 Extraction of features using statistical criteria

When no prior knowledge regarding which resonances are relevant for the given classification problem is available, one may consider extracting features based on statistical properties such

as the variability, similarity or dissimilarity within the data. Using automatic feature extraction methods, such as principal component analysis (PCA) or principal coordinate analyses (PCO), the data can be transformed so that the new variables/features best reflect the above properties. Moreover, only useful information is kept, while noise or artifacts are filtered out. This approach was considered when analyzing the AF spectra where no *prior* knowledge regarding the metabolites present in the data was available and, additionally, the spectra present high complexity (a very high number of metabolic peaks can be visually identified).

Principal component analysis

Principal component analysis (PCA) (Jolliffe, 2002) is an unsupervised multivariate technique introduced by (Pearson, 1901). It transforms a set of correlated features into a set of uncorrelated features, called principal components (PCs). The PCs are expressed as linear combinations of the original features.

PCA is based on the calculation of the eigenvalue decomposition of a data covariance matrix or singular value decomposition of a data matrix, usually after mean centering the data. After organizing our data as an n by m matrix, X^T, with zero empirical mean (the empirical (sample) mean of the distribution has been subtracted from the dataset), PCA finds the optimal linear transformation for extracting the subspace that has largest variance, by computing:

$$Y^T = X^T W = V\Sigma \tag{2.14}$$

where W is the $m \times m$ matrix of eigenvectors of XX^T, V is the $n \times n$ matrix of eigenvectors of $X^T X$, Σ is the rectangular diagonal matrix with non-negative real numbers on the diagonal and the singular value decomposition (SVD) of X is: $X = V\Sigma W^T$. The columns of Y^T represent the *"scores"* with respect to the PCs. This PCA transformation preserves the dimensionality in the sense that the same number of PCs as original variables is obtained. For a reduced-dimensionality representation of the data, X is projected into the reduced space defined by the first l singular vectors of W_l:

$$Y = W_l^T X = \Sigma_l V_l^T \tag{2.15}$$

The matrix W of singular vectors of X is equal to the matrix W of eigenvectors of the matrix of observed covariances $C = X X^T$.

In NMR spectroscopy it is assumed that most of the variance in the original dataset can be explained by a limited number of PCs. Therefore, the method is often considered, when analyzing MRS data, to reduce the multidimensional datasets to lower dimensions.

Principal coordinate analysis

Principal Coordinate Analysis (PCO) also known as Multidimensional Scaling (MDS) is a more general projection method than PCA as it can use any distance matrix. The method explores the similarities and dissimilarities of data (Borg and Groenen, 2005). With MDS the data are transformed by computing a matrix of item-to-item similarities/dissimilarities (= distance matrix) and assigns for each variable a location in an *N*-dimensional space, where *N* is specified a priori. MDS tries to find the main axes or principle coordinates (PCOs) through this matrix. Thus, having *n* objects, the dissimilarity matrix is defined as:

$$\Delta = \begin{pmatrix} d_{1,1} & d_{1,2} & \dots & d_{1,n} \\ d_{2,1} & d_{2,2} & \dots & d_{2,n} \\ \dots & \dots & \dots & \dots \\ d_{n,1} & d_{n,2} & \dots & d_{n,n} \end{pmatrix} \tag{2.16}$$

where $d_{i,j}$ is a distance function that computes the distance between the i^{th} and j^{th} objects. Then, MDS aims at finding n vectors $x_1, \dots, x_n$ by solving the following optimization problem:

$$\min_{x_1,\dots x_n} \sum (\|x_i - x_j\| - d_{i,j})^2 \tag{2.17}$$

where $\|\bullet\|$ is the distance function.

For some cost functions, minimizers can be stated analytically in terms of matrix eigendecompositions.

2.3 Conclusions

In this chapter the preprocessing steps used in this thesis for improving the quality of the MRS data, such as SNR improvement, frequency alignment, phase and lineshape correction, eddy currents correction, water suppression and baseline correction are presented. Feature extraction methods which either exploit the biomedical information embedded in the spectra, or extract features based on their statistical relevance are summarized.

Chapter 3

Pattern recognition methods in MRS

This chapter reviews the pattern recognition methods considered in this thesis for MRS data analysis. The supervised classification methods K-nearest neighbor, discriminant data analysis, support vector machines and canonical correlation analysis are outlined in section 3.1. In section 3.2 a few unsupervised classification methods are presented. Firstly, the clustering analyses method is briefly reviewed. Then, blind source separation techniques such as independent component analysis, non-negative matrix factorization and convex analysis methods are outlined and their behavior in NMR spectroscopic data analysis is discussed. A few classification performance measures are introduced in Section 3.3. Finally, the possibility of combining multimodal sources of information for improved classification and the modality of visualizing the classification results are presented.

3.1 Supervised classification

Machine learning techniques are commonly considered in the analysis of NMR data. Supervised classification uses a set of data defined a priori, called training dataset, and produces a function or a model called a classifier or a regression function. In this sections K-nearest neighbor (K-NN), linear discriminant analysis (LDA) and support vector machines (SVM) algorithms, which are able to produce reliable classifiers in the analyses of NMR spectroscopic data, are described. A special case of supervised classification is a model based canonical correlation analysis (CCA) approach, which uses a model defined a priori from a training set.

3.1.1 K-nearest neighbor

The k-nearest neighbor algorithm (K-NN) classifies objects by computing the distance between two objects using a distance function (Duda et al., 2001). Thus, having two objects, x and y, composed of N variables/features, such that $x = \{x_1 \ldots x_N\}$ and $y = \{y_1 \ldots y_N\}$, we can compute the distance between them using the function $d(x,y)$. Most commonly the Euclidian distance is considered:

$$d_E(x,y) = \sum_{i=1}^{N} \sqrt{x_i^2 - y_i^2} \tag{3.1}$$

When using the K-NN algorithm, data normalization is suggested as preprocessing step in order to avoid that the variable with the largest scale dominates the distance measure.

3.1.2 Linear discriminant analysis

Linear discriminant analysis (LDA) is a statistical technique which finds a linear combination of features which best separate two or more classes of objects. Thus, for comparing the correlation between variables and the class label, the *N*-dimensional input vector *x* is projected onto a line (Fisher, 1936):

$$y = w^T x \tag{3.2}$$

where *y* is a scalar and *w* is a weight vector. Considering y^{th} as a threshold, we classify *y* as class *A* if $y \geq y^{th}$ and as class *B*, otherwise. *w* is chosen to maximize the criterion *J(w)*:

$$J(w) = \frac{w^T S_B w}{w^T S_w w} \tag{3.3}$$

where S_B is the between-class covariance matrix and S_W is the total within-class covariance matrix, as defined in (Fisher, 1936).

3.1.3 Support vector machines

Support vector machines (SVM)s are a group of supervised learning methods that can be applied to classification or regression. The technique was originally developed for binary classification, but multi-class extensions are possible (Weston and Watkins, 1999). The idea behind SVMs is to map the original data points from the input space to a high dimensional feature space so that the classification problem becomes simpler in the feature space, by constructing a hyperplane with maximal distance between the two classes. Thus, the SVM

training algorithm builds a model which is a representation of the input points in space and based on this model it assigns the new data into one class or the other.

Given a set of training data $\{(x^i, y^i)\}_{i=1}^{Nt}$, where x^i vectors are the input data and $y^i \in \{-1,+1\}$ are the class label, SVM estimates a model of the form:

$$f(x) = sign(w^T \varphi(x) + b) \tag{3.4}$$

where φ denotes the function considered for feature mapping the *N*-dimensional input vector *x* from the input space to the *Nf*-dimensional feature space (Vapnik, 1998). *w* and *b* are unknowns. A data point *x* is assigned to the first class if *f (x) =+1* or to the second class if *f(x)=-1*.

3.1.4 Canonical correlation analysis

Canonical correlation analysis (CCA) was developed by Hotelling (1936) and is a multi-channel generalization of ordinary correlation analysis, which quantifies the relation between two random variables, *x* and *y,* by means of the so-called correlation coefficient:

$$\rho = \frac{Cov[x, y]}{\sqrt{V[x] * V[y]}} \tag{3.5}$$

with the correlation coefficient, ρ , a scalar taking values between -1 and 1. *Cov* stands for covariance and *V* for variance. The term "canonical" refers to the coordinate system in which the correlation is measured.

For zero mean variables Eq 3.5 reduces to:

$$\rho = \frac{E[x * y]}{\sqrt{E[x^2] * E[y^2]}} \tag{3.6}$$

where *E* stands for the expectation of a random variable. Being a multivariate method, CCA can be applied to multichannel signals. Thus, assuming two zero-mean multivariate random

vectors $x = [x_1, \ldots, x_m]^T$ and $y = [y_1, \ldots, y_n]^T$, where the superscript T denotes the transpose. One can define from these two vectors the following linear combinations of the components of x and y, which represent two new scalar random variables X and Y:

$$\begin{aligned} X &= \omega_{x_1} x_1 + \cdots + \omega_{x_m} x_m = \omega_x^T x \\ Y &= \omega_{y_1} y_1 + \cdots + \omega_{y_n} y_n = \omega_y^T y \end{aligned} \tag{3.7}$$

CCA computes the linear combination weight coefficients $\omega_x = [\omega_{x_1}, \ldots, \omega_{x_m}]^T$ and $\omega_y = [\omega_{y_1}, \ldots, \omega_{y_n}]^T$, known as regression weights, that maximize the correlation between X and Y. Then, ρ becomes:

$$\rho = \frac{E\left[(\omega_x^T x) * (\omega_y^T y)\right]}{\sqrt{E\left[(\omega_x^T x)^2\right] * E\left[(\omega_y^T y)^2\right]}} = \frac{\omega_x^T C_{xy} \omega_y}{\sqrt{(\omega_x^T C_{xx} \omega_x)(\omega_y^T C_{yy} \omega_y)}} \tag{3.8}$$

C_{xy} is an ($m \times n$) covariance matrix with the covariances between the variables in X and Y as elements. C_{xx} and C_{yy} are the corresponding matrices for the covariances between the variables within X and Y, respectively. It is possible to find min(m; n) pairs of variates, each maximally correlated, subject to the constraint that each pair is uncorrelated with the pairs that precede it.

In the standard CCA, the regression weights may take both negative and positive values. Non-negativity constraints on ω_x and ω_y can be imposed (Friman, 2003). Good detection performance can be obtained using a non-negativity constrained CCA, as shown in (Friman, 2003; De Vos et al., 2007).

CCA can also be considered for solving multivariate dataset problems by using a data driven approach (Correa et al., 2008, 2010; Li et al., 2009) or can be used to decompose one dataset into contributing sources in a BSS manner (De Clercq et al., 2006). For this, certain assumptions must be valid (De Vos, 2009). In this thesis the restricted CCA algorithm, with non-negativity constraints, proposed by (Friman, 2003) is used in order to compare two different datasets by quantifying the relation between them by means of correlation coefficients.

3.2 Unsupervised classification

When no training datasets along with the data class labels are available *a priori*, unsupervised learning techniques may be considered to describe the classes/groups within the data. One such technique is cluster analysis where the classification is based on some common properties, such as the similarities between the data within the same group and the dissimilarities between the data belonging to different groups. Blind source separation techniques may also be used for the unsupervised classification of MRS data as described bellow.

3.2.1 Cluster analysis in MRS

Cluster analysis is a form of unsupervised learning in the sense that the algorithm tries to partition a set of objects in more subsets in an optimal way, according to some common properties without any knowledge of group membership. The purpose is to make each subset (or cluster) as homogeneous as possible so that all objects in it have similar properties, while objects in different clusters should be as dissimilar as possible.

K-means clustering is predominantly used in a wide range of medical applications because of its simplicity and wide availability in standard software packages (Hartigan and Wong, 1979; Tavazoie et al., 1999; Rosen et al., 2005).

Given a pre-specified number k, the k-means algorithm partitions the dataset into k subsets (clusters $C_1 \ldots C_k$) by iteratively optimizing the sum, over all clusters, of the within-cluster sums of object-to-cluster-centroid distances:

$$S = \sum_{i=1}^{k} \sum_{x \in C_i} d(x, \mu_i) , \tag{3.9}$$

where $d(x, \mu_i)$ is the distance between x, an object in cluster C_i, and μ_i, the centroid of C_i (i.e., the average of all objects in the cluster). The choice of the distance measure, which will determine how the similarity of two objects is calculated, is important since it will influence the shape of the clusters, as some objects may be close to one another according to one distance and farther away according to another. In clustering the following distances are commonly considered: Euclidean distance, Mahalanobis distance, cosine distance, correlation distance, Hamming distance.

Cluster validation techniques can be used to measure the quality of clusters on the basis of the definition that objects within one cluster are similar to each other, while objects in different clusters are dissimilar with each other. In section 3.3, the validation techniques considered in this thesis are reviewed.

3.2.2 Blind signal separation

Blind source separation (BSS) techniques are often used in signal processing to extract a set of source signals from a set of mixed signals and to estimate the contribution of these sources to the measured mixture. There are different methods for blind signal separation, such as principal components analysis (PCA), independent component analysis (ICA), dependent component analysis (DCA), non-negative matrix factorization (NNMF), low-complexity coding and decoding, stationary subspace analysis. Because many data are by their nature non-negative, as for instance color intensities, chemical concentrations, frequency counts, etc., non-negativity is an important constraint that can be considered when analyzing these data. Therefore, since magnitude spectra, as well as the metabolite concentrations estimated from MRS data are non-negative data, in this thesis the focus lies on considering BSS techniques which are able to impose non-negativity constrains.

3.2.3 Non-negative matrix factorization

Non-negative matrix factorization (NNMF) is a mathematical technique that reveals hidden factors within a dataset of signals. It is also known under the name self modeling curve resolution (Lawton and Sylvestre, 1971) or positive matrix factorization (Paatero and Tapper, 1994). Given a matrix, X, with NNMF, X is factorized into two matrices, A and S. Other methods, such as vector quantization or principal component analysis (PCA), can be understood as factorizing a data matrix, as well. These methods are subject to different constraints such as "winner-takes-all" constraint, which results in clustering the data into mutually exclusive prototypes, with vector quantization, or orthogonality constraint for PCA. NNMF differs from these methods by constraining the factors A and S to be non-negative while minimizing the cost function:

$$f(A,S) = \|X - AS\|_F^2, \text{ with } A,S \geq 0 \tag{3.10}$$

Different cost functions can be considered. Commonly, the squared error, Frobenius norm and an extension of the Kullback-Leibler divergence to positive matrices are considered (Lee and Seung, 2001). Other approaches that propose alternative cost function formulations include but are not limited to (Guillamet et al., 2001; Wang et al., 2004; Cichocki et al., 2006; Hamza

and Brady, 2006; Pauca et al., 2006). Each approach leads to a different NNMF algorithm, usually minimizing the cost function using iterative update rules.

For solving the optimization problem in Eq. 3.10 one may consider alternating least squares algorithms (ALS) (Paatero and Tapper, 1994; Sajda et al., 2004), gradient descent algorithms (Chu et al., 2004; Lee and Seung, 2001) or multiplicative update algorithms (Lee and Seung, 1999, 2001). In (Lin, 2005) the use of a projected gradient bound-constrained optimization method seems to have better convergence properties.

In the standard NNMF algorithm, A and S are initialized with random non-negative values before the iteration starts. Alternate approaches for the algorithm in order to speed up or influence convergence to a desired solution have been proposed (Wild et al., 2003). Additionally, various authors have imposed additional constraints on A and/or S such as smoothness (Pauca et al., 2004; Chen and Cichocki, 2005, Sen and Yuntao, 2009) or sparsity (Hoyer, 2004, Kim and Park, 2007, 2008). The inclusion of such constraints is motivated by the problem itself and often reflects the need to compensate for the presence of noise or other data degradations in X. The additional constraints are typically considered via penalty terms. Thus, the cost function in Eq. 3.6 becomes:

$$f(A,S) = \left\|X - AS\right\|_F^2 + \alpha C_1(A) + \beta C_2(S) \tag{3.11}$$

where $C_1(A)$ and $C_2(S)$ are the penalty terms introduced to impose the additional constraints over A and S, and α and β are regularization parameters to balance the trade-off between the accuracy of the factorization and the constraints.

The product AS is an approximate factorization of rank at most k. Usually k is chosen such that $k << min(m, n)$ (Berry et al., 2006). An appropriate decision on the value of k is critical in practice and the choice of k is mostly problem dependent.

3.2.4 Independent component analysis

Independent component analysis (ICA) is a special case of blind source separation method in which the goal is to find a linear representation of non-Gaussian data so that the components are statistically independent, or as independent as possible. Through time the method found many applications and implementations and nice reviews of the method are provided in (Hyvärinen et al., 2001; Amari and Cichocki, 2002).

Classically, having an $m \times n$ matrix $X = (x_1, x_2, ..., x_m)^T$, with ICA we can decompose $X = AS$, where S contains the source signals as its rows $S = (s_1, s_2, ..., s_k)^T$ and A is the $m \times k$ mixing matrix. The cost function can be optimized with various algorithms. Usually, one of the

following four different criteria (Yuan, 2009) are considered: the maximization of non-Gaussianity, such as FastICA (Hyvärinen and Oja, 1997, Hyvärinen, 1999), minimizing mutual information (Zheng et al., 2006), maximum likelihood estimation (includes the so called infomax principle (Bell and Sejnowski, 1995) and natural gradient algorithm (Bell and Sejnowski, 1995; Amari, 1998; Oja, 1999)) and tensorial methods (Cardoso, 1989, 1990, 1999). ICA imposes the assumptions/restrictions of independence and/or non-Gaussianity.

Independence. Two variables x_1 and x_2 are considered independent if the information on the value of x_1 does not give any information on the value of x_2, and vice versa. Statistically speaking, independence can be defined by the probability densities. Thus, x_1 and x_2 are independent if and only if their joint probability density function (pdf), $p(x_1,x_2)$, is the product of two marginal probability density functions:

$$p(x_1, x_2) = p(x_1)p(x_2) \tag{3.12}$$

This definition can be extended for any number n of random variables, $x_1 \ldots x_n$, in which case the joint density must be a product of n terms.

Uncorrelation can also be seen as a weaker form of independence. For this, x_1 and x_2 are said to be uncorrelated if their covariance is zero. If the variables are independent, they are uncorrelated, but uncorrelation does *not* imply independence. Because of this, many ICA methods give uncorrelated estimates of the independent components since this reduces the number of free parameters and simplifies the problem (Hyvärinen and Oja, 2000).

Non-Gaussianity. From the different cost functions that can be considered, the most common are based on maximizing non-Gaussianity. A quantitative measure of non-Gaussianity is classically given by kurtosis or the fourth-order cumulant. Another measure of non-Gaussianity is given by negentropy.

Since the criterion of maximal non-Gausianity can be used as a measure of statistical independence, a vector w that maximizes the non-Gaussianity of $w^T X$ under one of the measures mentioned above is computed. Thus, each local maximum for the non-Gaussianity of $w^T X$ gives us one of the independent components.

Before applying the ICA algorithm, the observations (the rows of X) are usually assumed to be “white” or are transformed to be so. Through whitening, X is linearly transformed so that we obtain a new matrix whose rows are zero-mean, uncorrelated and their variances equal unity.

Additional constraints. Since in the real world many data are non-negative, additional non-negativity constraints on the linear ICA model can be added. Plumbley proposes in a series of

publications the combination of non-negativity and independence assumptions on the sources, referred to as non-negative independent component analysis (Plumbley, 2001, 2002, 2003, 2004a, 2004b). The concept proposed by Plumbley is that a "well-grounded" non-negative source, *s*, has non-zero pdf all the way down to zero. For this, using the probability function, Pr(.), a source is called non-negative if $Pr(s < 0) = 0$ and well-grounded if $Pr(s < \delta) > 0$ for any $\delta > 0$. One approach to find the sources is to whiten the non-zero-mean observations and make a rotation to positive factors; the obtained factors can then be seen as the sought sources (Plumbley, 2002). In (Oja and Plumbey, 2004) an orthogonal rotation of the whitened observation vector into non-negative outputs that give a positive permutation of the original sources is proposed and a gradient-based algorithm operating on pre-whitened data is used. A modified version of the FastICA Algorithm (Hyvärinen and Oja, 1997) for non-negative ICA with constraints that the sources are non-negative with probability one was also proposed (Yuan and Oja, 2004).

Although the classical application of the ICA is as blind source separation technique, in NMR the method often finds its application as a feature extraction technique (Szabo de Edelenyi et al., 2005) which is motivated by the theory of redundancy reduction.

3.2.5 Convex analysis of mixtures of non-negative sources

Convex analysis of mixtures of non-negative sources (CAMNS) is a recently developed non-negative BSS method (Cha et al., 2008). CAMNS is deterministic, requiring no source independence assumption and accounts for sparsity. The development is based on a special assumption called local dominance. This assumption, closely related to sparsity, states that each source exhibits a non-zero value for a certain feature for which all the other sources have a zero value. Under local dominance, the BSS criterion becomes a convex analysis problem, namely finding the extreme points of an observation-constructed polyhedral set. This problem can be solved using linear programming, and leads, in this setting, to a unique source separation with probability one. Thus, the source signals can be perfectly identified in a blind fashion (Cha et al., 2008).

Summarizing from (Cha et al., 2008), the CAMNS method first constructs from the data matrix X (whose rows, transposed, are denoted here by column vectors x_i) the mean vector $d = \frac{1}{m}\sum_{i=1}^{m} x_i$ and a matrix containing the first *k-1* principal components of the mean centered sample covariance matrix, namely the matrix of eigenvectors:

$$C = \left[q_1\left(UU^T\right), q_2\left(UU^T\right), \ldots, q_{k-1}\left(UU^T\right)\right] \tag{3.13}$$

where $U = [x_1 - d, ..., x_m - d]$, and $q_i(UU^T)$ stands for the eigenvector corresponding to the i^{th} largest eigenvalue of UU^T. Then the algorithm proceeds at finding the extreme points of the polyhedral set, Ω, containing all non-negative sums between the mean vector d and the linear combinations of the first k-1 principal components, which are the columns of C. Due to the local dominance assumption on the sources, it can be proven that the k extreme points of Ω are precisely the k non-negative sources that one may seek, as described in (Cha et al., 2008).

3.3 Performance measures

A common problem of unsupervised data classification is estimating the correct number of classes, k, existing in a dataset. For BSS experiments, the number of the sources, k, to be extracted has to be defined a priori. In defining k value, one approach is to test the performance of the proposed method for various values of k and setting k to that value for which best performance was obtained (Croitor Sava et al., 2011b). Clinical information regarding the number of groups expected in the data can also be considered in defining k.

Most clustering algorithms also require a user-defined input parameter k. Therefore is essential to have a correct estimation of k. The general approach to automatically determining this value is to estimate the quality of each solution provided by various k values and select the value of k that gives the best performance according to a quality criterion. Several approaches have been proposed to measure clustering performance for various k values. The performance measure methods considered in this thesis for estimating the correct number of classes to consider in the classification are introduced below.

3.3.1 Krzanovski-Lai index

The Krzanowski and Lai index (KL) is defined as (Krzanowski and Lai, 1985):

$$KL(k) = \left| \frac{Diff_k}{Diff_{k+1}} \right| \tag{3.14}$$

with

$$Diff_k = (k-1)^{2/m} W_{k-1} - k^{2/m} W_k \tag{3.15}$$

where m denotes the number of features in the dataset and W_k is calculated as the within-group dispersion matrix:

$$W_k = \sum_{i=1}^{k} \sum_{x_j \in C_i} (x_j - c_i)(x_j - c_i)^T \tag{3.16}$$

with x_j representing an object assigned to the j^{th} cluster, and c_i denotes the centroid of the i^{th} cluster. A value of k is optimal if it maximizes *KL(k)*.

3.3.2 The weighted inter-intra index

With the weighted inter-intra index, the optimal number of clusters within a given dataset is computed by maximizing intra-cluster similarity (Strehl, 2002; Strehl and Ghosh, 2003):

$$INTRA(X, \lambda, i) = \frac{2}{(n_i - 1)n_i} \sum_{\lambda_a = \lambda_b = i, b > a} S(x_a, x_b) \tag{3.17}$$

and minimizing inter-cluster similarity:

$$INTER(X, \lambda, i, j) = \frac{1}{n_i n_j} \sum_{\lambda_a = i, \lambda_b = j} S(x_a, x_b) \tag{3.18}$$

where i and j are cluster indices, n_i and n_j is the number of objects in the clusters i and j, respectively, λ is the n-dimensional label vector, and $S(x_a, x_b)$ is the similarity between two data-points x_a and x_b computed based on the Euclidian distance.

The quality measure is defined based on the ratio of weighted average inter-cluster to weighted average intra-cluster similarity:

$$\phi^Q(X, \lambda) = 1 - \frac{\sum_{i=1}^{k} \frac{n_i}{n - n_i} \sum_{j \in \{1,\ldots,i-1,i+1,\ldots k\}} n_j * INTER(X, \lambda, i, j)}{\sum_{i=1}^{k} n_i * INTRA(X, \lambda, i)} \tag{3.19}$$

Here, $\phi^Q \in [0,1]$ with $\phi^Q = 0$ meaning that the objects within a cluster are on average not more similar than samples from different clusters. On the other hand, $\phi^Q = 1$ describes a clustering where every pair of samples from different clusters has the similarity of zero and at least one sample pair from the same cluster has a non-zero similarity.

3.3.3 Silhouette index

Silhouette is a technique (Rousseeuw, 1987) that computes the compactness and separation of clusters by calculating the silhouette width for each object, average silhouette width for each cluster and overall average silhouette width for a total dataset, X. The optimal number of clusters is the one that gives the largest overall average Silhouette value (Kaufman and Rousseeuw, 1990; Chen et al., 2002). Thus, each cluster can be represented by a so-called silhouette, *S(i),* which is based on the comparison of its tightness and separation, and is computed as:

$$S(i) = \frac{(b(i) - a(i))}{\max\{a(i), b(i)\}} \tag{3.20}$$

where *a(i)* is the average dissimilarity of the i^{th}-object to all other objects in the same cluster; *b(i)* is the minimum of average dissimilarity of the i^{th}-object to all objects in another cluster. The dissimilarity is computed as the squared Euclidean distance between points in X. *S(i)* takes values in the interval [-1,1]. If the value is close to 1, the object is assigned to the appropriate cluster, while a value close to -1 means that the object is wrongly assigned and is somewhere between the clusters. A value that is close to *0* means that the object is equally far from more clusters.

3.3.4 Homogeneity and Separation index

Homogeneity index computes the compactness of the cluster as an average distance between the objects in the cluster and its respective centroid:

$$Hom = \frac{1}{N_o} \sum_i D(o_i, C(o_i)) \tag{3.21}$$

where o_i is the i^{th} object and $C(o_i)$ its centroid, N_o is the total number of objects and D is the distance function. In this thesis the Euclidian distance was used.

Separation index is a measure of between-cluster variance computed as the weighted average distance between clusters:

$$Sep = \frac{1}{\sum_{i \neq j} N_{ci} N_{cj}} \sum_{i \neq j} N_{ci} N_{cj} D(C_i, C_j) \tag{3.22}$$

where C_i and C_j are the centroids of i^{th} and j^{th} clusters, and N_{ci}, N_{cj} are the number of objects in the i^{th} and j^{th} clusters, respectivly.

Homogeneity and separation is a variation of the two indices suggested by (Shamir and Sharan, 2000):

$$HS = (1 - \sqrt{N_c}\frac{N_c}{N_o})(Hom - Sep) \tag{3.23}$$

where N_c and N_0 are the total number of clusters and total number of objects, respectively. Decreasing homogeneity index and increasing separation index suggest better clusters, thus this criterion is based on the minimization of *HS*.

3.3.5 Kruskal-Wallis test

The Kruskal-Wallis test is a one-way analysis of variance by ranks (their significance in separating between groups) (Kruskal and Wallis, 1952). It is a non-parametric alternative to the well-known one-way analysis of variance between groups (ANOVA) (Hollander and Wolfe, 1973; Neter, 1996). Unlike ANOVA, it does not assume a normal distribution for the data. The hypotheses for the comparison of two independent groups are: the null hypothesis of the test is that the samples come from identical populations (with equal medians); the alternative hypothesis is that the samples come from different populations.
The Kruskal-Wallis test statistic is formulated as:

$$\rho = (N-1)\frac{\sum_{i=1}^{g} n_i(\bar{r}_i - \bar{r})^2}{\sum_{i=1}^{g}\sum_{j=1}^{n_i}(r_{ij} - \bar{r})^2} \tag{3.24}$$

where n_i denotes the number of samples in group i, g is the total number of groups, r_{ij} represents the rank of sample j in group i after ranking all the cases of all groups, $\bar{r}_i$ is the average of the ranks r_{ij} over all samples j in group i, N is the total number of samples across all groups and: $\bar{r} = \frac{N+1}{2}$. When two or more values are equal, each of them receives a (noninteger) rank equal to the average of the integer ranks at which they are tied. Commonly, $\rho < 0.01$ suggests that the differences are statistically significant.

3.3.6 Tukey multiple comparison

In a one-way analysis of variance, one may test the hypothesis that several groups are all the same, against the general alternative that they are not all the same. Sometimes this approach is too general and one may need information about which pairs of means are significantly different and which are not. A test that can provide such information is called a multiple comparison procedure. This procedure provides a comparison interval. When the intervals overlap, there is no statistically significant difference between the groups, while if the intervals are disjoint, the difference can be considered as statistically significant.

Tukey's test is a single-step multiple comparison test, generally used in conjunction with a one-way analysis of variance analysis in order to find which means are significantly different from one another (Tukey, 1949).

Tukey's test is based on a formula very similar to that of the t-test, except that it corrects for experiment-wise error rate:

$$q_s = \frac{Y_A - Y_B}{SE} \tag{3.25}$$

where Y_A is the larger of the two means being compared, Y_B is the smaller of the two means being compared, and SE is the standard error of the data.

The q_s value can then be compared to a q value from the *studentized range* distribution (Pearson and Hartley, 1970). (A studentized range distribution is a continuous probability distribution that arises when estimating the mean of a normally distributed population in

situations where the sample size is small.) If the q_s value is larger than the $q_{critical}$ value obtained from the distribution, the two means are said to be significantly different.

3.4 Software

In this thesis, the supervised classifiers: K-NN, LDA and SVM were developed using Matlab Statistics toolbox. For the CCA implementation Matlab code from the developer (Friman, 2003) was considered. K-means clustering analysis was performed using the *kmean* function implemented in Matlab Statistics toolbox. For applying the proposed BSS methods we considered: an NNMF implementation in Matlab (Kim and Park, 2008), available online at http://www.cc.gatech.edu/~jingu; an adapted version for MRS spectra of the nICA code (Oja and Plumbley, 2004), available online at http://www.cs.helsinki.fi/u/phoyer and the CAMNS program package (Cha et al., 2008) available at http://mx.nthu.edu.tw/~tsunghan, which relies on the convex optimization software package SeDuMi (a free convex optimization solver (Sturm, 1999)).

To compute the validity indices: KL index, weighted inter-intra index, silhouette index and homogeneity and separation index a Matlab toolbox for estimating the number of clusters (http://www.mathworks.com/matlabcentral/fileexchange/13916) was considered.

SPID is a matlab graphical user interface (GUI) developed in our department which provides the user with tools capable to simulate, preprocess, process and classify *in vivo* and *ex vivo* MRS signals. AQSES-MRSI quantification method is embedded in SPID.

3.5 Fusion of several MR modalities

A large number of studies confirmed the power of *in vivo* MRS and MRSI spectroscopy techniques in disease diagnosis and prognosis. *Ex vivo* techniques, such as HR-MAS and high resolution MRS, have shown also to provide valuable information since, due to their high spectral resolution, they allow the identification of a high number of metabolites present in the data. Other NMR modalities, such as MRI imaging, diffusion- and perfusion-weighted MRI and functional MRI have gained lately much interest. Although all these NMR modalities are mostly considered separately for disease classification, the fusion of several NMR techniques can bring added value to the classification. As shown in (Croitor Sava et al., 2011d) *in vivo* and *ex vivo* MR spectroscopy and MR imaging techniques can complement each other.

The possibility of fusing multimodal NMR sources of information for brain tumor classification has firstly been tackled by Szabo De Edelenyi who proposes the use of a pattern recognition technique that combines MRI with spectroscopic information (Szabo De Edelenyi

et al., 2000). Later, various MRI image variables are fused with metabolic information for MRSI data classification (Simonetti et al., 2005; Laudadio et al,. 2005a, 2005b, 2008; Devos et al., 2005; De Vos et al., 2007; Luts et al., 2009a). These studies were motivated by the nature of MRSI data, which allows one to explore both spatial and metabolic information.

Another application where MRI and MRSI data can be combined is to consider MRI as additional information to estimate to what extent two adjacent voxels resemble each other. This information can help to decide how close the parameters of two adjacent voxels are, and to what extent a neighboring voxel influences the voxel under investigation. In (Laudadio et al., 2005b) for the classification of each MRSI voxel, information coming from its neighboring voxels was also considered. Still, in Laudadio's study no difference was made between two adjacent voxels belonging to different tissue types. In (Kelm, 2007), the author proposes to add an additional term in the cost function to ensure a certain smoothness in the parameter estimates, with a new regularization factor which finds a trade-off between the squared residual errors and the smoothness of the parameter's spatial maps. Moreover, based on the location of the voxels and the tissue type of each voxel, one can increase the accuracy of the feature extraction method for MRSI data by imposing proximity constraints on the spectral parameters within a MRSI grid based on MRI information. In (Croitor Sava et al., 2011a), optimized starting values and a penalty term that promotes a spatially smooth spectral parameter map were proposed. This approach showed to provide improved metabolite quantification results (Kelm, 2007; Croitor Sava et al., 2011a) and therefore more reliable metabolite estimates to be considered in the MRSI data classification.

In general, when working with supervised classification methods, the classifier has to learn the significant features, by means of a training procedure tuned to separate the different classes. Thus, in order to obtain reliable classifiers we need large and representative datasets for each class. Nevertheless, some clinically important tumors are sufficiently rare that even a large multicentre study would be unlikely to gather sufficient cases to define their metabolite profiles using in vivo MRS. Therefore, for rare brain tumors little is known biologically and a diagnosis on the basis of morphologic and metabolic appearance alone is controversial. Nowadays, large collaborative programmes exist for collecting frozen tissue from such tumors at surgery and placing them in a tumor bank. Biological studies using frozen tissues from tumor banks have been highly successful and HR-MAS could form part of such a study. In this context fusing HR-MAS information, MRSI, and MRI measurements can represent another promising approach to provide improved detection and classification of brain tumors (Croitor Sava et al., 2008; 2011d). These sources can complement each other both for the situation when we are confronted with a lack of information available for building a classifier, as well as for the situation when we have access to different sources of information and we use all these sources in building a robust classifier. In both circumstances, HR-MAS information can act as an added value, since combining multimodal heterogeneous sources of information can improve the classifier performance (Croitor Sava et al., 2011d).

3.6 From MRSI to nosologic imaging

The notion of nosologic image was first introduced in 2000 (Szabo De Edelenyi et al., 2000) to better visualize the classification results of an MRSI grid. As its term reflects, (*nosology* (in Greek *Nosos* = Disease) is a branch of medicine that deals with classification of diseases)) it refers to an image which indicates, using colors, the tissue types behind each MRSI voxel. These images can be easily interpreted by radiologists and physicians and therefore can improve the accuracy of the diagnosis, see Figure 3.1. Through time several authors considered visualizing the MRSI classification results using nosologic imaging (Szabo De Edelenyi et al., 2000; Simonetti et al., 2005; Laudadio et al,. 2005a, 2005b, 2008; Devos et al., 2005; De Vos et al., 2007; Luts et al., 2009a; Kelm et al., 2007). In all these studies both metabolic information coming from MRSI and imaging information from MRI were considered in the classification.

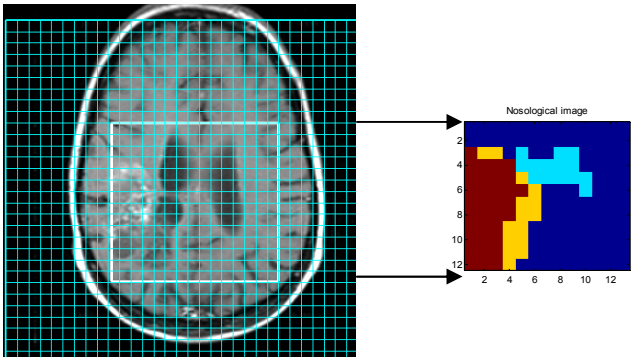


Figure 3.1 *The illustration of a T_2 weighted image of a brain affected by oligodendroglioma grade III (left). The tumor lesion is localized in the left middle area of the MRSI grid. Based on the MRSI information available from this patient each voxel is classified and the results are transformed into a nosologic image (right), where red and yellow represent grade III and grade II glioma, respectively. Dark blue stands for normal tissue and light blue for cerebrospinal fluid.*

Nosologic imaging has also been used to visualize the results of a classification approach where multimodal sources of information coming from *in vivo* and *ex vivo* MR data were considered (Croitor Sava et al., 2011d). Furthermore, nosologic images were drawn based on the abundance maps, reflecting the presence of necrosis, viable tumor cells or infiltrations in the MRSI grid, extracted using BSS techniques as described in details in Chapter 6, Section 6.2.

3.7 Conclusions

In this chapter an overview was provided of different algorithms that are used in the thesis for the classification of *in vivo* and *ex vivo* MR data. Using supervised and unsupervised classification methods as the ones described in this chapter one can obtain very accurate classification results. Nowadays in most hospitals data from an increasing number of modalities (MRS, MRSI, MRI, HR-MAS, etc.) are acquired. By means of advanced pattern recognition methods, such as CCA, we can combine them to improve the classification performance. BSS methods that respect the non-negativity of the MRS data are also gaining more and more interest these days since they can provide not only information regarding the tissue type present in the data, but also the abundance of each tissue type. To measure the performance of the classification and to identify the most appropriate number of classes, when this value has to be given *a priori* to the classification, several validity indices and performance tests are proposed. Moreover, nosologic images, which allow a user friendly visualization of the results, are introduced.

Chapter 4

AQSES-MRSI for the quantification of MRSI data using spatial information

Magnetic Resonance Spectroscopic Imaging (MRSI) provides MR spectra from multiple adjacent voxels within a body volume represented as a 2 or 3 dimensional matrix, allowing measurement of the distribution of metabolites over this volume. This chapter[1] describes an advanced metabolite quantification method for MRSI data, AQSES-MRSI, in which the available spatial information is exploited. A nonlinear least squares algorithm, where prior knowledge is included in the form of proximity constraints on the spectral parameters within a grid and optimized starting values, is proposed. A penalty term that promotes a spatially smooth spectral parameter map is added to the fitting algorithm. This method is adaptive, in the sense that several sweeps through the grid are performed and each solution may tune some hyperparameters at run-time. AQSES-MRSI has been tested on simulated MRSI data with several types of disturbances and on short echo time in vivo proton MRSI data. Moreover, AQSES-MRSI performance is compared against AQSES, QUEST and the quantification software LCModel.

4.1 Introduction

As opposed to single-voxel MRS measurements, the MRSI signals usually have a lower quality, due to the spatial/spectral trade-off for the available measuring time. Thus, retrieving accurate estimates of the most relevant metabolite concentrations remains a challenging computational task because of magnetic field inhomogenieties, relatively low signal-to-noise ratio (SNR) and physiological motion, compromising spectral resolution and leading to

[1] Croitor Sava AR, Sima DM, Poullet JB, Wright AJ, Heerschap A, Van Huffel S. Exploiting spatial information to estimate metabolite levels in two-dimensional MRSI of heterogeneous brain lesions. NMR in Biomedicine. 2011; 24(7): 824–835.
and
Sima DM, Croitor Sava A, Van Huffel S. Adaptive alternating minimization for fitting magnetic resonance spectroscopic imaging signals. Recent Advances in Optimization and its Applications in Engineering. Eds. M. Diehl, F.Glineur, W. Michiels., Lirias number: 265005. 2010: 511-520.

strongly overlapping metabolite peaks. Since MRSI provides measures of multiple metabolites simultaneously at each voxel, there is furthermore great interest in exploiting the available spatial information, as this is expected to improve the accuracy of quantification compared to processing the signals on an individual voxel basis.

Incorporating spatial prior knowledge to optimize processing of MRSI data has been addressed previously (Pels, 2005; Kelm, 2007; Bao and Maudsley, 2007). The prior knowledge that has been considered so far includes the assumption that the signals are perfectly aligned in frequency, and/or the phase of the resonances is constant over the grid under proper preprocessing (Pels, 2005), that the frequency, damping and phase parameters have spatially smooth variations (Kelm, 2007), that the metabolite composition of each tissue type is relatively constant over a local region, and MRI-derived tissue distribution functions can be used as prior knowledge for MRSI quantification (Bao and Maudsley, 2007). In all these approaches a common quantification solution is formulated for the whole MRSI grid assuming that many characteristics of the signals within the same grid are related. Still, differences in the signals may appear due to the heterogeneity of the tissue under investigation and inhomogeneities in the magnetic field applied in the scanner. It is well-known that some metabolite concentrations differ with tissue type. For example the compound N-Acetyl Aspartate (NAA) is reduced in voxels containing tumor tissue as compared to normal tissue (Howe et al., 2003b; Magalhaes et al., 2005). Moreover, T2 relaxation times of metabolite spin systems may also depend on tissue type (Frahm et al., 1989; Oros-Peusquens et al., 2008) and pathology (Kamada et al., 1994). At the same time, the spectral parameters such as damping and frequency are magnetic field-dependent. The process called shimming aims to obtain a constant magnetic field throughout the MRSI grid. Although an optimal shimming result is not guaranteed, it is reasonable to assume that there are no abrupt changes in the magnetic field between neighboring voxels and that possible variation in the damping and frequency parameters proceed smoothly over the considered MRSI grid. Exceptions could be the occurrence of abnormal features strongly affecting susceptibility, such as bleeds or cysts or for voxels at sharp boundaries like the borders of ventricles.

AQSES-MRSI is a novel approach: an alternating nonlinear least squares algorithm for fitting and modeling MRSI data, in which both the parameters' variability and similarity within an MRSI grid are considered. In the quantification of all voxels, penalties are added to promote, within neighboring regions, smooth parameters maps for frequency shifts and damping corrections, while allowing complete freedom to the metabolite amplitudes (metabolite concentrations). Due to the heterogeneity of the tissue that characterizes brain tumors, and to the variations induced by magnetic field inhomogeneities, a common optimization over the whole MRSI array is not explicitly formulated, as opposed to previous studies (Pels, 2005; Kelm, 2007; Bao and Maudsley, 2007). A dynamic approach, in which the bounds on the relevant values of the parameters are iteratively adapted, and/or the parameters of the model function take at each iteration a new starting values for each voxel, is considered. To assess the quality of the AQSES-MRSI method, an extensive Monte Carlo simulation study and several *in vivo* MRSI examples of brain tumor patients are presented.

4.2 The proposed method

AQSES-MRSI is a fully automated method to estimate metabolite levels in MRSI data, which includes spatial information of neighboring voxels. It is an important extension of the time-domain quantification method AQSES (Accurate Quantitation of Short-echo Time Magnetic Resonance Spectroscopic Signals) (Poullet et al., 2007a) for MRSI data. AQSES-MRSI fits the measured signal to a nonlinear model (Sima and Van Huffel, 2007), which is derived from metabolite profiles that are measured in vitro or quantum-mechanically simulated. The AQSES optimization problem, described in detail in Chapter 2, is further modified in order to account for the spatial prior knowledge available when dealing with MRSI data. AQSES-MRSI's enhanced performance with respect to the time-domain quantification methods AQSES and QUEST, both working on a single-voxel basis, is demonstrated. An analysis of MRSI data by LCModel software is also included for comparison reasons. The proposed method is embedded as a plug-in to the in-house software SPID (Poullet, 2008), a Matlab® (The MathsWorks™) platform for advanced spectroscopic signal preprocessing, processing and classification.

4.2.1 Modalities of exploiting spatial information

If one considers a voxel *c* within an MRSI grid of voxels, smooth parameter maps can be locally measured at voxel *c* by using the parameter value at the current location and the values in a certain neighborhood. AQSES-MRSI starts by individually fitting each signal in the grid using nonlinear least squares (Sima and Huffel, 2007; Poullet et al., 2007a). Then several sweeps through the grid are performed until convergence. At each sweep spatial information is taken into account in the fitting algorithm by imposing smoothness constraints in more steps, outlined below:

- 1st step: in this step changes are made to the starting values of the nonlinear parameters, θ_c (vector containing damping corrections and frequency shifts for voxel *c*), to be set to the median of the parameter values from the considered neighbors θ_s, obtained in the previous sweep ($s = 1,\ldots,S$, where S is the total number of voxels in the considered neighborhood).

- 2nd step: this step optimizes the bounds on the parameters' variability. An extra box constraint is added so that the parameters of the neighboring voxels do not present a high variability. The upper and lower bounds of this constraint are imposed by tightening the previous box based on the current information available in the neighboring voxels.

- 3rd step: in this step spatially smooth parameter maps for the frequency shifts and damping corrections are imposed. The nonlinear least squares problem is modified by adding

a penalty term, which builds a sum over the squared distances between the parameters of all neighboring voxels. The weight on the smoothness of individual parameters is adjustable.

Adaptive alternating minimization

The optimization problem is highly dimensional since in practice one may have grids of at least 16×16 voxels and at least 10 metabolite signals in the basis set, leading to a total of more than 5000 nonlinear variables. However, the objective function is a sum of squares, where each term contains only a few variables. Thus, the total optimization problem is a natural candidate for an alternating minimization procedure, where this type of subproblems is solved for each voxel in several sweeps through the grid, until convergence.

In a statistical setting, this type of alternating minimization has been introduced in the field of computer vision under the name iterated conditional modes (ICM). An extension of ICM to MRSI data is proposed in (Kelm, 2007; 2011).

Alternating minimization algorithms are known to converge under very mild conditions (Csiszar and G. Tusnady, 1984). Recently, convergence properties have been analyzed for the situation when the problem statement slightly changes from sweep to sweep (Niesen et al., 2009). In (Niesen et al., 2009) the variables are partitioned in only two sets, while here an adaptive alternative minimization with a large number of subsets (one subset per voxel) is applied. Slight changes in problem formulation are expressed, in our case, as modifications of the hyperparameters of the problem. The new subproblem at each sweep, for each voxel, is very similar to (Niesen et al., 2009), except that the box constraint may vary at each sweep, and so do the regularization factors.

The convergence

The convergence measure is defined at each sweep *i* as:

$$C_i = \frac{1}{PL} \sum_{l=1}^{L} \sum_{p=1}^{P} \frac{\left(\theta_l^{\,i}(p) - \theta_l^{\,i-1}(p)\right)^2}{\theta_l^{\,i}(p)^2} \tag{4.1}$$

Where $\theta_l^i(p)$ is the estimated parameter p of signal l in sweep i, P is the number of parameters per signal, L is the number of signals. The iterative algorithm continues until $C_i<0.001$ or a maximum of 10 sweeps is reached. Still we observed that the convergence is typically reached in less than 10 sweeps.

Starting values of the nonlinear parameters

In the single voxel implementation of AQSES, it was found convenient to set to zero all the initial values of the nonlinear parameters (frequency and damping corrections). In this way the optimization starts with no spectral correction with respect to the signals from the

metabolite basis set. The latter are assumed to be reasonably aligned to the *in vivo* signals. In AQSES-MRSI spatial information is introduced by initializing the nonlinear parameters of the voxel of interest with the median value of parameters in the previous sweep from the voxels considered in the selected neighborhood area. The first sweep uses initial values equal to zero.

$$\theta_c^i = median(\theta_s^{i-1}) \tag{4.2}$$

where θ_c^i represents the starting values of the nonlinear parameters at sweep *i* and θ_s^{i-1} represents the optimal parameters of the surrounding voxel *s* obtained at sweep *i-1*.

Spatial constraints

In the 2nd step an effective spatial constraint is introduced such that the parameters of the neighboring voxels do not yield a high variability. AQSES itself uses soft constraints (i.e., reasonable bounds on the damping and frequency corrections) of the form $d_k \in [0, A_d]$, $f_k \in [-A_f, A_f]$, where A_d and A_f are small scalar values. Recall that the nonlinear parameters represent corrections applied to the metabolite profiles. These soft constraints can be written in vector form as a box constraint: $\theta_c \in [B_{low}, B_{up}]$. The allowed parameter variation in this step of AQSES-MRSI is bounded by the following interval:

$$\theta_c^i \in [\overline{\theta}_s^{i-1} - \alpha^{i-1} B_{low}, \overline{\theta}_s^{i-1} + \alpha^{i-1} B_{up}] \tag{4.3}$$

where α^0 is a scalar value initially set to 0.25, $\overline{\theta}_s^{i-1}$ is computed at sweep *i* as the mean of the damping and, respectively, frequency of the voxels surrounding the voxel of interest and estimated in the sweep *i-1*. The value of α^i decreases with each sweep as $\alpha^i = \alpha^0 / i$, where *i* is the sweep counter.

Penalty term

Finally, in the 3rd step, inspired by (Kelm, 2007), a penalty term over the parameter maps is formulated. With AQSES-MRSI a complex optimization problem is considered by imposing a trade-off between solving the minimization problem and minimizing the nonlinear parameters variation within neighboring regions:

$$\min_{\theta_c} \frac{1}{N} \sum_{t=t_0}^{t_{N-1}} \left| y_c(t) - \hat{y}_c(t, \theta_c) \right|^2 + \sigma^2 \sum_{\theta_c \neq \theta_s} \varepsilon_s \beta_{cs} \left\| W(\theta_c - \theta_s) \right\|_2^2 \tag{4.4}$$

where the signal $y_c(t)$ corresponds to voxel *c* and the model $\hat{y}_c(t,\theta_c)$ is considered as a weighted sum of metabolite signals with nonlinear corrections θ_c. Spatial information is introduced via the second term, called penalty term, which encourages a smooth solution for the problem (Kelm, 2007). The penalty terms are multiplied by adjustable scalar penalty parameters ε_s, which account for the trade-off between an optimal fitting of the current signal and the penalty.

σ^2 is an estimate of the noise variance computed from the tail of the signal in the time domain in voxel *c*. β_{cs} is a weighting scalar which gives the influence of the parameters θ_s on the parameters θ_c, as described below. *W* is a diagonal weighting matrix, with $W \in R^{Km \times Km}$, which accounts for the scale differences between parameters, where *K* is the number of metabolite profiles and *m* is the number of parameters per metabolite. For example, for the Lorentzian model, *m=2* (damping and frequency), if one uses variable projection and solve for amplitude and phase in closed form. Thus *W* can be used to adjust the weight on the smoothness of certain individual parameter maps and even to turn off smoothing for some of the parameters by using a zero weight. In summary, all the parameters in the penalty term, ε_s, σ^2, *W* and β_{cs}, determine the trade-off between fitting the individual signals against smoothing the parameter maps.

The spatial model

Following the work of (Laudadio et al., 2005), a sliding window method is applied, i.e., the sweeps go through the voxels row-wise (a checker-board pattern or a spiral starting from the center of the grid are also possible). In choosing the geometry of the neighborhood, different models can be used for introducing spatial information in the optimization problem (Friman, 2003). Yet, based on the assumption that tissue and magnetic field inhomogeneities influence the parameter maps, spatial constraints are further considered only within the voxels surrounding the voxel of interest, restricting in this way the neighborhoods to small areas. Throughout the 2D experiments the "3x3 spatial model" (the adjacent voxels plus voxels on the diagonal are considered as neighbors, giving a total of 8 voxels (Friman, 2003), see Figure 4.1-a) is used. An extension to the 3D MRSI case could be possible. The selection of a fixed neighborhood (Friman, 2003; Laudadio et al., 2005) can be a disadvantage, in particular for very heterogeneous data. To overcome this limitation, an extra decision factor in the proposed method, β_{cs}, which makes the process of selecting the neighborhood more flexible, is introduced. In this way, AQSES-MRSI allows the user to account for both the similarities and the variability within an MRSI grid.

The spatial information is taken into account via:

$$\beta_{cs} = \beta_{cs}^{neighborhood} \beta_{cs}^{tissue} \tag{4.5}$$

where $\beta_{cs}^{neighborhood}$ is 0 or 1 depending on whether voxels *c* and *s* are neighbors according to, e.g., the "3x3 spatial model" for selecting the neighborhood area, see Figure 4.1 - a.

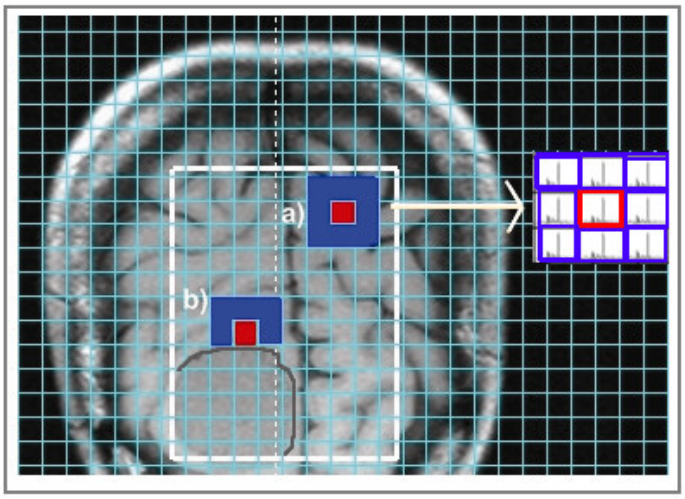


Figure 4.1 *Visualization of the neighborhood regions (blue color) that is taken into account in the spatial model for the parameter map of the voxel of interest (red color). In a) the neighborhood contains all the voxels selected with the "3x3" spatial model. In b) the neighborhood contains only the voxels selected with the "3x3" spatial model and belonging to the same tissue class.*

β_{cs}^{tissue} is based on tissue information and reflects how similar two voxels *c* and *s* are, independently from spatial consideration. The higher β_{cs}^{tissue}, the higher the influence of voxel *s* on voxel *c*, in other words, the closer the parameters θ_c and θ_s should be. To simplify, one can use $\beta_{cs}^{tissue} = 1$ if tissue type is similar, and $\beta_{cs}^{tissue} = 0$ otherwise. β_{cs}^{tissue} has to be available as prior information (Figure 4.1-b). It can be obtained in an prior step via MRI segmentation or classification. This segmentation procedure is not part of this study.

Choosing the weighting matrix *W*

The diagonal matrix *W*, which accounts for the different scales and variability of the parameters, can be used to adjust the smoothness of individual parameter maps. Let

$$W = \begin{pmatrix} W_d & 0 & \dots & 0 & 0 \\ 0 & W_d & \dots & 0 & 0 \\ \dots & \dots & \dots & \dots & \dots \\ 0 & 0 & \dots & W_f & 0 \\ 0 & 0 & \dots & 0 & W_f \end{pmatrix}$$

where $W \in R^{Km \times Km}$. Equal weights for all damping corrections and equal weights for all frequency shifts are considered. Both for simulation experiments as well as for *in vivo* data $W_d = 0.2$ is used for the Lorentzian damping parameters and $W_f = 2$ for the frequency maps (Kelm, 2007).

Choosing the penalty parameters ε_s

The positive scalar parameters ε_s accounts for the trade-off between fitting the model $\hat{y}_c$ to the signal y_c in least squares sense and imposing the minimization of the penalty term. ε_s is allowed to be adaptively chosen for each particular signal at each sweep by evaluating the current residual sum of squares $RSS = \frac{1}{N}\sum_{t=t_0}^{t_{N-1}} \left| y_c(t) - \hat{y}_c(t, \theta_c) \right|^2$ and the current penalty norm $penalty_s = \left\| W(\theta_c - \theta_s) \right\|_2^2$ and setting $\varepsilon_s = 0.1\sqrt{RSS} / \sqrt{penalty_s}$, which gives 90% importance to the fit and 10% importance to the penalty.

4.3 Experimental results using simulations and real-life examples

In this section, to evaluate the robustness and performance of the method, a simulation and an *in vivo* experiment were designed. Firstly, for several types of disturbances, Monte Carlo studies were performed on a series of MRSI simulated signals grouped in simulated MRSI grids of dimension 3x3 voxels. Tests on real life MRSI data are also performed and the method is compared with AQSES, QUEST and LCModel software.

4.3.1 Simulation experiments

The simulated MRSI signals were obtained as a linear combination of 11 metabolite profiles, which were individually shifted in frequency and broadened as described in the previous section: nine measured metabolite profiles: NAA, myo-inositol (Myo), creatine (Cr), phosphocholine (PCh), glutamate (Glu), lactate (Lac), alanine (Ala), glucose (Glc), taurine (Tau) plus two simulated lipids profiles: lipids at 1.3ppm (Lip1) and lipids at 0.9ppm (Lip2) The measured profiles were selected from a measured database acquired with a 1.5 T Philips NT Gyroscan using a PRESS sequence with an echo time of 23 ms, and a PRESS box of 2 *x* 2 *x* 2cm^3, as described in (Poullet et al., 2007a). 225 MRSI simulated signals grouped in 25 simulated MRSI grids of dimension 3x3 voxels were designed.

Noise disturbance

AQSES-MRSI performance for different levels of noise was measured. White Gaussian noise with different levels of SNR (10, 15, 20, 25 and 30) was added to the signals, see Figure 4.2. The signal power, P_{sig} , was measured for each signal as the squared Euclidean norm of the time-domain signal divided by the length of the signal, and transformed to dB through $P_{sig} = 10\log_{10}(P_{sig})$. Then the standard deviation of the added noise, *N(t),* for the different levels of SNR was computed as:

$$std_{N(t)} = \sqrt{10^{\left(\frac{P_{sig}-SNR}{10}\right)}} \tag{4.6}$$

For this experiment, damping, frequency and amplitude values were set to take values corresponding to the signals measured in normal brain tissue. These nominal values were chosen as in (Poullet et al., 2007a) and are within the intervals reported for *in vivo* MRSI (Howe et al., 2003b, Devos, 2005b). Typically, before quantifying *in vivo* MRSI data, a phase-correction preprocessing step is performed. Assuming phase-corrected *in vivo* MRSI data, within the same grid, the phase values are kept constant for the same metabolite profile. Randomly valued, but reasonably smooth (i.e., almost constant) parameter maps were considered for damping and frequency so that, for each metabolite, the distortions of the exponential damping factor are limited to ±15% from its nominal value *d* within the MRSI grid. Thus, the damping values for each metabolite uniformly cover the interval [*d – 0.15*d, d + 0.15*d*]. Similarly, frequency shifts are allowed a variation of ±10%, [*f–0.1*f, f+0.1*f*].

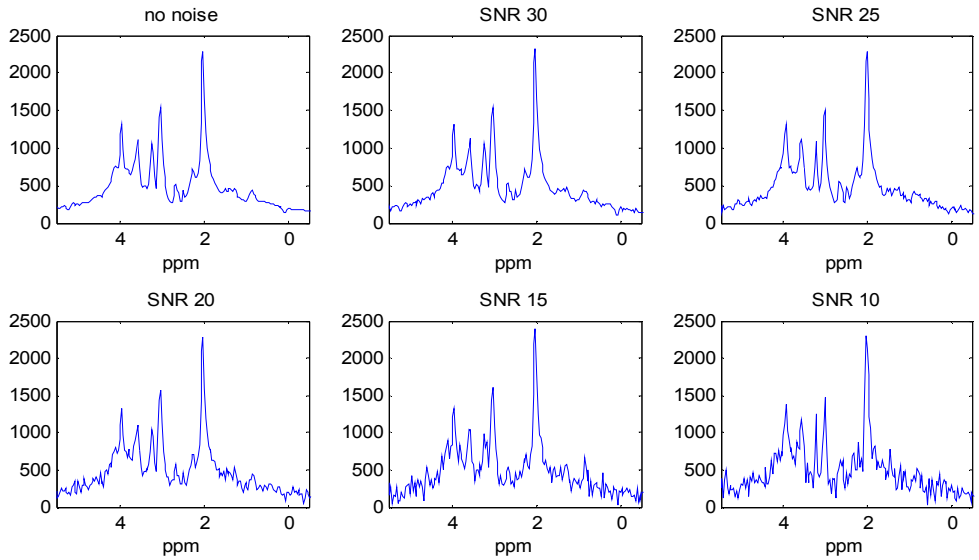


Figure 4.2 *Simulated MRSI spectra reflecting normal brain tissue profile and presenting different levels of noise (SNR = 30, 25, 20, 15, 10 and a noise free case).*

Magnetic field inhomogeneities disturbance

In order to analyze the effect of sharp edges versus smoothness and the influence of different levels of inhomogeneities on the performance of AQSES-MRSI, a 2nd simulation experiment was designed. For this purpose four MRSI datasets of 10x10 voxels have been generated with different parameter maps. Each simulated MRSI grid containing a region with normal-tissue-like spectra and a region with tumor-like spectra. The considered parameter maps present:

A. sharp edges but constant parameter values within a tissue region and different between the regions;

B. sharp edges with slightly varying random parameters values within the tissue region, but highly different between the regions;

C. sharp edges with smooth parameter map within the tumor region, and

D. smooth edges with smooth parameter maps over the whole grid.

Gaussian white noise of SNR = 15 was added to all signals.

Performance measurement
The relative mean-squared error (RMSE) was computed for each metabolite k within the simulated grid, as follows:

$$RMSE_k = \left(\frac{1}{L} \sum_{l=1}^{L} \frac{(\hat{a}_{k,l} - a_k^{sig})^2}{(a_k^{sig})^2} \right) \tag{4.7}$$

where $\hat{a}_{k,l}$ is the estimated amplitude of the l^{th} signal and a_k^{sig} is the true amplitude. L is the number of signals within the MRSI grid.

The performance over the whole grid and over all metabolites is computed as:

$$RMSE = \left(\frac{1}{K} \sum_{k=1}^{K} RMSE_k \right) \tag{4.8}$$

where K defines the number of metabolites.

For every specific test, the corresponding Cramer-Rao lower bounds (CRB) are computed from the Fisher information matrix corresponding to the true parameter values of the nonlinear model function. Then, the calculated RMSEs are compared to the theoretical CR bounds. This gives us an excellent indication of the gain in the accuracy that can be obtained by using AQSES-MRSI.

4.3.2 *In vivo* MRSI studies

To verify to which extent the conclusion drawn in the simulation studies are consistent with real conditions, in other words, to analyze whether the method preserves its robustness and accuracy when applied to real data, *in vivo* studies are performed. To this end the method is applied to several *in vivo* MRSI measurements.

The cases are extracted from the INTERPRET database (http://azizu.uab.es/INTERPRET/) and were acquired in the Radboud University of Nijmegen Medical Centre (RUNMC) on a 1.5T clinical MR system (Siemens Vision), using a 2D STEAM pulse sequence with the STEAM box positioned in a transversal plane through the brain showing the largest tumor

diameter in the Gd contrast enhanced image. The study was approved by the ethical committee of the UMCN and for tumor typing followed the rules of the World Health Organization (WHO). The MRSI parameters are: 16x16x1024 samples, TR/TE/TM=2000 or 2500/20/30 ms, slice thickness = 12.5 or 15 mm, FOV (field of view) = 200 mm, spectral width = 1000 Hz. The water suppressed MRSI signals are preprocessed as follows: filtering of k-space data by a Hanning filter of 50% using the LUISE software package (Siemens, Erlangen, Germany), zero filling to 32 x 32 and spatial 2D Fourier transformation to obtain time domain signals for each voxel, eddy current correction, water removal with HLSVD-PRO (Laudadio et al., 2002) and baseline correction performed as described in (Poullet, 2008). Finally, all spectra were normalized with respect to the amplitude of the water unsuppressed signal. The SNR of the preprocessed data is computed as the power of the signal, $P_{sig,}$ after extracting the estimated noise power, divided by the power of noise, $P_{noise,}$ computed from the last 180 points of the time-domain signals. For the considered data, SNR values are between 8 and 16 dB.

As in the simulation study, 9 measured metabolites and 2 simulated ones were considered for quantifying the data. The measured metabolite profiles were selected from a measured basis set acquired on a 1.5 T Siemens system, using a STEAM sequence with an echo time of 20 ms, and a STEAM box of 2x2x2 cm^3, as described in (Poullet et al., 2007a). These metabolites were chosen based on their potential as biomarkers to separate between different brain tissue types as well as to identify brain lesions. Another important aspect in the choice of a restricted basis set is that fitting metabolites that are actually not visible in the spectrum or that are too correlated with each other may increase the complexity of the problem and affect the accuracy of the algorithm (Poullet et al., 2007a). AQSES-MRSI can be combined with any other simulated or measured basis set under the same protocol as the considered *in vivo* data and the basis set given here is just a representative example.

The performance of AQSES-MRSI on *in vivo* MRSI cases is compared with the single voxel time domain quantification methods AQSES (Poullet et al., 2007a) and QUEST (Ratiney et al., 2005) as implemented in jMRUI Version 4.0, applied on individual voxels (Naressi et al., 2001). AQSES-MRSI results are also compared with LCModel (Provencher, 2003), which incorporates a functionality that allows the user to consider spatial information when analyzing multivoxel data. When quantifying the *in vivo* MRSI data with LCModel Version 6.2, the same metabolite basis set as for the other methods was considered. To asses the quality of the fit, the quantification results are translated into metabolic maps. Additionally, an analysis of the fit and of the residual is performed.

4.4 Results

4.4.1 AQSES-MRSI performance

Noise influence

AQSES-MRSI performance for different noise levels are presented in Figure 4.3. The results are compared with the single-voxel approach AQSES. This is done separately for the sequential steps of the algorithm (see Section 4.2.1) so that one can observe how each step, aimed at introducing spatial prior knowledge, influences the quantification results. For low level of noise both AQSES and AQSES-MRSI 1st, 2nd and 3rd step prove to be very robust and accurate as the RMSE curves almost converge to the CR bound values.

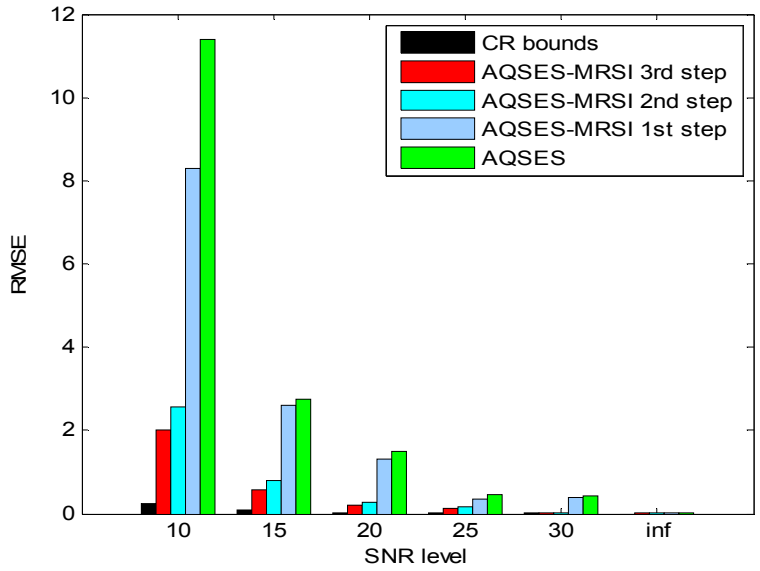


Figure 4.3 *Mean of the RMSE amplitude values computed for the 25 simulated MRSI grids of 3x3 voxels, for different levels of SNR (30, 25, 20, 15, 10 and a noise free case); the influence on the performance of each step within the AQSES-MRSI algorithm.*

For higher levels of noise, there is a clear difference between the individual voxel approach versus the multivoxel approach. From the results we can conclude that incorporating spatial information in the form of dynamic starting values for nonlinear parameters contributes in minor percentage to the final performance reached by AQSES-MRSI, as a small improvement in the accuracy is obtained after this step (see AQSES-MRSI$_{1st\ step}$). The gain in accuracy becomes obvious after the 2nd step where soft constraints on the damping and the frequency

parameter maps were imposed (see AQSES-MRSI$_{2nd\ step}$). After the 2nd step, the accuracy with respect to the single-voxel approach improves with up to 70% at low SNR. At high noise levels (see Figure 4.3), the last step, which imposes smoothness penalties, AQSES-MRSI$_{3rd\ step,}$ brings an improvement of 78% in the accuracy.

The performance of AQSES-MRSI for each metabolite individually is also investigated (Figure 4.4). A major improvement in estimating the overlapping metabolites (Lip1, Lip2, Lac and Ala) is obtained with the proposed method. Low standard deviation values with respect to the mean performance are registered with AQSES-MRSI proving that the problem of metabolite mis-quantification is reduced. Indeed, these peaks are strongly overlapping with other metabolites, thereby decreasing the robustness of metabolite estimation. In contrast, AQSES-MRSI still provides good estimates showing that by using spatial constraints in the fitting algorithm we are able to obtain robust parameter estimation of overlapping peaks; see Figure 4.5 for the RMSEs of these metabolites for a range of SNRs.

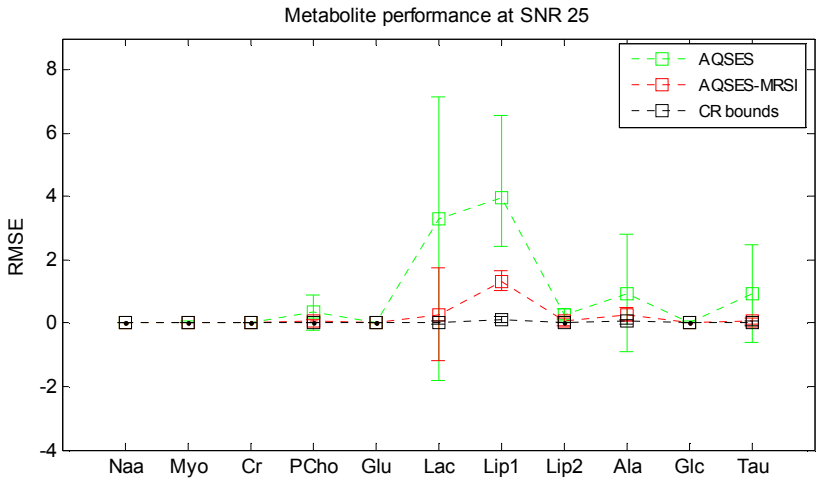


Figure 4.4 *Mean of the RMSE$_k$ amplitudes values computed for the 25 simulated MRSI grids of 3x3 voxels, for different metabolites. Vertical lines show the mean and the standard deviation values. SNR level is 25.*

Inhomogeneity influence

To analyze the impact of using spatial information in quantifying inhomogeneous data, the results obtained with AQSES-MRSI in the second experiment are further presented. Here four sets of simulated MRSI grids presenting different types of parameter maps were used. The results of this experiment are presented in Figure 4.6. Regardless of the degree of inhomogeneity, AQSES-MRSI outperforms the single voxel approach. The RMSE for

AQSES-MRSI stays constantly below 3 within the MRSI grid. For the voxels situated at the interference between the two considered tissue types we can notice some problems for the sharp edge maps (see map A and map B). Even if the error remains low in these regions, the performance of the algorithm is influenced by sudden parameters change.

The error in estimating the metabolite concentrations for map D are detailed in Figure 4.6.b-c. A percentage of improvement of up to 75% is reported when using AQSES-MRSI. The estimates obtained with AQSES-MRSI are very close to the true amplitudes regardless of the tissue type. AQSES performance shows to be tissue type dependent (see the error maps of the following metabolites: Cr, Lac, Lip1, Lip2, Ala, in Figure 4.6.b). This drawback is a consequence of the fact that metabolite concentration varies with the tissue type and, therefore, metabolites in low concentration in a certain region can not be estimated with high accuracy with a single voxel approach. With AQSES-MRSI this problem is reduced.

4.4.2 The effect of including spatial prior knowledge when analyzing *in vivo* MRSI data

In this section the performance of AQSES-MRSI on *in vivo* MRSI data is further analyzed.

Metabolic maps
The results obtained with AQSES-MRSI on different patients with different brain tumor types (a meningioma, a glioblastoma and an oligoastrocytoma tumor grade III) are illustrated and discussed. Since this study is not aimed at evaluating a preliminary MRI segmentation step, when defining the parameters β_{cs} tissue class prior knowledge is not included. This means that we impose the spatial constraints on all the voxels surrounding the voxel of interest as defined with the 3 x 3 spatial model (see Section 4.2.1). The resulting metabolite estimates are exported into metabolite maps. By analyzing these maps one can have a fast visual overview on the performance of the method. No post-smoothing has been performed on the metabolite map images.

Results show that the AQSES-MRSI method provides a much less noisy spatial metabolite distribution with well-contoured metabolic maps, as opposed to AQSES, QUEST and LCModel. Even for metabolites that are difficult to quantify with conventional approaches the proposed method gives good results, as can be seen in Figures 4.7, 4.8 and 4.9.

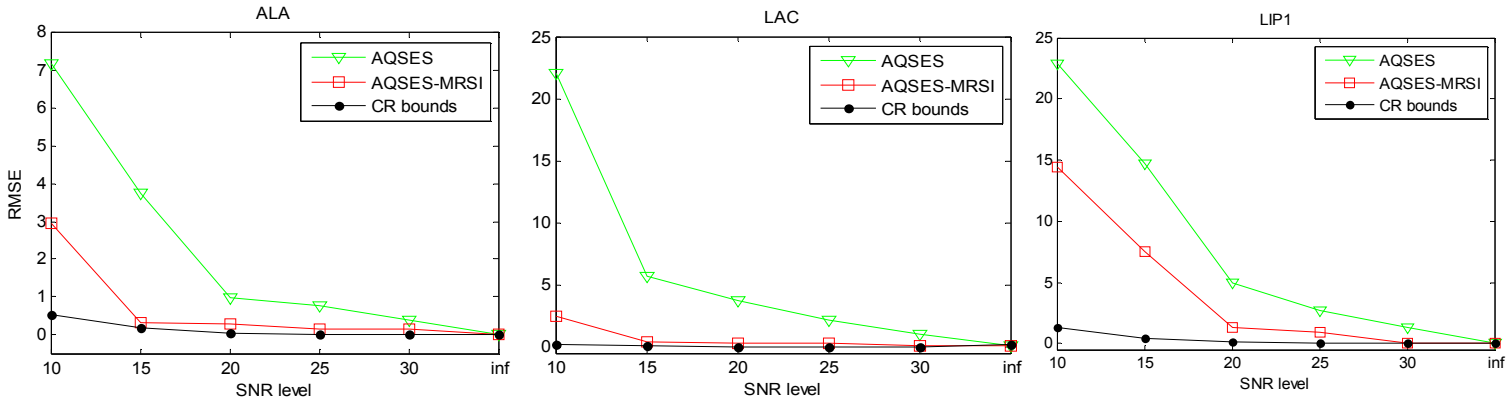


Figure 4.5 *Mean of the $RMSE_k$ amplitudes values of Ala, Lac and Lip1 computed for the 25 simulated MRSI grids of 3x3 voxels for different levels of SNR.*

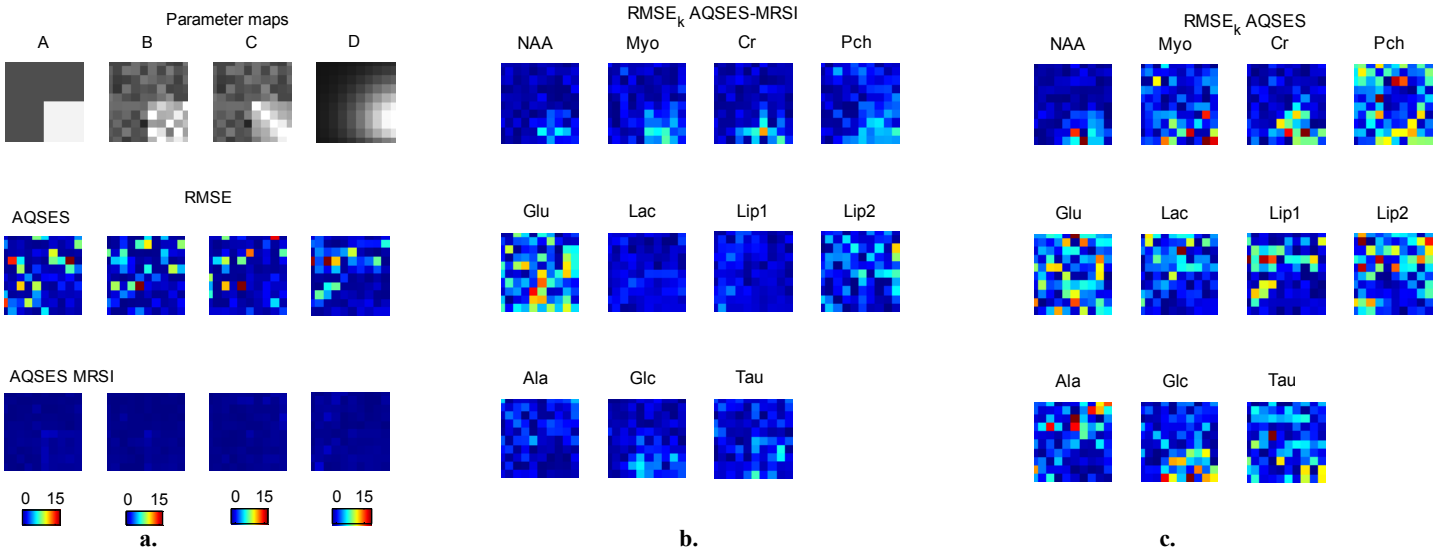


Figure 4.6 ***a.*** *Simulated MRSI grids with different parameter maps: A-D. 25% of the MRSI grid contains tumor like spectra (lower right corner) and 75% of the grid presents normal tissue like spectra. Color maps with the RMSE values for each voxel are presented for AQSES and AQSES-MRSI (see 2nd and 3rd row). In* ***b.*** *and* ***c****. the performance of AQSES-MRSI versus AQSES in estimating the metabolite concentrations for map D is detailed for each metabolite.*

For the meningioma patient, AQSES-MRSI results are in agreement with previous studies, (e.g. Maruyama et al., 1999; Fountas et al., 2000; Howe et al., 2003b) and in the tumor area the NAA, Cr and Myo levels are lower with respect to the non-affected area, while Glc levels are higher. The Myo and Glc metabolite maps drawn based on the results obtained with the single-voxel approaches are noisier and a clear differentiation between the normal and tumor tissue is not obtained when analyzing the levels of these compounds over the whole grid (Figure 4.7). A decrease in NAA and Cr in the tumor area is observed for all four approaches. Still, a smoother map is obtained when using spatial prior knowledge. Compared to LCModel, similar metabolite maps were obtained for NAA, Cr and Myo. The LCModel map for Glc is in disagreement with all the other results and with the literature (Maruyama et al., 1999).

For the patient with a glioblastoma (Figure 4.8), Ala and Lac concentration estimates with AQSES-MRSI are increased in the tumor region while NAA is low, which has been observed in previous studies for these tumors (e.g. Kinoshita and Yokota, 1997; Howe et al., 2003b). Lips levels are reported by all methods as elevated in the affected area, being very high towards the center of the tumor area which could be a sign of necrotic tissue (Kuesel et al., 1994; Howe et al., 2003b). Also in this example, the parameter maps obtained with AQSES, QUEST and LCModel are less smooth. For the single voxel approaches, high levels of Ala and Lac are present in isolated voxels in the normal tissue region, not likely to represent the true situation, but rather artifacts due to mis-fitting. Compared to AQSES-MRSI, LCModel, which considers spatial knowledge, provides smooth metabolites in the normal tissue region, while for the tumor region the maps are very noisy and present variations that seem to be above the limit of a normal inhomogeneity behavior (the metabolite value in a voxel within the tumor tissue region is closer to the mean of the metabolite value within the normal tissue region). A better fit is observed with AQSES-MRSI for the spectra coming from tumor regions, where the residual presents no contribution from the considered metabolites. With AQSES-MRSI the tumor region is nicely contoured and the metabolite maps are smooth through the whole MRSI grid. These results are also closer to the diagnosis agreed by the clinicians after the histopathology. Moreover, the metabolite maps seem more plausible when using the proposed spatial prior than without it, which is justified by comparing spectra of neighboring voxels.

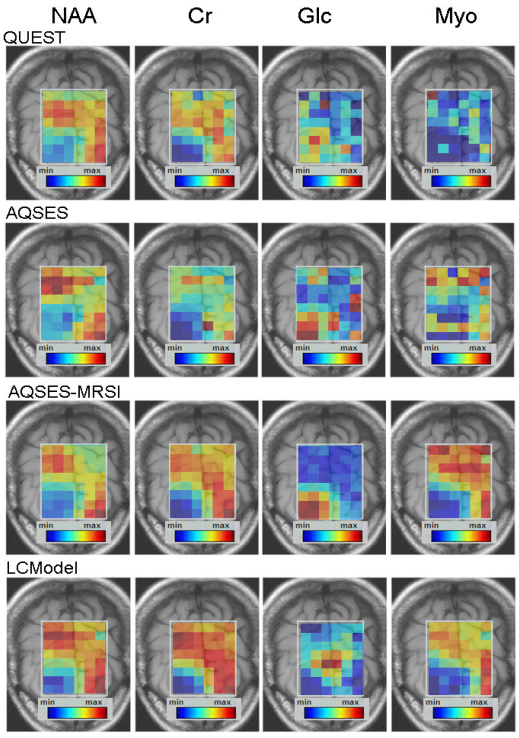


Figure 4.7 *Metabolic maps obtained after applying QUEST, AQSES, AQSES-MRSI and LCModel. The color scheme is relative to each metabolite. The patient is diagnosed to have a meningioma (lower left corner of the MRI image).*

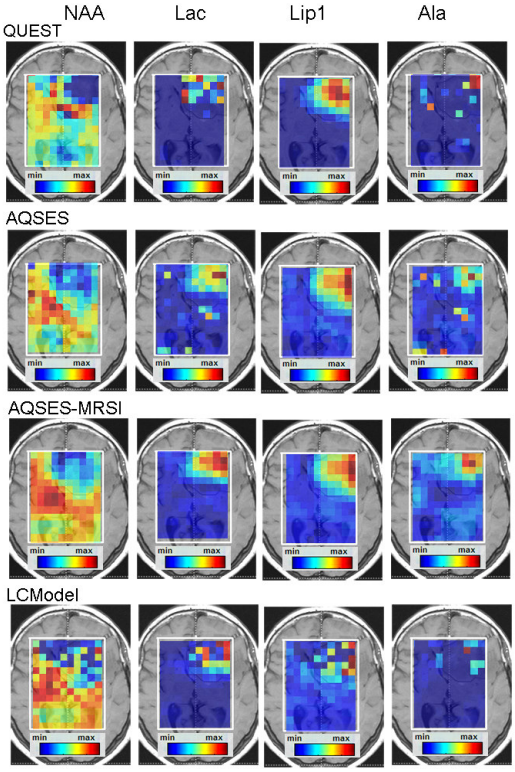


Figure 4.8 *Metabolic maps obtained after applying QUEST, AQSES, AQSES-MRSI and LCModel. The color scheme is relative to each metabolite. The patient is diagnosed to have a glioblastoma (upper right corner of the MRI image).*

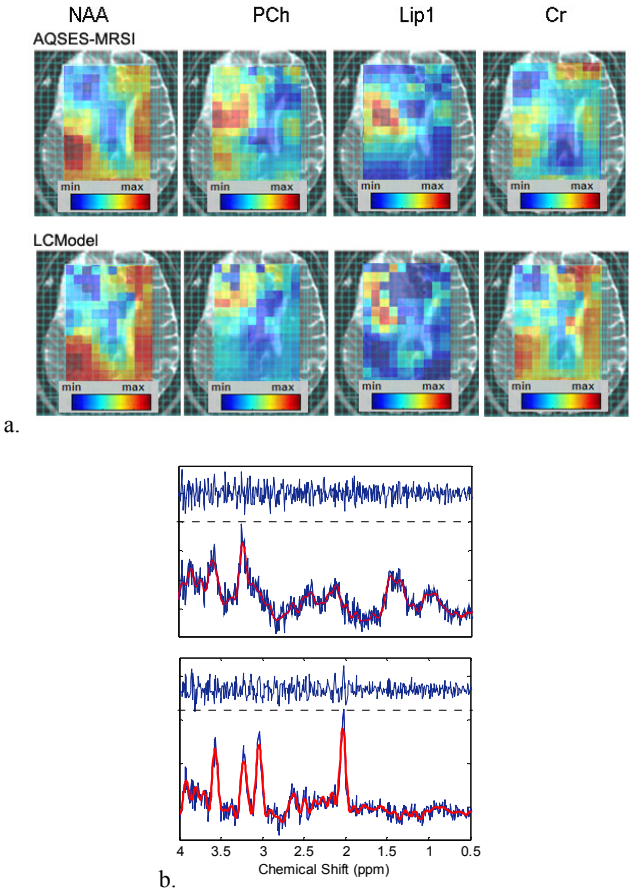


Figure 4.9 *In a. metabolic maps obtained with AQSES-MRSI and LCModel for a patient diagnosed with oligoastrocytoma tumor grade III (upper left corner of the MRSI grid). The color scheme is relative to each metabolite. In b. the quantification results obtained with AQSES-MRSI, for 2 selected spectra: the residual, the fit and the signal are visualized. Upper signal comes from the tumor region; lower signal comes from the normal tissue area.*

For the oligoastrocytoma case the quantification results allow us not only to separate between tumor and normal tissue region, but also to find the contour of the CSF zone. When analyzing AQSES-MRSI results from the quality-of-fit point of view we observe high performance both in the tumor and in the normal tissue region. As an illustration, two signals from different tissue regions are presented together with their AQSES-MRSI fit and the residual, see Figure 4.9. The residuals do not exhibit obvious unassigned metabolite peaks.

4.5 Discussion

Results show that an important advantage of using spatial prior knowledge in the quantification of MRSI spectra is that overlapping peaks as Ala, Lac and Lip_s can be better assessed independently, also in cases where single-voxel approaches fail to do so. This can represent a critical point in the quantification of MRSI data and further in the classification of brain tumors based on spectroscopic MR signals, as we know that these peaks are important biomarkers to discriminate different tissue types. In addition, resonances of metabolites present at relatively low concentration can be better estimated. This represents an added value in the analysis of MRSI data for the detection and characterization of brain lesions and disorders, as most of the classification algorithms are applied on feature vectors derived from tissue levels of relevant metabolites. Application of the new method to brain tumors, which can be very heterogeneous, showed improvements compared to conventional processing methods. Thus, it is expected that starting from more reliable spectral parameter estimates the accuracy and robustness to separate tumor and normal tissue and to differentiate between tumor types will be enhanced. AQSES-MRSI results can be used as more robust starting points towards improved tissue segmentation and classification.

The simulation studies showed that by exploiting spatial prior knowledge and by using information from the spectral parameters (frequencies, dampings) of spectra from surrounding voxels, statistically better results are obtained compared to processing the signals on an individual basis. The spectral resolution of the *in vivo* datasets was too low to permit proper differentiation between Glu and Gln; the CRB were larger than 50% for each of the two metabolites. However, the sum of Glu and Gln could be reasonably estimated.

Previous quantification studies that exploit spatial prior knowledge demonstrated that this information can improve the estimation of metabolite levels (Pels 2005; Kelm, 2007). The approach proposed in (Pels, 2005) extends the $AMARES_{ts}$ method (Advanced Method for Accurate, Robust and Efficient Spectral fitting - time series approach) (Vanhamme et al., 1999) and exploits the idea of processing the spectra within the MRSI grid simultaneously, while equating some spectral parameters across the grid. The problem is seen as a quantification of a series of MRS signals, which boils down to minimizing a cost function that includes more signals simultaneously. In (Pels, 2005) it is assumed that the frequencies and phases remain constant over the whole MRSI grid, thus equality relations between these parameters of the same type are imposed for all signals. The signals need to be preprocessed by eddy current correction and spectrum alignment such that these assumptions are sufficiently met. Then the model function is used for all the voxels, but the number of free model parameters is lowered due to the imposed equalities on frequencies and phases, respectively, across all voxels. However, the distortion of the nonlinear model parameters of *in vivo* MRS signals depends on magnetic field inhomogeneities. These are, in turn, also dependent on the heterogeneity of the tissue. Hence, such a simplified solution does not satisfy the complexity of the problem in realistic cases. To better meet such conditions, small

variations in the frequency shifts and damping corrections are allowed in AQSES-MRSI, but their parameter maps are imposed to be smooth.

In another study spatial information is being used by a hierarchy of neighborhood systems in the form of a generalized Gaussian Markov random field (GMRF) (Kelm, 2007; 2011). Instead of exact equality relations, softer constraints are considered in the form of spatially smooth parameter maps for the frequencies, dampings and phase variables. To this end, a Bayesian approach of specifying a prior distribution over the considered parameter maps is used (Chou and Brown, 1990). This means that penalty terms in the form of weighted distances between parameters of the same type are added to the nonlinear least squares fitting problem based on the classical model of a sum of damped exponentials. As in (Pels, 2005) the optimization function is modified so that several signals are fitted simultaneously and the method is not sensitive to the heterogeneity of the information contained in the MRSI grid. Although GMRF provides an elegant methodology, the structure of the GMRF is often a poor model of the true components underlying the data, especially if we deal with very heterogeneous data. Part of the problem stems from the Markov property that the relationship among adjacent voxel pairs is determined by the input features (Dietterich, 2007). First order (four neighbors) and second order (eight neighbors) hierarchies of neighborhood systems are used (Kelm, 2007). This makes the optimization problem very hard to solve because it requires a global adjustment and we deal with extremely high-dimensional data. This study shows that a computational cheaper approach for introducing spatial information can bring very satisfactory improvements in the quantification process. In our proposed adaptive method, AQSES-MRSI, a nonlinear least squares problem is solved only for the parameters of the current signal for each voxel at a time, and several sweeps through the MRSI grid are performed so that some of the hyperparameters of the problem are optimized at each sweep. Hence, as opposed to previous studies (Pels, 2005; Kelm, 2007), a common optimization for simultaneously fitting all the signals in the MRSI grid and simultaneously penalizing all their parameters was not explicitly needed in this study.

Quantification methods based on numerical optimization usually require excellent starting values for the model parameters. With AQSES-MRSI an intrinsic correction mechanism, to adapt the starting values and to correct the nonlinear parameters variability in the quantification of each signal at each sweep through the grid, is proposed. Thus, simply starting in the first sweep with zero corrections on the dampings and zero frequency shifts for all the metabolite profiles, still leaves the possibility of multi-start optimization, since starting values can change at each sweep according to the parameters of the neighboring voxels. An analysis of MRSI data by LCModel software, which also includes spatial information, showed a relatively low performance in tumor regions, suggesting that its accuracy is tissue type dependent, which could be a drawback in the processing of very heterogeneous MRSI data As in (Kelm, 2007), by adding a smoothing penalty term an improved solution is obtained. Another added value of AQSES-MRSI is the fact that neighboring regions could be dynamically chosen, giving the user the possibility to extend or to limit the neighborhood area by adding tissue prior knowledge when defining this area.

AQSES-MRSI, the methods proposed in (Pels, 2005; Kelm, 2007; 2011) and LCModel software have in common that the resolution of the parameter maps equals the resolution of the MRSI grid, although MRI information can be used for pre-assignment of voxels to a certain tissue type. An interesting different approach is considered by the recent *k*-space-time methods (Bao and Maudsley, 2007; Kornak et al., 2010), which use prior anatomical knowledge to reconstruct MRSI signals and metabolic maps at the resolution of the underlying MRI.

4.6 Conclusions

With AQSES-MRSI improved metabolite estimates of MRSI data can be obtained. This study demonstrates how essential it is to have a robust method for tuning the starting values, the soft constraints and the additional penalties involved in the optimization algorithm. Exploiting spatial prior knowledge is shown to improve the accuracy of quantification compared to processing MRSI voxels on an individual basis. It brings the advantage that overlapping peaks or peaks of compounds present at low concentration can be better resolved than in single-voxel approaches. Because of the automation of the method and its improved robustness to deal with spatial heterogeneity of spectral data, AQSES-MRSI is expected to be a better and more attractive tool to analyze clinical MRSI data, for patients with intracranial tumours, than single-voxel approaches.

Chapter 5

Classification of HR-MAS signals for tumor tissue typing in adult human gliomas

In gliomas one can observe distinct histopathological tissue properties, such as viable tumor cells, necrotic tissue or regions where the tumor infiltrates normal brain. A first screening between the different intratumoral histopathological tissue properties would greatly assist in correctly diagnosing and prognosing gliomas. In this chapter[2] the potential of ex vivo HR-MAS spectroscopy in characterizing these properties is analyzed and the biochemical differences between necrosis, high cellularity and border tumor regions in adult human gliomas are investigated. In Section 6.3 the statistical studies applied on sets of metabolite concentrations and metabolite ratios extracted from 52 HR-MAS recordings coming from patients with different grades of glial tumors are described. Then, in Section 6.4, the correlation between the histopathological tissue properties and the considered metabolic profiles is analyzed. The results are described in Section 6.5. Additionally, representative reference tissue models describing the metabolic behavior are extracted for characterizing the intratumoral tissue properties.

5.1 Introduction

Glial brain tumors are one of the most common brain tumors found among adults and are characterized by an extensive heterogeneity. This is reflected both at the level of the tumor type and grade, as well as at a microscale level, since along with viable tumor cells there may be necrotic regions. Moreover, glial tumors are highly infiltrative. Therefore, there may also be a contribution from normal brain tissue at the border of the affected area. These characteristics have posed serious difficulties in the diagnosis and prognosis of glial tumors.

[2] Croitor Sava AR, Martinez-Bisdal MC, Celda B, Cerda JM and Van Huffel S. Tissue typing within glial tumours. In Proc. of the European Society for Magnetic Resonance in Medicine and Biology Congress (ESMRMB). Antalya, Turkey. 2009; 471-472.
and
Croitor Sava AR, Martinez-Bisbal MC, Van Huffel S, Cerda JM, Sima DM, Celda B. Ex Vivo High Resolution Magic Angle Spinning Metabolic Profiles Describe Intratumoral Histopathological Tissue Properties in Adult Human Gliomas. Magnetic Resonance in Medicine. 2011; 65: 320-328.

As a result, many researchers are now focusing on understanding this disease from the metabolomic, genomic and proteomic points of view.

The potential of *ex vivo* and *in vivo* NMR spectroscopy has been lately extensively exploited in the separation between normal brain and brain tumors (Rutter at al., 1995; Howe et al., 2003), as well as for the characterization of different degrees of malignancy (Opstad et al., 2008a; McKnight, 2004; Negendank at al., 1996; Erb et al., 2008). The focus in most of the previous studies lies mainly on brain tumor characterization and typing, without describing the histopathological tissue properties at a microscale level. However, there is an increasing interest in determining the correlation between metabolic features derived from *ex vivo* high resolution magic angle spinning (HR-MAS) and histopathological properties, as the HR-MAS technique is becoming a metabolomic methodology with potential applications in supporting tumor classification and diagnosis. Previous studies have shown that HR-MAS can help in predicting the growth characteristic within different regions of a tumor (McKnight et al., 2007) and can help in differentiating between glial tumor grades (Erb et al., 2008). Moreover, with HR-MAS one can successfully reveal the status of tumor microheterogeneity (Cheng et al., 2000) and can observe metabolic alterations before they are morphologically detectable (Andronesi et al., 2008), which, in turn, can further be correlated to histopathological properties (Opstad et al., 2008a, 2008b). Nevertheless, these studies limit themselves at describing independent metabolite behavior while ignoring their interconnectivity. In this chapter a multivariate statistical study where sets of features coming from combinations of different metabolites and metabolite ratios are analyzed for assessing their relevance in correlating the HR-MAS spectra with the histopathological tissue properties is proposed.

Although HR-MAS is increasingly used to analyze tumor tissue biochemistry, nowadays histopathological analysis of the surgically extracted tumor tissue is usually considered as the gold standard for assigning the type and grade of the tumor, as well as the contribution of necrosis, high cellularity and normal brain tissue within the tumor area. Since HR-MAS spectra are obtained directly from the biopsy sample, HR-MAS can reveal a first level of correlation between metabolic profiles and biopsy tissue type, allowing for a better investigation of the tumor. Additionally, with *ex vivo* HR-MAS the tissue integrity is mostly conserved. This is a major advantage since it allows one to perform, on the same tissue sample, multimodal studies including subsequent genomic, proteomic or histopathological analyses and, therefore, to obtain a direct comparison between all these techniques. The added value of combining and comparing different techniques has been shown before (Cheng et al., 2000; ; Tzika et al., 2007; Andronesi et al., 2008; Righi et al., 2009). Such analyses, based on multiple data sources, can provide further insights into the biology of the brain tumors and improve the diagnosis.
In this chapter, the correlation between metabolic features derived from *ex vivo* HR-MAS and necrosis, high cellularity or infiltrations, which are common histopathological tissue properties, is evaluated. Therefore, both metabolomic and histopathological knowledge is considered. Compared to (Cheng et al., 2000), where similar conclusions are drawn from tissue samples coming from the same patient, this study employs a multicenter database of

frozen tissues extracted from 52 patients presenting different types of glial tumors (glioblastoma (GBM), grade III (GIII) and grade II (GII)).

The purpose of the study is threefold:

- First, to analyze whether with unsupervised classification methods predominant histopathological tissue property can be identified for each glial tumor type. As the highest heterogeneity is observed and confirmed by the histology in the GBM group, this group is firstly analysed. To this end, feature sets coming from various metabolites and metabolite ratios are tested as potential biomarkers for the considered clustering problem. The statistically significant correlation between the considered feature sets and the predominant histopathological tissue properties is also investigated.

- Second, to extract representative reference metabolic tissue models for each histopathological tissue property and to analyze which of the considered input feature values are most sensitive in revealing the predominant histopathological property.

- Finally, to test whether the conclusions drawn for the GBM group can be extended to other glial tumor groups, with different grades of malignancy.

5.2 Materials

5.2.1 HR-MAS data acquisition

Brain tumor biopsies were carried out on 52 adult patients presenting a glial tumor. Three hospitals provided the samples used in this study: Hospital La Ribera-Alzira (Valencia), Hospital Clínico Universitario (Valencia) and Instituto FLENI (Buenos Aires), all participating as partners in the eTUMOUR project (*www.etumour.net*). Initial diagnosis, done in each centre as a routine part for the standard patient management, assigns the considered cases to glial tumor group with different degree of malignancy: 27 grade IV glioblastoma tumor (GBM), 7 grade III glial tumor (GIII) and 18 grade II glial tumor (GII). The tissue specimens were snap-frozen in liquid nitrogen and stored at -80^0C until the time of spectroscopic analysis, when 1D PRESAT (pulse-and-acquire) data were acquired. HR-MAS experiments were conducted on 29/52 samples using a Bruker Avance DRX 600 spectrometer operating at a ^{1}H frequency of 600.13 MHz. The instrument was equipped with a 4 mm triple resonance ^{1}H/^{13}C/^{15}N HR-MAS probe with magnetic field gradients aligned with the magic angle axis. 23/52 samples underwent HR-MAS experiments using a Bruker Avance DRX 500 spectrometer operating at a frequency of 500.13MHz. The instrument was equipped with a 4mm triple resonance ^{1}H/^{31}P/^{13}C HR-MAS probe. A single-pulse 90^o pre-saturation

experiment was acquired in all the samples. Number of transients was 256 collected into 32 k data points for all the experiments. Water pre-saturation was used during one second along the recycling delay for solvent signal suppression. Spectral width was 8 kHz and 10 kHz for 600MHz and 500MHz NMR spectrometers, respectively. To keep the rotation sidebands out of the acquisition window, samples were spun at 5000 Hz in the DRX 600 spectrometer and at 4000 Hz in the DRX 500 spectrometer. Sample temperature was kept at 4^0C, using the cooling of the inlet gas pressures responsible for the sample spinning. Recycling delays were 1.5 seconds for all experiments. Each sample was introduced in a 4mm ZrO_2 rotor fitted with a 50 ml cylindrical insert, without any previous D_2O washing.

5.2.2 HR-MAS data preprocessing

The HR-MAS spectra were preprocessed as follows. Signals were truncated to the first 2048 points to reduce the computational load in the preprocessing steps. The water components were removed by HLSVD-PRO (Laudadio et al., 2002). Contributions outside the frequency interval [0.25, 4.2] ppm were filtered out in order to keep only the contribution of the metabolites of interest. Small variations in the chemical shift of peaks between HR-MAS experiments have been noticed. Therefore, all filtered 1D PRESAT were aligned with respect to the Alanine doublet at 1.47 ppm (Poullet et al., 2007b). Signals were then normalized (divided by the *L2* norm of the frequency domain signal between 0.25 and 4.2 ppm). A baseline correction was applied using an apodization function as described in Chapter 2, Section 2.1.8.

The concentrations of the following metabolites were measured for the study: the lipids group (Lips), N-acetylaspartate (NAA), Creatine (Cr) and total Choline group (tCho). Peak integration, see Chapter 2, Section 2.2.3, was used for extracting the concentration of these metabolites by considering the following integrated intervals in ppm: Lip1 [0.84, 0.91], Lip2 [1.255, 1.285], Lip3 [2.79, 2.81], NAA [2.0, 2.015], Cr [3.01, 3.03], Cho [3.19, 3.205], PCho [3.21, 3.22], GPCho [3.225, 3.235]. These areas were computed from the mean of all the available HR-MAS spectra. Specifically, the highest point in the area to be integrated was identified for each metabolite, then the area bounds were fixed for each metabolite individually to those ppm values at which peak slopes return to baseline, but keeping symmetric intervals with respect to the highest point.

Sets of metabolite features were tested along with metabolite ratio feature sets to determine which is most likely to preserve the tissue's histological information. Hence, the ratio set was composed of Lips, NAA and tCho with respect to Cr. Consequently, the considered features were real-valued numbers that can be represented as points in an n-dimensional space, where $n = 7$ for the concentrations case, and $n = 3$ for the ratios case.

5.2.3 Histological analysis

After performing the HR-MAS study, tumor specimens were snap-frozen and submitted for quantitative histopathological examinations. 37 out of the 52 biopsy samples (22 GBM, 6 GIII and 9 GII) were subject to histological examination performed on tissue samples taken from the same part used in the HR-MAS study. The analysis was done by an expert neuro-pathologist and the samples were classified according to the revised WHO criteria (Louis et al., 2007). The samples were fixed in 10% formalin, embedded in paraffin, serially sectioned, slide mounted and stained with Hematoxilyn and Eosine. Routine histological methodology has been used for evaluating the cell density and the percentage of necrosis. Based on the histology the samples are considered with variable content of highly cellular tumor tissue, infiltrations with normal tissue and/or necrotic tissue. The percentage of tissue with a predominant property was calculated for each sample by measuring the total area of the biopsy sections and then delineating the regions of interest. Each case was assigned as having a certain histopathological tissue property when its corresponding region was ≥ 50% from the total area and any of the other two properties was observed in a region < 20% from the total area. Nevertheless, for the largest part (approximativly 85%) of the high-cellularity samples, the histology post HR-MAS showed a percentage of cellularity ≥ 75%. See Table 5.1 for more details.

5.3 Methods

The steps involved in the statistical analysis of the HR-MAS data are: distribution analysis, clustering and validation, applied exclusively to the feature vectors described in Section 6.2.

Data distribution
For obtaining information about the location and the spread of the data, the variance within each tumor group by computing the median and the interquartile range (IQR) is studied. This representation, know as boxplots, is thus helpful to detect possible skewness in the data and existing outliers.

Data clustering
Cluster analysis is used to determine if the considered feature sets have the potential to predict histopathological tissue properties. The k-means clustering algorithm (Hartigan and Wong, 1979), see also Chapter 2, Section 3.2.1, is applied to the HR-MAS data to partition them into k subsets (clusters $C_1 \ldots C_k$). Each centroid is the component-wise mean of all the objects (feature vectors) in that cluster, after centering and normalizing the sequence of values within each object to zero mean and unit standard deviation.

Table 5.1 *Percentage of tissue contributions for each case according to the histopathological study. The index represents the number assigned at acquisition.*

Necrosis	Tumor	Border	Collagen	Normal	Index
			GBM		
80	20	0	0	0	2
0	0	0	0	100	3
10	70	0	20	0	4
0	0	5	0	95	5
100	0	0	0	0	6
0	0	100	0	0	7
10	90	0	0	0	8
0	90	0	10	0	9
0	90	0	10	0	10
0	90	0	10	0	11
75	0	0	25	0	12
0	50	0	50	0	13
0	20	80	0	0	14
20	50	0	30	0	15
0	0	10	90	0	16
25	75	0	0	0	21
25	75	0	0	0	22
100	0	0	0	0	23
30	70	0	0	0	24
0	0	100	0	0	25
20	80	0	0	0	26
30	70	0	0	0	27
			GIII		
50	50	0	0	0	28
0	20	80	0	0	29
0	25	35	40	0	30
0	80	0	20	0	32
0	20	0	80	0	33
0	75	0	25	0	34
			GII		
0	0	0	0	100	35
0	50	50	0	0	36
0	80	0	20	0	37
0	0	0	0	100	38
0	80	20	0	0	45
0	50	0	50	0	48
0	80	20	0	0	49
0	20	0	80	0	50
0	80	20	0	0	51

Since the similarity in shape between two feature vectors embodies the interest of this study, the correlation distance was considered most appropriate for the considered data. More precisely, the distance $d(x,\mu_i)$ is computed as (Cohen et al., 2003):

$$d(x,\mu_i) = 1 - \frac{(x-\bar{x})(\mu_i-\bar{\mu}_i)'}{\sqrt{(x-\bar{x})(x-\bar{x})'(\mu_i-\bar{\mu}_i)(\mu_i-\bar{\mu}_i)'}} \tag{5.1}$$

where the bar denotes a vector with all elements equal to the mean of the values in the given vector, and the prime denotes vector transposition (here, x and μ_i are row vectors).

Statistical validation

A critical parameter in clustering is the number of clusters, k. To minimize subjectivity when choosing the best number of clusters for the data, k is estimated with several statistical indices, which measure the quality of the clustering on the basis of the definition that objects within one cluster are similar to each other, while objects in different clusters are dissimilar with each other. The optimal number of clusters among different values of k is obtained by evaluating the solutions of the following proposed validity indices: weighted inter-intra index (Wint) (Strehl, 2002), Krzanovski-Lai index (KL) (Krzanowski and Lai, 1985), Silhouette index (Sil) (Rousseeuw, 1987) and Homogeneity and Separation index (Kaufman and Rousseeuw, 1990), which are described in details in Chapter 3, Section 3.3.

As a final measure of the statistical significance of the proposed data analysis, the cluster reliability, or the likelihood that the cluster structure is not formed by chance is measured. For this, Tukey multiple comparison (Tukey, 1949) is considered after performing the Kruskal-Wallis test (Hollander and Wolfe, 1973), see also Chapter 3, Section 3.3. This procedure provides a comparison interval for the mean value of the considered features allowing one to check if the metabolite alterations are statistically significant between the considered clusters.

5.4 Correlation with histopathology

After assigning each case to one of the clusters, the relationship of each cluster to histopathology is investigated. For labeling the clusters, the correlation between the cluster centroids μ_i and the metabolic profile coming from pure tissue samples (with the dominant histopathological tissue property more than 90% of the total region) is computed by means of correlation coefficients. Clusters are labeled considering the highest correlation coefficient value. Furthermore, reference metabolic models are proposed for necrotic, highly cellular and border tissue, by computing the mean of the feature vectors belonging to the same cluster after centering and normalizing the sequence of values within each feature vector to zero

mean and unit standard deviation. Only the cases with histopathological confirmation are used in this step.

Grade II and grade III gliomas tissue characterization
One purpose of this study is to analyze to which extent the molecular composition is dependent on the tumor grade. To this end, the metabolomic analysis, supported by histopathology, is extended to the GII and GIII glioma groups. For each case within the GII and GIII tumor groups the correlation coefficient between the feature vector extracted from the HR-MAS spectra and all the reference models obtained for the GBM group in the previous step is computed. This approach should grant further insight to whether the metabolic profiles from the GBM clusters change significantly with the tumor grade, and whether a similar molecular composition can be observed for necrosis, highly cellular or infiltrations, regardless of the grade of malignancy.

5.5 Results

Results of the statistical analyses
According to the histological exam, a great extent of tissue heterogeneity is observed for all the studied glial tumors and the high grade tumors appear to be more heterogeneous than low grade tumors. In particular for the GBM group, although all cases within this group were initially diagnosed in the hospital as high grade GBM tumor, they are highly variable in their composition as different content of necrotic, high cellularity or infiltrations with normal tissue, as reported by histopathology. Some samples contained up to 90-100% necrosis and some contained only areas of infiltrating tissue at the border of the tumor. The intergroup variability is reflected also at metabolic level (Figure 5.1). The metabolite concentration distributions are observed to be widely dispersed around the median values and outliers can be identified. The likelihood that the identified outliers cluster together as a new subgroup within the GBM group is investigated.

Using no prior knowledge, data clustering of the GBM group in 3 subgroups is indicated as the best solution by the Homogeneity-Separation, Sil and Wint indices (see Figure 5.2 a) and b)). According to these findings, $k = 3$ is further considered the optimal number of clusters for the k-means clustering algorithm. KL index suggests 4 as the best number of subgroups for data clustering. The 4^{th} cluster contains in fact only one case, which was considered by histopathology with over 90% contributions from normal tissue. The results of the clustering procedure are presented in Figures 5.3 and 5.4.

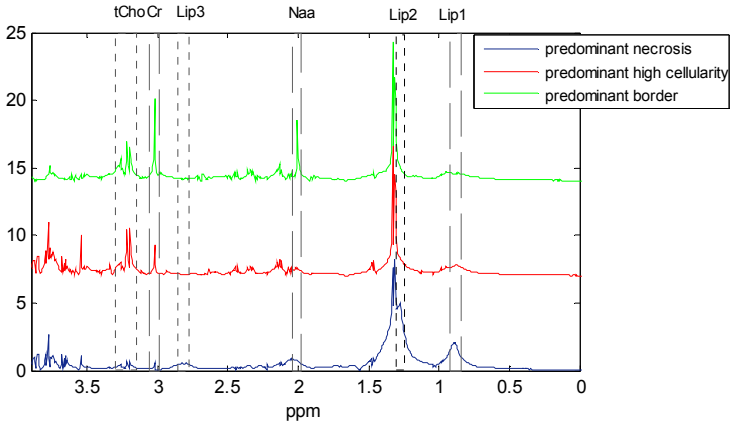


Figure 5.1 *HR-MAS spectra coming from GBM samples with different predominant tumor histopathological properties. The vertical lines highlight the region where the considered metabolites are located in ppm scale.*

One can visually observe considerably high differences in the metabolite profiles between the three clusters. The obtained clusters are homogeneous and clearly separable. μ_1 correlates best with infiltrative border tissue (corr = 0.84), μ_2 with the necrotic tissue (corr = 0.98) and μ_3 with the highly cellular tissue (corr = 0.85). Additionally, the relationship between these findings and the conclusions drawn from histology are assessed. A very good agreement between these two different techniques is obtained when working with the metabolite concentrations set, as 21 out of 22 histopathologically validated cases were found to contain tissue with the same predominant histopathological property, both with HR-MAS clustering analysis and with the histopathological procedure. The results are in agreement with literature since μ_1 is characterized by high levels of NAA, which are typically found at the border region of the tumor or in regions with infiltrative normal tissue (Peeling and Sutherland, 1993). μ_2 presents very high levels of Lip(s), which is an expected behavior for GBM tumors and is mainly associated with necrosis (Opstad et al., 2008), while μ_3 has high level of Cho(s), a generally accepted biomarker of active tumor cell growth (Tedeschi et al., 1997). The obtained clusters will be further referred to as border tissue (C_1), necrotic tissue (C_2) and high cellularity tissue (C_3), respectively. In Figure 5.4, all the GBM cases projected in a multidimensional scaled plane represented by the first three principal coordinates (PCOs) (Gower and Hand 1996) are shown.

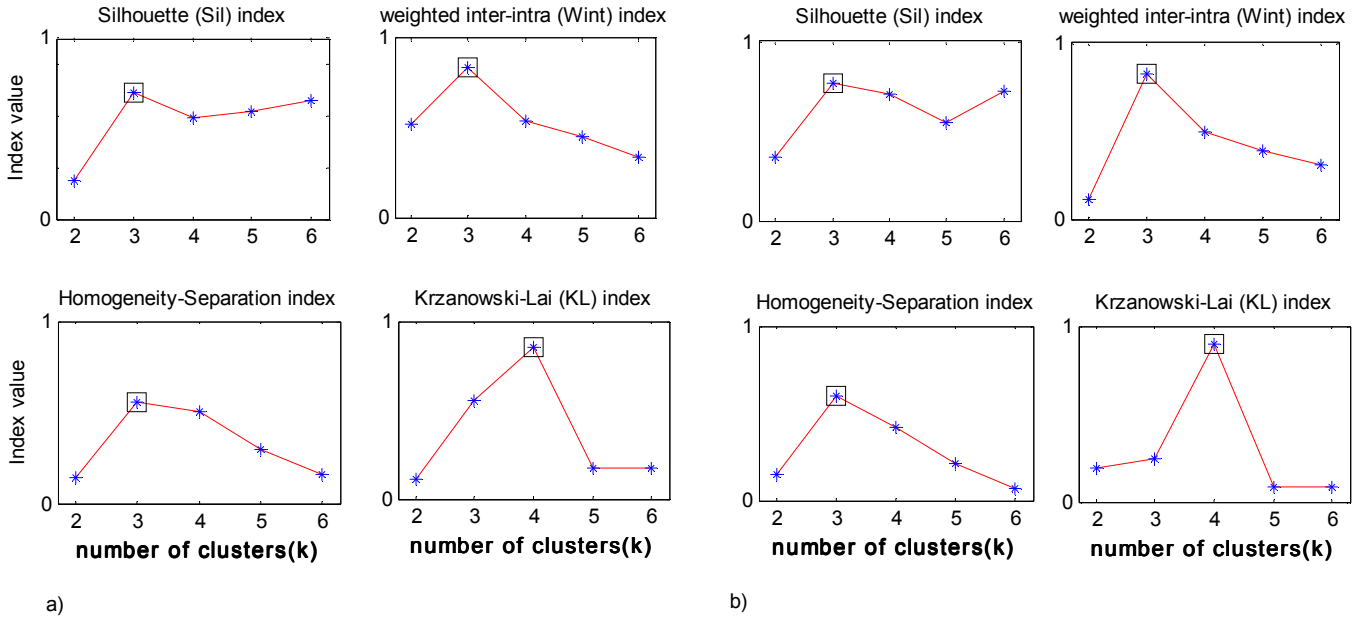


Figure 5.2 *Statistical indices for estimating best k for k-means when considering a) the metabolite concentrations as input features and b) the metabolite ratios as input features. The highest index value, indicating the optimal number of clusters, is contoured with black.*

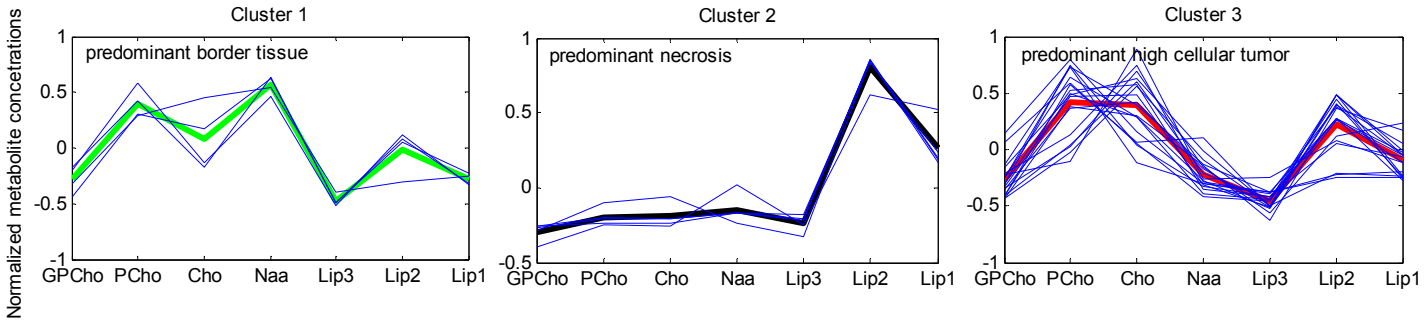


Figure 5.3 *Feature profiles of clusters for GBM samples: centroids are marked in bold, and objects within clusters are marked blue.*

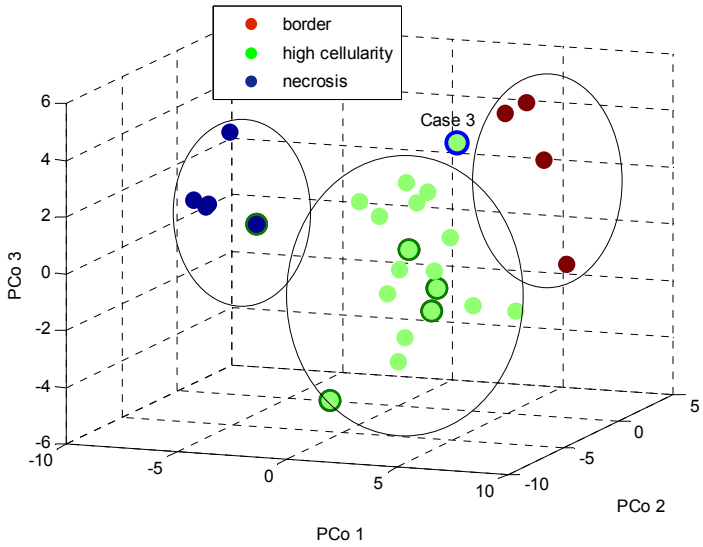


Figure 5.4 *Data visualization in the principal coordinates space. First three principal coordinates (PCo1, PCo2, and PCo3) of GBM samples were considered. The three black ovals drawn on the obtained image encompass the clusters' population.*

For case 3, indicated by a light blue circle in Figure 5.4, an agreement between the metabolic and the histopathological analysis was not obtained. It was clustered as predominantly highly cellular tumor, while histology reports this area to be composed primarily of normal tissue. As this tissue type is not considered in this study, case 3 is reported as an outlier and this could explain its location outside the 3 obtained clusters. The same case was assigned by the KL index to a separate cluster. The five cases for which no histopathological validation is available (indicated by a dark green circle in Figure 5.4 do not influence the clustering results, as they are evidently grouped with the other objects in their clusters.

When considering the metabolite ratios, an agreement with the histopathology was obtained for 18 cases out of 22. Three of the four cases without agreement cluster as predominantly border tissue when considering the ratios, while the histopathology reports a high percentage of active tumor cells. Case 3 was assigned, also when working with metabolite ratios, to predominantly highly cellular tumor tissue.

Grade II and grade III glioma characterization

For the GIII tumor group, 2 cases out of 7 are highly correlated with the border tissue model and 5 cases are highly correlated with the high cellularity tissue model, see Figure 5.5. These results are in agreement with the histology. A special situation is represented by case 28, for which the histopathology reveals equal percentage of highly cellular tumor tissue and

infiltrations (50%-50%). The metabolic profile of this case correlates most with predominantly border tissue. Still, a very high correlation with the highly cellular tissue model is also obtained. No case with predominantly necrosis was reported for this tumor group.
For the GII tumor group, the metabolic analysis indicated that 11 cases were highly correlated with the highly cellular tumor tissue model, 5 cases with the border tissue model and 2 cases with the necrotic tissue model, see Figure 5.5. A good agreement with the histology was obtained for 7 out of the 9 histopathologically validated cases. Histopathology confirms for one case within this tumor group some contributions from necrotic tissue. This apparent inconsistency (one grade II glioma presenting necrosis) could be a consequence of the fact the tissue sample analyzed with HR-MAS is not strictly coming from the same tumoral region as the one used for initial diagnosis. The two cases assigned by metabolic analysis to necrosis reveal high lipids levels. As in (Opstad et al., 2008a), lipids are observed to be present in non-necrotic biopsy samples. This could be, for example, due to hypoxia, since lipids may originate not only from regions of necrosis, but also from viable growth-arrested cells (Barba et al., 1999).

5.6 Discussion

The present work illustrates a significant correlation between the tumor microheterogenity as revealed by the histopathology and *ex vivo* HR-MAS sets of metabolite concentrations and ratios.

Combinatorial approaches, where different techniques are correlated for assessing the relation between clinically relevant cell processes and specific metabolites, have been previously proposed. In (Tzika at al., 2007) and (Righi et al., 2009), combining HR-MAS and genomic data provides insights into the biology of glial tumors. In (Cheng et al., 2000) HR-MAS of intact brain tumor biopsies are combined with histopathology for revealing tumor microheterogeneity. Specifically, the concentration of mobile Lips and Cho were reported to correlate linearly with the amount of necrosis and tumor cellularity, respectively, while higher levels of NAA are expected in the border region of the tumor with respect to the active tumor region. Still, the conclusions drawn in (Cheng et al., 2000) are coming from a limited number of samples originating from a single patient with GBM tumor. In this chapter a more complex study, where samples measured in different clinical centers and coming from different patients with glial tumor with different grades of malignancy are analyzed using advanced statistical methods. Results confirm that, by using only information coming from *ex vivo* HR-MAS data, clearly differentiate between histopathological tissue properties within glial brain tumors, regardless of the malignancy grade. An important finding is that the alterations in metabolite concentrations are correlated and not independent from each other. Based on this, representative tissue models describing metabolites' behavior for necrotic, highly cellular and border tumor tissue can be derived. To our knowledge this is the first study that derives the metabolic profiles of the three considered histopathological tissue properties.

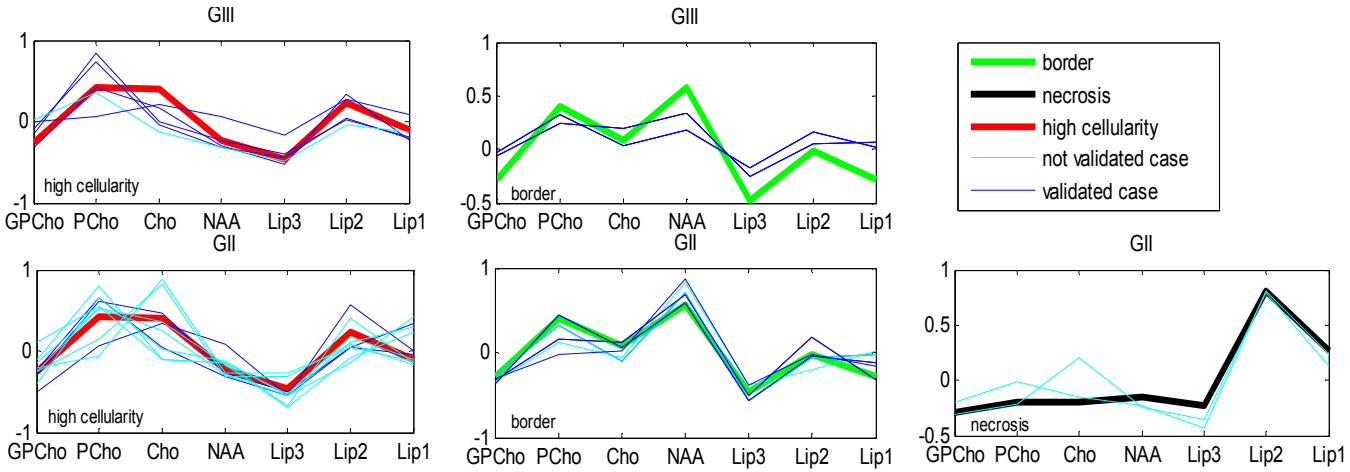


Figure 5.5 *Assignments based on highest correlation coefficient within GIII and GII glial tumor group, respectively.*

Best biomarkers for tissue differentiation and characterization

The results suggest that all the investigated metabolites and ratios are sensitive in identifying histopathological tissue properties. A *p*-value lower than 0.01, which is often considered in the literature to be the threshold value for declaring that the differences are at a high level of significance, was obtained for each feature considered in the study, see Figure 5.6. NAA, tCho group and Lips are interconnected. This interconnectivity gives rise for example to correlations between decreased Cho and Lips and increased NAA in the border region of the tumor. Better differentiation between necrotic, border and high cellularity tumor tissue is obtained when considering sets of features compared to independent features. In Figure 5.7, different metabolic subsets are chosen to describe the space in which the GBM data are analyzed. The Lips-to-tCho metabolite subset allows us to better differentiate necrosis from highly cellular tumor tissue, while best separation between all three tissue properties is given by the tCho-to-NAA subset and the Lips-to-NAA subset.

Characteristic features of necrosis are significantly increased concentrations of Lips and metabolite ratios of Lips/Cr compared to the respective levels in high cellularity and border tumor tissue. These results are in agreement with the conclusions formulated previously in the literature (Kuesel at al., 1994a; 1994b; Cheng et al., 2000; Opstad et al., 2008a). We additionally report for necrosis that NAA and NAA/Cr values are almost negligible and the concentrations of tCho and the tCho/Cr values are also very low. Having as reference the sum of all the considered metabolites, in necrotic tissue we observe NAA level <20%, while Lip(s) level >60% and Cho(s) level < 30%, see Figure 5.8.

A distinguishable characteristic of border tissue is the high level of NAA. These results are confirming the conclusions reported previously in the literature. Also Lips play an important role in separating border tissue from necrosis, and as well the tCho group. As seen in Figure 5.8, Lip(s) level < 40%, NAA level > 20%, Cho(s) level > 20% within the border tumor regions. Lips/Cr ratios are low or very low, the Cho/Cr, PCho/Cr and GPCho/Cr ratios are < 1.5 and NAA/Cr is not negligible.

tCho values are the highest in highly cellular tumor regions. The levels of NAA and its ratio to Cr is very low, the Lips and Lips/Cr are much lower compared to necrotic tissue but not varying too much from the values reported in border regions. As a conclusion of our results the Lip(s) level <50%, NAA level <20%, Cho(s) level > 40% in high cellular area and the Lips/Cr ratios are low or very low, the Cho/Cr, PCho/Cr and GPCho/Cr ratios are > or close to 1.5 and NAA/Cr is negligible.

Similar metabolic patterns were observed for the considered tissue properties, regardless of the grade of malignancy. The results demonstrate the biological relevance of MRS biomarkers in understanding the biology of the tumor, with potential in improving non-invasive diagnosis and in aiding clinicians in improving diagnosis and treatment and ongoing evaluation of the patients. Even if the diagnosis assignment is progressively improving by implementations of a variety of pattern recognition methodologies (Poullet et al., 2009), still difficulties remain in the grading of glial tumor. This may be due to the fact that the methodologies proposed are

not sensitive to the microheterogeneity of the tissue. Commonly, the tumor classification problem is limited to separating between different tumor grades, without considering the contributions of necrotic or normal tissue in the metabolic profile of the spectra under investigation. As it was shown in this study, there is a high variability within the HR-MAS data coming from the same tumor grade group. This intra-group metabolic variability is a consequence of the tumor microheterogeneity, since no biopsy procedure could guarantee the homogeneity of the sample under investigation. Ignoring a first separation between the three histopathological tissue properties will highly affect the performance of any classifier applied on HR-MAS data. Tissue microheterogeneity is expected to be reflected also in the spectral profile of *in vivo* MRS or MRSI measurements, where one will deal with large voxel volumes (the area under investigation is much larger than with HR-MAS).

The findings in this study could be translated to *in vivo* studies and, therefore, could aid in the interpretation of low resolution single-voxel MRS and multi-voxel MRSI. This is especially supported by previous works that reported for the metabolites considered here a high correlation between *ex vivo* and *in vivo* MRS (Celda et al., 2006; Martinez-Bisbal et al., 2004; Opstad et al., 2010). Moreover, there are situations in which prior knowledge on the intratumor tissue differences could add to the power of an accurate tumor classification, by improving the identification of the glial tumor grade (Erb et al., 2008) or in separating glioblastomas from metastasis (Fan et al., 2004; Luts et al., 2009b).

One should not neglect the fact that the examined tissue samples have a complex content being composed of a mix between two of the following: necrotic, border and high cellular tumor tissue, as reported by the histopathology. This characteristic could be observed also with HR-MAS data as some cases were very close to the border between two tissue types. Further studies on tissue source separation and quantification of the contribution (abundance) of each source within each tissue sample have been performed and are detailed in Chapter 6.

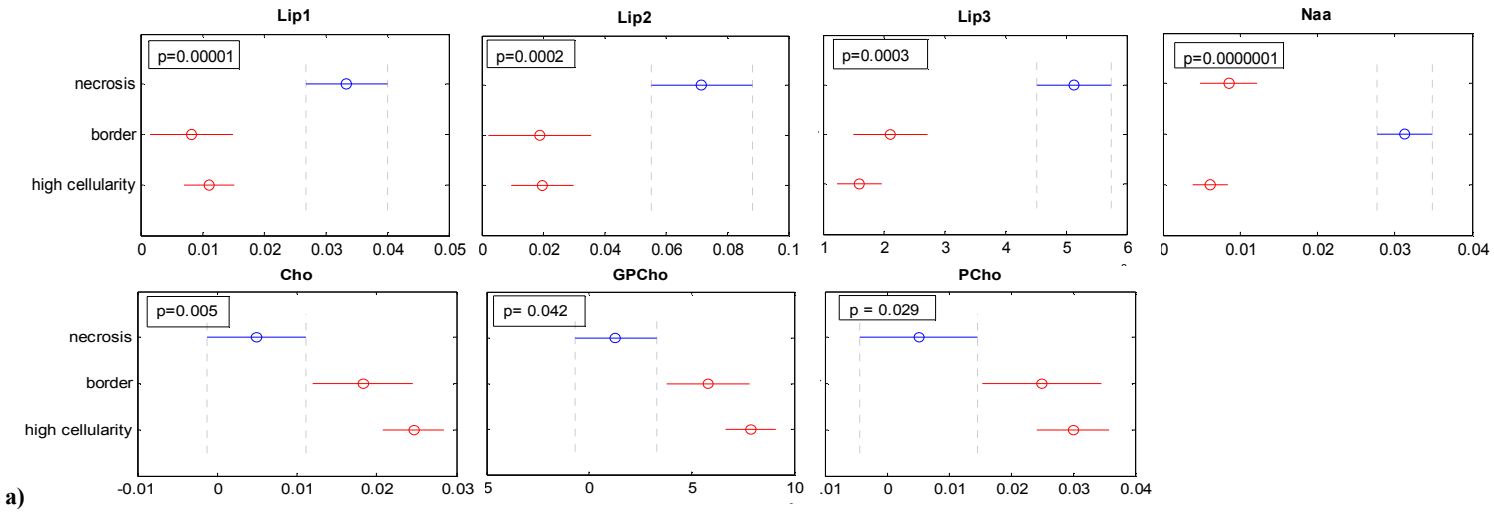


Figure 5.6 *Comparison plot after performing the Kruskal-Wallis test (p-value is indicated) and the Tukey multiple comparison. Differences between the three histopathological tissue properties for a) the metabolites considered in the study and b) for the metabolite ratio values are illustrated.*

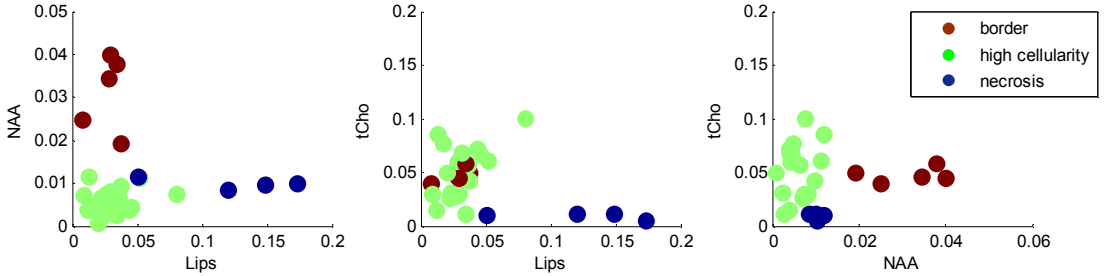


Figure 5.7 *All GBM cases plotted in the Lips-to-NAA, tCho-to-Lips and tCho-to-NAA space, respectively.*

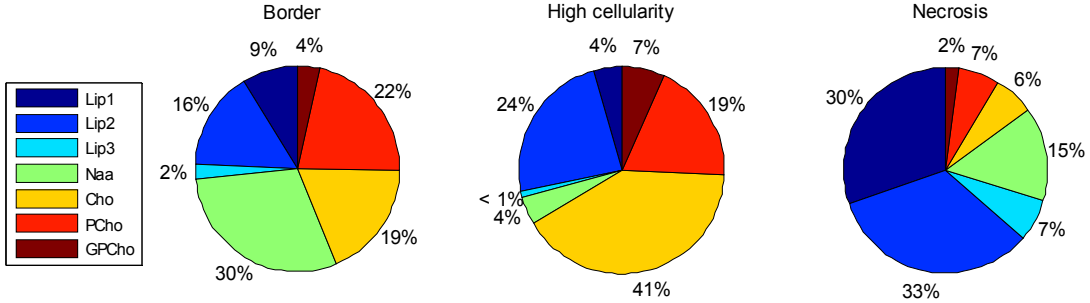


Figure 5.8 *Metabolites distribution for different histopathological tissue properties. The percentage values reflect the ratio between individual metabolite concentrations and the sum of all the considered concentrations.*

5.7 Conclusions

The statistical studies performed in this chapter show a strong correlation between the histopathological tissue properties and metabolic profiles coming from *ex vivo* HR-MAS in glial tumors. The results are in agreement with the pathology obtained by the histopathological examination that succeeded the high HR-MAS measurements A clear separation between necrotic tissue, high cellularity tumor tissue and border tumor tissue is obtained regardless of the malignancy grade. The metabolite concentration sets can better differentiate between the considered histopathological tissue properties than the ratios of the metabolites to Cr. The proposed metabolic profiles reflect that the metabolites behavior is interconnected, and typical biochemical patterns emerge for each histopathological tissue property. *Ex vivo* HR-MAS can therefore provide relevant metabolic information on the tumor tissue under investigation. Likewise, the adequate agreement between *ex vivo* metabolic characteristics, obtained from the HR-MAS classification and histopathology results, can aid in the interpretation of *in vivo* spectra and, therefore, increase their importance in non-invasive brain tumor classification.
The findings in this chapter could aid in a better understanding of glial tumor tissue metabolism, and therefore could improve in diagnosis and prognosis of the tumor type and grade.

Chapter 6

Non-negative blind source separation techniques for brain tumor tissue typing

This chapter[3] presents a study with the goal to differentiate between tumor tissue types by separating the different sources that contribute to the profile of each spectrum. Blind source separation techniques are applied for obtaining characteristic profiles for necrosis, high cellular tumor and border tumor tissue, and providing the contribution (abundance) of each of these tumor tissue types to the profile of each spectrum. The problem is formulated as a non-negative source separation problem. Non-negative matrix factorization, convex analysis of non-negative sources and non-negative independent component analyses methods are tested both on ex-vivo HR-MAS and in vivo MRSI data. The results are confronted with the pathology obtained by the histopathological examination that succeeded the HR-MAS measurements Firstly, in Section 6.1, an analysis to verify to which extent the dimension of the input space, the input features and the number of sources to be extracted from the HR-MAS data could influence the performance of the source separation is presented. In Section 6.2 the study is extended to in vivo MRSI data.

6.1 Application to *ex vivo* HR-MAS spectroscopy

6.1.1 Introduction

As shown in Chapter 5, a significant variability within the HR-MAS spectral profiles belonging to the same brain tumor tissue type can be observed (Croitor Sava et al., 2011b) due to the heterogeneity that characterizes brain tumors. Thus, the tissue under investigation might present contributions from

[3] Croitor Sava AR, Sima DM, Martinez-Bisbal MC, Celda B and Van Huffel S. Non-negative blind source separation techniques for tumor tissue typing using HR-MAS signals. In Proc. of the 32nd Annual International Conference of the IEEE Engineering in Medicine and Biology Society (IEEE EMB), Buenos Aires, Argentina. 2010; 3658-61.
and
Croitor Sava AR, Martinez-Bisbal MC, Sima DM, Calvar J, Esteve V, Celda B and Van Huffel S. Quantifying brain tumor tissue abundance in HR-MAS spectra using non-negative blind source separation techniques. Submited to the Journal of Chemometrics.

various tumor tissue types. The observed spectra are, therefore, a combination of different constituent sub-spectra, since the measured signal is the response to the stimulation of the entire tissue sample. The overall gain with which a tissue type contributes to a spectrum is proportional to its abundance, i.e., its proportion in the entire mixed tissue sample. As a result, multiple metabolites and tissue types may be present in a single HR-MAS spectrum.

This concept can be summarized by describing the spectra available from m samples, which are stacked as n-dimensional row vectors in an m by n matrix X, where n is the number of observations (or data points) in each spectrum:

$$X = AS \tag{6.1}$$

where S is a k by n matrix whose k rows are the unknown pure tissue spectra (also referred to as sources) and n the number of observations of each source. A, an m by k matrix, contains the concentrations, or abundances, of the constituent pure tissue sources in each sample.

The purpose of the study is to identify the pure components of the different tissues, S, and to estimate the concentration of each component, A. This problem is formulated as a blind source separation problem (BSS). BSS techniques have been previously considered when analyzing NMR spectroscopic data since they have shown some interesting properties such as: a straightforward interpretation and analysis of the data without the need for prior knowledge (no representative training set or representative models are required); a better interpretation of the complexity of the data by allowing one to resolve the partial volume effect caused by the heterogeneity of the brain tissue; decomposing the mixture of the spectra under investigation; easily interpretable results for clinicians. Previous studies mostly refer to the analyses of *in vivo* single voxel MRS (Lee et al., 2000; Ladroue et al., 2003) and multi-voxel MRSI brain data (Szabo De Edelenyi et al., 2005; Su et al., 2008; Wright et al., 2009). Still, in all these studies an empirical validation of the results obtained with the proposed BSS methods is proposed. This is due to the fact that is very difficult, if not impossible, to determine if the obtained components are really corresponding to spectra of pure tissue in the brain. Although for healthy tissue and necrosis it is possible to acquire spectra from voxels filled with only one tissue, for high cellular tumor tissue there is a weak probability to obtain such a direct validation. In the proposed study several BSS techniques are applied to *ex vivo* HR-MAS data to obtain the pure tissue sources and quantify their abundance in the analyzed spectra. With HR-MAS a straightforward validation of the results is available, since a histopathological analysis was performed post HR-MAS acquisition on the same tissue samples. Histopathology, which is often considered the ground-truth for brain tissue typing, provides detailed information on the mixture of tissues present in the data under investigation, as well as the concentration of each tissue.

An important constraint considered in this study is the nonnegativity. This solution is motivated by the nature of the NMR magnitude spectra, where one has to deal with non-negative signals. Blind separation of non-negative source approaches have been recently successfully used in many applications where the sources to be separated are of non-negative nature, e.g., biomedical imaging (Nuzillard D. and Nuzillard J.M., 1998), analytic chemistry (Malinowski, 2002), hyperspectral imaging (Nascimento and Dias, 2005) and biomedical signals (Su et al., 2008). The way to exploit the non-

negativity characteristic in non-negative BSS (nBSS) techniques is subjective to the data under analysis. Therefore numerous nBSS alternatives have been proposed. A class of nBSS methods utilizes the statistical property that the sources are mutually uncorrelated or independent. This class includes among others: non-negative independent component analysis (nICA) (Plumbley, 2002, 2003; Oja and Plumbey, 2004; Yuan and Oja, 2004), Bayesian positive source separation (BPSS) (Moussaoui et al., 2006). Another class of nBSS methods is represented by implementations which require no assumption on source independence or zero correlations. One such nBSS approach is the non-negative matrix factorization (NNMF). This method explicitly imposes source non-negativity and even mixing matrix non-negativity.

Compared to the previous studies on NMR spectroscopic data using BSS techniques (Lee et al., 2000; Szabo De Edeleny et al., 2005; Su et al., 2008; Wright et al., 2009), where only the performance of one method was reported, in this chapter a comparative study is proposed where three different methods, based on different mathematical principles, but having in common the non-negativity constraint are considered. NNMF, nICA and convex analysis for blind separation of mixtures of non-negative sources (CAMNS) (see Chapter 3 for their detailed description) are applied on the full magnitude HR-MAS spectra. In this way characteristic profiles for necrosis, high cellular tumor and border tumor tissue are obtained, and the contributions (abundances) of each tumor tissue to the profile of the spectra are provided. The study has a multifold purpose and evaluates:

- which of the considered nBSS methods performs best.
- which is the best feature input space to consider, i.e., the results on the full magnitude HR-MAS signals and on dimensionally reduced features spaces are compared.
- how the choice of the parameters for the considered nBSS methods influences the results, mainly focusing on the: robustness when the algorithms are applied to different datasets the number of sources to be calculated.
- whether the nBSS methods could provide similar results to histopathology, which could further be easily interpretable by the clinicians.

6.1.2 Materials

The HR-MAS spectra of brain tissue samples from 52 adult patients presenting a glial tumor with different degree of malignancy were considered. Based on the initial diagnosis (i.e., before histopathological examination) the data were split in three subgroups: 27 grade IV glioblastoma tumor (GBM), 7 grade III glial tumor (GIII) and 18 grade II glial tumor (GII). Data acquisition and preprocessing was performed as described in Chapter 5, Section 5.2.1.

Post HR-MAS experiments 37 out of the 52 biopsy samples (22 GBM, 6 GIII and 9 GII) were submitted for quantitative histopathological examinations. This analysis revealed that the samples

present different histopathological tissue properties reflected in a variable content of highly cellular tumor tissue, infiltrations with normal tissue and/or necrotic tissue. Additionally, for each sample the percentage of each tissue property was calculated by measuring the total area of the biopsy sections within a sample and then delineating the regions of interest. The values are revealed in Chapter 5, Table 5.1.

In a classical classification approach, each of the 52 HR-MAS spectra would have been assigned to one and only one of the considered tumor subgroups, without identifying the contributions from necrotic tissue and normal tissue within each case. However, a strong correlation between the histopathological tissue properties and metabolic profiles coming from *ex vivo* HR-MAS has already been observed in glial tumors (Croitor Sava et al., 2011b); see also the discussion in Chapter 5. Therefore, for diagnosis purposes, it would be useful to decompose the HR-MAS spectra and identify the components reflecting pure highly cellular tumor tissue, border tissue (with infiltrations from normal brain tissue) and/or necrotic tissue and then determine their concentrations in each spectrum.

6.1.3 Methods

Non-negative matrix factorization

The principles of the methods are described in Chapter 3. For this study an NNMF implementation with sparseness constraints (NNMFSC) on the sources, *S*, is considered as in (Kim and Park, 2007). Thus the following optimization problem is solved.

$$\min_{A,s}\left\{\|X - AS\|_F^2 + \eta\|A\|_F^2 + \beta\sum_{j=1}^{n}\|S(:,j\|_1^2\right\} \quad \text{subject to } A, S \geq 0 \tag{6.2}$$

where *S(:,j)* is the j^{th} column vector of *S*, $\eta > 0$ is a parameter meant to control the size of $\|A\|_F^2$ and $\beta > 0$ balances the trade-off between the accuracy of the approximation and the sparseness of *S*. For this study the default values $\eta = 0.2$ and $\beta = 0.1$ were considered (Kim and Park, 2007).

NNMF is not a unique decomposition. Thus, (Kim and Park, 2007) propose an alternating non-negativity constrained least squares implementation which is fast and guaranteed to converge to a stationary point of the problem. The algorithm begins with the initialization of *A* with non-negative values and then several sweeps (up to a maximum of 100) are performed till convergence by computing:

$$\min_{S}\left\|\begin{pmatrix} A \\ \sqrt{\beta}\, e_{1xk} \end{pmatrix} S - \begin{pmatrix} X \\ 0_{1xn} \end{pmatrix}\right\|_F^2 \quad \text{subject to } S \geq 0 \tag{6.3}$$

$$\min_{A} \left\| \begin{pmatrix} S^T \\ \sqrt{\eta}\, I_k \end{pmatrix} A^T - \begin{pmatrix} X^T \\ 0_{kxm} \end{pmatrix} \right\|_F^2 \quad \text{subject to } A \geq 0 \tag{6.4}$$

where *k* is the number of sources, e_{1xk} is a row vector with all components equal to one and 0_{1xn} is a *0* vector. I_k is an identity matrix of *kxk* and 0_{kxm} a zero matrix of size *kxm*. Each subproblem of the type (6.3) or (6.4) is solved with a non-negative linear least squares active set method (Kim and Park, 2008).

CAMNS

Another novel approach that accounts for sparsity and non-negativity is convex analysis of mixtures of non-negative sources (CAMNS) (Cha et al., 2008). It is a recently developed nBSS framework. CAMNS is deterministic and is based on a special assumption called local dominance, which is closely related to sparsity and states that each source exhibits a non-zero value for a certain feature for which all the other sources have a zero value. Under the local dominance principle, the BSS criterion becomes a convex analysis problem and can lead to a unique source separation with probability one, as detailed in Chapter 3. Thus, the source signals can be perfectly identified in a blind fashion as described in (Cha et al., 2008).

nICA

One possible approach to the complexity of the spectra is to assume that the different tissue types are statistically independent. Following this principle, ICA has been previously considered in biomedical signal processing and analyses of single voxel MRS (Lee et al., 2000; Ladroue et al., 2003) and multi-voxel MRSI data (Szabo De Edelenyi et al., 2005; Su et al., 2008; Wright et al., 2009). These studies have shown that ICA can provide an effective way to reduce the dimensionality of MR spectra. In the study presented in this chapter a non-negative implementation of ICA which is based on a gradient algorithm operating on pre-whitened data, as suggested by (Ola and Plumbey, 2004), is considered. This approach is related to the 'nonlinear PCA' algorithms investigated by (Oja, 1999). The independent sources are considered to be non-negative and well-grounded (see Chapter 3). The algorithm is guaranteed to find a permutation of the well-grounded, non-negative sources. The idea behind this is that an orthogonal rotation of the whitened observation vector into non-negative outputs gives a positive permutation of the original sources. The proposed cost function minimum coincides with the non-negative solutions (Oja and Plumbey, 2004).

Prior to applying nICA the dimension of the data was reduced. This step ensures the stability of the algorithm when the size of the dataset is small compared to the dimension of the data as was emphasized in (Hyvarinen, 1999). Commonly PCA and SVM are use to reduce dimension (Hyvärinen and Oja, 2000; Kolenda, 2002). As in (Kolenda, 2002) the number of ICs was controlled by an initial PCA projection from the original data onto a *k* dimensional subspace.

6.1.4 Application to HR-MAS

The feature input space

The proposed nBSS techniques are applied on the magnitude HR-MAS spectra and on sets of features obtained from the spectra. For the spectra *n=716* points representing the magnitude HR-MAS signal in the region of interest between 0.25 ppm and 4.2 ppm were used. For the feature case, two experiments are designed. One where the concentration of 19 most visible metabolite peaks (see Table 6.1) are considered (*n=19*) and one where the concentration of the most representative metabolites for characterizing histopathological tissue properties (*n=8*) (Croitor Sava et al., 2011b; Cheng et al.1998), are used. Although visible, Alanine (Ala) and Lactate (Lac) were not added to the set due to their sensitivity to snap-freezing the samples, the temperature conditions and the unavoidable period of ischemia during the biopsy procedure, which significantly alters them when using HR-MAS (Opstad et al., 2008b; 2010).

Peak integration, a feature reduction method typical in NMR analysis (see Chapter 2, Section 2.2.3), was used for extracting the concentration of the considered metabolites. Namely, the highest point in the area to be integrated was identified for each metabolite, then the area bounds were fixed for each metabolite individually to those ppm values at which peak slopes return to baseline, but keeping symmetric intervals with respect to the highest point. Other metabolite quantification methods may also be considered and should not influence the results, subject to the condition that they provide reliable metabolite estimates. See Table 6.1 for a description of the metabolites considered in the two experiments where 19 and respectively 8 metabolic features were used as input space and the integration intervals considered for each metabolite.

Parameters to be considered

The study also questions the robustness of the considered algorithms when applied to slightly different datasets, i.e., different input matrices *X*. Thus, firstly we build the matrix *X* from the 27 measured GBM cases. Afterwards, we consider as input matrices *X* information coming from the available GII and GIII glial tumor subgroups separately. Finally, the whole dataset of 52 cases (GII, GIII, and GBM) is considered together as a single dataset.

For every experiment, the number of the sources, *k*, to be extracted has to be chosen. How the value of *k* influences the results and the performance of the algorithms is also investigated. A logical assumption is to choose *k* equal to the number of histological groups, if one presumes that the inter-patient variability is not too large. Thus, for the GBM group if one requires *S* to have 3 components, then these components should ideally represent the pure sources for necrotic, highly cellular and border tumor tissue. *A* contains the coefficients of the linear combinations of the found sources and reflects the abundance of the obtained sources within each sample. For GII and GIII glial tumor datasets, since the samples mainly contain highly cellular tumor tissue and border tumor tissue, we started from *k=2*. When considering all 52 cases, a *k* value up to 5 was tested. This choice is motivated by the high inter-patient variability, since in addition to the histopathological tissue variability the samples present different grades of tumor aggressiveness.

Table 6.1 *Metabolites*

Metabolite	Metabolite abreviation	Integration area in ppm	Experiment n=19	Experiment n=8
Lipid	'Lip1'	0.84 - 0.91	x	x
Lipid	'Lip2'	1.255 - 1.285	x	x
Lipid	'Lip3'	2.79 - 2.81	x	x
N-acetyl-aspartate	'Naa'	2.0 - 2.015	x	x
Creatine	'Cr'	3.01 - 3.03	x	x
Choline	'Cho'	3.19 - 3.205	x	x
Phosphocholine	'Pcho'	3.21 - 3.22	x	x
Glycero-phosphocholine	'GPCho'	3.225 - 3.235	x	x
Glutamate	'Glu'	2.1 - 2.12	x	
Glutamine	'Gln'	2.12 - 2.13	x	
Glutamate	'Glu2'	2.3 - 2.33	x	
Glutamine	'Gln2'	2.41 - 2.44	x	
Taurine	'Tau'	3.245 - 3.265	x	
Myo-inositol	'Myo1'	3.49 - 3.525	x	
Glycine	'Gly'	3.53 - 3.55	x	
Myo-inositol	'Myo2'	3.58 - 3.61	x	
Glutamine + Glutamate group	'Glx'	3.76 - 3.78	x	
Alpha glucose	'Glcalf'	3.83 - 3.86	x	
Beta glucose	'Glcbet'	3.86 - 3.89	x	

Performance measurement

Firstly, to evaluate the accuracy of the proposed nBSS methods in identifying the pure tumor tissue sources, a measure of the separation quality is performed. The nBSS results are validated by comparing them against the histology findings (the standard reference on which diagnosis is based nowadays). To this aim the spectra coming from samples classified as pure highly cellular tumor tissue, infiltrations with normal tissue and necrotic tissue (more than 90% of the sample area is covered by one tissue type) are considered as reference spectra. Then, the correlation coefficient, ρ **,** between the sources obtained with NNMFSC, CAMNS and nICA, respectively, and the reference HR-MAS tissue models is computed:

$$\rho = \frac{\mathrm{cov}(M_k, S_k)}{\sigma_M \sigma_S} \tag{6.5}$$

where *cov* stands for covariance, M_k for the k^{th} reference HR-MAS tissue model, S_k for the k^{th} obtained sources and σ is the standard deviation. The correlation coefficient takes a value between -1 and 1,

where a value close to -1 indicates a negative correlation, close to 0 indicates that sources are uncorrelated and close to 1 that the sources are highly correlated with the reference tissue.

Secondly, based on the mixing coefficients representing the contribution (abundance) of each source to the spectra we can assign each case, based on the highest abundance, to the predominant tissue type class. Additionally, for each case the percentage of necrosis, tumor cell density and infiltrations with normal tissue is computed. For this, the source with the smallest abundance for each case was set to zero and the percentage of the other two sources is then computed based on the new abundance matrix. This choice was motivated by the glial brain tumor growth behavior where necrotic regions are surrounded by highly cellular tumor cells and infiltrations from normal tissue are present at the border of the affected area. Thus, as observed also in the histopathological study, necrotic and border tissue are not present simultaneously in the analyzed biopsy samples. Moreover, this approach will allow us to verify if the abundance matrix obtained with the considered BSS methods is correct with respect to the tumor growth behavior. The results are then compared with the histopathological study and the mean squared error (MSE) for the percentage assignment is computed as:

$$MSE = \frac{1}{k}\sum_{1}^{k} (\overset{\%}{S}_k - \overset{\%^{his}}{S}_k)^2 \tag{6.6}$$

where $\overset{\%}{S}_k$ is the estimated percentage and $\overset{\%^{his}}{S}_k$ is the percentage according to the histological analysis, and k=3.

6.1.5 Results

Source detection performance

For each experiment conducted in this study, a set of source components, S, has been obtained. All three considered methods, nICA, CAMNS and NNMFSC respectively, provide consistent results and mostly similar sources. In Figure 6.1 the components extracted from the GBM group, for an input of 8 metabolic features, when asking for three components are shown. For this test we observe that the mutual correlation coefficients between the similar components obtained with CAMNS, NNMFSC and nICA are very high for necrotic and tumor tissue types (over 0.95). The border tissue component obtained with nICA presents more contributions from tLips and tCho compared to the component obtained with the other two methods.

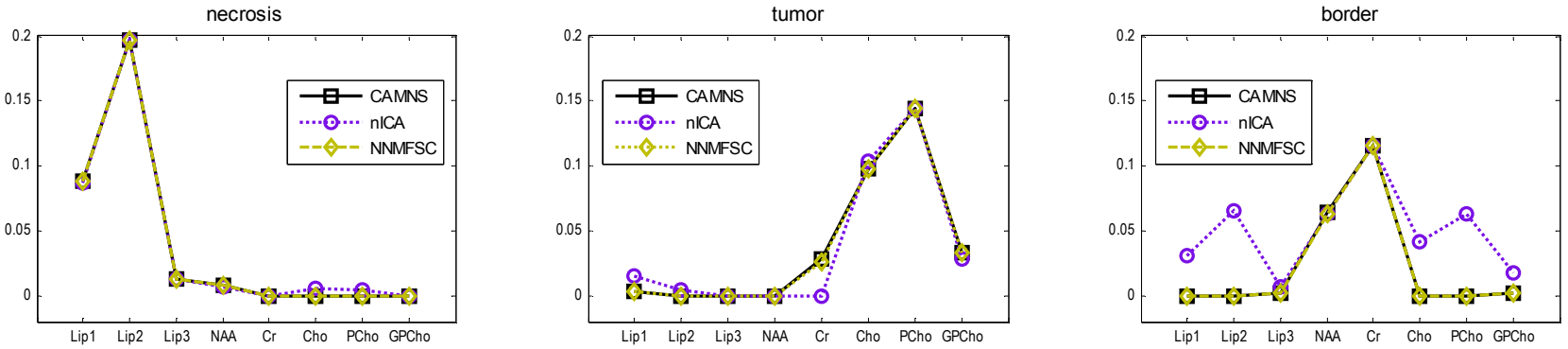


Figure 6.1 *Constituent tumor tissue source profiles identified with CAMNS, nICA and NNMFSC.*

As one aspect of the study is to analyze to which extent the feature input space could influence the results, Table 6.2 presents the results of the experiments conducted on the GBM group, when working on the whole magnitude spectra (n=716) or on a reduced feature input space (n=8 or n=19, as defined in Section 6.1.4). The accuracy of each method in extracting pure tissue sources, computed by means of correlation coefficients between the obtained nBSS sources and the reference spectra are illustrated.

Table 6.2 *The correlation between the obtained tissue sources and the reference tissue models for different input feature spaces*

	n=716	**n=19**	**n=8**
NNMFSC			
necrotic	0.97	0.97	0.99
tumor	0.69	0.65	0.72
border	0.91	0.92	0.91
CAMNS			
necrotic	0.98	0.97	0.99
tumor	0.62	0.61	0.71
border	0.89	0.54	0.88
nICA			
necrotic	0.81	0.93	0.98
tumor	0.68	0.67	0.73
border	0.83	0.51	0.68

All methods identify with a very high accuracy the necrotic tissue pure component, as the correlation with the reference model is mostly higher that 0.95 for all the considered feature input spaces. The sources obtained on the full magnitude spectra (n=716), as well as on the extracted metabolic features are clearly separated and are in agreement with the conclusions drawn in the literature (Cheng et al., 1998). See Figure 6.1 and 6.2, where one can observe that the obtained necrotic tumor tissue source is characterized by elevated peaks of lipids (Lip1, Lip2), while the rest of the metabolites are present in very low concentrations.

For extracting the border tissue component, NNMFSC outperforms the other two methods. With NNMFSC, the correlation with the histopathology reaches more than 0.9 out of 1. The sources present characteristic high peaks of NAA and Cr. The border tissue source obtained with CAMNS when applied on full spectra reveals some contributions from tCho as well as high Gly concentrations which would be typical for a highly cellular tumor tissue. With nICA, the border tissue component obtained on the full magnitude spectra presents contributions from tLips and tCho. This phenomenon is noticeable

also based on 8 features; see Figure 6.1, where the estimated source for border tissue appears in fact as a mixture of tumor, necrosis and border tissue, although with a predominant contribution from border tissue.

All methods are less accurate in extracting a component that would correspond to spectra of pure tumor tissue in the brain. With CAMNS, the tumor tissue source presents levels of Cr that are higher than what is concluded in the literature (Tong et al., 2004, Majos et al., 2004, Wright et al. 2009) and with nICA, Lips are present in the source. Again, overall best performance is obtained with NNMFSC. As one can see in Figure 6.2, Ala and tCho metabolic components are more elevated in the tumor compared to the other sources.

Looking at the overall performance of the considered methods, results show that with NNMFSC the obtained sources are the closest to the reference tissue models. Additionally, best overall accuracy for NNMFSC, as shown in Table 6.2, is obtained when considering an input feature space consisting only of the most representative metabolites ($n=8$), followed closely by the full magnitude spectra input space.

Interpretation of the abundance matrix

For each spectrum we obtain the mixing coefficients representing the contribution (abundance) of each source within the spectrum. Thus, we can identify for each case, based on the highest abundance, the predominant tissue class, as well as to compute the approximate concentration contribution from each tissue type. These mathematical results were compared with the histopathological results. For this comparison only the histopathologicaly confirmed cases could be considered (22 GBM, 6 GIII and 9 GII). NNMFSC can accurately identify the predominantly tissue class for 19 out of the 22 histopathologically confirmed GBM cases. With CAMNS and nICA 16 and 17, respectively, out of 22 histopathologically confirmed GBM cases, were correctly assigned to the predominant tissue class. These results were also reflected in the percentages of contribution of each source to the cases, as a good agreement was obtained between histology and the methods proposed in this study. The MSE is mostly below 10 when considering the NNMFSC algorithm, see Figure 6.3.

Choosing the number of sources, *k*

In Figure 6.4 the results obtained on the dataset represented by all 52 glial tumors are presented, when using NNMFSC for different k values ($k=2,\ldots,5$). For $k=2$, the necrotic tissue component is accurately detected. The second component presents characteristics which reveal a mixture between border and highly cellular tumor tissue. For $k=3$, the three obtained sources present a high correlation with the reference models for pure necrotic, highly cellular and border tumor tissue, respectively. For a $k>3$ necrotic and border tissue remain relatively stable, while the other components can not be clinically or histopathologically interpretable. First source detectable is the one corresponding to necrotic tissue. Its profile does not change radically for different k values. Thus, adding another component does not influence the results. For $k=3$ all the obtained sources present a histopathological meaning. These results confirm our assumption that the best k value is the one that reflects the number of histopathological components present in the data. By choosing a smaller k, one would obtain impure sources which would present contribution from more than one tissue type, while by choosing a higher k, one would obtain components that do not have a histopathological interpretation.

These results are also confirmed by similar experiments performed when considering each glial tumor subgroup separately. For the GBM dataset, most meaningful sources were also obtained when considering *k=3*. For the GII and GIII subgroups best performance is given for *k=2*. This can be explained by the fact that the necrotic tissue type is not represented in these subgroups, as revealed by the histopathological analyses (see Table 5.1 in Chapter 5). The two sources extracted from GII and GIII groups, respectively, are highly correlated with border and highly cellular tumor tissue models.

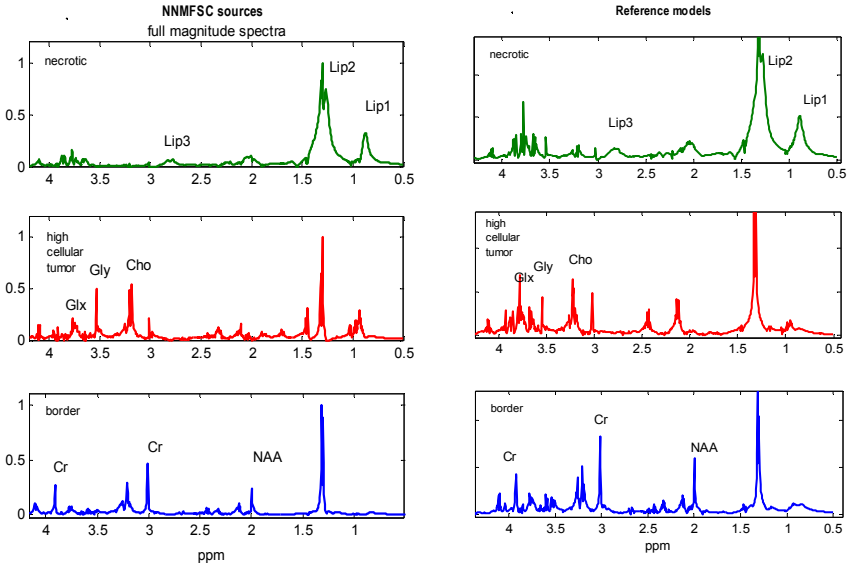


Figure 6.2 *Tumor tissue sources obtained with NNMFSC, when applied on the magnitude spectra (left column). Right column plots illustrate pure tissue samples, as indicated by histopathology.*

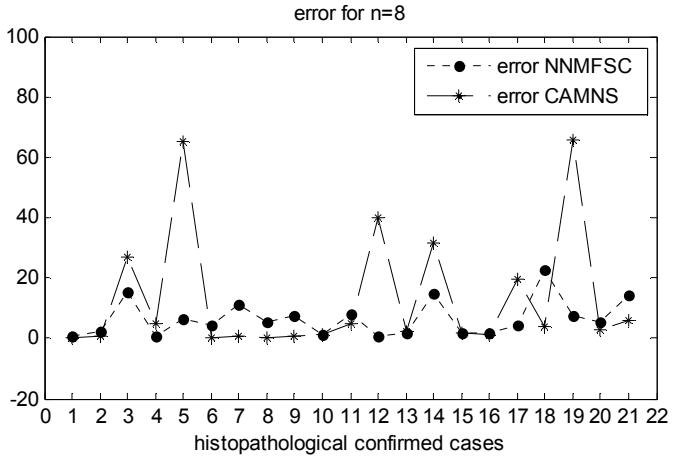


Figure 6.3 *The MSE computed as in Eq. 6.6 obtained with NNMFSC and CAMNS, respectively, on feature vectors (n=8). The error corresponding to nICA (not shown) is higher overall.*

Additionally, a relatively high similarity can be observed between the sources obtained with NNMFSC on the different tumor groups or on all 52 spectra. See Figure 6.5 where plots displaying the sources extracted from all cases and from each glial tumor subgroup, respectively, are illustrated. The metabolite feature space is represented by the 8 most representative metabolites.

Thus, the performance of the algorithm is not influenced by the number of available cases used as input matrix. Nevertheless, the method will always identify only those histopathological classes that are well represented in the data.

6.1.6 Discussion

In this study nBSS methods are used for obtaining characteristic profiles for each tissue subtype and their concentrations within a spectrum. The interpretation of the results is strongly supported by an extensive histopathological study. We show that NNMFSC, CAMNS and nICA can reliably answer the problem of source separation when analyzing HR-MAS data. Still, NNMFSC overall outperforms the other two methods, followed very closely by CAMNS. The similarity in the results obtained with NNMFSC and CAMNS could be a due to the fact that the methods rely on the same principles, i.e., they do not assume any independence or correlation, but sparsity is imposed. Still with CAMNS the assumption of sparsity (namely the local dominance property) is too strong, in the sense that, when a source exhibits a non-zero value for a certain feature, all the other sources must have a zero value. With NNMSC, a trade-off between the accuracy of the approximation and the sparseness of S is allowed. This is mainly important since for some metabolites it can happen that they exhibit peaks of different concentration in more than one source.

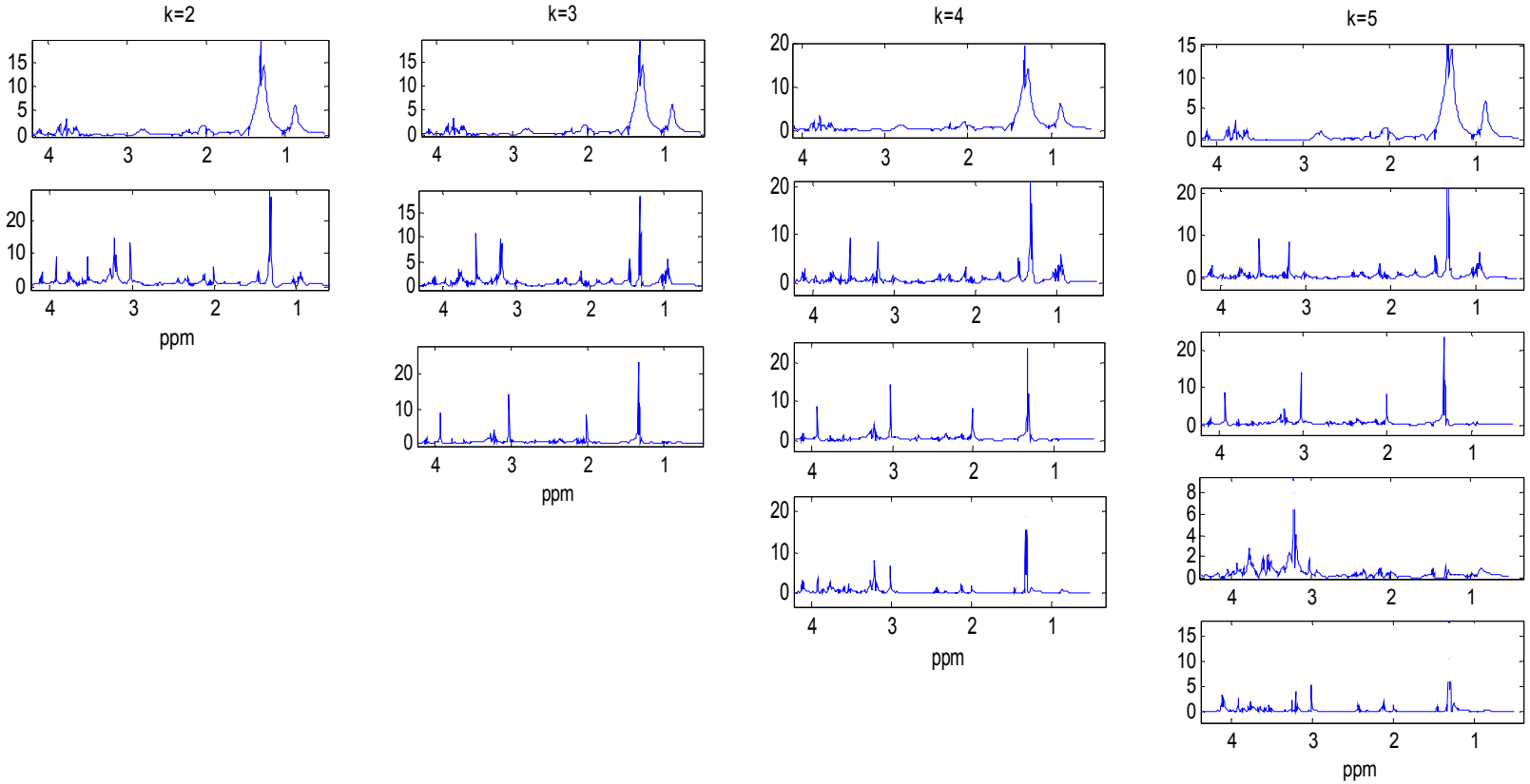


Figure 6.4 *NNMFSC components calculated for the full dataset of 52 magnitude spectra, for k = 2,3,4, and 5.*

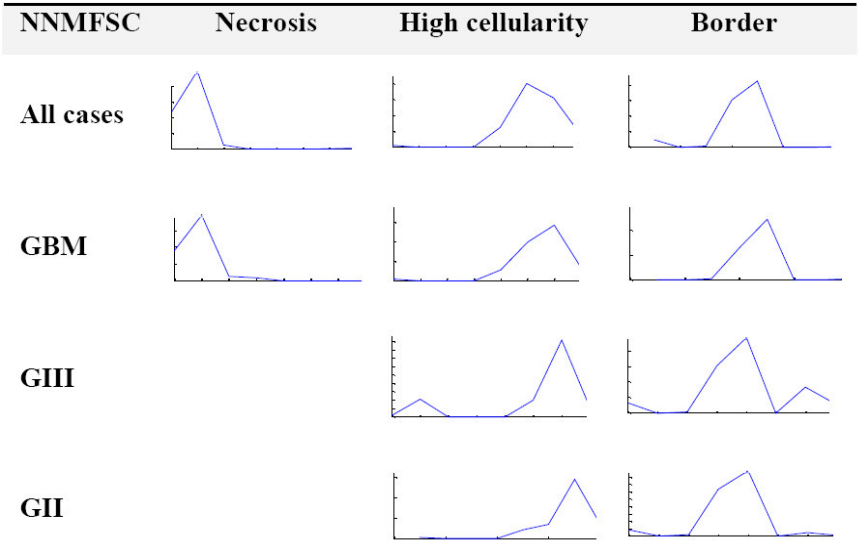


Figure 6.5 *NNMFSC components calculated for 8 metabolic features, for GII, GIII, GBM and all glial tumor datasets.*

For nICA one imposes a strong assumption of independence and consequently uncorrelation. Taking into consideration the nature of HR-MAS data, where correlations in the metabolic profiles may still be present to some degree between the spectra form different tissue types, such an approach is not the most suitable for our problem, as could be concluded from the results. In reality, it would be hard to identify a 100% pure highly cellular tissue in glial tumours. This tissue type will mostly exhibit some contribution from normal tissue or some necrotic cells. Moreover, the metabolites describing the histopathological tissue properties are correlated as shown in Chapter 5, (Croitor Sava et al., 2011b). Therefore, the extracted tumor tissue source would always correlate to some extent to the other two histopathological tissue types.

Choosing the correct k is not as important as one might expect. It has been observed that once a component is well represented in the data, it will be correctly identified by the proposed nBSS algorithms, regardless of the value of k. These conclusions are in agreement with (Szabo De Edelenyi et al., 2005). Also the dimension of the input space (the number of spectra used for extracting the sources) is not influencing the results as proven by the experiments described in Section 6.1.5.

With respect to the best input feature space to be considered, for best separation between necrotic, high cellular tumor tissue and infiltrations, our results are in agreement with the literature and show that NAA, Cr, Lips and tCho group are most representative for solving this classification problem. Adding extra information will not bring any added value in the performance of the considered nBSS methods. Additionally, by increasing the dimensionality of the matrices (case n=19 and n=716), the problem becomes more expensive and also prone to provide a solution that is less meaningful for the given problem. A reduction of the input feature space to the most representative features would bring a two-fold advantage. On one side, it reduces the computational time, and, secondly, we avoid bringing irrelevant information into the problem.

Using the mixing coefficients we can compute the percentage of necrosis, tumor cellularity and infiltrations with normal tissue for each case. This approach presents the advantage that the results are closer in what concerns their interpretation to the histopathological output and to the clinical interpretation.

Brain tumor tissue classification problems arising from *in vivo* magnetic resonance spectroscopy can benefit from a similar approach, as described in Section 6.2.

6.2 Application to *in vivo* MRSI data

6.2.1. Introduction

As shown in Chapter 5 and in Section 6.1 of this chapter, there is a significant variability between the *ex vivo* spectra coming from glial brain tumours as an effect of intra-tumoral heterogeneity. This phenomenon, explained in detailed by histopathological studies, is also reflected at the metabolic level. By applying nBSS methods on HR-MAS data one can obtain characteristic profiles for each tumor tissue subtype and their abundance within a spectrum. This finding provides relevant additional information for a better interpretation and classification of brain tumor tissue. Brain tumor tissue classification problems arising from *in vivo* MRS can benefit from a similar approach. Therefore this section will further extend the study presented in Section 6.1 to MRSI data.

Although the MRSI technique is very interesting due to its non-invasive nature as well as due to the possibility of exploring spatial information, the accuracy of MRSI in differentiating and grading glial brain tumors is limited by the significant variability of *in vivo* spectra as an effect of intra-tumoral heterogeneity. In gliomas one can observe distinct histopathological tissue properties, such as viable tumor cells, necrotic tissue or regions where the tumor infiltrates normal brain.

This study proposes a screening between these intratumoral histopathological tissue properties within MRSI data by quantifying the abundance within each MRSI voxel for each intratumoral histopathological tissue property. We assume that such an approach would greatly assist in an improved diagnosis, prognosis and treatment planning in gliomas. From the BSS methods analyzed in Section 6.1 NNMFSC will further be considered for this study, as it has been shown to be most accurate in solving the addressed problem. Additionally, nosologic images are drawn based on the extracted abundance maps, reflecting the presence of necrosis, viable tumor cells or infiltrations in the MRSI grid.

6.2.2 Data

MRSI data of 7 patients with gliomas, histopathologically confirmed according to WHO classification, were acquired at the University Hospital of Leuven (UZLeuven) on a 3T Philips scanner (Achieva and Intera, Philips, Best, The Netherlands), using a PRESS pulse sequence as the volume selection technique. The acquisition parameters are: FOV: 16cm x 16cm, VOI: 8cm x 8cm , samples size: 2048, number of signal averages: 1, shimming: pencil beam shimming, first and second order. For each patient both water suppressed and unsuppressed proton MRSI data were acquired as well as MR images (T_1-weighted MRI without contrast, T_2-weighted MRI, T_1-weighted MRI with contrast, FLAIR, DWI with sequence b-value of 0 mm/s² , DWI with sequence b-value of 1000 mm/s²).

The spectra were preprocessed using the Matlab platform and by water removal with HLSVD-PRO (Laudadio et al., 2002), baseline correction and normalization (see Chapter 2, Sections 2.1.7 and 2.1.8, respectivly). The baseline was corrected using an apodization function as described in Chapter 2 and the normalization was performed with respect to the water signal. Magnitude spectra are computed by taking the absolute value of the Fourier transformed time-domain signals. Contributions outside the frequency interval [0.25, 4.2] ppm were filtered out in order to keep only the contribution of the metabolites of interest and to avoid expensive computations.

6.2.3 Methods

For each MRSI grid, NNMFSC is applied separately on the magnitude MRSI spectra in the region of interest between 0.25 ppm and 4.2 ppm and on sets of features obtained from the spectra.

A two step approach is implemented. This choice is motivated by the high heterogeneity of the data reflected both at MRSI grid level as well as at the intra-tumoral level. Also, since there are different tumor types and grades, in the first step we separate normal brain tissue voxels from voxels with abnormal brain tissue, which should therefore contain predominant tumor tissue. For this step, the value of k is set to 2 and the two obtained NNMFSC components should typically represent the normal brain tissue and the abnormal tissue pattern. Then, based on the highest abundance, each voxel is assigned to normal or abnormal tissue. For selecting the abnormal tissue voxels one may use MRI images. Still, as shown in previous studies, glial tumors are highly infiltrative and the area surrounding the enhancing region in glioblastoma and the region where the gliomas infiltrate, appeared normal on the MRI. Additionally, for the infiltrated non-enhancing/non-$T2$ hyperintense areas, abnormal Cho/NAA ratio levels were reported for gliomas (Di Costanzo et al., 2008). Elevated levels of Cho were also observed in the surrounding region for gliomas in (Fan et al., 2004).

The NNMFSC results are validated by comparing them against MRI intensity enhancement and by evaluating the Cho/NAA peak-area ratios within the grid. Spectra from areas with obvious intensity enhancements were selected as tumor spectra.

In the second step, NNMFSC is applied within the region with abnormal tissue with the purpose of identifying for each voxel within this region its predominant intratumoral histopathological property corresponding to necrotic, high cellular or infiltrations. The results are then used to construct nosologic images, by assigning each voxel to the tumor tissues type with the highest abundance coefficient. In this step the number of components to be extracted, k, is set to 3.

As mentioned above, two types of experiments were designed in this study. One where we work with the full magnitude spectra and one where we work with metabolic features

extracted from each spectra. For the second case AQSES-MRSI (Croitor Sava et al., 2011a), an advanced metabolite quantification method for MRSI data, with which the available spatial information is exploited, was considered. The method is described in details in Chapter 4.

For the metabolite features case, we considered a different number of metabolites for each step. Thus, 11 observations, representing the concentration of the most representative metabolites in separating tumor from normal tissue (NAA, Glu, Cre, PCh, Glc, Lac, Ala, Myo, Tau and Lips at 0.9 and 1.3ppm), were used in the first step. Only 6 observations representing the concentration of the most representative metabolites in identifying intratumoral histopathological variability (Lips at 0.9 and 1.3ppm, Lac, Cr, NAA and PCh) were further considered in the second step. This choice was based on the conclusion drawn in previous studies which showed that there is a high correlation between the concentrations of Lips, Cr, NAA and PCh group and the histopathological tissue properties (Croitor Sava et al., 2009; 2011b; Cheng et al. 2000; Andronesi et al., 2008; Opstad et al., 2008a). Additionally, as shown in Section 6.1, NNMFSC best performance in separating between histopathological tissue types was reported for this set of metabolites. When conducting *ex vivo* MRS studies, Lac levels might be highly affected by the sample handling procedure, such as changing the sample volume in the MAS rotor, snap-freezing the samples, the temperature conditions. With *in vivo* MRS these conditions do not occur and therefore Lac levels can be reliably detected in the profile of the spectra. Thus, since Lac levels are reported in (Cheng et al., 2000) to correlate with the level of necrosis, it was also considered in this study.

To compare the obtained sources with the ones obtained in the study described in Section 6.1 we computed the correlation between the histopathological tissue sources extracted with the NNMFSC algorithm on the MRSI data and the ones extracted on HR-MAS data in Section 6.1.4.

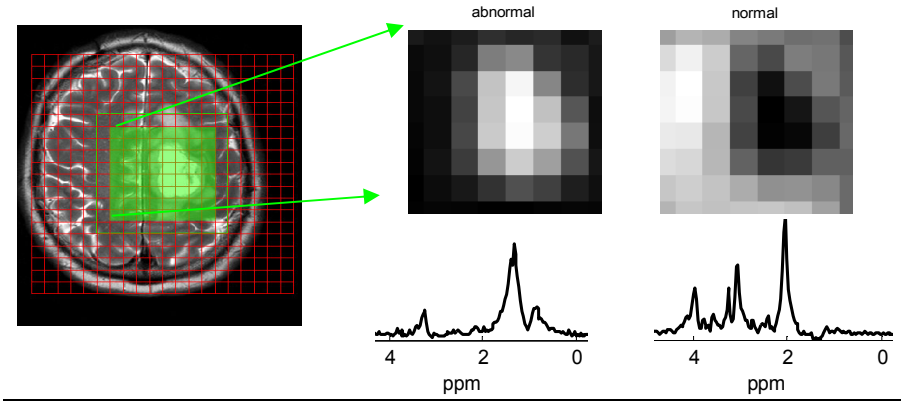
Although a direct validation of the results using histopathological analysis is not feasible when analyzing *in vivo* MRSI data, for all voxels, the results were confronted with the tissue labeling proposed by the expert spectroscopists.

6.2.4 Results

For each individual MRSI examination, a set of two components have been obtained in the first step, as well as an abundance matrix. The results on a MRSI image of a patient with glioblastoma are presented in Figure 6.6 which displays the extracted components and the two corresponding maps where the abundance of each component for the different voxels is displayed. The abundance matrix is drawn using a grey scale map showing the values of each component for the different voxels. It takes values between 0 and 1, represented by black and white, respectively, as shown in Figure 6.6.b.

The contour of the abnormal tissue area is very similar to the contour reflected in the MRI image. The first component is present in high concentrations in the center of the tumor, in the necrotic area. Its metabolic profile is very different from the normal tissue component. It presents elevated levels of Lips and Lac, while the concentration of the other metabolites is very low. The abnormal tissue area contains many voxels where a mixture of these two components is obtained. The second component, the normal tissue component, is present only in the healthy part of the brain and shows a high degree of similarity with the measured spectra obtained from healthy tissue, with high NAA/Cho levels and with metabolic profiles very close to the conclusions reported in the literature (Devos, 2005b).

We also compare the results obtained on the full magnitude spectra with the results on the extracted features. See Figure 6.7, where each voxel is labeled based on the highest abundance component. Results obtained on magnitude spectra and metabolite feature space show that with both approaches we obtain very similar tissue assignment.



a. b.

Figure 6.6 *a. MRI T2-weighted image of a glioblastoma patient. The contour of the MRSI grid is marked with green on the image. In b. the results of the first step using NNMFSC are visualized: abundance maps showing the voxels identified as abnormal tissue and predominantly normal brain tissue (the upper part of the image); lower part shows the component profiles as identified with NNMFSC.*

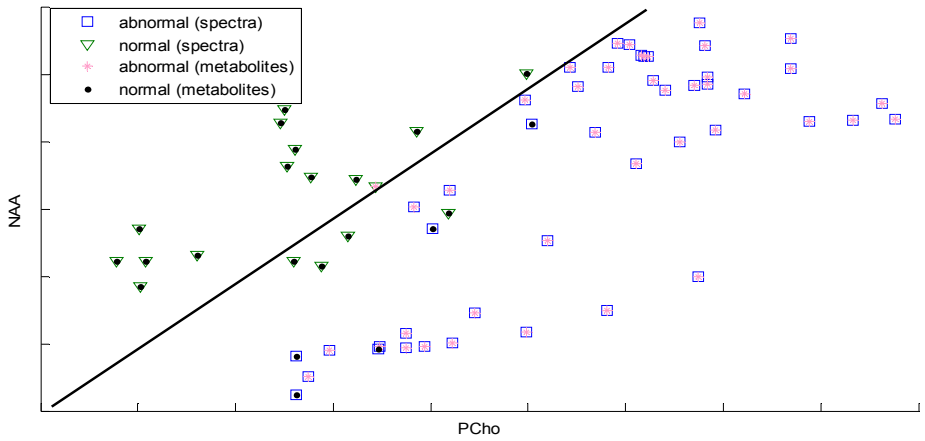
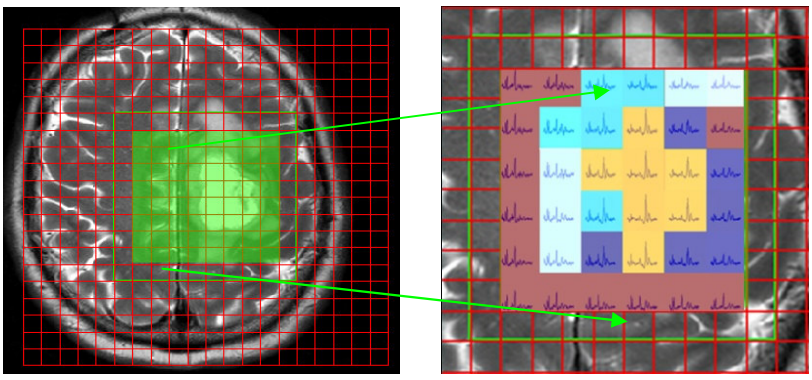


Figure 6.7 *Plot showing the label of each voxel, within the MRSI grid, based on its highest abundance component. Results on magnitude spectra and metabolite feature space are compared.*

In the second step, NNMFSC results applied in the abnormal tissue region, for *k=3,* are converted to nosologic images. The voxels identified as predominantly necrotic tissue, voxels with viable tumor cells and voxels with predominant normal brain tissue are visualized. Each histopathological tissue class is represented by a different color and therefore the images are easily interpretable. See Figure 6.8, where the results on the GBM patient after the second step are presented.



b.

Figure 6.8 a. *MRI T2-weighted image of a glioblastoma patient. The contour of the MRSI grid is marked with green on the image. b. Nosologic image showing the voxels identified as predominantly necrotic tissue (orange color), voxels with viable tumor cells (blue color; dark*

blue stands for high cellularity; lighter blue reflects higher levels of infiltrations from normal tissue, the lighter the blue the higher the percentage of infiltrations) and voxels with predominantly normal brain tissue (dark red). This image was created using NNMFSC, with metabolite concentrations as features.

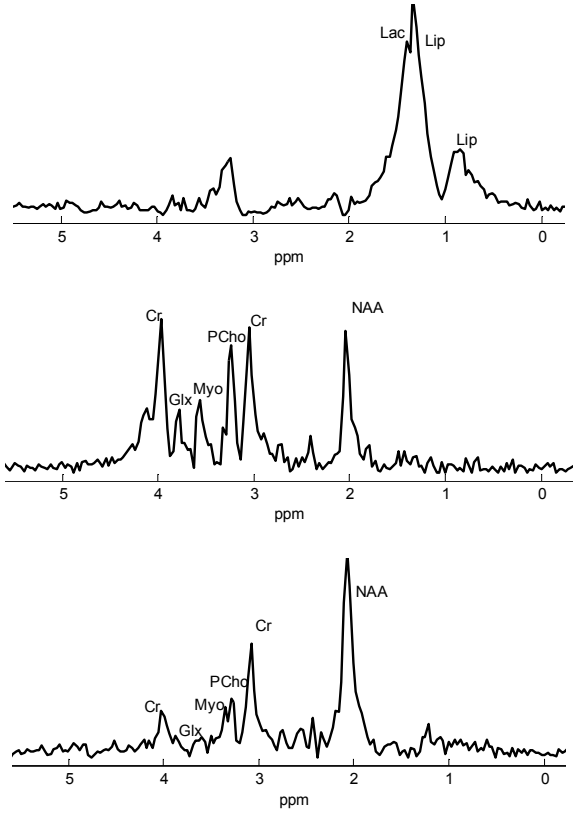


Figure 6.9 *The NNMFSC 2nd step sources obtained for k=3.*

Figure 6.9 illustrates the components obtained in the second step. Using as reference the tissue models defined in Section 6.1 as necrotic, border and highly cellular tissue we can assigned each component to a histopathological tissue class. The necrotic tissue component is very similar to the abnormal tissue component identified in the first step, with the mutual correlation coefficients of 0.96, and is present in high concentrations in the center of the tumor area. The border and the highly cellular tissue component are surrounding the necrotic tissue area. Where the infiltrations with normal tissue are high, also the levels of NAA and Cr are elevated, while in the highly cellular regions high levels of PCho are observed.

6.3 Conclusions

The nBSS methods proposed in Section 6.1 for obtaining characteristic profiles for each tissue subtype and the abundance of each source within a spectrum can reliably answer the problem of source separation when analyzing HR-MAS data. Moreover, we can decompose the observed MRSI grid into constituent tumor tissue sources with different predominant intratumoral histopathological properties and further quantify the abundance of each considered tissue source which can then be explored as nosologic images. This approach can provide relevant additional information for a better interpretation and classification of *in vivo* MRSI data and therefore enhance its contribution to brain tumor classification. In particular, this method can be of added value in addressing difficult questions such as the grading of glial tumors or differentiating metastasis from glioblastoma. Also it requires no previous training set, which often can be a problem when dealing with new measurements or with rare tumors.

The finding in this study can provide relevant additional information for a better interpretation and classification of brain tumor tissue in *ex vivo* high resolution MRS and *in vivo* MRS(I), respectively.

Chapter 7

Fusing *in vivo* and *ex vivo* NMR for brain tumor classification

This chapter[4] describes a study on classifying short echo-time brain magnetic resonance spectroscopic imaging (MRSI) data by applying a model-based canonical correlation analysis (CCA) algorithm and by using, as prior knowledge, multimodal sources of information coming from high resolution magic angle spinning (HR-MAS), MRSI and magnetic resonance imaging (MRI). The potential and limitations of fusing in vivo and ex vivo nuclear magnetic resonance (NMR) sources to detect brain tumors is investigated. Various modalities for multimodal data fusion are presented, the effect and the impact of using multimodal information for classifying MRSI brain glial tumors data is studied and an analysis on which parameters influence the classification results is performed by means of extensive simulation and in vivo studies. Special attention is drawn to the possibility of considering HR-MAS data as a complementary dataset when dealing with a lack of MRSI data needed to build a classifier.

7.1 Introduction

Several *in vivo* and *ex vivo* NMR techniques are commonly used in the diagnosis and prognosis of brain tumors. Among them, conventional MRI techniques essentially assess anatomy, but they are often not able to characterize the heterogeneous growth of cancer tissue and to identify tumor type or grade. To address these issues, MR spectroscopy (MRS), and especially its multi-voxel approach, MRSI allows the spatial mapping of metabolites. *Ex vivo* high resolution NMR techniques are also often considered if one is interested in an accurate biochemical profile of brain tissue. Since a good correlation between *ex vivo* HR-MAS and *in vivo* MRS has been reported (Opstad et. al., 2010) one can consider using HR-MAS to improve the interpretation of the metabolic biomarkers that are visible with *in vivo* NMR. Additionally, with *ex vivo* HR-MAS the tissue integrity is not extremely damaged (Martínez-Bisbal et al., 2010) and this is an advantage since it allows one to perform, on the same tissue

[4] Croitor Sava AR, Martinez-Bisbal MC, Laudadio T, Piquer J, Celda B, Heerschap A, Sima DM and Van Huffel S. Fusing *in vivo* and *ex vivo* NMR sources of information for brain tumor classification. Accepted for publication in Journal of Measurement Science and Technology. 2011.

sample, multimodal studies including subsequent genomic, proteomic or histopathological analyses and, therefore, to obtain a direct comparison between all these techniques.

Nowadays multiple acquisitions of the brain with different techniques are getting very common. Combinatorial approaches, where different techniques are correlated or compared for assessing the tumor type and grade have been previously proposed (Barton et al., 1999; Cheng et al., 2000; Tugnoli, et al., 2006; Tzika et al, 2007; Righi et al, 2009; Wright et al., 2009; Lopez-Gines et al., 2009, 2010; Ferrer-Luna et al., 2009, 2010). These studies, where multiple data sources are considered, can provide further insights into the biology of the brain tumors and improve the diagnosis. Still, in all these studies the multimodal sources of information are explored individually and then overlaid to demonstrate the relationship between them. It has been shown in (Simonetti et al., 2003, 2005; Devos et al., 2005a; De Vos et al., 2007; Luts et al., 2009a; Laudadio et al., 2005, 2008) that fusing MRI and MRSI information improves brain tumor classification compared to the use of information of each source alone.

In this chapter a multi-center study where multimodal sources of information coming from HR-MAS, MRSI and MRI are integrated for the classification of glial brain tumors is proposed. The novelty of the approach relies on fusing various sources of information, demographically heterogeneous and acquired using different biomedical data acquisition protocols. The purpose is to explore the common features as well as the complementarity in the data, and, therefore, to take advantage of both metabolic and anatomical information.

In order to fuse multimodal sources of NMR information, reliable and robust classification strategies must be considered. The classification methodology proposed in this study is based on the canonical correlation analysis (CCA) algorithm (Golub and Van Loan, 1996). CCA has been shown to be a good framework for fusing multimodal biomedical data and it has already successfully been applied to brain data (De Vos, et al., 2007; Laudadio et al. 2005; Correa et al., 2008, 2010; Li et al., 2009). CCA allows us to perform a multivariate analysis where different sources of information are integrated in the classification algorithm. For this study a model-based CCA approach based on investigating the goodness-of-fit of the data to some prior knowledge is considered.

Since in supervised classification one may have to deal with complications such as the limited number of samples available for analysis, firstly, the problem of lack of data available *a priori* for building a model for the analyses based on the CCA algorithm was tackled. Then, the possibility of using HR-MAS data as a complementary dataset for building the models was explored. Two different approaches for improving the classification results by fusing multimodal information are proposed: integrating multiple datasets or multi-channel modeling. Additionally, for both approaches the model accounts for inter-patient variability. To assess the quality of the proposed method and to investigate which parameters influence the classification results, an extensive simulation study is carried out and several *in vivo* MRSI examples of brain tumor are analyzed.

7.2. Materials

7.2.1 Tumor data description

***Ex vivo* HR-MAS data**
For this study a dataset of HR-MAS measurements acquired on 52 patients as part of the eTUMOUR project was considered. The details on the acquisition and the preprocessing of these data are described in Chapter 5.

Although all samples were initially labeled as glial brain tumors with different degree of malignancy (27 glioblastomas (GBM), 7 grade III glioma (GIII), 18 grade II glioma (GII)), the histopathological analysis performed post HR-MAS analysis on the same tissue part used in the HR-MAS analysis revealed a high variability in the content of each sample. Therefore, they present variable contributions from highly cellular tumor tissue, infiltrations with normal tissue and/or necrotic tissue. 12 of the 52 samples presented very high infiltrations (over 70%) from normal tissue, revealing metabolic patterns that are typical for normal brain tissue, as described in (Croitor Sava et al., 2011b). Since the HR-MAS spectra coming from these samples were not representative for the tumor tissue types considered in this study they were grouped separately. The other 40 out of 52 spectra within the HR-MAS datasets were then split in three subgroups as follows: 13 GII, 5 GIII and 22 GBM.

***In vivo* MRI and MRSI data**
In vivo NMR measurements on 25 patients with a brain tumor were performed in the Radboud University of Nijmegen Medical Centre (RUNMC). The study was approved by the ethical committee of the RUNMC. Each patient tumor type was determined by expert consensus and histopathological validation followed the rules of the World Health Organization (WHO). Since for one of the patients no consensus was reached, the data from this patient were not used. Therefore for the statistical study 24 patients were considered.

For each patient both water suppressed and unsuppressed proton MRSI data and a set of MR images were acquired. The latter consisted of T1 weighted (TE/TR=15/644ms), T2 weighted (TE/TR=16/3100ms), proton density weighted (TE/TR=98/3100ms) and Gadolinium (Gd) enhanced T1 (15 ml 0.5 M Gd-DTPA) images. The acquisition was performed on a 1.5T clinical MR system (Siemens Vision), using 2D STEAM pulse sequence with the STEAM box positioned in a transversal plane through the brain showing the largest tumor diameter in the Gd contrast enhanced image. The MRSI parameters are: 16x16x1024 samples, TR/TE/TM=2000 or 2500/20/30ms, slice thickness = 12.5 or 15 mm, FOV (field of view) = 200 mm, spectral width = 1000 Hz and NS=2.

All water suppressed MRSI spectra were semi-automatically preprocessed as follows: filtering of k-space data by a Hanning filter of 50% using the LUISE software package (Siemens, Erlangen, Germany), zero filling to 32 x 32 and spatial 2D Fourier transformation to obtain time domain signals for each voxel, eddy current correction, water removal with

HLSVD-PRO (Laudadio et al., 2002), frequency alignment using a semi-automatic procedure as described in (Simonetti et al., 2003) and baseline correction using an apodization function as described in (Poullet, 2008). Zero-order phase was already corrected during eddy current correction. Manually, all first order phases were adjusted. Finally, all spectra were normalized with respect to the unsuppressed water signal. For more details on these preprocessing steps see also Chapter 2, Section 2.1.

From each patient, several spectra from voxels located in the tumor area of the MRSI grid, as well as from normal appearing regions were selected, resulting in a total of 379 spectra. Spectra with the same pathology were then grouped, resulting in an MRSI dataset of 176 spectra for GII, 57 spectra for GIII, 70 GBM spectra and 76 spectra for normal tissue from patients.

7.2.2 Harmonization of multimodal data

A multi-center study in which multimodal data (HR-MAS, MRSI and MRI) are combined is proposed. The fusion of multimodal datasets is a challenging problem since the data are dissimilar in nature. In addition the considered datasets are heterogeneous in demographics and data acquisition protocols. To overcome this problem we propose a feature-based approach.

For harmonizing the spectral information coming from MRSI and HR-MAS data, a dimensionality reduction of the available data is performed, by quantifying the most important metabolite concentrations using peak integration. We emphasize that all spectroscopic data are based on hydrogen proton (^{1}H). The following 10 metabolites were considered: *Lip1* (lipids at *0.9ppm*), *Lip2* (lipids at 1.3 ppm), *Lac* (lactate), *Ala* (alanine), *NAA (*N-acetyl-aspartate), *Glx group* (glutamine - *Gln* and glutamate - *Glu*), *Cr* (creatine), *Cho* (choline), *Tau* (taurine), *Myo* (myo-inositol) + *Gly* (glycine). The chosen metabolites are important biomarkers for separating different tissue types within the brain and present a high correlation in *ex vivo* and *in vivo* measurements (Opstad, 2010). Thus, for each MRSI and HR-MAS spectrum, a vector with 10 metabolite concentrations, further called spectral feature vector, is obtained.

The linewidth and SNR differences between *in vivo* and *ex vivo* spectra make us reasonably think that different strategies are required to extract relevant features. Thus, different integration intervals are considered for HR-MAS and MRSI spectra, respectively (see Table 7.1).

Due to peak overlap and relatively low spectral resolution that characterize the MRSI measurements at the clinical field strength considered in this study, *Lac, Ala* and *Lip2* were extracted as one feature, *Glu* and *Gln* were also grouped, the same for Myo and *Gly*, as well as *Glu, Gln* and *Ala,* which overlap around 3.74 ppm.

Table 7.1 *Integration intervals: MRSI vs HR-MAS spectra*

Metabolite	MRSI	HR-MAS
Lip1	[0.835-0.965] ppm	[0.860-0.920] ppm
Lac + Ala +Lip2	[1.265-1.395] ppm	[1.320-1.340] ppm (Lac) [1.450-1.490] ppm (Ala) [1.300-1.320] ppm (Lip)
NAA	[1.955-2.085] ppm	[1.955-2.085] ppm
Glu+Gln	[2.135-2.265] ppm	[2.090-2.170] ppm (Gln) [2.390-2.50] ppm (Glu)
Cr	[2.955-3.095] ppm	[3.010-3.030] ppm
Cho	[3.135-3.265] ppm	[3.135-3.245] ppm
Tau	[3.375-3.505] ppm	[3.390-3.420] ppm
mI+Gly	[3.495-3.625] ppm	[3.500-3.620] ppm
Glu+Gln+Ala	[3.685-3.815] ppm	[3.720-3.800] ppm
Cr	[3.885-4.015] ppm	[3.910-3.940] ppm

For HR-MAS, the considered metabolites were quantified separately. Peaks which were grouped together in short-echo time ^{1}H MRSI spectra were grouped in the same manner in HR-MAS spectra, by summing up their corresponding integrated areas into one feature.

Spectral information is also combined with imaging information coming from MRI measurements and the harmonization of these sources is performed, as described in (Simonetti et al., 2003), by lowering the resolution of the MR images to the MRSI voxel size. Specifically, the images with 4 contrasts are aligned with respect to the MRSI image and the MR pixel intensities within each spectroscopic voxel are averaged out to achieve the low resolution of the MRSI grid. Hence, this yields for each MRSI voxel one vector of 4 variables, further called the image feature vector. The image intensities were normalized by dividing each intensity value by the highest intensity in its corresponding MRI image.

Finally the resulting MRSI, HR-MAS and MRI feature vectors are scaled to be in the same numerical range. More precisely, the arithmetic mean of each feature vector is subtracted from its elements, so that the new elements are centered around zero, and the new vector is scaled by division to its Euclidean norm.

After performing the dimensionality reduction of the data using the above-described feature-based approach, three new datasets are obtained: one consisting of 379 MRSI spectral feature vectors, S_{MRSI}, one of 379 image feature vectors, S_{MRI} and one of 52 HR-MAS spectral feature vectors, S_{HR-MAS}.

7.3 Methods

7.3.1 Model-based CCA

To illustrate the idea of fusing *ex vivo* HR-MAS, *in vivo* MRSI and MRI information, several simulated and *in vivo* experiments were designed. In all these experiments a model-based approach of the statistical method CCA, which is explained in details in Chapter 3, is considered. This method has recently been successfully applied to classify prostate and brain MRSI data (De Vos et al., 2006; Laudadio et al., 2005, 2008).

During an MRSI acquisition, spectra are measured in a grid of voxels. Inspired by (Laudadio et al., 2005), we want to assign each voxel to a certain tissue type by computing the maximum canonical correlation coefficient between the information available for the voxel of interest (x) and the tissue models obtained based on the information available a priori (y). Since there is a high probability that the voxel under investigation belongs to the same tissue type as the neighboring voxels, when defining the components of x spatial information coming from the voxels surrounding the voxel of interest is included. To this aim a symmetric 3x3 spatial model was considered (the adjacent voxels plus voxels on the diagonal are considered as neighbors, giving a total of 8 voxels). This means that, for example, for classifying the voxel on position 5 shown in Figure 7.1, we compute the x variable as: $x = [x_5, (x_1 + x_9)/2, (x_2 + x_8)/2, (x_3 + x_7)/2, (x_4 + x_6)/2]^T$, where for each position i we denote the corresponding feature vector with x_i.

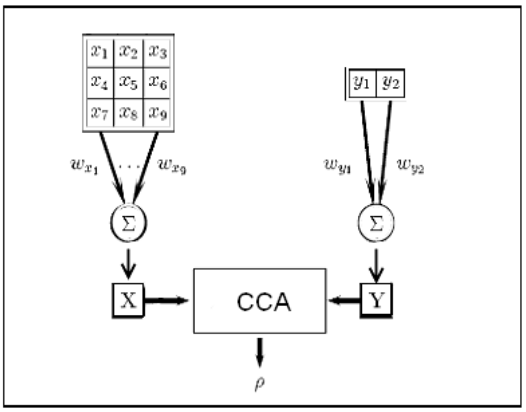


Figure 7.1 *Schematic representation of CCA when applied to a 3x3 region of MRSI voxels.*

Since for each voxel we have access to both, MRSI and MRI information, x_i, where $i = 1,\ldots,9$, is defined as a feature vector containing 14 entries by concatenating 10 metabolite estimates extracted from the spectrum of the i^{th} voxel and 4 image intensities extracted as described in Section 7.2.2, alongside each other.

For each tissue class considered in this study a model, y, so-called subspace model, is computed by two vectors:

$$y = \begin{cases} y_1 = [\overline{S}, \overline{S}_{MRI}] \\ y_2 = [1^{st} PC_{[\widetilde{S}, \widetilde{S}_{MRI}]}] \end{cases} \tag{7.1}$$

where $\overline{S}$ represents the mean of all the considered spectral feature vectors, *S*, extracted from the a priori available datasets of validated S_{MRSI} and/or $S_{HR\text{-}MAS}$ data. $\overline{S}_{MRI}$ is the mean of all the available S_{MRI} data. Thus, y_1 consists of 14 entries: 10 spectral features and 4 image intensities concatenated alongside each other. In order to model the natural inter-patient variability, a second component (y_2) is defined as the first principal component, 1st PC, computed by performing principal component analysis (PCA) separately on the matrices $\widetilde{S}$ and $\widetilde{S}_{MRI}$. These were obtained by mean centering the previously considered matrices *S* and $S_{MRI.}$ For each tissue type a distinct subspace model is defined by considering only the a priori available information belonging to the same tissue type.

Once x and y have been defined, CCA is applied to each voxel so that a correlation map is obtained for each tissue type. These correlation maps are then compared, assigning to each voxel the tissue type corresponding to the largest canonical correlation coefficient. The results are then visualized using nosologic images, which are constructed such that all voxels of the same tissue type are visualized with the same color (Szabo de Edelenyi et al., 2000). These images can be easily interpreted by radiologists and physicians and, along with clinical and radiological information, can improve the accuracy of the diagnosis.

7.3.2 Simulation study

Several simulated experiments are performed to test the performance of the methods for differently sized datasets used in building the subspace model. Additionally, different modalities to combine multimodal information are considered, as further described in this section.

For the simulation study the available datasets are randomly split in two subsets: one used for building the MRSI simulated grids and one used for building the a priori model. This procedure is repeated 30 times for each experiment and thus the results presented in this study will be the average CCA performance over 30 simulated MRSI grids (10 for each tumor type (GII, GIII and GBM)). Also new subspace models are computed with each repetition since different a priori information is considered.

All simulated MRSI grids present two tissue regions: a region of 5x5 tumor voxels in the upper left corner and normal tissue in the remaining ones. When defining the voxels x_i and the subspace models y, spectral features and imaging features are merged in one vector, see (7.1). Thus, each voxel consists of 14 features (10 metabolite concentrations and 4 image intensities). In Figure 7.2, a simulated MRSI grid is visualized.

Performance for differently sized datasets used in building the tissue subspace model
The behavior of CCA for different size datasets used in building the tissue subspace model is analyzed. We tested the performance of CCA when considering large datasets by using all the available MRSI and MRI information (i.e. 176 GII, 57 GIII, and 70 GBM) and, then, gradually and randomly reducing the size of the dataset to 10 GII, 10 GIII and 10 GBM.



Figure 7.2 *Feature vectors of a simulated MRSI grid. Left upper corner square (red contour): GBM tissue; rest of the grid: normal tissue.*

Adding complementary information coming from HR-MAS

With this experiment we tackle the problem of lack of data needed to build the subspace models. We analyze to which extent HR-MAS can complement MRSI in building the subspace models and help in improving the classification results, when this problem is encountered. One approach is to merge MRSI and HR-MAS information by stacking the feature vectors extracted from the two types of spectra into one matrix, $S = [S_{MRSI_{1...10}}; S_{HR-MAS}]^T$, and afterwards to compute each subspace model, *y,* for each tissue type, including the MRI image features from the S_{MRI} dataset, as well, as defined in (7.1). This approach is further called *data integration*.

Another approach is to consider different channels of multimodal sources of information coming from both the MRSI and HR-MAS datasets when computing *y*. Thus, a subspace model from each data source is computed separately and then both are merged into a final subspace model. Thus a subspace model where the y variable now contains 4 components, 2 coming from the MRSI data and 2 coming from the HR-MAS data, is obtained:

$$y = \begin{cases} y_1 = [\overline{S}_{MRSI}, \overline{S}_{MRI}] \\ y_2 = 1^{st} PC_{[\widetilde{S}_{MRSI}, \widetilde{S}_{MRI}]} \\ y_3 = [\overline{S}_{HR-MAS}, \overline{S}_{MRI}] \\ y_4 = 1^{st} PC_{[\widetilde{S}_{HR-MAS}, \widetilde{S}_{MRI}]} \end{cases} \tag{7.2}$$

This modality of computing the subspace model is further referred to as *multichannel approach*.

The performance of CCA for the two approaches proposed for building the subspace model is analyzed and compared for various scenarios where HR-MAS information is added gradually. Thus, various combinations of (l_1,l_2), where l_1 represents the number of MRSI data and l_2 the number of HR-MAS data, are considered in the subspace model: (0,0), (5,0), (10,0), (all,0), (0,10), (5,10), (10,10), (all,10), (0,30), (5,30), (10,30), (all,30), (0,all)), (5, all), (10,all), (all, all).

Performance measurement
Each voxel within the simulated MRSI grids is classified applying CCA and the performance of the classification is evaluated by computing the area accuracy rate (AAR) and the weighted accuracy rate (WAR) (Guyon, 2006a; 2006b; Lewicki and Hill, 2006), as defined in (7.3) and (7.4) below. The AAR value provides information on the degree of reliability of the method in detecting the tumor region; WAR provides information on the method's ability in differentiating the tissue types characterizing the lesion, i.e., in assigning each voxel to the right tissue class.

$$AAR = \left(\frac{a+b+c+d}{A+B+C+D} \right) \tag{7.3}$$

$$WAR = \frac{1}{N}\left(\frac{a}{A} + \frac{b}{B} + \frac{c}{C} + \frac{d}{D} \right) \tag{7.4}$$

where a, b, c and d represent the number of correctly predicted outcomes for normal, GII, GIII and GMB tissue respectively. A, B, C and D represent the number of voxels belonging to normal, GII, GIII and GBM, respectively. N is the total number of classes (in our case N = 4, as we have 4 tissue types).

7.3.3 *In vivo* study

In order to verify to which extent the conclusions drawn in the simulation studies are consistent with real conditions, we further test the approaches described above on real-life case studies. Thus, for the *in vivo* study several patients from the 24 patients with MRSI measurements described in Section 2 were selected. As already mentioned, CCA assigns each voxel to a tissue class based on the highest canonical correlation coefficient value. Nosologic images are drawn, where each voxel is colored according to the tissue class it belongs to as

follows: dark blue is used for normal tissue, and yellow, red and orange are used to color the tumor voxels of GII, GIII and GBM tissue, respectively. The results obtained by all considered approaches used in building the subspace model are reported and compared against the clinical outcome.

7.4. Results

7.4.1 Simulation study

Influence of the size of the dataset used to build the tissue subspace model

A decrease in performance is observed when building the subspace models from a small number of data, see Figure 7.3. In particular, the WAR value presents a decrease from 91.4 % (for a dataset with more than 50 data) to 76.2% (for a dataset of 10 data) when analyzing the GII simulated MRSI grids. Generally, the accuracy of the classifier shows to be positively correlated to the number of available data used to build the subspace model: the more samples we include, the better performance we achieve.

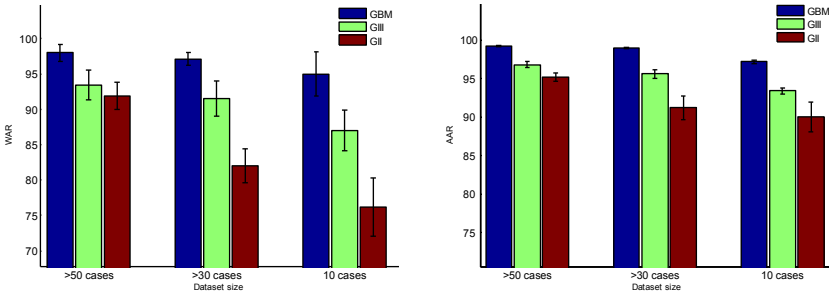


Figure 7.3 *WAR (left) and AAR (right) mean values obtained over 10 simulated MRSI grids for each tissue type are presented for different sizes datasets used to build the tissue subspace models. The black error bars indicate the maximum and minimum value of WAR and AAR during the repeated radomized simulations.*

Adding HR-MAS information when building the subspace model

Results show that both approaches considered for adding complementary HR-MAS information when building the subspace model, *data integration* and *multichannel approach*, respectively, improve CCA classification results when not enough MRSI data are available. Especially for the GII tumor group an improvement in accuracy up to 8% is obtained when adding extra information coming from HR-MAS, compared to the case when considering a dataset of 10 or less MRSI data, see Figure 7.4. For the GIII case, the increase in accuracy is not significant. This can be explained by the fact that we have a set of only 5 HR-MAS

signals for this type of tumor. Therefore, even by complementing the 10 data of the MRSI dataset with 5 new HR-MAS data, we are still dealing with a small size dataset used to build the tissue subspace model.

The general trend is that when not enough information of one source (e.g., MRSI) is available for one or more tissue classes, then, using complementary information coming from HR-MAS data when building the subspace model keeps the performance of CCA to a reliable level. On the other hand, when sufficiently large datasets of one source (e.g., MRSI) are available for one or more tissue classes, then adding extra HR-MAS information to the MRSI datasets does not bring any statistically significant improvement to the classification results when considering the *data integration* approach. On the contrary, with the *multichannel approach* for GII tumor classification an increase in the WAR value to almost 96% is obtained, see Figure 7.5. This could be due to the fact that by considering *a multichannel approach* when building the subspace model a four-dimensional subspace as in eq. (7.2) is built instead of a two-dimensional subspace (1). Consequently, 4 coefficients ω_y instead of only 2 are optimized such that the correlation between *X* and *Y* is maximized. This offers more flexibility in exploring all correlations between each of the two types of information used for building the model and the data.

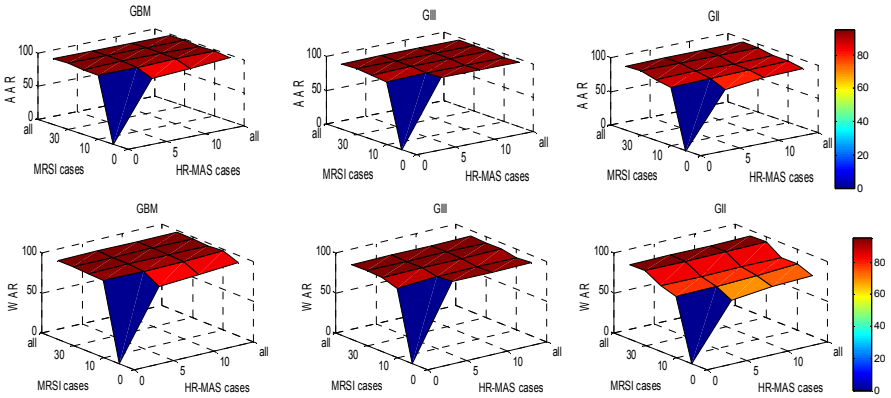


Figure 7.4 *AAR (top) and WAR (bottom) mean values obtained over 10 simulated MRSI grids for each tumour type, for different number of MRSI and HR-MAS data considered in building each subspace model. Data integration approach was considered in building the subspace model. (For GIII we have a total of 5 HR-MAS data and, therefore, the values are not changing through the plot for HR-MAS when considering 10 and all available data.)*

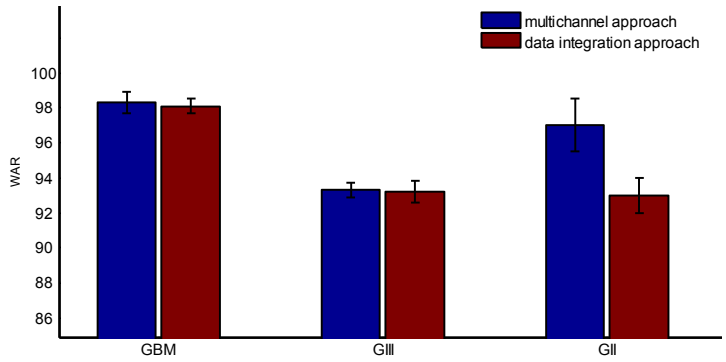


Figure 7.5 *WAR mean value over 10 simulated MRSI grids for each tissue type: comparison between the multichannel approach and data integration approach when considering large MRSI and HR-MAS datasets. The black error bars indicate the maximum and minimum value of WAR during the repeated randomized simulations.*

When using only HR-MAS data to compute the tissue subspace models (in Figure 7.4, note the values corresponding to 0 MRSI cases), the accuracy of the classifier is relatively high, especially for classifying GIII and GBM tumor types. Although the performance for this specific situation does not reach the level of performance obtained with a subspace model computed from large representative MRSI datasets (see in Figure 7.4 the values corresponding to the scenario (0, all) against (all, 0)), we can still build a classifier that is able to provide satisfactory results for classifying MRSI data. Thus, results show once more that these two NMR techniques (HR-MAS and MRSI) can complement each other.

7.4.2 *In vivo* study

Nosologic images

An example of application on an MRSI grid from a patient with low grade astrocytoma (GII) is shown in Figure 7.6. The tumor lesion is localized in the left upper corner of the MRSI grid. The results obtained with CCA are translated into nosologic images and are presented in Figure 7.6.b-e. The area of the tumor is correctly detected by all the considered approaches (CCA where only MRSI data are used in building the model, only HR-MAS data are used in building the model, all MRSI and HR-MAS data are used in building the model with the *data integration approach* and all MRSI and HR-MAS data are used in building the model with the *multichannel approach* for 7.6.b, 7.6.c, 7.6.d and 7.6.e, respectively) and no isolated tumor voxels appear in the healthy tissue area. Regarding the accuracy level for detecting the tumor type, differences can be noticed between the considered approaches. Both 7.6.b and 7.6.c assign some voxels to GIII. This can be explained by the fact that the spectra within

these voxels present higher levels of Cho and lower levels of NAA compared to the rest of the tumor area, which is typical for aggressive grade tumor and/or high cellularity tumor tissue. In 7.6.d the entire area of the tumor is assigned to GII. Still, some voxels of normal tissue are detected inside the area of the tumor. The result closest to the clinical validation is the nosologic image obtained for 7.6.e.

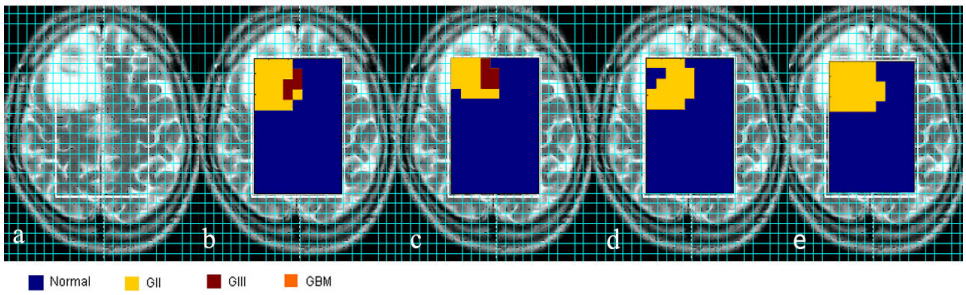


Figure 7.6 *a. T2 MRI image of a brain affected by tumor; nosologic images obtained with CCA for b. all MRSI cases used in building the subspace model, c. only HR-MAS cases are used in building the model, d. all MRSI+HR-MAS cases are used in building the model with data integration approach e. all MRSI and HR-MAS cases are used in building the model with multichannel approach.*

The CCA performance for the real-life case studies is similar to the performance obtained in the simulated studies and results are in consensus with the clinical outcome.

7.5 Discussion

For this study, as we had access to three different sources of information, the input space (i.e., prior available database) could be either spectral information coming from MRSI data, information coming from HR-MAS spectra, a set of image intensities coming from MRI data, or the combination of all described sources. It is very common to consider a classification using these sources separately. Since each of the input data sources can add extra information to the classification problem, a multimodal approach for fusing all the available information seemed as a reasonable solution in this study. Previous reports have shown that, when classifying MRSI data, a significant improvement in the performance of the classifier is obtained by taking into account MRI information as well (Devos et al., 2005a; De Vos et al., 2007; Luts et al., 2009a; Laudadio et al., 2005, 2008). We further explored this idea for analyzing the behavior of a classification method that combines information coming from MRSI, HR-MAS and MRI measurements. As results show, fusing multimodal sources represents a promising approach to improved brain tumor classification.

A challenging problem in this study was the harmonization of all the input spaces due to the fact that we have to manage the use of very different sources of information/data, obtained with different measurement techniques, as well as the use of data coming from different clinical centers. The problem was overcome by considering a feature-based CCA approach, where common characteristic features from all the different data types are extracted and a normalization of the data was performed.

Since the performance of the model-based CCA algorithm proposed for this study is directly dependent on the prior available observations used in building the model, special attention is paid to the possibility of using HR-MAS data as a complementary dataset when dealing with a lack of MRSI data needed to build a classifier. It is worthwhile to stress that the model choice dictates the detection performance. We evaluate the CCA performance when solving the aforementioned problem either by adding HR-MAS data to the in vivo database, or considering only HR-MAS datasets for building the subspace model, see Section 7.3. For the latter case we obtain lower performance than when considering also MRSI information in building the subspace model. Still, taking into consideration the fact that totally different datasets coming from different centres and acquired with different techniques (HR-MAS data for building the model and MRSI data for testing the performance) were used, these results show the potential of combining heterogeneous sources of information for tissue typing (e.g., in brain tumour recognition) which is particularly interesting when no information of one source (e.g. MRSI) is available for one or more tissue classes. Thus, by determining metabolite concentrations from the tissue samples with HR-MAS and using this information to define the MRS metabolite profiles found can help to the construction of *in vivo* MRS classifiers. For the GII tumor, the performance of CCA is lower than for the other two tumor types. We believe that there are many factors that can explain these results. First of all, when analyzing tissue samples, i.e., HR-MAS data, the sampling procedure is crucial for homogeneity. In most NMR experiments, pH and temperature must be tightly regulated to ensure homogeneity across peak positions and amplitude, as there is a strong dependence between a spin resonance frequency and its local environment (Waters et al., 2000). Some experimental variables, like the effects of changing the sample volume in the MAS rotor, snap-freezing the samples, the temperature could have an influence on the estimated concentration of some metabolites. On the other hand, the variability among the glial tumor spectra may be large due to the fact that the same type of tumor may include molecular subgroups which may greatly affect the concentrations of some metabolites.

We have explored two approaches for building the model that combines both sources of information. *Data integration approach* is straightforward, in the sense that no distinction is made between the sources of information, because the extracted features are treated in common. Therefore, feature vectors from MRSI and from HR-MAS are grouped into a single dataset, from which the mean and the first principal component are extracted as model y. This approach might loose specificity in the case when there is some incongruence between the two sources of information. For that reason we introduced a second approach, the *multichannel approach*, where the two sources of data are not averaged together, but are

considered as different directions to which the data to be classified might align to. We have seen that this approach led to a better classification of the simulated GII cases.

The idea presented in this study can be extended to any type of tumor, especially to the rare ones for which a biopsy is normally performed, and to any pattern recognition method/system that makes use of a learning procedure or uses reference tissue models. This could be very interesting for distinguishing between rare tumors and between rare and common tumors of clinical importance. Such a system can afterwards be applied to classify other MRSI data non-invasively, thereby avoiding the need of new biopsies.

7.6. Conclusions

Fusing multimodal sources of information coming from MRSI, HR-MAS and MRI measurements represents a promising approach to provide improved detection and classification of brain tumors since each source has its own advantages and limitations and, therefore, they can complement each other. This approach can add value to the process of tumor diagnosis, both for the situation when we are confronted with a lack of information available for building a classifier as well as for the situation when we have access to different sources of information and we use all these sources in building a robust classifier. Additionally, results show that HR-MAS information can act as an added value in the process of classifying MRSI data. An improvement in the accuracy of CCA is observed for all tissue types when a limited number of MRSI data, needed to build the subspace model, are available in the database and HR-MAS data are used as a complementary dataset. Moreover, our simulation and *in vivo* studies show that when we have access to various types of information describing the same population, combining multimodal heterogeneous sources of information can also improve the performance of CCA in detecting correctly the tumor type and the tumor region.

Chapter 8

High resolution ^{1}H NMR spectroscopy for the classification of fetuses with congenital diaphragmatic hernia

High resolution ^{1}H NMR spectroscopy is performed to compare amniotic fluid from fetuses with congenital diaphragmatic hernia (CDH) undergoing temporary tracheal occlusion (TO) or its reversal (rTO) against healthy controls. Signal processing techniques are applied to improve the data quality. Then, feature reduction methods which explore the variability in the data are separately considered in combination with automated classification techniques for differentiating the complicated pregnancies. The potential of NMR spectroscopy in separating CDH at TO from CDH at rTO is also investigated.

8.1 Introduction

Congenital diaphragmatic hernia (CDH) is a condition that can be targeted in utero, i.e., by performing surgery on the fetus during pregnancy, hence, precise information on the possible disease condition of the fetus is needed. In this study, we analyze, using high resolution ^{1}H NMR spectroscopy, the human amniotic fluid (AF) from fetuses with CDH and try to differentiate between CDH cases at the time of undergoing temporary tracheal occlusion (TO) with an inflatable balloon to stimulate lung development and CDH cases after reversal TO against healthy controls. The purpose is to spot the potential and limitations of using NMR spectroscopy in differentiating the CDH groups.

High-resolution NMR spectroscopy of human AF or fetal organs has the prospect of becoming a valuable technique for the evaluation of fetal health and development. Previous studies have already shown that NMR spectra of human AF can reflect fetal status and development as well as maternal health. Metabolic correlations with disorders such as spina bifida (Bock, 1994; Groenen et al., 2004), Down syndrome (Bock, 1994) and congenital malformations (Graca et al., 2009) in fetuses and cystic fibrosis (Le Moyec, 1994) and diabetes (McGowan, 1999) in mothers were reported. Further information on changes in metabolic patterns related to fetal lung (Clifton et al., 2006; Pearce et al., 1993) and kidney maturation (Bock, 1994) exist. Moreover normative values were suggested for the second and third trimester (Cohen et al., 2009). Still, very limited information is available for comparing normal and complicated pregnancies. Also a limited number of samples were usually

considered in the previous studies and only particular resonances in the NMR spectra were exploited. Although it has recently been shown that at high field NMR spectroscopy up to 75 different compounds can be identified in human AF (Graca et al., 2008), for many minor compounds, which were detected, no assignment could be achieved. This leaves out potentially valuable spectral information, unknown *a priori*, and which could be exploited when NMR spectroscopy is performed. Thus, in the proposed study, automatic feature reduction methods, which do not imply prior knowledge, were considered. Principal Component Analysis (PCA) (Pearson, 1901) and Multidimensional Scaling (MDS) (Borg and Groenen, 2005) were separately applied to reduce the dimension of spectral patterns and select the most relevant features. Then, classifiers were developed and tested for differentiating the CDH groups. Different combinations of feature extraction methods and classification techniques were applied.

8.2 Materials

84 AF samples from 54 healthy fetuses, 20 CDH cases at the time-point of TO and 10 CDH fetuses at the reversal of TO were collected at the Department of Obstetrics and Gynecology, University Hospital Gasthuisberg, Leuven, Belgium, from November, 2009 to April 2011. The samples were acquired during invasive fetal procedures such as: amniocentesis for healthy fetuses and at the moment of the TO intervention or during cesarian section for the CDH fetuses. Only AF samples with normal fetal karyotype were used for NMR analysis and no known infectious material was collected. Informed consent was obtained at all times and the study was approved by the ethical committee of the KU Leuven.

The gestational age ranged from 15-38 weeks, 21-35 weeks and 31-35 weeks in fetuses of the control, CDH at TO and CDH at TO reversal group, respectively. No first trimester samples were included, as amniocentesis is not performed that early in gestation. Besides amniocentesis, samples were gained during invasive fetal procedures as described for CDH or cesarian sections. Only AF samples with normal fetal karyotype were used for NMR analysis and no known infectious material was collected. Informed consent was obtained at all times and the study was approved by the ethical committee of the KU Leuven.

High resolution ^{1}H NMR spectra of AF were acquired at 37°C using an Avance 400 MHz NMR spectrometer (Bruker Biospin, Rheinstetten, Germany) after diluting 0.4ml amniotic fluid with 0.1ml D_2O in a 5mm NMR tube. The water signal was partially suppressed by means of selective excitation by using pulse field gradients. One-dimensional spectra were acquired with a spectral width of 12 ppm and using 16 k data points. Free induction decays were averaged over 8 k accumulations. A relaxation delay of 2sec was allowed. An exponential function was applied prior to Fourier transformation, resulting in a line broadening of 0.1 Hz. NMR spectra were phase and baseline corrected using the Topspin software (Bruker Biospin).

8.3 Methods

The data are preprocessed, processed and statistically analyzed using Matlab platform. To improve the quality of the spectra, an additional baseline correction, using splines, was performed using the '*msbackadj'* function from the Matlab Bioinformatics toolbox, followed by frequency alignment and normalization with respect to external sodium 3-(trimethylsiyl) propane sulfonate at 0.0 ppm. For the statistical study the magnitude spectra in the region between 0.0 and 4.2 ppm were considered.

Due to the complexity of the spectra, since we have to deal with a very high number of peaks reflecting the presence of different metabolites in the amniotic fluid, firstly a feature reduction step is performed in order to extract relevant features that will be considered as inputs for classifying the CDH groups. By considering only particular resonances we could leave out potential valuable information. Moreover, no metabolic assignment was achieved so far for CDH. Therefore, automatic feature reduction methods, which do not imply any prior knowledge, are considered. Principal Component Analysis (PCA) (Pearson, 1901) and Multidimensional Scaling (MDS) (Borg and Groenen, 2005) were separately applied on the full region of interest of the magnitude spectrum to reduce the dimension of spectral patterns.

With PCA the data are linearly transformed for extracting a set of uncorrelated variables (features), called principal components (PCs). Since in NMR spectroscopy it is assumed that most of the variance in the original dataset can be explained by a limited number of PCs, the method is commonly used as a feature reduction technique.
Multidimensional scaling (MDS), also known as Principal Coordinates Analysis (PCO), is a more general projection method than PCA since it uses any distance matrix. PCO determines a set of synthetic variables (feature) called principal coordinates (PCo(s)) that best represent the pairwise distances between data. The number of PCo(s) to be extracted is specified *a priori.* For this study the correlation distance was considered for computing the distance matrix.

Binary classifiers are developed and tested for all pairwise differential diagnoses involving control, all CDH cases, CDH at TO and CDH at rTO. Three different classification algorithms, namely linear discriminant analysis (LDA), k-nearest-neighbor method (KNN) and a linear support vector machine method (SVM), are considered and compared. The effect of the feature extraction methods in combination with the proposed classifiers is investigated, for different number of features. Since 98% of the variability of the data is described by the first 10 PCs, for comparison with MDS method, the maximum number of features to be considered was set to 10. To estimate the error of the classifiers, 10-fold cross-validation was applied.

8.4 Results and discussion

Results on the different combinations of feature extraction methods and classification techniques considered for the study show that the best performance is obtained when using the MDS features as input. With MDS all the considered binary classification tasks are solved with high accuracy. Table 8.1 and 8.2 summarize the results for the pairwise classifiers in combination with the first 6 PCs and 6 PCo(s) respectively, since for this number of features we obtain the overall best performance.

The best classifier among control and the CDH groups achieves an accuracy up to 94%, when considering KNN in combination with MDS. When having the PCs as input, for the proposed classifiers the accuracy is mostly lower, around 75%. For the differentiation between the CDH at TO and rTO, when using the PCo(s) as input features the accuracy reached 88%, in contrast to PCA which reached an accuracy of 72%. Similar performance were obtained with KNN and SVM algorithms.

Cohen et al., 2009 reported metabolic differences in the AF coming from the 2nd and 3rd trimester, respectively. The data considered in this study also cover a wide range of gestational ages raising the question whether the classifiers are not predisposed in predicting the age rather than the disease. Because we do not have a homogeneous age distribution through all the groups (the control group is represented by AF samples collected at the beginning of the 2^{nd} trimester of pregnancy, while the CDH groups contain AF samples collected in the end of the 2^{nd} trimester and the 3^{rd} trimester), a straightforward manner to clarify this supposition was not possible. One approach would be to identify the spectral regions that contribute to the successful classification; assign the respective metabolites and compare them with the literature. In this way we could identify the metabolites that are prone to alter due to the presence of the complication in the pregnancy and not due to the gestational age. For differentiating between CDH at TO and at rTO, the cases are very close in gestational age. On the other hand, maturation of organs as the lung will greatly increase in the end of pregnancy; therefore, basically we cannot answer whether the observed differences are due to age or disease.

Table 8.1 *Mean classification accuracy over 100 runs of repeated random sampling for the differentiation of complicated and control pregnancies, for 6 PCo(s). HC stands for healthy controls, CDH_TO for CDH fetuses at TO and CDH_rTO for CDH fetuses at TO reversal*

	MDS+LDA	MDS+KNN	MDS+SVM
HC vs all CDH	0.85	0.94	0.91
HC vs CDH_TO	0.86	0.94	0.90
HC vs CDH_rTO	0.81	0.94	0.91
CDH_TO vs CDH _rTO	0.86	0.88	0.86

Table 8.2 *Mean classification accuracy over 100 runs of repeated random sampling for the differentiation of complicated and control pregnancies, for 6 PCs. HC stand for healthy controls, CDH_TO for CDH fetuses at TO and CDH_rTO for CDH fetuses at TO reversal*

	PCA+LDA	PCA+KNN	PCA+SVM
HC vs all CDH	0.70	0.74	0.77
HC vs CDH_TO	0.68	0.75	0.76
HC vs CDH_rTO	0.70	0.77	0.78
CDH_TO vs CDH _rTO	0.64	0.72	0.72

Using automatic feature reduction methods, such as PCA and MDS, brings the advantages that no prior knowledge with respect to the particular resonances that are relevant for the given classification problems, is required. Additionally, by using only particular resonances, we could leave out potential valuable information, while with PCA and MDS the data are projected into a new space that explores the most variability and differences in the data. On the other hand, although the extracted features reflect most of the variability and similarity or dissimilarities in the data, the metabolic meaning is lost.

Using feature ranking methods, such as Kruskal-Wallis test, we can identify which features are more likely to differentiate CDH. Based on the null hypothesis that all samples are drawn

from the same population, the test gives for each point in the spectra the measure of its weight in separating between the groups, called rank. The higher the rank the more significant is the feature in separating between the groups, while for a low rank value the feature does not contribute in the separation, see Figure 8.1. A threshold to keep only the first *n* features with the highest rank or only the features that have a rank higher than a certain value can be imposed.

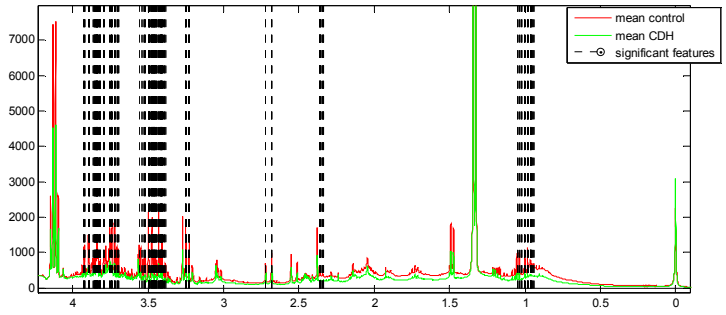


Figure 8.1 *Kruskal-Wallis test results in ranking of each point of the spectra for differentiating CDH from control group. The first 50 spectral points with the highest rank are highlighted with black-dotted lines.*

8.5 Conclusions

Results show that dimensionality reduction methods in combination with automated classifiers when analyzing ^{1}H NMR spectra have a high potential in identifying CDH pregnancies. Still, before drawing reliable conclusions, the age vs. disease problem is a major limitation and needs further investigation. Overall we can conclude that NMR spectroscopy can represent an attractive tool which in later clinical applications could be combined with routine fetal magnetic resonance imaging and thus help to obtain a more detailed picture of fetuses with CDH. The experiments proposed in this study represent an interesting investment in future technologies. Moreover, these findings can then be further investigated for their potential in diagnosis and prognosis of the disease. Deeper understanding of the pathophysiology of CDH will be the basis for more effective therapies.

Chapter 9

Conclusions and future work

In this chapter the main conclusions and contributions of this thesis are outlined. Then a few open problems and possible leads to solve them are outlined.

9.1 Summary

Chapters 1-3 contain background material required in the thesis. In Chapter 1, firstly, the basic concepts of NMR spectroscopy were presented and the NMR modalities which were considered throughout the thesis were introduced. Thus, a theoretical overview of MR imaging, MR spectroscopy, MR spectroscopic imaging and *ex vivo* high resolution MR techniques such as HR-MAS was provided. The research presented in this thesis finds its application in diagnosing brain tumors and abnormal pregnancies. Hence, a short overview of these two medical case studies, underlying the potential of NMR techniques in their diagnosis and prognosis was provided.

Before analyzing NMR spectroscopic data, several processing and preprocessing steps are required in order to improve the quality of the data and to facilitate accurate classification. In Chapter 2 an overview of the typical processing and preprocessing steps was given by focusing on those techniques that are considered in the studies presented in this thesis. SNR improvement, frequency alignment, phase, eddy currents and lineshape correction, water suppression, baseline correction and normalization preprocessing methods were outlined. Automatic feature extraction methods such as MDS and PCA, as well as quantification methods that exploit the biomedical information embedded in the spectra, such as AQSES, QUEST and LCModel were presented.

In Chapter 3 different classification algorithms considered throughout the studies presented in this thesis were overviewed. The supervised classification methods K-nearest neighbor, linear discriminant analysis, support vector machines and canonical correlation analysis are presented along with the unsupervised cluster analysis and BSS methods such are NNMF, ICA and CAMNS. Performance measure tests, such as Krzanovski-Lai index, the weighted inter-intra index, Silhouette index, Homogeneity and Separation index, Kruskal-Wallis test and Tukey multiple comparison were introduced.

Chapters 4-8 contain the main personal contributions of the thesis. In Chapter 4 an advanced metabolite quantification method for MRSI data, AQSES-MRSI, in which the available

spatial information is exploited, is presented. AQSES-MRSI uses an NLLS algorithm and prior knowledge is included in the form of proximity constraints on the spectral parameters within a grid, optimized starting values and a penalty term that promotes a spatially smooth spectral parameter map is added to the fitting algorithm. AQSES-MRSI results on simulated MRSI data with several types of disturbances and on short echo time *in vivo* proton MRSI data shows improved accuracy of quantification compared to processing MRSI voxels on an individual basis with methods such as AQSES, QUEST and LCModel. Overlapping peaks or peaks of compounds present at low concentration can be better resolved than in single-voxel approaches.

Chapter 5 is a study on the distinct histopathological tissue properties, such as viable tumor cells, necrotic tissue or regions where the tumor infiltrates normal brain in gliomas. A cluster analysis on HR-MAS recordings coming from patients with different grades of glial tumors is presented and confronted with histopathology. The results when applying the method on sets of metabolite concentrations and metabolite ratios show that with HR-MAS a strong correlation between the histopathological tissue properties and the metabolic information are obtained and that the metabolite concentration sets can better differentiate between the considered histopathological tissue properties than the ratios of the metabolites to Cr. With the proposed approach representative reference tissue models describing the metabolic behavior are extracted for characterizing the intratumoral tissue properties. These models can be considered as prior knowledge to other studies.

In Chapter 6 the problem of correctly identifying the distinct histopathological tissue properties is further explored and blind source separation techniques are considered for obtaining characteristic profiles for necrosis, highly cellular tumor and border tumor tissue, and providing the contribution (abundance) of each of them to the profile of each spectrum. Non-negative matrix factorization, convex analysis of non-negative sources and non-negative independent component analysis methods are tested on *ex-vivo* HR-MAS. Since the ultimate goal is to obtain a similar differentiation when using non-invasive methods, an extension of the proposed approach to *in vivo* MRSI data is proposed. The results show that BSS can reliably answer the problem of source separation and provide answers that are very close to histopathology.

Chapter 7 describes a study using model-based canonical correlation analysis (CCA) algorithm for the classification of short echo-time brain magnetic resonance spectroscopic imaging (MRSI) when using, as prior knowledge, multimodal sources of information coming from high resolution magic angle spinning (HR-MAS), MRSI and magnetic resonance imaging (MRI), which are demographically heterogeneous and acquired using different biomedical data acquisition protocols. An extensive simulation study on different scenarios regarding multimodal data availability and data fusion approaches shows that that HR-MAS information can act as an added value in the process of classifying MRSI data. The study is extended to *in vivo* experiments and proves similar results.

Chapter 8 proposes a pilot study for correlating metabolic information coming from high resolution MRS with the congenital diaphragmatic hernia (CDH) condition in fetuses. Automatic feature extraction methods as MDS and ICA in combination with LDA, SVM and K-NN are considered for the goal of differentiating amniotic fluid from fetuses with CDH undergoing temporary tracheal occlusion (TO) or its reversal (rTO) from healthy controls.

9.2 Future work

Data fusion

NMR spectroscopy, as shown also in this thesis, has a tremendous potential in improving the diagnosis and prognosis of a large range of clinical conditions. Nowadays, MRI is routinely considered for successfully identifying the brain tumor area and to some extent predicts the tumor type. MR spectroscopy is still not commonly used for brain tumor diagnosis. This is mainly due to the reluctance of the clinicians to the technique since interpreting spectroscopic data requires special knowledge. Therefore, developing advanced classifiers to be embedded in a friendly user interface is a key factor to the success of the method. Moreover, it is often happening that during an *in vivo* NMR experiment various data are collected such as MRI images of different contrast, DWI, DTI and MRSI. Analysing all these sources of information separately is the common approach and is time expensive. Having advanced classifiers which are able to fuse multimodal sources of information can improve the classification results and, as shown in Chapter 7, one could simultaneously benefit from the different knowledge embedded in MRI and spectroscopic data. An interesting future approach would be to develop classifiers based on even more sources of information such as DTI, DWI, MRI and functional MRI in combination with classical MRI and spectroscopy. Moreover, during the eTumour project a very large database of different measurements including DNA microarray were collected to study the brain tumors. Combining NMR spectroscopic information with gene sequence information and trying to identify the correlation between these two different techniques could lead to a better understanding of the disease.

Fusing multimodal sources of information could be an interesting lead to follow also for improved metabolite quantification. As shown in Chapter 4, when quantifying multivoxel MRSI data coming from brain tumors, including spatial knowledge improves the results. Adding information from MRI could be an interesting track to further research. Thus, as described in Chapter 4, AQSES-MRSI quantifies each voxel by considering information from the neighboring voxel. Using MRI information one could redefine the neighboring area in a more dynamic way. One way is to embed in the quantification advanced imaging segmentation steps. Another approach would be to consider BSS methods as a quick way to approximate the percentage of contribution of each tissue type to each voxel and use this information to initialize the neighborhood areas prior to the quantification.

BSS methods

Due to the heterogeneity of brain tumors, quantifying histopathological tissue properties within the tumor area provides a better interpretation of the complexity of the disease. As shown in this thesis, NNMF can resolve the partial volume effect and provide results close to the histopathology and easily interpretable by clinicians. Additionally, these methods do not require any training data. An interesting future application would be to consider NNMF methods for an automatic delimitation of the necrotic area within the MRSI measurements and identifying the infiltrative regions. To this aim, a more detailed study on the potential and limitation of BSS methods in solving this problem, by comparing various NNMF implementations could be an interesting future research work. Moreover, one may consider more than one source of information when applying NNMF, and try to fuse spectral information with imaging information from MRI, DTI and DWI data.

MRSI quantification

The multi-voxel quantification approach proposed in this thesis, AQSES-MRSI, is more accurate than individually fitting each signal in the grid. Still, some issues must be further studied, such as what smoothness measure is more appropriate for *in vivo* data, or how to automatically safeguard against decreasing the constraint box too much; ideas from trust region methods could be adapted for this purpose. Additionally, an extension of AQSES-MRSI to 3D MRSI data still needs to be implemented. Moreover, although developed and tested on brain data, AQSES-MRSI can be considered in quantifying other types of MRSI measurements. Still, to do so, some adjustments and modifications in the algorithm might be needed. For the quantification of prostate MRSI data one might have to deal with the coil artifact. Thus, accounting for the decrease in metabolite intensities when far away from the coil could improve the quantification of prostate MRSI data.

AF analysis

In Chapter 8 we propose a pilot study that shows that the metabolic information contained in the AF coming from CDH fetuses reflects the status of the disease. Further research to identify metabolites that are, as detected by MRS, differently existent in CDH compared to non-CDH fetuses could help to define new markers and methods for diagnostic and prognostic purposes in fetuses with CDH. Therefore, advanced feature selection methods that allow identifying clinical relevant features could be considered and tested. To this aim, one may analyse several automatic statistical methods such as Fisher discriminant criterion, the Kruskal-Wallis test, Relief-F or an enhanced forward selection algorithm as described in (Nikulin et al., 1998). Moreover, the study presented in Chapter 8 is part of larger project which deals with other complicated pregnancies such as twin-twin transfusion syndrome (TTTS). Since about this clinical condition little is known from the metabolic point of view, a study to identify the potential of using MRS in the diagnosis and prognosis of TTTS could be of high interest. To improve the classification results, clinical information (sex, age, etc) can also be included. MRS, in contrast to other techniques can potentially be applied in a non-invasive fashion and could give functional information about the fetus. Thus, an extension of the results obtained on the *ex vivo* data to MRSI *in vivo* measurements is an interesting approach for the future.

Bibliography

Allais DC. The problem of too many measurements in pattern recognition. IEEE International Recreation Center. 1966; 124-130.

Amari S. Natural gradient works efficiently in learning. Neural Computation.1998; 10:251-276.

Amari SI and Cichocki A. Adaptive Blind Signal and Image Processing. John Wiley & sons, Inc. 2002.

Andronesi OC, Blekas KD, Mintzopoulos D, Astrakas L, Black PM and Tzika AA. Molecular classification of brain tumor biopsies using solid-state magic angle spinning proton magnetic resonance spectroscopy and robust classifiers. International Journal of Oncology. 2008; 33(5):1017-1025.

Antoine JP, Coron and Dereppe JM. Water peak suppression: time-frequency vs time-scale approach. Journal of Magnetic Resonance. 2000; 144:189-194.

Antoine JP, Chauvin C and Coron A. Wavelets and related time-frequency techniques in magnetic resonance spectroscopy. NMR in Biomedicine. 2001; 14:265-70.

Ardon H. Dendritic cell-based tumor vaccination for high-grade gliomas. PhD thesis. Faculty of Medicine, K.U.Leuven, 2011.

Barba I, Cabañas ME and Arús C. The relationship between nuclear magnetic resonance-visible lipids, lipid droplets, and cell proliferation in cultured C6 cells. Cancer Research. 1999; 59:1861-1868.

Bao Y and Maudsley AA. Improved Reconstruction for MR Spectroscopic Imaging. IEEE Transactions on Medical Imaging. 2007; 26: 686-695.

Barton SJ, Howe FA, Tomlins AM, Cudlip SA, Nicholson JK, Bell BA and Griffiths JR. Comparison of in vivo ^{1}H MRS of human brain tumours with ^{1}H HR-MAS spectroscopy of intact biopsy samples in vitro. Magnetic Resonance Materials in Physics, Biology and Medicine.1999; 8:121-128.

Bartha R, Drost DJ, Menon RS and Williamson PC. Spectroscopic lineshape correction by QUECC: combined QUALITY deconvolution and eddy current correction. Magnetic Resononance in Medicine. 2000; 44(4):641-645.

Bartha R, Drost DJ, Menon RS and Williamson PC. Factors affecting the quantification of short echo in-vivo 1H MR spectra: prior knowledge, peak elimination, and filtering. NMR in Biomedicine. 1999; 12(4):205-216.

Bartholdi E and Ernst RR. Fourier spectroscopy and the causality principle. Journal of Magnetic Resonance. 1973; 11:9-19.

Barkhuysen H, de Beer R, van Ormondt D. Improved algorithm for noniterative time-domain model fitting to exponentially damped Magnetic Resonance Signals. Journal of Magnetic Resonance. 1987; 73:553-557.

Bell AJ and Sejnowski TJ. An information-maximization approach to blind separation and blind deconvolution. Neural Computation. 1995; 7:1129-1159.

Berry MW, Browne M, Langville AN, Pauca VP and Plemmons RJ. Algorithms and applications for approximate nonnegative matrix factorization. Computational Statistics and Data Analysis. 2006; 155-173.

Bock JL. Metabolic profiling of amniotic fluid by proton nuclear magnetic resonance spectroscopy: correlation with fetal maturation and other clinical variables. Clinical Chemistry. 1994; 40(1):56-61.

Borg I and Groenen P. Modern Multidimensional Scaling: theory and applications (2nd edition). New York: Springer-Verlag. 2005; 207-212. ISBN 0387948457.

Brown DE. Fully automated baseline correction of 1D and 2D NMR spectra using Bernstein polynomials. Journal of Magnetic Resonance. 1995; 114:268-70.

Callot V, Galanaud D, Le Fur Y, Confort-Gouny S, Ranjeva JP and Cozzone PJ. 1H MR spectroscopy of human brain tumours: a practical approach. European Journal of Radiology. 2008; 67(2):268-274.

Cardoso JF. Source separation using higher order moments. In Proceedings of IEEE International Conference on Acoustics, Speech and Signal Processing (ICASSP'89). 1989; 2109-2112.

Cardoso JF. Eigen-structure of the fourth-order cumulant tensor with application to the blind source separation problem. In Proceedings of IEEE International Conference on Acoustics, Speech and Signal Processing (ICASSP'90). 1990; 2655-2658.

Cardoso JF. High-order contrasts for independent component analysis. Neural Computation. 1999; 11(1):157-192.

Cavassila S, Deval S, Huegen C, van Ormondt D and Graveron-Demilly D. Cramér-Rao bound expressions for parametric estimation of overlapping peaks: influence of prior knowledge. Journal of Magnetic Resonance. 2000; 143:311-20.

Celda B, Monleón D, Martínez-Bisbal MC, Esteve V, Martínez-Granados V, Pinero E, Ferrer R, Piquer J, Martí-Bonmati L, Cervera J and López-Guerrero LA. New trends in Cancer for the 21st century. Advances in Experimental Medicine and Biology. 2006; 587:285-302.

Cha H, Ma WK, Chi CY and Wang Y. A convex analysis framework for blind separation of non-negative sources. IEEE Transactions on Signal Processing. 2008; 56(10):5120-5134.

Chandrasekaran B and Jain AK. Quantization Complexity and Independent Measurements. IEEE Transactions on Computers. 1974; 23:102-106.

Cheng LL, Chang LW, Louis DN and Gonzalez G. Correlation of high-resolution magic angle spinning proton magnetic resonance spectroscopy with histopathology of intact human brain tumor specimens. Cancer Research. 1998; 58:1825-1832.

Cheng LL, Anthony DC, Comite AR, Black PM, Tzika AA and González RG. Quantification of microheterogeneity in glioblastoma multiforme with ex vivo high-resolution magic-angle spinning (HR-MAS) proton magnetic resonance spectroscopy. Neurooncology. 2000; 2:87-95.

Chen H, Van Huffel S, van Ormondt D and de Beer R. Parameter estimation with prior knowledge of known signal poles for the quantification of NMR spectroscopy data in the time domain. Journal of Magnetic Resonance. 1996; 119:225-34.

Chen Z and Cichocki A. Nonnegative matrix factorization with temporal smoothness and/or spatial decorrelation constraints. Laboratory for Advanced Brain Signal Processing, RIKEN, Technical Report. Available online. 2005.

Chou PB, Brown CM. The theory and practice of Bayesian image labelling. International Journal of Computer Vision. 1990; 4:185-210.

Chu M, Diele F, Plemmons R and Ragni S. Optimality, computation, and interpretations of nonnegative matrix factorizations. Available online. 2004.

Cichocki A, Zdunek R and Amari S. Csiszar's divergences for non-negative matrix factorization: Family of new algorithms. In Proceeding of the 6th International Conference on Independent Component Analysis and Blind Signal Separation. Charleston, USA. 2006.

Clifton MS, Joe BN, Zektzer AS, Kurhanewicz J, Vigneron DB, Coakley FV, Nobuhara KK and Swanson MG. Feasibility of magnetic resonance spectroscopy for evaluating fetal lung maturity. Journal of Pediatric Surgery. 2006; 41(4):768-773.

Cohn BR, Joe BN, Zhao S, Kornak J, Zhang VY, Iman R, Kurhanewicz J, Vahidi K, Yu J, Caughey AB and Swanson MG. Quantitative Metabolic Profiles of 2nd and 3rd Trimester Human Amniotic Fluid Using 1H HR-MAS Spectroscopy. Magnetic Resonance Materials in Physics. 2009; 22:343-352.

Cohen J, Cohen P, West SG, Aiken LS. Applied multiple regression/correlation analysis for the behavioral sciences. Lawrence Erlbaum Associates; 2003.

Correa N, Li YO, Adalı T and Calhoun VD. Canonical correlation analysis for feature-based fusion of biomedical imaging modalities and its application to detection of associative networks in schizophrenia. The Journal of Selected Topics in Signal Processing. 2008; 2(6):998-1007.

Correa N, Adalı T, Li YO, and Calhoun VD. Canonical Correlation Analysis for Data Fusion and Group Inferences. IEEE Signal Processing Magazine. 2010; 27(4):39-50.
Cobas JC, Bernstein MA, Martin-Pastor M and Garcia-Tahoces P. A new general-purpose fully automatic baseline-correction procedure for 1D and 2D NMR data. Journal of Magnetic Resonance. 2006; 183:145-151.

Croitor Sava AR, Laudadio T, Poullet JB, Monleon D, Martinez-Bisbal MC, Celda B and Van Huffel S. Combining HR-MAS and In Vivo MRI and MRSI Information for Robust Brain Tumor Recognition. In Proc. of the 4th European Conference of the International Federation for Medical and Biological Engineering (ECIFMBE 2008). Antwerp, Belgium. 2008: 340-343.

Croitor Sava AR, Martinez-Bisdal MC, Celda B, Cerda JM and Van Huffel S. Tissue typing within glial tumours. In Proc. of the European Society for Magnetic Resonance in Medicine and Biology Congress (ESMRMB). Antalya, Turkey. 2009; 471-472.

Croitor Sava AR, Sima DM, Poullet JB, Wright AJ, Heerschap A and Van Huffel S. Exploiting spatial information to estimate metabolite levels in two-dimensional MRSI of heterogeneous brain lesions. NMR in Biomedicine. 2011a; 24(7): 824–835.

Croitor Sava AR, Martinez-Bisbal MC, Van Huffel S, Cerda JM, Sima DM and Celda B. Ex Vivo High Resolution Magic Angle Spinning Metabolic Profiles describe intratumoral histopathological tissue properties in adult human gliomas. Magnetic Resonance in Medicine. 2011b; 65:320-328.

Croitor Sava AR, Sima DM, Martinez-Bisbal MC, Celda B and Van Huffel S. Non-negative blind source separation techniques for tumor tissue typing using HR-MAS signals. In Proc. of the 32nd Annual International Conference of the IEEE Engineering in Medicine and Biology Society (IEEE EMB). Buenos Aires, Argentina. 2011c: 3658-3661.

Croitor Sava AR, Martinez-Bisbal MC, Laudadio T, Piquer J, Celda B, Heerschap A. and Van Huffel S. Fusing in vivo and ex vivo NMR sources of information for brain tumor classification. Accepted for publication in Measurement Science and Technology. 2011d. Available online.

Cross KJ. Improved digital filtering technique for solvent suppression. Journal of Magnetic Resonance. 1993; 101:220–24.

Csiszar I and Tusnady G. Information geometry and alternating minimization procedures. Statistics & Decisions. Supplement Issue. 1984; 1: 205-237.

Cudalbu C, Cavassila S, Rabeson H, van Ormondt D and Graveron-Demilly D. Influence of measured and simulated basis sets on metabolite concentration estimates. NMR in Biomedicine. 2008; 21(6):627–636.

Cudalbu C, Mlynarik V, Xin L and Gruetter R. Quantification of in vivo short echo-time proton magnetic resonance spectra at 14.1 T using two different approaches of modelling the macromolecule spectrum. Measurement Science and Technology. 2009; 20(10):104034 (7pages).

De Beer D and van Ormondt D. NMR basic principles and progress. Springer. 1992; 26.

De Clercq W, Vergult A, Vanrumste B, Van Paesschen W and Van Huffel S. Canonical correlation analysis applied to remove muscle artifacts from the encephalogram. IEEE Transactions on Biomedical Engineering. 2006; 53: 2583-2587.

De Graaf AA. QUALITY: quantification improvement by converting lineshapes to the Lorentzian type. Magnetic Resonance in Medicine. 1990; 13:343–357.

De Graaf RA. In vivo NMR Spectroscopy Principles and Techniques. Wiley: Chichester, 2007.

den Hollander JA, Evanochko WT and Pohost GM. Observation of cardiac lipids in humans by localized ^{1}H magnetic resonance spectroscopic imaging. Magnetic Resonance in Medicine 2005; 32:175–180.

Deprest J, Gratacos E and Nicolaides KH. FETO Task Group. Fetoscopic tracheal occlusion (FETO) for severe congenital diaphragmatic hernia: evolution of a technique and preliminary results. Ultrasound Obstet Gynecol. 2004; 24: 121–126

De Vos M, Laudadio T, Simonetti AW, Heerschap A and Van Huffel S. Fast nosologic imaging of the brain. Journal of Magnetic Resonance. 2007; 184 : 292-301.

De Vos M. Decomposition methods with applications in neuroscience. PhD thesis. Faculty of

Engineering. K.U.Leuven, Leuven, Belgium. 2009.

Devos A, Lukas L, Suykens JAK, Vanhamme L, Tate AR, Howe FA, Majos C, Moreno-Torres A, Van der Graaf M, Arus C and Van Huffel S. Classification of brain tumours using short echo time 1H MRS spectra. Journal of Magnetic Resonance. 2004; 170:164-175.

Devos A, Simonetti AW, van der Graaf M, Lukas L, Suykens JAK, Vanhamme L, Buydens LMC, Heerschap A and Van Huffel S. The use of multivariate MR Imaging Intensities versus metabolic data from MR Spectroscopic Imaging for brain tumour classification. Journal of Magnetic Resonance. 2005a; 173: 218-228.

Devos A. Quantification and classification of Magnetic Resonance Spectroscopy data and applications to brain tumour recognition. PhD thesis. Faculty of Engineering. K.U.Leuven Leuven, Belgium. 2005b.

Dezortova M and Hajek M. 1H MR spectroscopy in pediatrics. European Journal of Radiology. Clinical 1H MR Spectroscopy. 2008; 67(2):240-249.

Di Costanzo A, Scarabino T, Trojsi F, Giannatempo GM, Popolizio T, Catapano D, Bonavita S, Maggialetti N, Tosetti M, Salvolini U, d'Angelo VA, Tedeschi G. Multiparametric 3T MR approach to the assessment of cerebral gliomas: tumor extent and malignancy. Neuroradiology. 2006;48(9):622-31.

Dietrich W, Rudel CH, and Neumann M. Fast and precise automatic baseline correction of one- and two-dimensional NMR spectra. Journal of Magnetic Resonance. 1991; 91:1–11.

Dietterich TG. Structural, Syntactic and Statistical Pattern Recognition. Lecture Notes in Computer Science, chapter Machine Learning for Sequential Data. 2007; 15-30.

Dodge Y. The Oxford Dictionary of Statistical Terms. 2003; OUP. ISBN 0-19-850994-4.

Dorrius MD, Pijnappel RM, Jansen-van der Weide MC, Jansen L, Kappert P, Oudkerk and Sijens PE. Determination of Choline Concentration in Breast Lesions: Quantitative Multivoxel Proton MR Spectroscopy as a Promising Noninvasive Assessment Tool to Exclude Benign Lesions. Radiology. 2011; 259(3):695-703.

Duda RO, Hart PE and Stork DG. Pattern Classification. 2nd Edition. Wiley-Interscience, Chichester, West Sussex, England. 2001

Ebel A, Dreher W and Leibfritz D. Effects of zero-filling and apodization on spectral integrals in discrete Fourier-transform spectroscopy of noisy data. Journal of Magnetic Resonance. 2006; 182(2):330-8.

Elster V, Schubert F, A Link, Walzel M, Seifert F and Rinneberg H. Quantitative magnetic

resonance spectroscopy: Semi-parametric modeling and determination of uncertainties. Magnetic Resonanance in Medicine. 2005; 53: 1288–96.

Erb G, Elbayed K, Piotto M, Raya J, Neuville A, Mohr M, Maitrot D, Kehrli P and Namer IJ. Toward Improved Grading of Malignancy in Oligodendrogliomas Using Metabolomics. Magnetic Resonance in Medicine. 2008; 59(5):959-65.

Fan G, Sun B, Wu Z, Guo Q and Guo Y. In vivo single-voxel protonMR spectroscopy in the differentiation of high-grade gliomas and solitary metastases. Clinical Radiology. 2004; 59:77–85.

Ferrer E, Capdevila A and Arus C. Towards a method for automated classification of 1H MRS spectra from brain tumours. NMR in Biomedicine. 1998; 11:177–191.

Ferrer-Luna R, Mata M, Núñez L, Calvar J, Dasí F, Arias E, Piquer J, Cerdá-Nicolás M, Taratuto AL, Sevlever G, Celda B and Martinetto H. Loss of heterozygosity at 1p-19q induces a global change in oligodendroglial tumor gene expression. Journal of Neurooncology. 2009; 95(3):343-54.

Ferrer-Luna R, Núñez L, Piquer J, Arias E, Dasí F, Cervio A, Arakaki N, Sevlever G, Celda B and Martinetto H. Whole-genomic survey of oligodendroglial tumors: correlation between allelic imbalances and gene expression profiles. Journal of Neurooncology. 2011; 103(1):71-85.

Fisher R.The Use of Multiple Measurements in Taxonomic Problems.Annals of Eugenics. 1936; 7:179-188.

Fountas KN, Kapsalaki EZ, Gotsis SD and Kapsalakis JZ. In vivo proton magnetic resonance spectroscopy of brain tumors. Stereotactic and Functional Neurosurgery. 2000; 74:83-94.

Frahm J, Bruhn H, Gyngell ML, Merboldt KD, Hänicke W and Sauter R. Localized proton NMR spectroscopy in different regions of the human brain in vivo. Relaxation times and concentrations of cerebral metabolites. Magnetic Resonance in Medicine.1989; 11:47–63.

Frederick BD, Lyoo IK, Satlin A, Ahn KH, Kim MJ, Yurgelun-Todd DA, Cohen BM and Renshaw PF. In vivo proton magnetic resonance spectroscopy of the temporal lobe in Alzheimer's disease. Progress in Neuro- Psychopharmacology and Biological Psychiatry. 2004; 28(8):1313-1322.

Friman O. Adaptive Analysis of Functional MRI Data. PhD thesis. Linköping University, Sweden, 2003.

Gabr RE, Ouwerkerk R and Bottomley PA. Quantifying in vivo MR spectra with circles. Journal of Magnetic Resonanance. 2006; 179:152–163.

Galloway CM, Le Ru EC and Etchegoin PG. An iterative algorithm for background removal in spectroscopy by wavelet transforms. Applied Spectroscopy. 2009; 63(12):1370–1376.

Golub GH, Van Loan CF. Matrix computations. The Johns Hopkins University Press, Baltimore. 1996.

Golub GH, Pereyra V. Separable nonlinear least squares: the variable projection method and its applications. Inverse Problems. 2003; 19:1–26.

Golotvin S, Williams A. Improved baseline recognition and modeling of FT NMR spectra. Journal of Magnetic Resonance. 2000; 146 (1):122–125.

Govindaraju V, Young K and Maudsley A. Proton NMR chemical shifts and coupling constants for brain metabolites. NMR in Biomedicine. 2000; 13:129–153.

Gower JC and Hand DJ. Biplots. Chapman & Hall, London, UK. 1996; ISBN 0412716305.

Graveron-Demilly D, Diop A, Briguet A and Fenet B. Product-operator algebra for strongly coupled spin systems. Journal of Magnetic Resonance. A. 1993; 101:233–39.

Graca G, Duarte IF, Goodfellow BJ, Barros AS, Carreira IM, Couceiro AB, Spraul M and Gil AM. Potential of NMR spectroscopy for the study of human amniotic fluid. Analitical Chemistry. 2007; 79(21):8367–8375.

Graca G, Duarte IF, Goodfellow BJ, Carreira IM, Couceiro AB, Domingues MR, Spraul M, Tseng LH and Gil AM. Metabolite profiling of human amniotic fluid by hyphenated nuclear magnetic resonance spectroscopy. Analitical Chemistry. 2008; 80(15):6085–6092.

Graça G, Duarte IF, Barros AS, Goodfellow BJ, Diaz S, Carreira IM, Couceiro AB, Galhano E and Gil AM. (1)H NMR based metabonomics of human amniotic fluid for the metabolic characterization of fetus malformations. Journal of Proteome Research. 2009; 8(8):4144-50.

Groenen PMW, Engelke UF, Wevers RA, Hendriks JCM, Eskes TKAB, Merkus HMWM and Steegers-Theunissen RPM. High-resolution 1H NMR spectroscopy of amniotic fluids from spina bifida fetuses and controls. European Journal of Obstetrics & Gynecology and Reproductive Biology. 2004; 112(1):16–23.

Gruber S, Stadlbauer A, Mlynarik V, Gatterbauer B, Roessler K and Moser E. Proton magnetic resonance spectroscopic imaging in brain tumor diagnosis. Neurosurgery Clinics of North America. 2005; 16:101-114.

Guillamet D, Bressan M and Vitria J. A weighted non-negative matrix factorization for local representations. In: Proc. 2001 IEEE Computer Society Conference on Computer Vision and

Pattern Recognition. 2001; 1: 942–947.

Guyon I, Alamdari ARSA, Dror G and Buhmann JM. Performance Prediction Challenge. In: IJCNN ’06 international joint conference on neural networks. 2006a; 1649–1656.

Guyon I, Gunn S, Nikravesh M and Zadeh LA. Feature Extraction: Foundations and Applications (Studies in Fuzziness and Soft Computing), Springer. 2006b.

Günther UL, Ludwig C and Rüterjans H. Wavewat-improved solvent suppression in NMR spectra employing wavelet transforms. Journal of Magnetic Resonance. 2002; 156:19–25.

Hajek M, Dezortova M and Krsek P. 1H MR spectroscopy in epilepsy. European Journal of Radiology. 2008; 67(2):258 – 267.

Hartigan JA and Wong MA. A K-means clustering algorithm. Applied Statistics. 1979; 28:100–108.

Hamza AB and Brady D. Reconstruction of reflectance spectra using robust non-negative matrix factorization. IEEE Transactions on Signal Processing. 2006; 54:3637-3642.

Hiltunen Y, Ala-Korpela M, Jokisaari J, Eskelinen S, Kiviniitty K, Savolainen M, Kesäniemi YA. A lineshape fitting model for 1H NMR spectra of human blood plasma. Magnetic Resonance in Medicine. 1991; 21:222–232.

Hiltunen Y, Kaartinen J, Pulkkinen J, Häkkinen AM, Lundbom N, Kauppinen RA. Quantification of human brain metabolites from in vivo 1H NMR magnitude spectra using automated artificial neural network analysis. Journal of Magnetic Resonance. 2002; 154:1–5.

Hyvarinen A and Oja E. A fast fixed-point algorithm for independent component analysis. Neural Computation. 1997; 9(7):1483-1492.

Hyvarinen A. Fast and robust fixed-point algorithms for independent component analysis. IEEE Transactions on Neural Networks. 1999; 10(3):626-634.

Hyvärinen A and Oja E. Independent component analysis: algorithms and applications. Neural Networks. 2000; 13(4-5):411-30.

Hyvärinen A, Karhunen J. and Oja E. Independent Component Analysis. John Wiley & Sons, 2001.

Hoch J and Stern A. NMR data processing. John Wiley & Sons. 1996.

Hollander M and Wolfe DA. Nonparametric Statistical Methods. NewYork: Wiley. 1973.

Howe FA and Opstad KS. 1H MR spectroscopy of brain tumours and masses. Nuclear Magnetic Resonance in Biomedicine. 2003a; 16:123–131.

Howe FA, Barton SJ, Cudlip SA, Stubbs M, Saunders DE, Murphy M, Wilkins P, Opstad KS, Doyle VL, McLean MA, Bell BA, Griffiths JR. Metabolic profiles of human brain tumours using quantitative in vivo ^{1}H magnetic resonance spectroscopy. Magn Res Med 2003b; 49:223–232.

Hoyer P. Non-negative Matrix Factorization with Sparseness Constraints. J. of Machine Learning Research. 2004; 5:1457–1469.

Huang Y, Lisboa PJ and El-Deredy W. Tumour grading from magnetic resonance spectroscopy: a comparison of feature extraction with variable selection. Medical Statistics. 2003; 22:147–64.

Hwang JH, Graham GD, Behar KL, Alger JR, Prichard JW and Rothman DL. Short echo time proton magnetic resonance spectroscopic imaging of macromolecule and metabolite signal intensities in the human brain. Magnetic Resonance in Medicine. 1996; 35(5):633-639.

Jiru F. Introduction to post-processing techniques. European journal of radiology. 2008; 67(2):202–217.

Jolliffe IT. Principal Component Analysis, second edition, New York: Springer-Verlag New York, Inc.; 2002

Kasprian G, Balassy C, Brugger PC and Prayer D. MRI of normal and pathological fetal lung development. European Journal Radiology. 2006; 57(2):261-70.

Kamada K, Houkin K, Hida K, Matsuzawa H, Iwasaki Y, Abe H and Nakada T. Localized proton spectroscopy of focal brain pathology in humans: significant effects of edema on spin-spin relaxation time. Magnetic Resonance in Medicine. 1994; 31:537–540.

Kaufman L and Rousseeuw PJ. Finding Groups in Data: An Introduction to Cluster Analysis. Wiley; 1990.

Kelm BM. Evaluation of Vector-Valued Clinical Image Data Using Probabilistic Graphical Models: Quantification and Pattern Recognition. PhD Thesis. Heidelberg, Germany. 2007

Kelm BM, Kaster FO, Henning A, Weber MA, Bachert P, Boesiger P, Hamprecht FA, Menze BH. Using spatial prior knowledge in the spectral fitting of MRS images. NMR in Biomedicine. 2011. Published online.

Kinoshita Y, Yokota A. Absolute concentrations of metabolites in human brain tumors using in vitro proton magnetic resonance spectroscopy. NMR in Biomedicine. 1997; 10 : 2-12.

Kim H and Park H. Sparse Non-negative Matrix Factorizations via Alternating Non-negativity-constrained Least Squares for Microarray Data Analysis. Bioinformatics. 2007; 23-12:1495-1502.

Kim H and Park H. Nonnegative Matrix Factorization Based on Alternating Nonnegativity Constrained Least Squares and Active Set Method. SIAM Journal on Matrix Analysis and Applications. 2008; 30:713-730.

Klose U. In vivo proton spectroscopy in presence of eddy currents. Magn. Reson. Med. 1990; 14:26–30.

Kornak J, Young K, Soher BJ and Maudsley AA. Bayesian k-Space-Time Reconstruction of MR Spectroscopic Imaging for Enhanced Resolution. IEEE Transactions on Medical Imaging. 2010; 29:1333-1350

Kolenda T. Adaptive tools in virtual environments: Independent component analysis for multimedia. PhD Thesis.Kongens Lyngby, Denmark. 2002.

Krzanowski J and Lai YT. A criterion for determing the number of groups in a data set using sum-of-squares clustering. Biometrics 1985; 44:23–34.

Kruskal and Wallis. Use of ranks in one-criterion variance analysis. Journal of the American Statistical Association. December 1952; 47 (260): 583–621.

Kuesel AC, Donnelly SM, Halliday W, Sutherland GR and Smith ICP. Mobile lipids and metabolic heterogeneity of brain tumours as detectable by ex vivo 1HMR spectroscopy. NMR in Biomedicine. 1994a; 7:172–180.

Kuesel AC, Sutherland GR, Halliday W, Smith ICP. 1H MRS of high grade astrocytomas: mobile lipid accumulation in necrotic tissue. NMR Biomed. 1994b; 7:149–155.

Ladroue C, Tate AR, Howe FA and Griffiths JR. Independent component analysis. For automated decomposition of in vivo magnetic resonance. Magnetic Resonanance in Medicine. 2003; 50:697–703.

Laudadio T, Mastronardi N, Vanhamme L, Van Hecke P and Van Huffel S. Improved Lanczos algorithms for blackbox MRS data quantitation. Journal of Magnetic Resonance. 2002; 157:292-297.

Laudadio T, Pels P, De Lathauwer L, Van Hecke P and Van Huffel S. Tissue segmentation of MRSI data using Canonical Correlation Analysis. Proc. of the Second International Conference on Computational Intelligence in Medicine and Healthcare. Lisbon, Portugal. 2005a.

Laudadio T, Pels P, De Lathauwer L, Van Hecke P, Van Huffel S. Tissue segmentation and classication of MRSI data using canonical correlation analysis. Magnetic Resonance Medicine. 2005b; 54:1519-1529.

Laudadio T, Martinez-Bisbal MC, Celda B and Van Huffel S. Fast nosological imaging using canonical correlation analysis of brain data obtained by two-dimensional turbo spectroscopic imaging. NMR in Biomedicine. 2008; 21: 311–321.

Lawton WH and Sylvestre EA. Self modeling curve resolution. Technometrics. 1971; 13(3): 617-622.

Le Moyec L, Muller F, Eugene M and Spraul M. Proton magnetic resonance spectroscopy of human amniotic fluids sampled at 17-18 weeks of pregnancy in cases of decreased digestive enzyme activities and detected cystic fibrosis. Clin. Biochem. 1994; 27(6): 475–483.

Lee Y, Huang Y, El-Deredy W, Lisboa PJ, Ards C, Harris P. Robust methodology for the discrimination of brain tumours from in vivo magnetic resonance spectra. In: IEEE Proceedings—Science Measurement and Technology. 2000; 147: 309–314.

Lee D, Seung H. Learning the Parts of Objects by Non-Negative Matrix Factorization. Nature. 1999; 401:788–791.

Lee D and Seung H. Algorithms for Non-Negative Matrix Factorization. Advances in Neural Information Processing Systems. 2001; 13:556–562.

Lewicki P.and Hill T. Statistics: Methods and Applications. StatSoft. 2006.

Lemmerling P, Vanhamme L, in 't Zandt H, Van Huffel S, Van Hecke P. Time-domain quantification of short-echo-time proton MRS. MAGMA. 2002; 15:178–179.

Leclerc X, Huisman T, Sorensen A. The potential of proton magnetic resonance spectroscopy (1H-MRS) in the diagnosis and managemen. Journal of Current opinion in onlcology. 2002;14:292-298.

Li B, Wang H and Gonen O. Metabolite ratios to assumed stable creatine level may confound quantification of proton brain MR spectroscopy. Magnetic Resonance Imaging. 2003; 21: 923–928.

Li YO, Wang, Adalı T and Calhoun VD. Joint blind source separation by multi-set canonical correlation analysis. IEEE Trans. Signal Processing. 2009; 57(10):3918–3929.

Lin CJ. Projected gradient methods for non-negative matrix factorization. Neural Computation, 19(2007), 2756-2779.

Lindon JC and Ferrige AG. Digitisation and data processing in Fourier transform NMR. Prog. NMR Spectrosc. 1980; 14:27–66.

Liu H and Motoda H. Computational methods of feature selection. Chapman & Hall. Data Mining and Knowledge Discovery Series. 2007.

Louis DN, Ohgaki H, Wiestler OD and Cavenee WK. World Health Organization Classification of Tumours of the Central Nervous System. IARC, Lyon, 2007. ISBN 9283224302.

Lopez-Gines C, Gil-Benso R, Faus C, Monleon D, Mata M, Morales JM, Cigudosa JC, Gonzalez-Darder J, Celda B and Cerda-Nicolas M. Metastasizing anaplastic ependymoma in an adult. Chromosomal imbalances, metabolic and gene expression profiles. Histopathology. 2009; 54(4):500-4.

Lopez-Gines C, Gil-Benso R, Ferrer-Luna R, Benito R, Serna E, Gonzalez-Darder J, Quilis V, Monleon D, Celda B and Cerdá-Nicolas M. New pattern of EGFR amplification in glioblastoma and the relationship of gene copy number with gene expression profile. Modern Pathology. 2010; 23(6):856-65.

Luka L, Devos A, Suykens J, Vanhamme L, Howe F, Majos C, Moreno Torres A., van der Graaf M, Tate A, Arus C and Van Huffel S. Brain Tumour Classification based on long echo proton MRS signals. Artificial Intelligence in Medicine. 2004; 31(1):73–89.

Luts J, Laudadio T, Idema AJ, Simonetti AW, Heerschap A, Vandermeulen D, Suykens JAK and Van Huffel S. Nosologic imaging of the brain: segmentation and classification using MRI and MRSI. NMR in Biomedicine. 2009a; 22(4):374-90.

Luts J, Laudadio T, Martinez-Bisbal MC, Van Cauter S, Molla E, Piquer J, Suykens JAK, Himmelreich U, Celda B and Van Huffel S. Differentiation between brain metastases and glioblastoma multiforme based on MRI, MRS and MRSI. Proc. of the 22nd IEEE International Symposium on Computer-Based Medical Systems (CBMS). Albuquerque, New Mexico. 2009b; 1-8.

Machann J, Stefan N and Schick F. 1H MR spectroscopy of skeletal muscle, liver and bone marrow. European Journal of Radiology. 2008; 67(2):275 –284.

Mader I, Rauer S, Gall P and Klose U. 1H MR spectroscopy of inflammation, infection and ischemia of the brain. European Journal of Radiology. 2008; 67(2):250 – 257, 2008.

Magalhaes A, Godfrey W, Shen Y, Hu J and Smith W. Proton magnetic resonance spectroscopy of brain tumors correlated with pathology. Academic Radiology. 2005; 12:51-57.

Majos C, Margarida Julia-Sape M, Alonso J, Serrallonga M, Aguilera C, Acebes JJ, Arus C, Gili, K. Brain tumor classification by proton MR spectroscopy: comparison of diagnostic accuracy at short and long TE. American Journal of Neuroradiology. 2004; 25:1696–1704.

Malinowski ER. Factor Analysis in Chemistry. New York: John Wiley. 2002.

Martinez-Bisbal MC, Marti-Bonmati L, Piquer J, Revert A, Ferrer P, Llacer JL, Piotto M, Assemat O and Celda B. 1H and 13C HR-MAS spectroscopy of intact biopsy samples ex vivo and in vivo 1H MRS study of human high grade gliomas. NMR in Biomedicine. 2004; 17(4):191-205.

Martinez-Bisbal MC, Esteve V, Martinez-Granados B, Cerda M and Celda B. Magnetic resonance microscopy contribution to interpret high-resolution magic angle spinning metabolomic data of human tumor tissue. Proceedings of ESMRMB 2008. Available online.

Martinez-Bisbal MC, Esteve V, Martínez-Granados B and Celda B. Magnetic resonance microscopy contribution to interpret high-resolution magic angle spinning metabolomic data of human tumor tissue. Journal of Biomedical Biotechnology. Published online. 2010.

Maruyama I, Sadato N and Waki A. Hyperacute changes in glucose metabolism of brain tumors after stereotactic radiosurgery: a PET study. Journal of Nuclear Medicine. 1999; 40:1085–1090.

Mann PS. Introductory Statistics. 2nd Edition, Wiley.1995 ISBN 0-471-31009-3.

Maudsley AA, Wu Z, Meyerho DJ and Weiner MW. Automated processing for proton spectroscopic imaging using water reference deconvolution. Magnetic Resonance in Medicine. 1994; 31(6):589–595.

Maudsley AA. Spectral lineshape determination by self-deconvolution. Journal of Magnetic Resonance. B. 1995; 106(1):47–57.

Mandelshtam VA, Taylor HS and Shaka AJ. Application of the filter diagonalization method to one- and two-dimensional NMR spectra, Journal of Magnetic Resonance. 1998; 133:304–312.

Manton DJ, Lowry M, Blackband SJ and Horsman A. Determination of proton metabolite concentrations and relaxation parameters in normal human brain and intracranial tumours. NMR Biomed. 1995; 8:104–112.

Marion D, Ikura M and Bax A. Improved solvent suppression in one- and twodimensional NMR spectra by convolution of time-domain data. Journal of Magnetic Resonances.1989; 84:425–30.

McKnight TR, Lamborn KR, Love TD, Berger MS, Chang S, Dillon WP, Bollen A, Nelson SJ. Correlation of magnetic resonance spectroscopic and growth characteristics within grades II and III gliomas. Journal of Neurosurgery. 2007; 106:660–666.

McKnight TR. Proton magnetic resonance spectroscopic evaluation of brain tumor metabolism. Seminars in Oncology. 2004; 31:605-617.

McGowan PE, Reglinski J, Wilson R., Walker JJ, Wisdoms S and McKillop JH. Journal of Pharmaceutical and Biomedical Analysis. 1993; 11:629-632.

McGowan PE, Lawrie WC, Reglinski J, Spickett CM, Wilson R, Walker JJ, Wisdom S, Maclean MAH. NMR as a noninvasive probe of amniotic fluid in insulin dependant diabetes mellitus. Journal of Perinatal Medicine. 1999; 27(5): 404–408.

Meyer R, Fisher M, Nelson S and Brown T. Evaluation of manual methods for integration of in vivo phosphorus NMR spectra. NMR in Biomedicine. 1988; 1(3): 131–135.

Menze BH, Lichy MP, Bachert P, Kelm BM, Schlemmer HP and Hamprecht FA. Optimal classification of long echo time in vivo magnetic resonance spectra in the detection of recurrent brain tumors, NMR Biomed. 2006; 19:599–609.

Mierisová S and Ala-Korpela M. MR spectroscopy quantitation: a review of frequency domain methods. NMR Biomed. 2001; 14: 247–259.

Morris GA. Compensation of instrumental imperfections by deconvolution using an internal reference signal. J. Magn. Reson. 1988; 80:547–552.

Morris GA, Barjat H and Horne TJ. Reference deconvolution methods. Progress in Nuclear Magnetic Resonance Spectroscopy. 1997; 31:197–257.

Moussaoui S, Brie D, Mohammad-Djafari A and Carteret C. Separation of non-negative mixture of non-negative sources using a Bayesian approach and MCMC sampling. IEEE Transactions on Signal Processing. 2006; 54(11): 4133–4145.

Mukherji S. Clinical Applications of Magnetic Resonance Spectroscopy. Wiley-Liss. 1998.

Mueller-Lisse UG and Scherr MK. Proton MR spectroscopy of the prostate. European Journal of Radiology. 2007; 63(3):351 – 360.

Murphy M, Loosemore A, Clifton A, Howe F, Tate A, Cudlip S, Wilkins P, Griffiths J and Bell B. The contribution of proton magnetic resonance spectroscopy (1H MRS) to clinical brain tumour diagnosis. Magn. Reson. Med. 1993; 30:518–519.

Naressi A, Couturier C, Castang I, De Beer R and Graveron-Demilly D. Java-based graphical user interface for mrui, a software package for quantitation of in vivo/medical magnetic resonance spectroscopy signals. Computers in Biology and Medicine. 2001; 31:269–286.

Nascimento JMP and Dias JMB. Does independent component analysis play a role in unmixing hyperspectral data? IEEE Transactions on Geoscience and Remote Sensing. 2005; 43(1): 175–187.

Negendank WG, Sauter R, Brown TR, Evelhoch JL, Falini A, Gotsis ED, Heerschap A, Kamada K, Lee BC, Mengeot MM, Moser E, Padavic-Shaller KA, Sanders JA, Spraggins TA, Stillman AE, Terwey B, Vogl TJ, Wicklow K and Zimmerman RA. Proton magnetic resonance spectroscopy in patients with glial tumors: a multicenter study. Journal of Neurosurgery. 1996; 84(3):449-58.

Neter J, Kutner MH, Nachtsheim CJ and Wasserman W. Applied linear statistical models. McGraw-Hill, Boston. 1996.

Niesen U, Shah D and Wornell GW. Adaptive alternating minimization algorithms. IEEE Transactions on Information Theory. 2009; 3:1423–1429.

Nuzillard D and Nuzillard JM. Application of blind source separation to 1-D and 2-D nuclear magnetic resonance spectroscopy. IEEE Transactions on Signal Processing. 1998; 5(8):209–211.

Oja E. Nonlinear PCA criterion and maximum likelihood in independent component analysis. In Proceedings of International Workshop on IndependentComponent Analysis and Blind Signal Separation (ICA'99), Aussois, France. 1999; 143-148.

Oja E and Plumbley MD. Blind Separation of Positive Sources by Globally Convergent Gradient Search. Neural Computation. 2004; 16:1811-1825.

Opstad KS, Ladroue C, Bell B.A, Griffiths JR and Howe FA. Linear discriminant analysis of brain tumour 1H MR spectra: a comparison of classification using whole spectra versus metabolite quantification. NMR in Biomedicine. 2007; 20:763–770.

Opstad KS, Bell BA, Griffiths JR and Howe FA. An investigation of human brain tumour lipids by high-resolution magic angle spinning 1H MRS and histological analysis. NMR Biomed 2008a 21(7):677-685.

Opstad KS, Bell BA, Griffiths JR, Howe FA: An assessment of the effects of sample ischaemia and spinning time on the metabolic profile of brain tumour biopsy specimens as determined by high-resolution magic angle spinning (1)H NMR. NMR Biomed 2008b. 21:1138-1147

Opstad KS, Wright AJ, Bell BA, Griffiths JR and Howe FA. Correlations between in vivo (1) H MRS and ex vivo (1) H HRMAS metabolite measurements in adult human gliomas. Journal of Magnetic Resonance Imaging. 2010; 31:289-297.

Oros-Peusquens AM, Laurila M and Shah NJ. Magnetic field dependence of the distribution of NMR relaxation times in the living human brain. MAGMA. 2008; 21:131–147.

Osorio-Garcia MI, Sima DM, Nielsen FU, Himmelreich U and Van Huffel S. Quantification of magnetic resonance spectroscopy signals with lineshape estimation. Journal of Chemometrics. 2011; 25(4):183–192.

Paatero P and Tapper U. Positive matrix factorization: A non-negative factor model with optimal utilization of error estimates of data values. Environmetrics.1994; 5:111–126.

Pauca P, Piper J and Plemmons R. Nonnegative matrix factorization for spectral data analysis. Linear Algebra and Its Applications. 2006; 416(11): 29-47.

Pauca V, Shahnaz F, Berry M, Plemmons R. Text Mining Using Non-Negative Matrix Factorizations. In Proceedings of the 4th SIAM International Conference on Data Mining, Lake Buena Vista, FL. 2004; 22-24.

Pearce JM, Krone JT, Pappas AA and Komoroski RA. Analysis of saturated phosphatidylcholine in amniotic-fluid by P-31 NMR. Magn. Reson. Med. 1993; 30(4):476–484.

Pearson ES. Hartley, H.O. Biometrika Tables for Statisticians.Cambridge. 1970; 1:3.

Pearson K. On Lines and Planes of Closest Fit to Systems of Points in Space (PDF). Philosophical Magazine 1901; 2(6):559–572.

Pels P. Analysis and Improvement of Quantification Algorithms for Magnetic Resonance Spectroscopy. PhD Thesis. Leuven, Belgium. 2005.

Peeling J and Sutherland G. High-resolution 1H NMR spectroscopy studies of extracts of human cerebral neoplasms. Magn Reson Med. 1992; 24:123–136.

Piper J, Pauca VP, Plemmons RJ and Giffin M. Object Characterization from Spectral Data using Nonnegative Factorization and Information Theory. In Proceedings of the AMOS Technical Conference. Maui, Hawaii, USA. September 2004; 1-12.

Pijnappel W, Van den Boogaart A, De Beer R and van Ormondt D. SVD-based quantification of magnetic resonance signals. J. Magn. Reson. 1992; 97:122–134.

Plumbley MD. Adaptive lateral inhibition for nonnegative ICA. In: Proceedings of the

International Conference on Independent Component Analysis and Blind Signal Separation. San Diego, CA. 2001; 516-521.

Plumbley MD. Conditions for nonnegative independent component analysis. SPLetters. June 2002; 9(6): 177-180.

Plumbley MD. Algorithms for Nonnegative Independent Component Analysis. IEEE Transactions on Neural Networks. 2003; 4(3):534-543.

Plumbley MD. Optimization using Fourier expansion over a geodesic for non-negative ICA. In: Proceedings of the International Conference on Independent Component Analysis and Blind Signal Separation (ICA'04).Granada, Spain. 2004a; 49-56.

Plumbley MD and Oja E. A nonnegative PCA algorithm for independent component analysis. IEEE Transactions on Neural Networks. 2004b; 15(1):66 -76.

Podo F. Tumour phospholipid metabolism. NMR Biomed. 1999; 12:413–439.

Poullet JB, Sima DM, Simonetti AW, De Neuter B, Vanhamme L, Lemmerling P and Van Huffel S. An automated quantitation of short echo time MRS spectra in an open source software environment: AQSES. NMR in Biomedicine. 2007a; 20:493-504.

Poullet JB, Martinez-Bisbal MC, Valverde D, Monleon D, Celda B, Arus C and Van Huffel S. Quantification and classification of high-resolution magic angle spinning data for brain tumor diagnosis. In Proceedings of IEEE Engineering in Medicine and Biology Society. 2007b; 5407-5410.

Poullet JB. Quantification and Classification of Magnetic Resonance Spectroscopic Data for Brain Tumor Diagnosis. PhD Thesis. Leuven, Belgium. 2008

Poullet JB, Sima DM and Van Huffel S. Metabolite quantification in MRS and pattern recognition. Encyclopedia of Magnetic Resonance. John Wiley. 2009; 1-9.

Poullet JB, Pintelon R and Van Huffel S. A new FIR filter technique for solvent suppression in MRS signals. Journal of Magnetic Resonance. 2009; 196: 61-73.

Preul M, Caramanos Z, Collins D, Villemure J, Leblanc R, Olivier A, Pokrupa R and Arnold D. Accurate, noninvasive diagnosis of human brain tumors by using magnetic resonance spectroscopy. Nature Medicine. 1996; 2(3):323–325.

Provencher S. Estimation of metabolite concentrations from localized in-vivo proton NMR spectra. Magn. Reson. Med. 1993; 30:672–679.

Provencher SW. Automatic quantitation of localized in vivo 1H spectra with LCModel. NMR

in Biomedicine. 2001; 14:260-264.

Rabeson H, Fauvelle F, Testylier G, Foquin A, Carpentier P, Dorandeu F, van Ormondt D and Graveron-Demilly D. Quantitation with QUEST of brain HRMAS-NMR signals: application to metabolic disorders in experimental epileptic seizures. Magn Reson Med. 2008; 59(6):1266-73.

Ratiney H, Coenradie Y, Cavassila S, van Ormondt D and Graveron-Demilly D. Time-domain quantitation of 1H short echo-time signals: background accommodation. MAGMA. 2004; 16(6):284:296.

Ratiney H, Sdika M, Coenradie Y, Cavassila S, van Ormondt D and Graveron-Demilly D. Time-domain semi-parametric estimation based on a metabolite basis set. NMR Biomed. 2005; 18(1):1-13.

Righi V, Roda JM, Paz J, Mucci A, Tugnoli V, Rodriguez-Tarduchy G, Barrios L, Schenetti L, Cerdan S and Garcia-Martin ML. ^{1}H HR-MAS and genomic analysis of human tumor biopsies discriminate between high and low grade astrocytomas. NMR Biomed. 2009; 22:629-637.

Rosen JE, Costouros NG, Lorang D, BurnsAL, Alexander HR, Skarulis MC, Cochran C, Pingpank JF, Marx SJ, Spiegel AM and Libutti SK. Gland Size Is Associated With Changes in Gene Expression Profiles in Sporadic Parathyroid Adenomas. Annals of Surgical Oncology. 2005; 12(5):412-416.

Ross BD, Ernst T, Kreis R, Haseler LJ, Bayer S, Danielsen E, Blüml S, Shonk T, Mandigo JC, Caton W, Clark C, Jensen SW, Lehman NL,Arcinue E, Pudenz R and Shelden CH. 1H MRS in acute traumatic brain injury. Journal of Magnetic Resonance Imaging. 1998; 8(4):829–840.

Rousseeuw PJ. Silhouettes: a Graphical Aid to the Interpretation and Validation of Cluster Analysis.
Journal of Computational and Applied Mathematics. 1987; 20:53-65.

Rutter A, Hugenholtz H, Saunders JK and Smith ICP. Classification of Brain Tumors by Ex Vivo ^{1}H NMR Spectroscopy. Journal of Neurochemistry. 1995; 64:1655-1661.

Sajda P, Du S, Brown TR, Shungu RSDC, Mao X and Parra LC. Nonnegative matrix factorization for rapid recovery of constituent spectra in magnetic resonance chemical shift imaging of the brain. IEEE Transactions on Medical Imaging. 2004; 23:1453-1465.

Seeger U, Klose U, Lutz O and Grodd W. Elimination of residual lipid contamination in single volume proton MR spectra of human brain. Magn. Reson. Imag. 1999; 17(8):1219-

1226.

Seeger U, Mader I, Naegele T, Grodd W, Lutz O and Klose U. Reliable detection of macromolecules in single-volume 1H NMR spectra of the human brain. Magn. Reson. Med. 2001; 45(6):1522-2594.

Seeger U, Klose U, Mader I, Grodd W, and Naegele T. Parameterized evaluation of macromolecules and lipids in proton MR spectroscopy of brain diseases. Magn. Reson. Med. 2003; 49(1):19–28.

Sen J and Yuntao Q. Constrained Nonnegative Matrix Factorization for Hyperspectral Unmixing. IEEE transactions on geoscience and remote sensing. 2009; 47(1).

Shamir R and Sharan R. Algorithmic approaches to clustering gene expression data. Current Topics in Computational Biology. 2001; 269-300.

Shamir R and Sharan R. Click: A clustering algorithm for gene expression analysis. In Proceedings of the 8th International Conference on Intelligent Systems for Molecular Biology (ISMB ’00). 2000; 8:307-16.

Sima D. Regularization Techniques in Model Fitting and Parameter Estimation, PhD thesis, Faculty of Engineering, K.U.Leuven. Leuven, Belgium. 2006.

Sima DM and Van Huffel S. Separable nonlinear least squares fitting with linear bound constraints and its application in magnetic resonance spectroscopy data quantification. Journal of Computational and Applied Mathematics. 2007; 203:264-278.

Sima D, Osorio Garcia MI, Poullet J, Suvichakorn A, Antoine JP, Van Huffel S and van Ormondt D. Lineshape estimation for Magnetic Resonance Spectroscopy (MRS) signals: self-deconvolution revisited. Measurement Science and Technology. 2009; 20:(10):104031-104043.

Sima DM, Croitor Sava AR and Van Huffel S. Adaptive alternating minimization for fitting magnetic resonance spectroscopic imaging signals. Recent Advances in Optimization and its Applications in Engineering. Springer. 2010; 511-520.

Simonetti AW, Melssen WJ, Szabo de Edelenyi F, van Asten JA, Heerschap A and Buydens LMC. Combination of feature-reduced MR spectroscopic and MR imaging data for improved brain tumor. NMR Biomed. 2005; 18(1):34-43.

Simonetti AW, Melssen WJ, van der Graaf M, Heerschap A and Buydens LMC. A chemometric approach for brain tumor classification using magnetic resonance imaging and spectroscopy. Analytical Chemistry. 2003; 75:5352–5361.

Sims CJ, Fujito DT, Burholt DR, Dadok J and Wilkinson DA. Comparison of metabolite levels in second and third trimester human amniotic fluid samples using proton magnetic resonance spectroscopy. Journal of J Matern Fetal Invest. 1996; 6(2):62–66.

Slotboom J, Boesch C and Kreis R. Versatile frequency domain fitting using time domain models and prior knowledge. Magn Reson Med. 1998; 39:899 –911.

Smith SA, Levante TO, Meier BH and Ernst RR. Computer simulations in magnetic resonance. An object-oriented programming approach. J. Magn. Reson. A. 1994; 106:75–105.

Smith I and Stewart L. Magnetic resonance spectroscopy in medicine: clinical impact. Progress in Nuclear Magnetic Resonance Spectroscopy .2002; 40:1–34.

Sodano P and Delepierre M. Binomial frequency response to non-binomial pulse sequences for efficient water suppression. Journal of Biomolecular NMR. 1993; 3:471–7.

Soher BJ, Young K and Maudsley AA. Representation of strong baseline contributions in 1H MR spectra. Magnetic Resonance in Medicine. 2001; 45:966–972.

Stadlbauer A, Moser E, Gruber S, Buslei R, Nimsky C, Fahlbusch R and Ganslandt O. Improved delineation of brain tumors: an automated method for segmentation based on pathologic changes of 1H-MRSI metabolites in gliomas. NeuroImage. 2004; 23:454-461.

Stadlbauer A, Gruber S, Nimsky C, Fahlbusch R, Hammen T, Buslei R, Tomandl B, Moser E and Ganslandt O. Preoperative grading of gliomas by using metabolite quantification with high-spatial-resolution proton MR spectroscopic imaging. Radiology. 2006; 238(3):958-69.

Stephenson DS and Binsch G. Automated analysis of high-resolution NMR spectra. II. Illustrative applications of the computer program DAVINS. J.Magn. Reson.1980; 37:409–30.

Stoica P, Sandgren N, Selén Y, Vanhamme L and Van Huffel S.. Frequency domain method based on the singular value decomposition for frequency-selective NMR spectroscopy. J. Magn. Reson.2003; 165:80–8.

Strehl AJ. Relationship-based Clustering and Cluster Ensembles for High-dimensional Data Mining. Ph.D thesis. Austin, 2002.

Strehl AJ. Ghosh J. Relationship-based Clustering and visualization for High-dimensional Data Mining. 2002. INFORMS Journal on Computing.Spring. 2003; 15(2):208-230.

Sturm JF. Using SeDuMi 1.02, a MATLAB toolbox for optimization over symmetric cones. Optimization Methods and Software. 1999; 11-12: 625–653.

Sundin T, Vanhamme L, Van Hecke P, Ioannis Dologlou I and Van Huffel S. Accurate

quantification of 1H spectra: From finite impulse response filter design for solvent suppression to parameter estimation. J. Magn. Reson.1999; 139:189–204.

Su Y, Thakur SB, Karimi S, Du S, Sajda P, Huang W and Parra LC. Spectrum separation resolves partial-volume effect of MRSI as demonstrated on brain tumor scans. NMR Biomed. 2008; 21:1030–1042.

Szabo de Edelenyi F, Rubin C, Esteve F, Grand S, Decorps M, Lefournier V, Le Bas JF and Remy C. A new approach for analyzing proton magnetic resonance spectroscopic images of brain tumors: nosologic images. Nature Medicine. 2000; 6:1287–1289.

Szabo De Edelenyi F, Simonetti AW, Postma G, Huo R and Buydens LMC. Application of independent component analysis to 1H MR spectroscopic imaging exams of brain tumours. Analytica Chimica Acta. 2005; 544(1-2):36-46.

Tate A, Crabb S, Griffith J, Howells S, Mazucco R, Rodrigues L and Watson D. Lipid Metabolite Peaks in Pattern Recognition Analysis of Tumour in vivo MR Spectra. Anticancer Research 1996; 16:1575–1580.

Tate A, Griffiths J, Martinez-Perez, Moreno I, Barba A, Cabanas I, Watson M, Alonso D, Bartumeus J, Isamat F, Ferrer F, Villa I, Ferrer F, Capdevila E and Arus C. Towards a method for automated classification of 1H MRS spectra from brain tumours. NMR Biomedicine. 1998; 11:177–191.

Tate A, Majos C, Moreno A, Howe F, Griffiths J and Arus C. Automated classification of short echo time in in vivo 1H brain tumor spectra: a multicenter study. Magn. Reson. Med. 2003; 49:29–36.

Tavazoie S, Hughes JD, Campbell MJ, Cho RJ and Church GM. Systematic determination of genetic network architecture. Nature Genetics. 1999; 22:281-285.

Tedeschi G, Lundbom N, Raman R, Bonavita S, Duyn JH, AlgerJR and Di C. Increased choline signal coinciding with malignant degeneration of cerebral gliomas: a serial proton magnetic resonance spectroscopy imaging study. Journal of Neurosurgery. 1997; 87:516–524.

Tong Z, Yamaki T, Harada K and Houkin K. In vivo quantification of the metabolites in normal brain and brain tumors by proton MR spectroscopy using water as an internal standard. Magnetic Resonance Imaging. 2004; 22:735–742.

Tugnoli V, Schenetti L, Mucci A, Parenti F, Cagnoli R, Righi V, Trinchero A, Nocetti L, Toraci C, Mavilla L, Trentini G, Zunarelli E and Tosi MR. Ex vivo HR-MAS MRS of human meningiomas: a comparison with in vivo ^{1}H MR spectra. International Journal of Molecular Medicine. 2006; 18:859–869.

Tukey JW. Comparing individual means in the analysis of variance. Biometrics 1949; 5:99–114.

Tukey J W. Box-and-Whisker Plots. Exploratory Data Analysis. 1977; 39-43.

Tzika AA, Astrakas L, Cao H, Mintzopoulos D, Andronesi OC, Mindrinos M, Zhang J, Rahme LG, Blekas KD, Likas AC, Galatsanos NP, Carroll RS and Black PM. Combination of high-resolution magic angle spinning proton magnetic resonance spectroscopy and microscale genomics to type brain tumor biopsies. International Journal of Molecular Medicine. 2007; 20(2):199-208.

Upton G and Cook I . Understanding Statistics. Oxford University Press. 1996. ISBN 0199143919.

Usenius JP, Tuohimetsa S, Vainio P, Ala-Korpela M, Hiltunen Y and Kauppine R. Automated classification of human brain tumours by neural network analysis using in vivo 1H magnetic resonance spectroscopic metabolite phenotypes. Neuroreport. 1996; 7(10):1597–1600.

.

Usenius JP, Vainio P, Hernesniemi J and Kauppinen RA. Choline containing compounds in human astrocytomas studied by 1H NMR spectroscopy in vivo and in vitro. Journal of Neurochemistry. 1994; 63:1538–1543.

Van der Veen WC, De Beer WC, Luyten PR and van Ormondt D. Accurate quantification of in vivo 31P NMR signals using the variable projection method and prior knowledge. Magnetic Resonance in Medicine. 2005; 6:92-98.

Vanhamme L, Van den Boogaart A and Van Huffel S. Improved Method for Accurate and Efficient Quantification of MRS Data with Use of Prior Knowledge. Journal of Magnetic Resonance. 1997; 129:35-43.

Vanhamme L, Van Huffel S, Van Hecke P and van Ormondt D. Time domain quantification of series of biomedical magnetic resonance spectroscopy signals. Journal of Magnetic Resonance. 1999; 140:120-130.

Vapnik VN. Statistical Learning Theory. Wiley, New York. 1998.

Young K, Soher BJ, and Maudsley AA. Automated spectral analysis II: application of wavelet shrinkage for characterization of non-parameterized signals. Magn. Reson. Med. 1998; 40:816–21.

Yuan Z and Oja E. A FastICA Algorithm for Nonnegative Independent Component Analysis. In Proceedings of the Fifth International Symposium on Independent Component Analysis and Blind Signal Separation (ICA 2004) Granada, Spain, 2004; 1-8.

Yuan Z. Advances in independent component analysis and nonnegative matrix factorization. PhD thesis. Helsinki University of Technology. Espoo, Finland. 2009.

Waters NJ, Garrod S, Farrant RD, Haselden JN, Connor SC, Connelly J, Lindon JC, Holmes E and Nicholson JK. High-Resolution Magic Angle Spinning ^{1}H NMR Spectroscopy of Intact Liver and Kidney: Optimization of Sample Preparation Procedures and Biochemical Stability of Tissue during Spectral Acquisition. Analytical Bio. 2000; 16-23.

Wang Y, Jiar Y, Hu C and Turk M. Fisher non-negative matrix factorization for learning local features. In: Asian Conference on Computer Vision. Korea. 2004; 27-30.

Webb P, Spielman D and Macovski A. Inhomogeneity correction for in vivo spectroscopy by high-resolution water referencing. Magn. Reson. Med. 1992; 23(1):1–11.

Wehrens R, Simonetti AW and Buydens LMC. Mixture modelling of medical magnetic resonance data. Journal of Chemometrics. 2002; 16:274–282.

Weston J and Watkins DC. Multi-class support vector machines. ESANN'99, Brussels. D-Facto publications. 1999.

Williamson DC, Hawesa H, Thacker NA and Williams SR. Robust quantification of short echo time 1H magnetic resonance spectra using the Pad´e approximant. Magn. Reson. Med. 2006; 55:762–771.

Wild S, Curry J and Dougherty A. Motivating Non-Negative Matrix Factorizations. In: Proceedings of the Eighth SIAM Conference on Applied Linear Algebra. July 2003; 15-19.

Wright AJ, Fellows G, Byrnes TJ, Opstad KS, McIntyre DJ, Griffiths JR, Bell BA, Clark CA, Barrick TR, Howe FA. Pattern recognition of MRSI data shows regions of glioma growth that agree with DTI markers of brain tumor infiltration. Magn Reson Med. 2009; 62(6):1646-51.

Wright AJ, Fellows GA, Griffiths JR, Wilson M, Bell BA; Howe FA. Ex-vivo HRMAS of adult brain tumours: metabolite quantification and assignment of tumour biomarkers. Molecular cancer. 2010: 9: 66. Published online

Zheng CH, Huang DS, Sun ZL, Lyu MR and Lok TM. Nonnegative independent component analysis based on minimizing mutual information technique. Neurocomputing.2006; 69: 878 – 883.

Zhu X, Schuff N, Kornak J, Soher B, Yaffe K, Kramer JH, Ezekiel F, Miller BL, Jagust WJ and Weiner MW. Effects of alzheimer disease on fronto-parietal brain n-acetyl aspartate and

myo-inositol using magnetic resonance spectroscopic imaging. Alzheimer Disease & Associated Disorders. 2006; 20:7785.

Publications list

Awards

1. Young scientist award for the best oral-poster presentation.
   Award received at the 6th European Symposium on Biomedical Engineering (ESMBE 2008), Chania, Greece for the work "Data Fusion of HR-MAS and in-vivo Information with Application in Brain Tumor Recognition" by Croitor Sava AR, Laudadio T, Poullet JB, Monleon D, Martinez-Bisbal MC, Celda B, Van Huffel S.

Papers in international journals and book chapters

2. Sima DM, Croitor Sava AR and Van Huffel S. Adaptive alternating minimization for fitting magnetic resonance spectroscopic imaging signals. Recent Advances in Optimization and its Applications in Engineering. Springer. 2010; 511-520.

3. Croitor Sava AR, Sima DM, Poullet JB, Wright AJ, Heerschap A and Van Huffel S. Exploiting spatial information to estimate metabolite levels in two-dimensional MRSI of heterogeneous brain lesions. NMR in Biomedicine. 2011; 24(7):824-835.

4. Croitor Sava AR, Martinez-Bisbal MC, Van Huffel S, Cerda JM, Sima DM and Celda B. Ex Vivo High Resolution Magic Angle Spinning Metabolic Profiles describe intratumoral histopathological tissue properties in adult human gliomas. Magnetic Resonance in Medicine. 2011; 65:320-328.

5. Croitor Sava AR, Martinez-Bisbal MC, Laudadio T, Piquer J, Celda B, Heerschap A. and Van Huffel S. Fusing in vivo and ex vivo NMR sources of information for brain tumor classification. Accepted for publication in Measurement Science and Technology. 2011. ePub ahead of print.

6. Osorio Garcia MI, Croitor Sava AR, Sima DM, Nielsen FU, Himmelreich U and Van Huffel S. Quantification improvements of 1H MRS signals. Accepted for publication in Magnetic Resonance Spectroscopy. ISBN 978-953-307-771-0.

Papers in proceedings of (inter)national conferences

7. Croitor Sava AR, Laudadio T, Poullet JB, Monleon D, Martinez-Bisbal MC, Celda B and Van Huffel S. Combining HR-MAS and In Vivo MRI and MRSI Information for Robust Brain Tumor Recognition. In Proc. of the 4th European Conference of the International Federation for Medical and Biological Engineering (ECIFMBE

2008). Antwerp, Belgium. 2008: 340-343.

8. Croitor Sava AR, Laudadio T, Poullet JB, Monleon D, Martinez-Bisbal MC, Celda B, Van Huffel S. Data Fusion of HR-MAS and in-vivo Information with Application in Brain Tumor Recognition. In Proc. of the 6th European Symposium on Biomedical Engineering (ESMBE 2008), Chania, Greece. 2008:1-4.

9. Croitor Sava AR, Laudadio T, Sima DM, Osorio-Garcia MI, Martinez-Bisbal MC, Celda B, Heerschap A and Van Huffel S. Incorporating in vivo and ex vivo NMR sources of information for modeling robust brain tumor classifiers. Proc. IEEE workshop on Imaging Systems and Techniques (IST 2010), Thessaloniki, Greece. 2010; 353 - 356.

10. Croitor Sava AR, Sima DM, Martinez-Bisbal MC, Celda B and Van Huffel S. Non-negative blind source separation techniques for tumor tissue typing using HR-MAS signals. In Proc. of the 32nd Annual International Conference of the IEEE Engineering in Medicine and Biology Society (IEEE EMB). Buenos Aires, Argentina. 2011: 3658-3661.

Abstracts for (inter)national conferences

11. Croitor Sava AR, Laudadio T, Poullet JB and Van Huffel S. Data fusion of HR-MAS and in-vivo information with application in brain tumor recognition. 25th Annual Meeting of the European Society for Magnetic Resonance in Medicine and Biology 2008 (ESMRMB). Valencia, Spain. October, 2008.

12. Croitor Sava AR, Sima D, Poullet JB and Van Huffel S. Exploiting Spatial Information for Estimating Metabolite Concentration in MRSI. 17th Annual meeting & Exhibition of the International Society for Magnetic Resonance in Medicine (ISMRM) 2009. Honolulu, Hawai. Apr 2009.

13. Croitor Sava AR, Martinez-Bisdal MC, Celda B, Cerda JM and Van Huffel S. Tissue typing within glial tumours. 26th Annual Meeting of the European Society for Magnetic Resonance in Medicine and Biology 2008 (ESMRMB). Antalya, Turkey. Oct. 2009.

14. Croitor Sava AR, Sima D, Poullet JB, A. Heerschap and Van Huffel S. Improved quantification of MRSI data using spatial constraints. 26th Annual Meeting of the European Society for Magnetic Resonance in Medicine and Biology 2008 (ESMRMB). Antalya, Turkey. Oct. 2009.

15. Croitor Sava AR, Sima DM, Celda B and Van Huffel S. Non-Negative Matrix Factorization for MRS data analysis. Leuven Statistical day 2010, Leuven, Belgium. May, 2010.

16. Croitor Sava AR, Martinez-Bisdal MC, Celda B and Van Huffel S. Identifying constituent tumor tissue subclasses in HR-MAS spectra using advanced blind source separation techniques. 18th Annual meeting & Exhibition of the International Society for Magnetic Resonance in Medicine (ISMRM) 2011. ISMRM-ESMRMB, Stockholm, Sweden. May, 2010.

17. Croitor Sava AR, Sima DM, Celda B and Van Huffel S. Tumour tissue typing in HR-MAS spectra using blind source separation techniques. 2nd Annual meeting of the Benelux ISMRM chapter. Utrecht, Netherlands. Jan. 2010.

18. Croitor Sava AR, Celda B, Sima DM, Li Y and Van Huffel S. Non-negative matrix factorization for high resolution magic angle spinning data analysis. National day on Biomedical Engineering. Brussels, Belgium. Nov. 2010.

19. Croitor Sava AR, Van Cauter S, Sima DM, Osorio Garcia M, Himmelreich U and Van Huffel. S. Non-negative blind source separation techniques for describing intratumoral histopathological tissue properties within MRSI measurements. 3rd Annual meeting of the Benelux ISMRM chapter, Hoeven, The Netherlands. January, 2011.

20. Croitor Sava AR, Beck V, Sandaite I, Deprest J, Claus F, Van Huffel S and Himmelreich U. High resolution ^{1}H NMR spectroscopy successfully discriminates fetuses with congenital diaphragmatic hernia from normal pregnancies. 3rd Annual meeting of the Benelux ISMRM chapter, Hoeven, The Netherlands. January, 2011.

21. Croitor Sava AR, Van Cauter S, Sima DM, Osorio Garcia M, Himmelreich U and Van Huffel. Non-negative blind source separation techniques for describing intratumoral histopathological tissue properties within MRSI measurements. 19th Annual meeting & Exhibition of the International Society for Magnetic Resonance in Medicine (ISMRM). Montreal, Quebec, Canada. May, 2011.

22. Croitor Sava AR, Beck V, Sandaite I, Deprest J, Claus F, Van Huffel S and Himmelreich U. High resolution ^{1}H NMR spectroscopy successfully discriminates fetuses with congenital diaphragmatic hernia from normal pregnancies. 19th Annual meeting & Exhibition of the International Society for Magnetic Resonance in Medicine (ISMRM). Montreal, Quebec, Canada. May, 2011.

Submitted papers

23. Croitor Sava AR, Martinez-Bisbal MC, Sima DM, Calvar J, Esteve V, Celda B and Van Huffel S. Quantifying brain tumor tissue abundance in HR-MAS spectra using non-negative blind source separation techniques. Submitted to the Journal of chemometrics. August 2011.

Curriculum vitae

Anca Ramona Croitor Sava was born on 14th of April 1980, in Suceava, Romania. In June 2004 she received the degree in engineering in electronics and telecommunications from the Polytechnic University Timisora, Romania. Her thesis was a joint study with the Technical Institute Oulu, Finland where she participated in an Erasmus exchange program (January-May 2004). In June 2007 she received the master degree in computer science from the West University, Timisoara, Romania.

In August 2007 she joined the research group BIOMED at the Department of Electrical Engineering (ESAT), Katholieke Universiteit Leuven, Belgium under the supervision of Sabine Van Huffel. Here she was involved in Health Agents IST–2004–27214), ETumour (FP6-2002-LIFESCIHEALTH-503094) and FAST (MRTN-CT-2006-035801) European projects. She mainly worked on the development of advanced methods for the interpretation and preprocessing of magnetic resonance (MR) data as well as for developing advanced classifiers with adaptive learning abilities combining segmentation, signal processing and pattern recognition with application in diagnosis, prognosis and treatment selection of adult's brain tumor as well as the prediction of certain complicated pregnancies using NMR techniques.